THE OXIDATION BEHAVIOUR OF SINTERED IRON

IAN ALASTAIR BRUCE

Doctor of Philosophy

THE UNIVERSITY OF ASTON IN BIRMINGHAM

February 1991

THE OXIDATION BEHAVIOUR OF SINTERED IRON

Ian Alastair Bruce

Doctor of Philosophy
February 1991

THESIS SUMMARY

The oxidation behaviour of porous, sintered iron was studied by thermo-gravimetric analysis (TGA), at temperatures between 300°C and 700°C, in a flowing atmosphere of $20\%O_2/80\%N_2$. Samples for TGA tests were compacted from pure iron powder, at 150MPa to 550MPa, and vacuum sintered at 1120°C. The mass gain of samples during oxidation was recorded continuously for a period of 24 hours.

It was found that the oxidation mass gain of PM samples depended on the permeability of the pore structure and the temperature. At low temperatures, the oxidising gas was able to permeate through the pore structure, causing the oxidation of a large active surface area. At high temperatures the active surface area was smaller, because oxygen diffusing into the pore structure, from the external atmosphere, was adsorbed by pore surfaces close to the external surface of the compact. Although the weight of the external oxide scale on compacts increased with increasing oxidation temperature, the absence of oxide in the core porosity in compacts oxidised at higher temperatures resulted in smaller mass gains than were observed for compacts oxidised at lower temperatures.

The heat generated by the oxidation of the large active surface areas of porous samples was studied by thermo-calorimetric analysis (TCA). It was determined that this phenomenon could raise the core temperature of samples significantly above the ambient furnace temperature, affecting the morphology of the oxide scale formed.

The effects (on oxidation behaviour at 500°C) of small, elemental alloy additions of Al, Cu, P and Si to pure iron powder were studied. It was found that elements that promote pore rounding during sintering caused a significant reduction in the mass gain rate of the PM alloys, compared to the PM pure iron. The oxidation resistance due to these elements prevented pore closure by oxide growth, so that the active surface area of these PM alloys remained high. The PM alloys were also studied by thermo-mechanical analysis (TMA, dilatometry), to determine their dimensional stability during sintering and subsequent elevated temperature service.

The oxidation experiment was augmented with optical and electron microscopy, and X-ray analysis of alloy and scale compositions.

KEY WORDS:
OXIDATION IRON POWDER_METALLURGY PERMEABILITY

ACKNOWLEDGEMENTS

I would like to thank Mr. Len Crane, my Supervisor, for his help and support during the writing of this thesis. I am grateful to Backer Electric CO. Ltd., of Rotherham, for their financial support, and to Aluminium Corporation Ltd, of Dolgarrog in North Wales, who gave me the time to finish writing-up.

There are a lot of people who have earned a lot of my gratitude for their help and friendship whilst I was working on this thesis. I hope I will not offend any of those friends, if I single-out, for special mention, Cathy Hollis.

CONTENTS

TABLES

FIGURES

PLATES

Section 1
INTRODUCTION

Powder metallurgy (PM) is a relatively recent manufacturing technology, the bulk of its development having occurred since the 1920's. The global market for net or near-net shape PM components is now in excess of $5 billion, with a growth rate between 8 and 12 per cent annually [1].

Towards the end of 1984, Backer Electric Co. Ltd., of Rotherham, were developing a sintered, porous iron, electric hot plate for use on domestic cookers and hobs. The hot plate was compacted using a novel technique, in which an electric heating element was embedded within the iron powder mass, before sintering as a near net-shaped component. Life testing of experimental hot plates, at heating-element temperatures of 300°C to 700°C, revealed problems with the oxidation of the porous iron mass, which led to the failure of components by cracking. Backer Electric approached Mr. L. W. Crane, Aston University, for a solution to this problem. It became apparent that very little was known about the oxidation behaviour of PM iron

A research project was planned, to study the factors affecting, and the kinetics of the oxidation of sintered porous iron. The main experiment would be thermo-gravimetric analysis, to examine the way in which the mass of samples changes as they are oxidised. Initially, samples compacted of pure iron powder would be studied, to establish the basic processes involved. The next stage would investigate how alloying the pure iron powder could be used to control the oxidation of PM samples.

Combined with this experiment would be the study of the microstructures of samples, both unoxidised and oxidised, using optical and electron microscopy. X-ray analysis and X-ray diffraction techniques would be used to determine the phases produced by sintering and oxidising powder alloys.

The goal of the research was to gain sufficient scientific understanding to be able to determine an iron-based PM alloy composition, that could be used for the manufacture

of the electric hot plate. The properties required of this alloy were resistance to oxidation, combined with dimensional stability during sintering and subsequent elevated temperature service. Therefore, a thermo-mechanical analysis experiment, using a dilatometer, was also planned, to study the dimensional stability of alloys developed in the thermo-gravimetry experiment.

Section 2
OXIDATION THEORY
Literature Review

Metals generally occur naturally in the oxidised state, and usually have to be reduced to the metallic state to be of technological value. In contact with oxidising elements during service, metallic components will tend to revert to the oxidised state, usually with detrimental effects for their designed purpose.

The most common oxidising element is oxygen, which makes up about 23% (by mass) of the Earth's atmosphere, 86% of the hydrosphere and 50% of the crust [2].

This chapter considers the oxidation of solid metallic surfaces exposed to an atmosphere in which oxygen is the only reactive agent (in practice, the process is complicated by the presence of other oxidising agents, such as sulphur and chlorine).

2.1 INITIAL PHENOMENA

The first stage in the oxidation of a clean metal surface is the bonding of oxygen to the metal surface, by the process of adsorption, to form a two-dimensional oxide film. This process eventually leads to the nucleation of a three-dimensional oxide scale.

2.1.1 Adsorption

Adsorption occurs in two phases, firstly physical bonding ('physisorption') due to the Van der Waals force, and secondly chemical bonding ('chemisorption') of the oxidative gas atoms, following dissociation of their parent molecules. Chemisorption requires the ionisation of the adsorbed species, which occurs by the transfer of electrons from the metal. Figure 2.1 illustrates the energies associated with these two processes.

Physisorption requires no activation energy, and proceeds as fast as gas molecules (both reactive and inert) impinge on the surface. The equilibrium rest position of

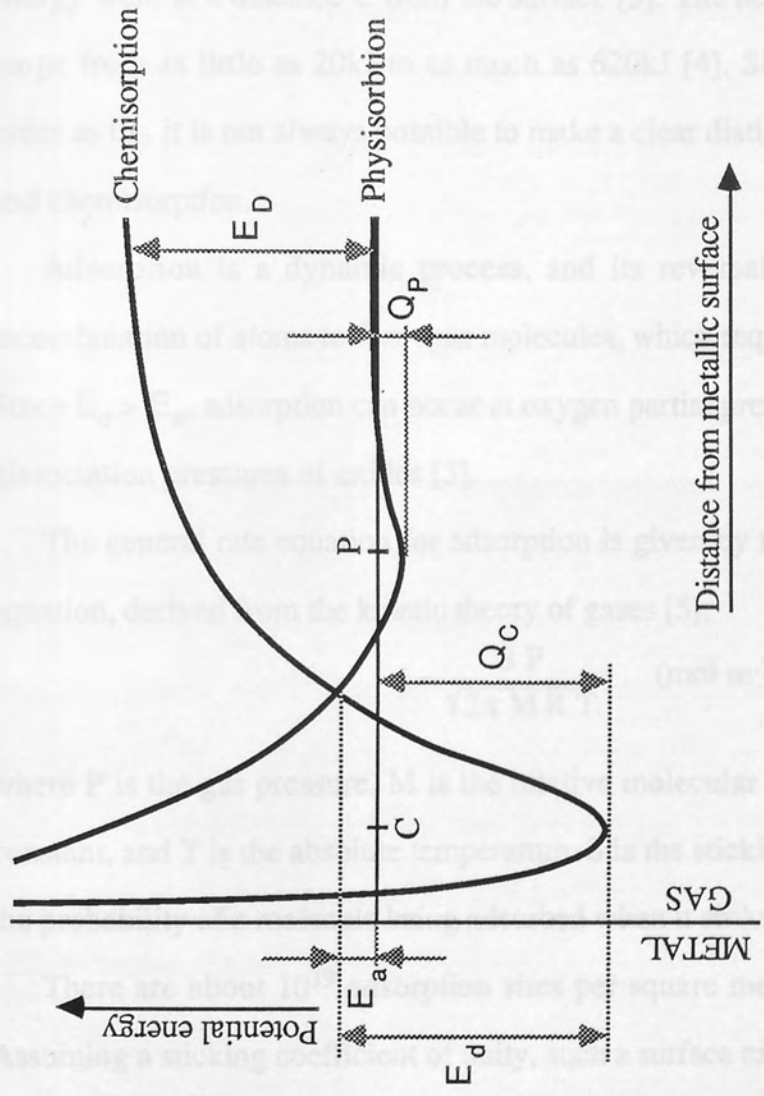

Figure 2.1. Potential energy wells associated with adsorption on a metal surface.

physisorbed molecules is at the bottom of a potential energy well, at a distance P from the surface [3]. The the heat of physisorption, Q_P, rarely exceeds 20kJ [4].

The energy required for dissociation, characterised by the magnitude of E_D, decreases as the gas molecules approach the surface. Chemisorption of the dissociated atoms may require an activation energy E_a, so it tends to be slower than physisorption. The equilibrium rest position of chemisorbed atoms is at the bottom of a potential energy well, at a distance C from the surface [3]. The heat of chemisorption, Q_C, can range from as little as 20kJ to as much as 620kJ [4]. Since Q_C may be of the same order as Q_P it is not always possible to make a clear distinction between physisorption and chemisorption.

Adsorption is a dynamic process, and its reversal, desorption, occurs by the recombination of atoms to form gas molecules, which requires an activation energy E_d. Since $E_d > E_a$, adsorption can occur at oxygen partial pressures significantly below the dissociation pressures of oxides [5].

The general rate equation for adsorption is given by the Hertz-Knudsen-Langmuir equation, derived from the kinetic theory of gases [5],

$$j = \frac{S\,P}{\sqrt{2\pi\,M\,R\,T}} \quad (\text{mol m}^{-2}\,\text{s}^{-1}) \qquad \text{Eq. 2.1}$$

where P is the gas pressure, M is the relative molecular mass of the gas, R is the gas constant, and T is the absolute temperature. S is the sticking coefficient, and represents the probability of a molecule being adsorbed when it strikes the surface [3].

There are about 10^{19} adsorption sites per square metre of a clean metal surface. Assuming a sticking coefficient of unity, such a surface exposed to gaseous oxygen at a pressure of $0.2\text{x}10^5$Pa at 293K would form a monolayer of adsorbed oxygen in about 9ps. In practice, the sticking coefficient will be less than unity because not every incident molecule can be adsorbed, and it will further decrease during the reaction as the number of vacant adsorption sites is reduced.

The adsorption stage of oxidation comes to an end when the metal surface is

completely saturated with oxygen, and a monolayer of adsorbed atoms has formed. Formation of the monolayer can be delayed or prevented by solution of oxygen in the metal. Most pure metals do not dissolve large amounts of oxygen, so that generally this effect can be neglected, though the presence of impurities and alloying elements can significantly modify this state of affairs [6].

2.1.2 Two-Dimensional Oxide Films

The layer formed by adsorption has a thickness that is unlikely to exceed one atomic diameter, and so may be considered in terms of only two spatial dimensions [7]. Adsorption at one site wholly or partly inhibits adsorption on adjacent sites, giving the layer a periodic structure [3, 8], although this bears little relation to the structure of the oxide film formed subsequently [7].

There is evidence that layers several atoms thick can be formed without the nucleation of three-dimensional oxide [9]. Multi-layer formation requires the exposure of metal ions at the surface as fresh adsorption sites, and usually starts before completion of the mono-layer. This is brought about by the place-exchange of oxygen and metal ions, and may be activated by the heat of chemisorption. The continuing high heat of chemisorption during multi-layer formation, suggests that metal ions in the two-dimensional film behave like the original metallic surface [8, 9]. Place-exchange becomes more difficult after completion of a mono-atomic adsorbed layer. Subsequent movement of oxygen ions into the metal will require an activation energy, and so they will remain on the surface for longer [9].

This stage of oxidation, when the oxide exists in two dimensions only, amounts to an incubation period, during which there is some movement of surface atoms, and a few atoms are chemisorbed when restructuring (by place exchange) of the mono-layer permits.

2.1.3 Nucleation of Three-Dimensional Oxide Films

The transition from two-dimensional oxide to the three-dimensional growth of an oxide film, by the apparently random formation of nuclei has yet to be satisfactorily explained, and the nature of the diffusing species remains to be determined. The simplest hypothesis assumes that classical theories of nucleation apply: a three-dimensional nucleus becomes stable when the local concentration of oxygen reaches some critical value [3].

The temperature, gas pressure and atomic structure of the metal are all found to have an effect on the number of nuclei formed, but once created their number appears to remain constant. The presence of surface imperfections appears to have little effect on the formation of nuclei, except at low temperatures, when thermal energy alone is insufficient to activate nucleation. At high temperatures, on the other hand, nucleation has all the characteristics of being homogeneous [7].

When a nucleus appears, the surrounding two-dimensional oxide is destabilised, and there is a continuous movement of matter across the surface towards the centre of growth (Figure 2.2). The removal of oxygen from the zone surrounding each nucleus may explain why the number of nuclei remains approximately constant during their growth, which occurs primarily by surface diffusion [3, 7].

The nucleation stage of oxidation comes to an end when the nuclei have completely covered the metal surface with a thin, continuous three-dimensional oxide film. The metal and atmosphere are now spatially separated by a barrier and the reaction can continue only if ions and electrons are able to migrate through the oxide layer.

2.2 POINT DEFECTS

All metal oxides are ionic, that is, they are composed of metal cations and oxygen anions bonded together by electrostatic attraction, to form a three-dimensional lattice. The electrostatic repulsion between like-charged ions prevents them occupying neighbouring sites, so that the ionic lattice has a periodic structure. Sodium chloride

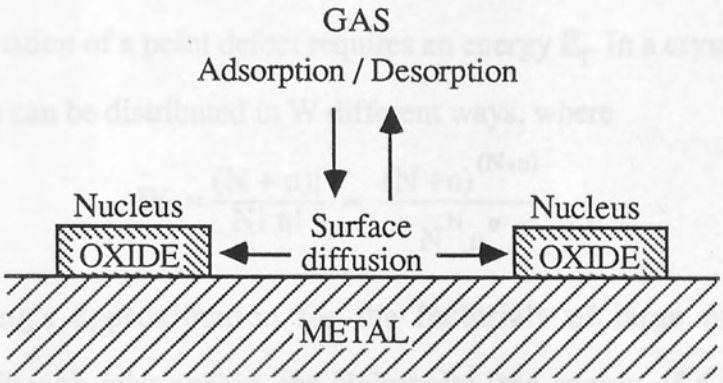

Figure 2.2. Lateral growth of three-dimensional oxide nuclei on a metal surface.

(NaCl) is a common example of the simple cubic ionic structure, with the Na^+ cations and Cl^- anions occupying alternate lattice sites. This periodicity allows the ionic structure to be considered in terms of interpenetrating sub-lattices of anions and cations (Figure 2.3).

Migration of ions through the oxide requires the creation of point defects in the ionic lattice. These point defects can take the form of vacant lattice sites, or interstitial ions occupying a volume in between ions occupying lattice sites. An ion with the requisite energy can exchange places with a neighbouring point defect site in its own sub-lattice. This process is usually considered in terms of the movement of the point defect.

The formation of a point defect requires an energy E_f. In a crystal of $(N + n)$ sites, n point defects can be distributed in W different ways, where

$$W = \frac{(N + n)!}{N!\, n!} \approx \frac{(N+n)^{(N+n)}}{N^N n^n} \qquad \text{Eq. 2.2}$$

using Stirling's approximation for the factorials of large numbers. Using the Boltzmann-Planck relationship, the Helmholtz free energy of a crystal containing n defects, relative to the free energy of the perfect crystal is given by

$$F = dE - T\,dS = n\,E_f - k\,T\,\ln W \qquad \text{Eq. 2.3}$$

at constant temperature and volume. Differentiating,

$$\frac{dF}{dn} = E_f - k\,T\,\ln\left(\frac{(N+n)}{n}\right) \qquad \text{Eq. 2.4}$$

The equilibrium value of n is defined by $dF/dn = 0$. Hence the defect fraction at equilibrium is

$$\frac{n}{N+n} = \exp\left(\frac{-E_f}{k\,T}\right) \qquad \text{Eq. 2.5}$$

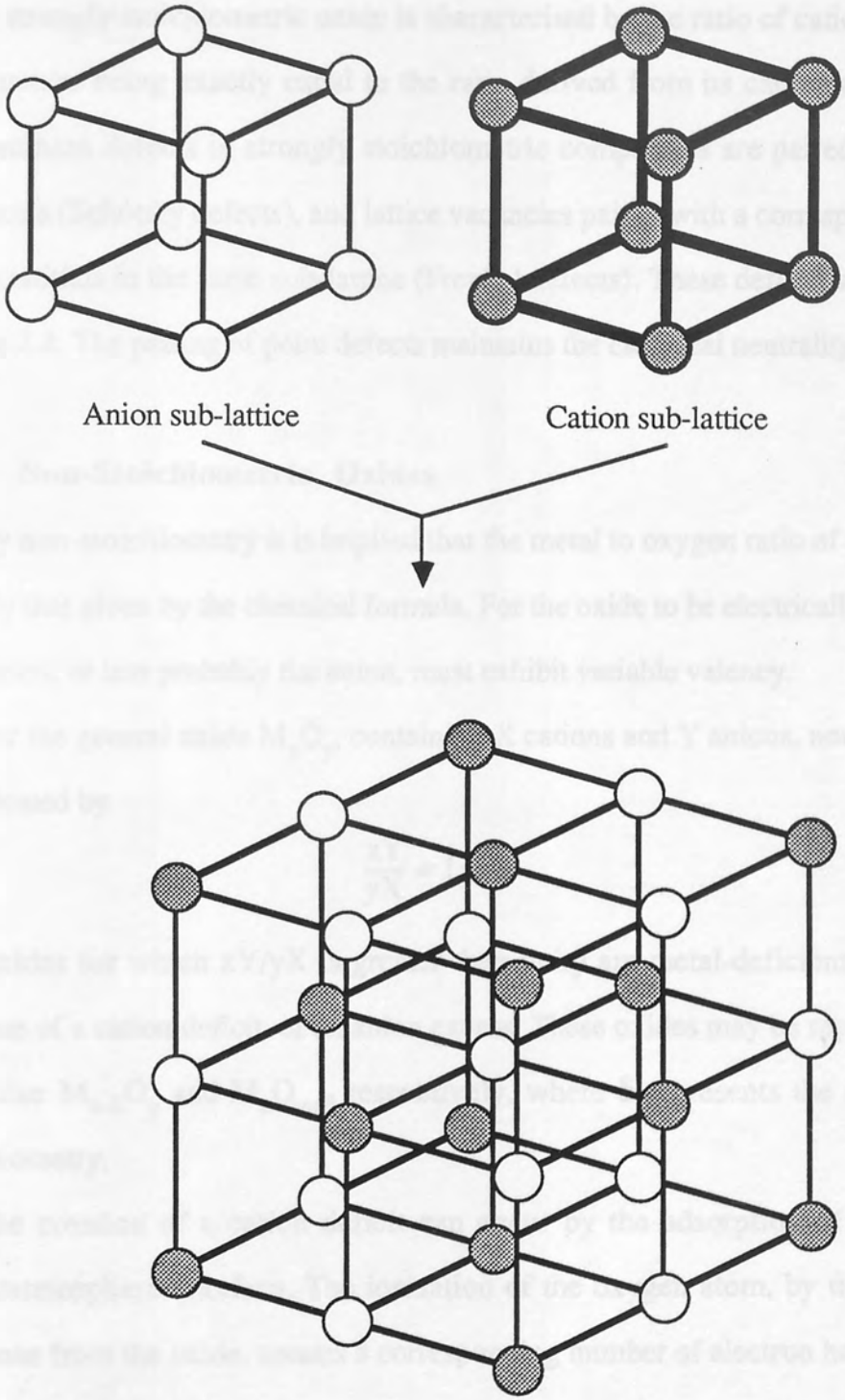

Figure 2.3. Simple cubic ionic lattice, composed of interpenetrating sub-lattices of anions and cations.

2.2.1 Strongly Stoichiometric Oxides

A strongly stoichiometric oxide is characterised by the ratio of cations to anions in its structure being exactly equal to the ratio derived from its chemical formula. The predominant defects in strongly stoichiometric compounds are paired oxygen-metal vacancies (Schottky defects), and lattice vacancies paired with a corresponding number of interstitials in the same sub-lattice (Frenkel defects). These defects are illustrated in Figure 2.4. The pairing of point defects maintains the electrical neutrality of the oxide.

2.2.2 Non-Stoichiometric Oxides

By non-stoichiometry it is implied that the metal to oxygen ratio of the oxide is not exactly that given by the chemical formula. For the oxide to be electrically neutral, either the cation, or less probably the anion, must exhibit variable valency.

For the general oxide M_xO_y, containing X cations and Y anions, non-stoichiometry is indicated by

$$\frac{xY}{yX} \neq 1 \qquad \text{Eq. 2.6}$$

Oxides for which xY/yX is greater than unity are metal-deficient, and can arise because of a cation deficit, or an anion excess. These oxides may be represented by the formulae $M_{x-\delta}O_y$ and $M_xO_{y+\delta}$ respectively, where δ represents the deviation from stoichiometry.

The creation of a cation deficit can occur by the adsorption of oxygen at the oxide/atmosphere interface. The ionisation of the oxygen atom, by the transfer of n electrons from the oxide, creates a corresponding number of electron holes. A vacancy is created on the cation sub-lattice when a metal ion moves out to the surface to partner the oxygen ion. This process can be represented by the equation

$$^1/_2O_2 = O_O + nh^+ + V_M^{n-} \qquad \text{Eq 2.7}$$

where O_O represents an oxygen ion occupying an anion sub-lattice site, V_M represents a vacancy on the cation sub-lattice (carrying an effective charge n-, to preserve electrical

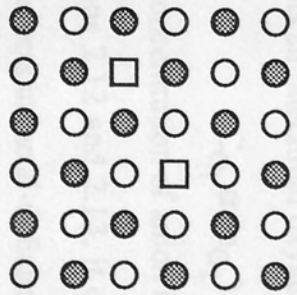

a) Schottky defect
(paired vacancies on the
cation and anion sub-lattices).

Cation

Anion

Vacant lattice site

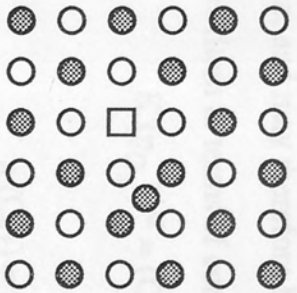

b) Frenkel defect
(cation vacancy paired with
an interstitial cation).

Figure 2.4. Schottky and Frenkel defects.

neutrality) and h^+ is an electron hole. The equilibrium constant, K, for this reaction is given by

$$K\,(p_{O_2})^{1/2} = (a_{h^+})^n\, a_{V_M} \qquad \text{Eq. 2.8}$$

where p_{O_2} is the partial pressure of oxygen in the atmosphere, and a_{h^+} and a_{V_M} are the activities of the electron holes and cation vacancies respectively. These defects are in very dilute solution, and may therefore be assumed to obey Henry's Law. Equation 2.8 can therefore be rewritten in terms of concentrations. Hence,

$$K\,(p_{O_2})^{1/2} = (C_{h^+})^n\, C_{V_M} \qquad \text{Eq. 2.9}$$

Since

$$n\,(C_{h^+}) = C_{V_M} \qquad \text{Eq. 2.10}$$

Equation 2.9 may be rewritten

$$K\,(p_{O_2})^{1/2} = n^n\,(C_{V_M})^{n+1} \qquad \text{Eq. 2.11}$$

Since K and n are constant,

$$C_{V_M} \alpha\, (p_{O_2})^{1/(2(n+1))} \qquad \text{Eq. 2.12}$$

Thus the concentration of vacancies on the cation sub-lattice is proportional to the partial pressure of oxygen.

An oxygen excess can be caused by the creation of oxygen ion interstitials, with the simultaneous creation of a number of electron holes, to preserve electrical neutrality. This may be represented by

$$^1/_2O_2 = O_i + nh^+ \qquad \text{Eq 2.13}$$

where O_i represents an interstitial oxygen ion. Hence,

$$C_{O_i} \alpha\, (p_{O_2})^{1/(2(n+1))} \qquad \text{Eq. 2.14}$$

where C_{O_i} is the concentration of anion interstitials.

From Equations 2.12 and 2.13, it can be seen that, at constant temperature, the number of point defects in metal-deficient oxides falls, as the partial pressure of oxygen in the atmosphere is decreased.

Oxides for which xY/yX (Eq. 2.6) is less than unity are oxygen-deficient, and may be due to an anion deficit, or a cation excess. These oxides may be represented by the formulae $M_{x+\delta}O_y$ and $M_xO_{y-\delta}$ respectively.

An anion deficit can arise through the desorption of an oxygen ion, creating a vacancy on the oxygen sub-lattice, V_O. This may be represented by

$$O_O = V_O^{n+} + ne^- + {}^1/_2O_2 \qquad \text{Eq 2.15}$$

where e^- represents a quasi-free electron; these electrons are not free in the sense of free electrons in metals, but may be transferred between oxygen vacancies, captured by cations, or used to ionise a newly-adsorbed oxygen atom. For this reaction, it can be shown that

$$C_{V_O} \alpha (p_{O_2})^{-1/(2(n+1))} \qquad \text{Eq. 2.16}$$

The desorption of an oxygen ion can also cause a metal excess, through the creation of a cation interstitial, M_i, by the reaction

$$MO = M_i^{n+} + ne^- + {}^1/_2O_2 \qquad \text{Eq 2.17}$$

For this reaction,

$$C_{M_i} \alpha (p_{O_2})^{-1/(2(n+1))} \qquad \text{Eq. 2.18}$$

Equations 2.16 and 2.18 show that, at constant temperature, the number of point defects in oxygen-deficient oxides rises, as the partial pressure of oxygen in the atmosphere is decreased.

2.3 SELF-DIFFUSION

Diffusion is the movement of solute particles (molecules, atoms or ions) through a solution, which pre-supposes that the diffusing species can occupy any available vacant site. However, in ionic structures, the mobile ions can occupy only the vacant sites on their own sub-lattice, which is more correctly considered in terms of self-diffusion. Investigations of self-diffusion usually use a solute consisting of a radioactive isotope element, in a solvent which is a non-radioactive isotope of the same element [10].

Self-diffusion is a structure-sensitive process, and is expected to increase with increasing lattice irregularity. An ion can jump into an adjacent lattice site if:

(i) the neighbouring site is vacant, for which the probability goes as $\exp(-E_f/kT)$,

(ii) it has the requisite activation energy, E_a, for the jump, for which the probability

goes as $\exp(-E_a/kT)$.

The total energy required to activate the movement of an ion through its sub-lattice is therefore $E_f + E_a = E_d$. The self-diffusion coefficient, D*, is given by

$$D^* = D_0 p_{O_2}^{1/n} \exp\left(\frac{-E_d}{k T}\right) \quad (m^2 s^{-1}) \qquad \text{Eq. 2.19}$$

where D_0 is a frequency factor, and n is related to the charge on the point defect.

2.4 ELECTRICAL CONDUCTION

The ionisation of oxygen atoms at the oxide/atmosphere interface during adsorption requires a supply of electrons, which must originate in the metal. Oxides do not have free electrons, as in a metal, so their migration requires some mechanism by which they can be transported across the oxide.

Strongly stoichiometric oxides are usually composed of ions with fixed valencies, and the formation of Frenkel and Schottky defects maintains electrical neutrality without the need for the transfer of electrons. Electrons therefore migrate through the oxide at about the same rate as the ions to which they are bound, which is a relatively slow process. Adsorption of oxygen at the oxide/atmosphere interface is thus restricted, and these oxides often have negligible oxidation rates (for example, Al_2O_3).

Electrical neutrality in non-stoichiometric oxides can only be reconciled by assuming that either the anion or, more probably, the cation exhibits variable valency. Electrons may be transferred between point defects and/or ions of different valence, and can thus migrate rapidly across the oxide to the oxide/atmosphere interface. Oxides generally contain a large number of point defects, so electron transport is rarely a controlling factor in the oxidation of all but the most strongly stoichiometric oxides.

Electron transfer between point defects and/or ions, although considerably faster than the carriage of electrons bound to the ions in a stoichiometric oxide, is very much slower than the migration of free electrons through a metal. Oxides are therefore classified as semi-conductors. Semi-conductors are sub-classified as P-type, in which the conduction of electrical charge appears to occur by the migration of positive charge

carriers (electron holes), and N-type, in which the electrical charge is conducted by negative carriers (electrons).

2.4.1 P-Type Semiconductors

Positive, or P-type, semiconduction occurs in metal-deficient oxides. A vacant cation lattice site, surrounded by anions, is effectively a site of high negative charge, to which electron holes may be attracted:

$$(V_M)^{n-} + nh^+ = V_M \qquad \text{Eq. 2.20}$$

An interstitial anion has a site of high negative charge, and may also attract holes:

$$(O_i)^{n-} + nh^+ = O_i \qquad \text{Eq. 2.21}$$

2.4.2 N-Type Semiconductors

Negative, or N-type, semiconduction occurs in oxygen-deficient oxides. An interstitial cation is a site of high positive charge, and it may attract free electrons:

$$(M_i)^{n+} + ne^- = M_i \qquad \text{Eq. 2.22}$$

A vacant oxygen ion site, surrounded by cations represents a site of high positive charge, to which free electrons may be attracted:

$$(V_O)^{n+} + ne^- = V_O \qquad \text{Eq. 2.23}$$

2.4.3 Conductivity in Oxides

The electrical conductivity, χ, of an oxide is proportional to the concentration of charge carriers. From Equations 2.7 and 2.13, it can be shown that for a given concentration of electron holes in a metal-deficient oxide,

$$\chi \propto C_{h^+} \propto (p_{O_2})^{1/(2(n+1))} \qquad \text{Eq. 2.24}$$

From Equations 2.15 and 2.17, it can be shown that for a given concentration of quasi-free electrons in an oxygen-deficient oxide,

$$\chi \propto C_{e^-} \propto (p_{O_2})^{-1/(2(n+1))} \qquad \text{Eq. 2.25}$$

Thus as the partial pressure of oxygen in the atmosphere decreases, the electrical

conductivity of a metal-deficient oxide will fall, whilst for an oxygen-deficient oxide it will rise.

2.5 OXIDE GROWTH RATE

When the surface of a metal is covered by a continuous oxide film, the chemical reaction between solid and gas is initiated by chemisorption of the gas on the oxide. Since most oxides are semiconductors because of their non-stoichiometry [11] the process is generally very complex, and should be treated as a three-dimensional process [8].

2.5.1 The Space Charge

When electrons are able to move through the oxide faster than cations, the ionisation of adsorbed oxygen atoms at the oxide/atmosphere interface will create a negative electro-static charge at the oxide surface. This charge, known as the space charge, attracts metal ions to the oxide surface. When the oxide film thickness is less than some critical value, x_c, the space charge can accelerate oxidation by acting directly on ions in the metal substrate. When the oxide film is thicker than x_c and the space charge is remote from the metal substrate, subsequent diffusion into the oxide must rely on thermal energy for activation [8].

Oxidation systems can be generally divided into two categories according to the dependence of growth kinetics on the space charge; *thin films*, in contradistinction to *thick films*, grow to a maximum thickness of the the order of x_c. The variation of the value of x_c between different oxidation systems makes this distinction somewhat vague, but a value of around 1μm appears to be commonly accepted [12].

2.5.2 Thin Films

Thin films are formed when there is inadequate thermal energy to excite diffusion, and consequently initially rapid growth may become very slow or even negligible when the film thickness has exceeded the range of the space charge (i.e. when film thickness $x > x_c$). Such behaviour typically occurs at low temperatures of up to about 400°C [3 - 5, 8].

When films are less than about 1μm in thickness, the concept of electrical neutrality within the film is unreliable. Theories of thin film growth must take account of atom jumps in the presence of large electric fields, and there have been several different approaches, as reviewed by Kofstad [4], Lawless [8] and Kubachewski and Hopkins [11]. There appears to be no consensus on what assumptions are reasonable for thin films, so there are numerous theories and a corresponding number of different kinetic expressions (for example, logarithmic, inverse logarithmic, cubic and parabolic).

2.5.3 Thick Films

In contradistinction to thin films, thick films are characterised by the continued rapid growth of the oxide film long after its thickness has exceeded the range of the space charge, and because diffusion must therefore be thermally activated, such films usually occur at temperatures above 400°C [3 - 5, 8].

In the initial stage of thick film formation (ie. when it is still very thin), ion diffusion through the oxide is rapid, and virtual equilibrium with the metal is established. With a metal activity of nearly unity at the oxide surface, the rate controlling factor is the adsorption of oxygen, so that this stage of oxidation proceeds at a uniform rate. To maintain a steady flux of ions across the film as it thickens, there has to be a constant activity gradient. As a result, the metal activity at the oxide/atmosphere interface must fall as the film thickens (see Figure 2.5), and will eventually approach equilibrium with the atmosphere. Since the metal activity cannot fall below equilibrium, further film thickening must result in a decrease of the activity gradient, and

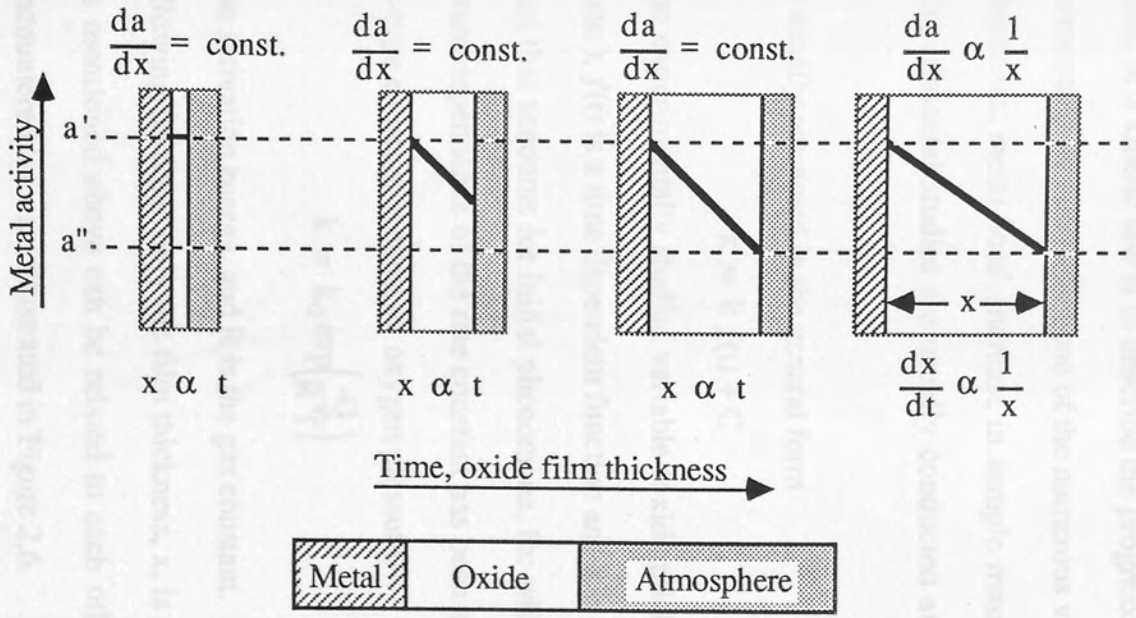

Figure 2.5. Dependence of metal activity and oxidation rate, on oxide film thickness.

consequently there is a reduction of the ionic flux and the oxidation rate. When equilibrium is established at the oxide/atmosphere interface, the ionic flux is inversely proportional to the film thickness, and subsequent oxide growth is usually found to conform to a parabolic law.

2.6 KINETIC LAWS

The purpose of a kinetic law is to describe the progress of oxidation, which can be studied experimentally by correlating one of the numerous variables (such as increase in oxide film thickness, metal 'loss', increase in sample mass, or oxygen consumption) with time. Experimental studies are usually conducted at constant temperature and pressure.

Laws are usually presented in the general form

$$x = k f(t) + C \qquad \text{Eq. 2.26}$$

where x is the experimentally studied variable (oxide thickness, weight gain per unit surface area etc.), $f(t)$ is a time dependent function and k is the oxidation rate constant. C is a constant that accounts for initial phenomena, for which the law does not apply. The temperature dependence of the rate constant has been shown, empirically, to obey an Arrhenius-type equation at constant oxygen pressure,

$$k = k_0 \exp\left(\frac{-Q}{R\,T}\right) \qquad \text{Eq. 2.27}$$

where Q is the activation energy, and R is the gas constant.

In the following sections, only the film thickness, x, is considered, although all of the variables mentioned above can be related to each other (eg. see [5]).The most commonly encountered laws are illustrated in Figure 2.6.

2.6.1 Logarithmic Kinetics

Theories relating to thin film growth are necessarily complex because of the need to consider atom jumps in the presence of large electric fields. The most frequently quoted

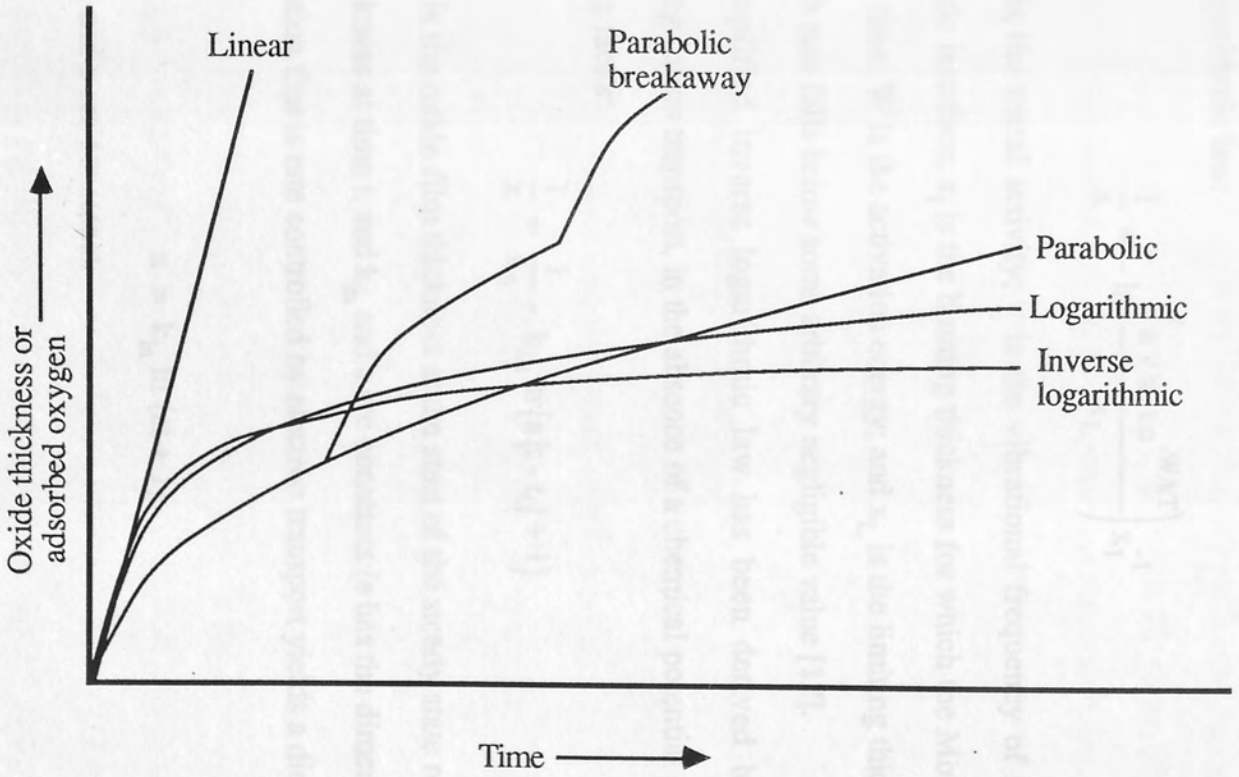

Figure 2.6. Oxidation laws.

work in this area is that of Cabrera and Mott [13], and it has accordingly received considerable attention by other authors (eg. see [8, 12, 14]). Cabrera and Mott assumed that the rate-controlling process is the injection of point defects into the oxide at one of the film interfaces. This assumption leads to slightly different results depending on the type of defect and the interface at which it is injected [12]. For the case of metal interstitials injected at the metal/oxide interface, an approximate solution produces an inverse logarithmic law:

$$\frac{1}{x} \approx -\ln\left(\frac{a \nu x_1 t e^{-W/kT}}{x_L}\right) x_1^{-1} \qquad \text{Eq. 2.28}$$

where a is the metal activity; ν is the vibrational frequency of metal atoms at the metal/oxide interface; x_1 is the limiting thickness for which the Mott-Cabrera theory is valid; t is time; W is the activation energy; and x_L is the limiting thickness above which the growth rate falls below some arbitrary negligible value [12].

A simplified inverse logarithmic law has been derived by Evans [14], by considering cation transport, in the absence of a chemical potential gradient, as the rate controlling factor:

$$\frac{1}{x} = \frac{1}{x_0} - k_{ln} \ln\left(a(t - t_0) + 1\right) \qquad \text{Eq. 2.29}$$

where x_0 is the oxide film thickness at the start of the steady state reaction at time t_0, x is the thickness at time t, and k_{ln} and a are constants (a has the dimensions $[\text{Time}]^{-1}$).

Oxidation that is rate controlled by electron transport yields a direct logarithmic law [14]:

$$x = k_{ln} \ln(at + 1) \qquad \text{Eq. 2.30}$$

where k_{ln} and a are constants.

2.6.2 Parabolic Kinetics

The parabolic law may be derived (for highly idealised conditions) from the assumption that a non-stoichiometric oxide film will have a concentration gradient of

defects across its thickness [5]. For example, a metal-deficient oxide will have a higher metal concentration at the metal/oxide interface than at the oxide/atmosphere interface. For a given concentration gradient the outward cation flux, j_c, is equal and opposite to the inward flux of cation vacancies, j_{V_c}. Since the rate of thickening of the oxide film is proportional to the cation flux,

$$k'' \frac{dx}{dt} = j_c = -j_{V_c} = D_{V_c} \frac{C''_{V_c} - C'_{V_c}}{x} \qquad \text{Eq. 2.31}$$

where k" is a constant. D_{V_c} is the self-diffusion coefficient for cation vacancies, and C'_{V_c} and C''_{V_c} are the cation vacancy concentrations at the metal/oxide and oxide/atmosphere interfaces respectively. Assuming thermodynamic equilibrium at each interface, the concentration gradient ($C''_{V_c} - C'_{V_c}$) is constant, and therefore

$$\frac{dx}{dt} = \frac{k'}{x} \qquad \text{Eq. 2.31}$$

Integrating, and noting that x = 0 at t = 0,

$$x^2 = k_p t \qquad (m^2 s^{-2}) \qquad \text{Eq. 2.32}$$

where k_p is the parabolic scaling constant.

In Section 2.2.2 (Equation 2.12), it was shown that the cation vacancy concentration is related to the oxygen partial pressure, so it follows that

$$k_p \alpha \left[(p_{O_2})^{1/n} - (p'_{O_2})^{1/n} \right] \qquad \text{Eq. 2.33}$$

where p'_{O_2} and p_{O_2} are the oxygen partial pressures at the metal/oxide and oxide/atmosphere interfaces respectively, and n is related to the valency of the diffusing species. The oxygen partial pressure at the metal/oxide interface, p'_{O_2}, is usually negligible compared to p_{O_2}.

Wagner's theorem [15] of thick film growth is the best known and most thoroughly tested theory of parabolic growth at elevated temperatures [8]. The theory provides a means by which the rate of film growth can be related to measurable transport properties of the film, such as diffusion coefficients.

2.6.3 Linear Kinetics

A linear oxidation rate,

$$x = k t \qquad \text{Eq. 2.34}$$

is usually observed when a phase boundary process is the rate determining step for the reaction. Such a process, the adsorption of oxygen at the oxide/atmosphere interface during the early stages of thick film growth, is described in Section 2.4.3. Another example is when the metal forms a volatile oxide, when the the controlling step is whichever process of evaporation and adsorption is the slower.

2.6.4 Cubic Kinetics

There is no fundamental explanation for cubic oxidation kinetics; cubic laws are usually derived from empirical observation, and may arise when two or more kinetic laws are combined [6].

2.7 MULTI-LAYER OXIDE SCALES

If a metal forms several stable oxides, the oxide richest in metal will be nearest the metal/oxide interface, and the oxide richest in oxygen will be nearest the oxide/atmosphere. In the ideal case, each oxide will constitute a separate layer, within which the concentration of metal decreases from the inside to the outside [11].

Several authors have analysed the simultaneous growth of multi-layer scales (eg. [16 - 20]). With the exception of Howe *et al* [18] the various theories have been based on the assumption of steady-state parabolic growth kinetics, and therefore apply generally to the formation of multi-layer scales at high temperatures. The majority of these theories have considered the formation of two layers, and have approached the problem as a two stage parabolic process, giving rise to two parabolic rate constants, one for each layer, which are related to the overall rate constant for scale formation. Gesmundo and Viani [16] have derived expressions for a three oxide scale.

The two layer model considered by Yurek *et al* [20] is shown in Figure 2.7, in

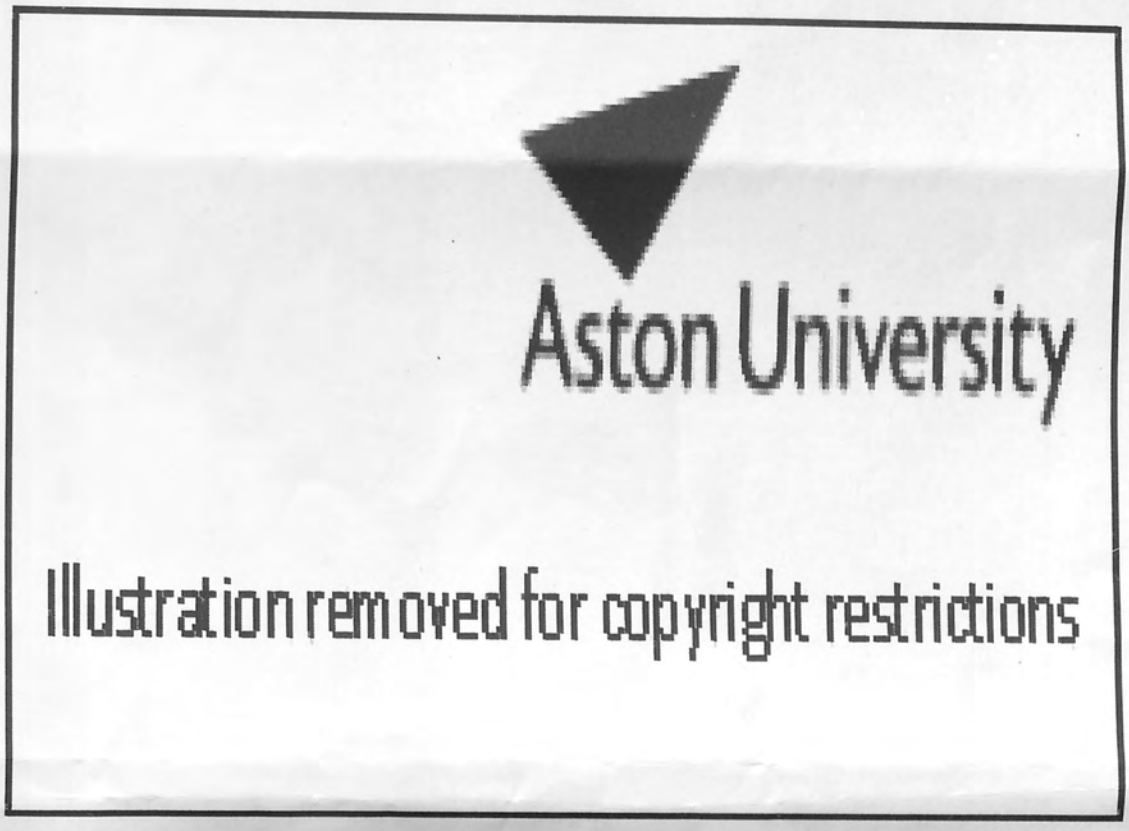

Figure 2.7. Model for two-layer oxide scale growth (Yurek et al [20]).

which the diffusion of anions is assumed to be negligible so that the reaction is rate-controlled by the outward diffusion of cations, the flux of which is assumed to be independent of the distance from the metal. The overall oxidation reaction is given by

$$(\nu\, w + \delta\, y)M + {}^{1}/_{2}\,(w + y)\,O_2 \rightarrow w\,M_{\nu}O + y\,M_{\delta}O \qquad \text{Eq. 35}$$

where w and y are the fractions of the scale of compositions $M_{\nu}O$ and $M_{\delta}O$ respectively.

The rates of thickening of each layer are given by

$$\frac{d\xi}{dt} = \frac{k_{p(M_{\nu}O)}}{\left(1 + \frac{\delta\, y}{\nu\, w}\right)} \qquad \text{and} \qquad \frac{d\eta}{dt} = \frac{k_{p(M_{\delta}O)}}{\eta\left(1 + \frac{w}{y}\right)} \qquad \text{Eq. 2.36(a), (b)}$$

where $k_{p\,(M_{\nu}O)}$ and $k_{p\,(M_{\delta}O)}$ are the parabolic rate constants for the respective oxides. The overall parabolic rate constant, K_p, for the growth of the entire scale, can be derived in terms of either oxide layer's rate constant, thus

$$K_p = \frac{(1 + \eta/\xi)^2}{\left(1 + \frac{\delta\, V_{M_{\nu}O}}{\xi\, V_{M_{\delta}O}}\right)} k_{p(M_{\nu}O)} = \frac{(1 + \xi/\eta)^2}{\left(1 + \frac{\xi\, V_{M_{\delta}O}}{\eta\, V_{M_{\nu}O}}\right)} k_{p(M_{\delta}O)} \qquad \text{Eq. 2.37}$$

where $V_{M_{\nu}O}$ and $V_{M_{\delta}O}$ are the molar volumes of the two oxides [20].

The relative thicknesses of the various layers mainly depend on diffusion rates in the different oxides, and also on the differences between the chemical potentials at the interfaces. If diffusion in a particular oxide is slow, then the thickness of the corresponding layer in the oxide scale will be very thin, although in theory, it should not disappear completely. The relative thicknesses of the layers are found to be independent of time.

The model proposed by Howe *et al* [18] takes into consideration initial phenomena of nucleation and lateral growth of nuclei for a two layer system, as well as the subsequent steady-state reaction for the outward growth of oxide. This theory was developed to describe the oxidation of iron at 350°C to 500°C, in which the nucleation

and lateral growth of the second, and most protective layer (Fe_2O_3), lags behind the development of the first layer (Fe_3O_4).

2.8 STRESSES IN OXIDE SCALES

Oxides are less dense than their parent metal. If the oxide forms as an adherent layer, interfacial strains will exist which produce stresses in the metal and oxide. It is also probable the metal and oxide will have different coefficients of thermal expansion, and thus if coherency is to be maintained at all times, further interfacial strains will be induced upon any change in temperature. The magnitude of growth stresses, and thermal stresses, may be greater than the fracture stress of the oxide [21]

In 1923, Pilling and Bedworth [22] proposed that the formation of a continuous, or discontinuous (porous), oxide layer could be predicted from the relative volumes of the metal ions and oxide molecules. Their proposal (commonly known as the 'Pilling-Bedworth Ratio') was based on the assumption that oxides grew by the inward diffusion of anions, and that the transition from metal to oxide occurred by an homogeneous dilation of the metal lattice. The Pilling-Bedworth Ratio is given by

$$PBR = \frac{\text{volume per metal ion in the oxide}}{\text{volume per metal atom in the metal}} = \frac{M_{oxide}}{\rho_{oxide}} \cdot \frac{\rho_{metal}}{M_{metal}} \qquad \text{Eq. 2.38}$$

where M_{metal} and M_{oxide} are the atomic and molecular weights of the metal and oxide, and ρ_{metal} and ρ_{oxide} are their densities.

A PBR of greater than unity indicates that the oxide will be in compression if it remains attached to the metal, and thus should form a continuous film. If the PBR is less than unity, the oxide film will be under tension, and may break up into a discontinuous, porous layer.

Subsequent authors have made use of the PBR to predict the growth stresses induced by the change in volume occurring during the transition from metal lattice to oxide sub-lattice [23, 24]. Assuming that this dilation is more or less isotropic, the sign and relative magnitude of the stress are given by (1 - PBR). However, as Stringer [24] and numerous others have pointed out, the PBR does not accurately predict the stresses

in many oxidation systems, and will be invalid for oxides that grow by the outward diffusion of cations. Nevertheless, in most cases it correctly predicts the sign of the stress in both cation diffusion- and anion diffusion-predominant oxidation systems (i.e. negative for compressive stresses, positive for tensile stresses) at least, and is thus a useful rule of thumb.

In theory, oxides that grow by cation diffusion should be stress free, since oxide formation occurs at the oxide/atmosphere interface where there is no restraint on relaxation. However, many such oxides are found to be under a compressive stress, and it has been suggested [25] that this is due to the ingress of anions and formation of new oxide at grain boundaries. Speight and Harris [26] believe that such a mechanism is untenable, arguing that (assuming diffusion occurs by a vacancy mechanism) it would lead to the paradoxical situation of oxide forming at a perfect vacancy source. In their view, growth stresses in oxides in which the diffusion of cations predominates, must arise from the growth of oxide in cracks and pores, as only these types of defects could provide the finite number of vacancies necessary.

Other sources of stress during isothermal oxide scale growth, besides the volumetric effect noted by Pilling and Bedworth [22], are considered in reviews by Stringer [24] and Taniguchi [27]. In brief these are:

(i) Oxygen solution in the metal - which since oxygen is usually the larger ion, dilates the metal lattice, creating a compressive stress in the metal surface, or a tensile stress in the oxide film;

(ii) Imperfect epitaxy - while oxide films are thin, an epitaxial relationship is generally maintained between the oxide and the substrate. Since perfect epitaxy is improbable because of lattice mismatch, the metal and oxide lattices must both undergo some strain;

(iii) Point defects - vacancies and interstitial ions both cause some local lattice distortion. Growing oxides always contain a concentration gradient of these defects, associated with the material flux, so that stresses will tend to be

concentrated at interfaces;

(iv) Local heterogeneities - metal grain boundaries, for example, often oxidise faster than grains and produce a thicker oxide, which results in either the formation of oxide ridges or oxide penetration between grains;

(v) Oxide growth within the oxide layer - the ingress of the oxidising atmosphere into defects in the oxide film can create new (oxygen rich) oxide, the continued growth of which produces a compressive stress in itself and the surrounding oxide;

(vi) Formation of multi-layer scales - this type of reaction, and any associated volumetric changes, take place at the interface of two solid phases, rather than the oxide/atmosphere interface where the solid phase is free to relax by expanding outwards; and

(vii) Composition changes in the oxide - changes in composition often take place during the oxidation of alloys, because the alloy components have different affinities for oxygen and do not diffuse at the same rate in the alloy and oxide. Another possibility is the formation of an oxide with a wide range of stoichiometry on a pure metal (although this can be ascribed equally to the effects of point defect concentration gradients).

Thermal stresses may arise during heating and cooling, due to differences between the thermal expansion coefficients of the metal and oxide, or between oxide layers. There may also be volumetric changes due to phase transformations in the metal and oxide scale.

The mechanical characteristics of the oxide and metal also have an effect on stress development. For example, a compressive stress in the oxide may be relaxed to some extent by the elastic expansion of the metal substrate. Plastic deformation by creep mechanisms can play a part in stress relaxation by allowing the oxide to expand at free surfaces, especially at high temperatures.

2.8.1 Stress-Induced Defects

U.R.Evans [28] has made a detailed study of the influence of lateral compressive stresses in oxide films, and has classified three different types of rupture: blistering, flaking and shear cracking (Figure 2.8). The compressive stress within the oxide is assumed to be proportional to the thickness of the film, so that when the oxide has grown to some critical thickness, one of the above mentioned defects will form, depending on the oxide's adherence to the metal substrate and the coherence of the bulk oxide. The formation of cavities, by vacancy condensation, at the metal/oxide interface of iron has been found to reduce the oxide scale's adherence to the substrate [29], so adhesion must be, at least in part, time dependent.

Stress related defects are most commonly encountered when the oxide growth rate remains significant for long periods of time, so that generally they occur at high temperatures and with parabolic growth kinetics.

2.9. POROSITY IN OXIDE SCALES

Many oxide scales that grow by the outward diffusion of cations are found to be porous, especially in the layers closest to the metal. Although small voids formed by vacancy injection and condensation in the scale may account for some porosity, it seems that most of it stems from the growth of fresh oxide beneath detached scales in conditions of low oxygen pressure [5, 30].

2.9.1 Vacancy Condensation

A metal ion entering the oxide at the metal/oxide interface leaves behind a residual metal vacancy. Classical theories of oxidation ignore the existence of these vacancies and assume that they are annihilated *in situ* to preserve ideal contact between oxide and metal [30]. In fact this does not happen to all vacancies, and the number of vacancies remaining at the interface depends on the availability of vacancy sinks. The nature of the vacancy sinks is not well understood, but is thought to involve dislocation type entities

Figure 2.8. Stress-induced defects in oxide scales (after Evans [28]).

located at or close to the metal/oxide interface [31]. Caplan and Cohen [32] have shown that cold working iron prior to oxidation, which increases the concentration of dislocations in the metal, improves the adherence of scales.

H.E.Evans [31] points out that it is the number of vacancy sinks at the metal/oxide interface, rather than their nature, that is important. Vacancies will be annihilated at the interface if

$$\lambda_S \leq \lambda_V \ll z \qquad \text{Eq. 2.39}$$

where λ_S is the mean distance between vacancy sinks; λ_V is the mean distance between vacancies; and z is the mean migration distance of an interfacial vacancy before it is injected into the metal or oxide. Aggregation of vacancies leading to the formation of interfacial voids will occur if

$$\lambda_S \gg \lambda_V \ll z \qquad \text{Eq. 2.40}$$

It is important to note that the overlying oxide may be able to collapse into voids at the metal/oxide interface, thereby annihilating the vacancies and forming a dislocation loop which will act as a vacancy sink [30].

Vacancies will be predominantly injected into the metal if

$$\lambda_S \gg \lambda_V \gg z \qquad \text{Eq. 2.41}$$

where they may condense to form voids within grains or at grain boundaries. Intra-granular voids are not always associated with second phase particles, and it appears that their nucleation is not a difficult process [31].

The diffusion of vacancies into the metal produces a vacancy concentration gradient, which decreases with increasing depth below the metal/oxide interface [33]. In the case of a very thick metal substrate, as assumed by H.E.Evans [31], this gradient will remain more or less constant, as will the flux of vacancies into the metal. However, for thin metal substrates, the absence of vacancy sinks will lead to a steady rise in the the vacancy concentration, and the reduction of the vacancy gradient [33]. The flux of vacancies away from the interface is thus reduced, and the mean migration distance, z, of vacancies at the interface will correspondingly increase. The formation of interfacial

cavities in thin metal specimens is therefore much more probable than in thick ones.

An interesting phenomenon associated with this is that whilst the scale formed on one side of a thin metal strip becomes detached, the scale on the opposite side remains attached. Dunnington *et al* [33] have proposed that this is due to the cavity beneath the detached scale acting as a vacancy sink for the concentration gradient of vacancies originating at the opposite metal/oxide interface. This has been confirmed by Tylecote and Mitchell [34], who found that the scale remained attached on both sides of an iron sheet if vacancy sinks were present at the mid-thickness of the metal (the vacancy sinks consisted of holes drilled parallel to the surfaces of the metal sheet, and sealed prior to oxidation).

The formation of cavities does not represent a process of vacancy destruction. Cavities are simply repositories for voids which, under favourable circumstances, can also act as vacancy sources, and their presence does not reduce the number of metal lattice sites [31].

The formation of cavities in the metal near the metal/oxide interface has yet to be satisfactorily explained. Harris [35] has proposed that the formation of inter-granular voids in the metal is due to a creep mechanism, driven by the tensile stress induced by a compressed oxide scale, rather than by vacancy condensation. A recent study of the formation of voids in Ni-Cr alloys [36] has shown that at 1000°C cavities are formed almost exclusively at grain boundaries, whilst at 1200°C cavities are also formed within grains. This suggests that the formation (whether heterogeneous or homogeneous) of intra-granular voids requires some critical vacancy concentration to be exceeded. Since grain boundaries contain more heterogeneities than grains, it would be expected that the vacancy concentration required for inter-granular void formation is considerably less than that for intra-granular formation. Therefore, it seems probable that the formation of inter-granular cavities is, at least in part, due to vacancy condensation.

2.9.2 Oxide Growth Beneath Detached Scales

Large areas of the oxide scale can become partially detached from the metal when many small cavities coalesce, or when stress-induced defects grow laterally at the metal/oxide interface. If the cavity is open to the atmosphere, as in the case of flaking, the newly exposed metal and oxide surfaces will both oxidise. Spalling will occur if the stress in the scale is great enough to cause fracture around sections of the scale, but the action of some external force (eg. gravity) may be necessary for their removal. Detached flakes remaining on the metal surface may be engulfed by continued oxide growth.

Following separation of the metal and oxide, the flux of metal ions from the substrate into the separated scale is curtailed. However, the migration of cations across the scale can continue, driven by the high metal activity at the newly created void/oxide interface. This cation flux reduces the metal concentration and so the metal activity falls, with a corresponding rise in the oxygen activity [5, 37, 38].

If the void remains sealed against attack by the external atmosphere, the oxide at the void/oxide interface will dissociate to maintain the local equilibrium, supplying cations to the oxide and creating a partial pressure of oxygen in the void. The partial pressure of oxygen will rise as the oxygen activity increases with decreasing metal activity [37].

However, taking as an example the dissociation of ferric oxide in a cavity at the metal/oxide interface, at a temperature of 10^3K, the reaction

$$4Fe_3O_4 + O_2 = 6Fe_2O_3 \qquad \text{Eq. 2.42}$$

will proceed right-to-left at a partial pressure of oxygen of about 10^{-10}Pa or less. Using Equation 2.1 (Section 2.1.1), the molecular oxygen flux at the metal surface will be approximately 7.7×10^{-14}mol m^{-2} s^{-1}. Assuming 10^{19} oxygen sites per square metre, this would give an oxidation rate of approximately 10^{-8} atom layers per second, or in other words it would take more than 3 years to form an adsorbed layer of oxygen on the metal surface. Such growth rates are negligible, and cannot explain the formation of fresh oxide on the exposed metal surface in an apparently sealed cavity (as, for

example, is suggested by Juenker *et al* [37]). Gaseous oxygen must therefore be able to penetrate the oxide scale.

Mrowec [39] has proposed a mechanism by which pores could form at grain boundaries in the scale situated above interfacial cavities. Dissociation of the oxide is faster at grain boundaries than at grain surfaces and, because of the oxygen potential gradient in the scale, micro-channels through the scale are created [39]. This process is shown in Figure 2.9. Although there will be some tendency for these pores to heal by the lateral growth of oxide [12], complete closure may not occur if, at some residual level of porosity, the gas pressure gradient in the micro-channel becomes equal to the oxygen potential across the scale [30]. Lines of equal oxygen activity will then be parallel to the metal/scale interface, and since diffusion fluxes are normal to the iso-activity contours there will no longer be a net flow of cations to the sides of the micro-channels. The existence of pores connecting interfacial cavities to the external atmosphere has been confirmed by Brückman, Emmerich and Mrowec [40].

Figure 2.10 illustrates the formation of fresh oxide on a metal surface exposed by scale separation. New crystals of oxide grow at a very slow rate in a low oxygen pressure close to the equilibrium pressure, and the continual variation of the oxygen activity at the void/scale interface prevents the completion of a continuous layer of oxide on the metal surface before another is initiated on top. Over a period of time the growth of successive incomplete layers will take on the appearance of a discontinuous, porous oxide scale [5].

The separated oxide can continue to grow only by the adsorption of oxygen, which will occur at the external surface, and possibly also at the internal (void/scale interface) surface. Contact between the metal substrate and a detached scale can be re-established by the growth of fresh oxide in an interfacial cavity. In multi-layer scale systems (eg. iron and copper), the presence of gaseous oxygen can cause the formation of higher oxides than the oxide in the scale surrounding an interfacial cavity.

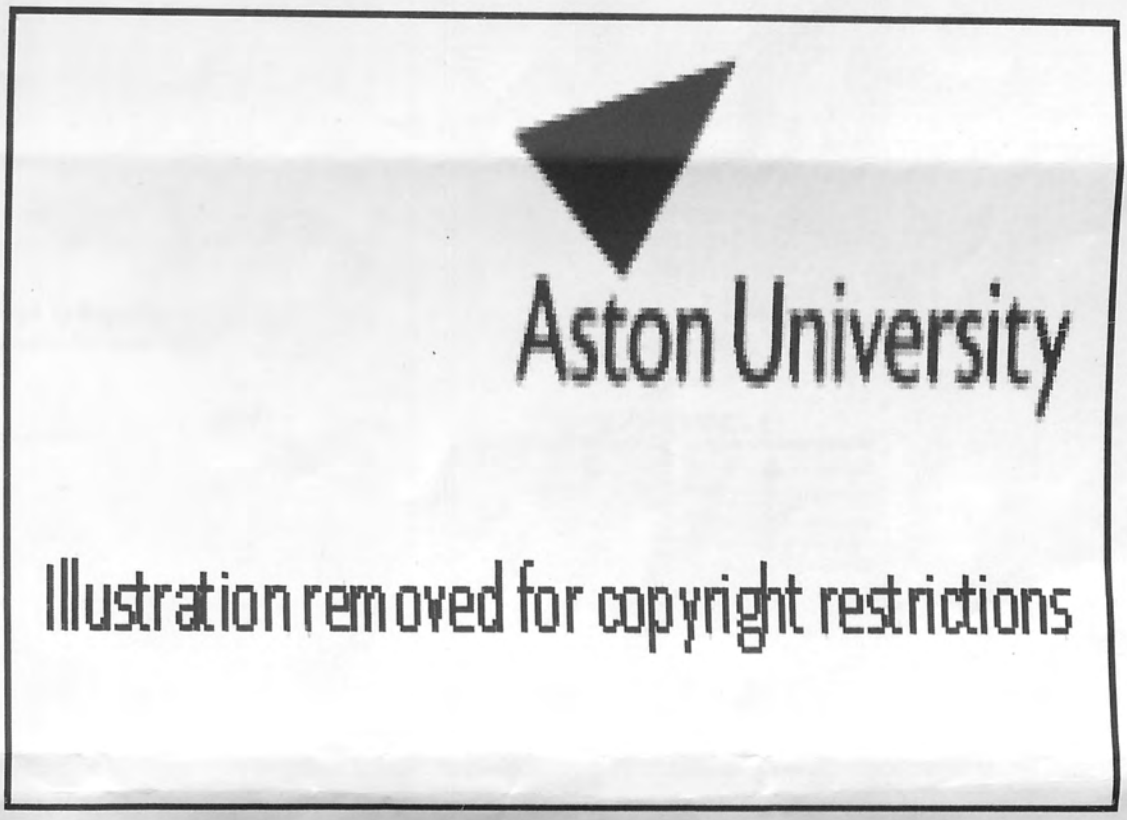

Figure 2.9. Development of micro-channels above an interfacial void, showing cation and gaseous oxygen fluxes (after Gibbs and Hales [r91]). Dashed lines represent contours of equal oxygen activity in the oxide scale.

Figure 2.10. Formation of a porous layer beneath a separated oxide scale (after Birks and Meier [5]).

2.9.2 Duplex Oxide Growth

In contradistinction to the growth of a multi-layer scale of two chemically distinct oxide phases parallel to the substrate on a pure metal, the term 'duplex oxide' is used to describe the simultaneous growth of a particular phase of the oxide in two structurally distinct layers [12]. Duplex oxide layers on alloys may have slightly different chemical compositions, because of the different diffusion rates of alloying elements in the two layers.

The conditions required for duplex growth are not yet fully understood, but it occurs only in those oxides that grow by the outward migration of cations, and then most commonly on impure or alloyed metals. The outer layer of a duplex oxide usually has a columnar structure, whilst the inner is more equi-axed, and may be porous. In many cases the boundary between the layers lies at the position of the original, unoxidised metal surface [12].

The critical steps that initiate duplex growth during oxidation are thought to be the separation of the metal and oxide, followed by inward gaseous transport of oxygen along fissures in the scale [12, 30]. Oxide nuclei are formed at the metal/scale interface by the direct oxidation of the metal. The condensation of metal vacancies undercuts these nuclei, exposing fresh metal surfaces for oxidation, producing a porous equi-axed structure (Figure 2.11).

The distinctive feature of duplex oxide scales is that growth occurs in opposite directions at the metal/oxide and oxide/atmosphere interfaces. Cations continue to migrate to the outer scale, through the interconnecting equi-axed oxide grains of the inner layer, whilst the continual undercutting and formation of oxide nuclei on the metal surface causes the metal/oxide interface to retreat.

Figure 2.11. Growth of duplex oxide scale (after Atkinson [12]).

2.10 SHORT CIRCUIT DIFFUSION

There is a considerable body of evidence that supports the basic correctness of the classical Wagner [15] theory. However, this evidence comes from studies of oxidation systems for which the transport mechanisms are reasonably well understood, and with fairly high growth rates (with a parabolic rate constant k_p greater than about 10^{-10} cm^2 s^{-1}). Oxides with slower growth rates cannot be explained by the theory, and in general the observed growth rates tend to be much greater than the predicted rates [41].

Although almost any departure from the basic assumptions in Wagner's theory could explain such discrepancies, the reasons for oxidation being faster than expected are most likely to stem from the transport of ions along pathways that short circuit lattice diffusion; diffusion is a structure-sensitive property, and therefore is expected to increase with increasing lattice irregularity. Grain boundaries, dislocations and interconnected porosity all constitute possible routes for the rapid diffusion of ions [41, 42].

In simple terms, the effect of short circuit diffusion will be to modify the diffusion coefficient, D, of the oxide, thus

$$D_{(effective)} = (1 - f)\, D_{(lattice)} + f\, D_{(short\ circuit)} \qquad \text{Eq. 2.43}$$

where f is the fraction of diffusion sites in the low resistance pathways [43].

2.11 MODIFICATION OF OXIDATION KINETICS

2.11.1 Effect of Defects

Defects can either decrease or accelerate the oxidation rate, depending on whether they reduce the flux of metal ions into the scale, or allow the atmosphere to attack the metal directly.

A cavity at the metal/oxide interface will obstruct the transport of metal ions into the separated scale. Metal ions may still enter the detached scale from its attached edges, but the restricted supply will result in an increasing oxygen content as gaseous oxygen continues to be adsorbed.

From H. E. Evans work [31] (see Section 2.9.1), it is apparent that the formation of cavities by vacancy condensation should occur at a uniform rate. The effect on oxidation kinetics will therefore reduce the rate constant gradually, as an increasing number of cavities are formed. On the other hand, cavity formation by blistering, which will occur only after the oxide film has grown to some critical thickness, will have a more abrupt effect, and the oxidation kinetics may be altered to take the form of a logarithmic law [28].

Defects that permit the ingress of the atmosphere (flaking, and blistering in which the bending stress in the scale is sufficient to cause fracture and spalling) will lead to the direct oxidation of the metallic substrate. Since the areas of the scale affected by this type of defect expose clean metal surfaces to the atmosphere, continued oxidation will produce the critical thickness for rupture in about the same time as it took the original growth of oxide [28]. A periodic return to fast initial oxidation kinetics, followed by a decrease in growth rate as the oxide film thickens in the sub-critical range, is a characteristic of this type of defect. It usually takes the form of parabolic breakaway growth (see Figure 2.6), although the time between periods of breakaway growth can be so brief that a plot of film thickness against time will appear to be linear [14].

2.11.2 Geometrical Effects

All the preceding arguments have assumed that oxidation is taking place on an infinite plane metal surface. Thus boundary effects can be ignored, and there are no external forces to prevent the oxide scale subsiding, to maintain contact with the retreating metal surface.

In practice, surfaces are rarely smooth, they may be curved, and they invariably have edges and corners. Whilst the diffusion coefficients of reactants in a planar oxide scale are constant (neglecting compositional effects), they can vary in curved layers [38]. Concave surfaces will produce a thicker scale (increasing the diffusion path length), and convex surfaces a thinner one (reducing the length of the diffusion path),

than a planar surface for the same amount of oxidised metal [44].

Geometrical features of the surface can concentrate or relax stresses already inherent in the scale. They may provide the foundations for the growth of stable oxide structures which could, for example, prevent the scale subsiding to maintain contact with the retreating metal surface.

Defects that arise as a result of surface geometry can be separated into those that are due to compressive stresses (typically in oxides that grow predominantly by the diffusion of cations), and those due to tensile stresses (often associated with oxides that grow mainly by anion diffusion) [45, 46]. These defects are illustrated in Figures 2.12 and 2.13.

The most commonly encountered geometrical features are edges and corners, where metal impoverishment produces a thinner scale than is found on the main surfaces; the small volume of metal in the corner has to supply cations to a large volume of oxide (see Figures 2.12a and 2.13a). When growth of the oxide produces a compressive stress, sheets of scale meeting at edges and corners will tend to support each other, preventing subsidence to the metal surface, whilst the surrounding scale is able to maintain contact (Figure 2.12a).

Many discrepancies in published kinetic data can be explained in terms of the different sample geometries used by different workers. Romanski [44] has identified three factors (specific area, shrinkage of the metal core, and the shape and size of the sample) that must be taken into account in experimental studies of oxidation.

2.11.3 Specific Surface Area

The specific surface area of a sample is the ratio of surface area to mass. Oxidation is generally exothermic, and the heat produced by the reaction, which is directly proportional to the area over which it occurs, will be added to that of the experimental conditions.

Experimenting with the sulphidation of 18.6mm diameter iron discs at 700°C,

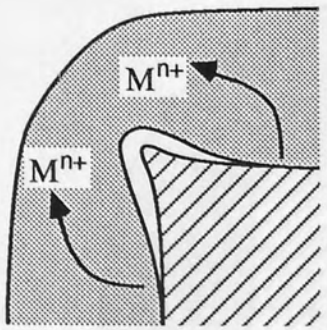

a) Corners and edges - the oxide is supported by surrounding scale. Scale subsidence is prevented, and the oxide becomes detached as the metal surface retreats.

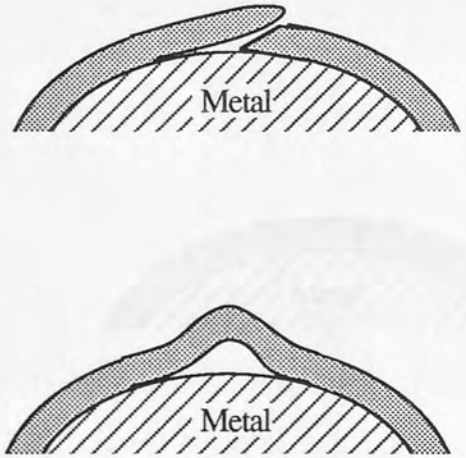

b) Convex surfaces - compressive stresses cause fracture or blistering.

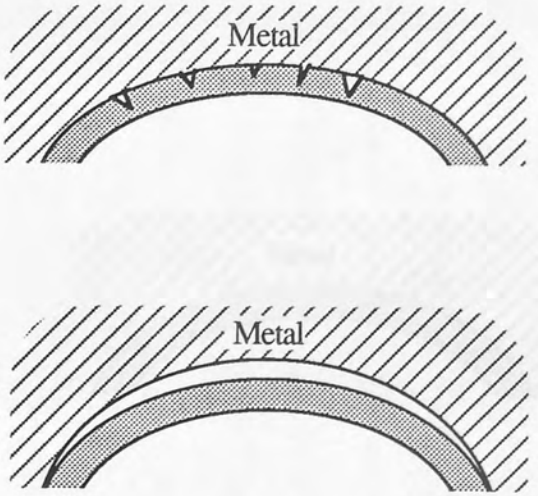

c) Concave surfaces - the retreating metal surface initiallty relaxes the compressive stress. Subsequent metal surface retreat places the oxide scale in tension, causing cracking or separtion.

Figure 2.12. Effects of surface geometry on an oxide scale growing under a compressive stress.

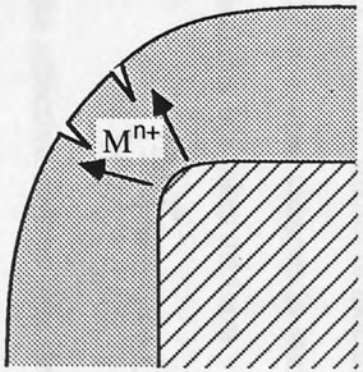

a) Corners and edges - tensile stresses hold the oxide scale against the metal surface. Tension cracking occurs in the vicinity of the edge radius.

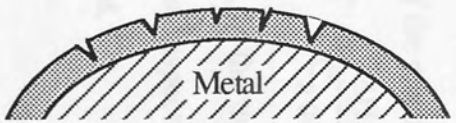

b) Convex surfaces - tension cracking.

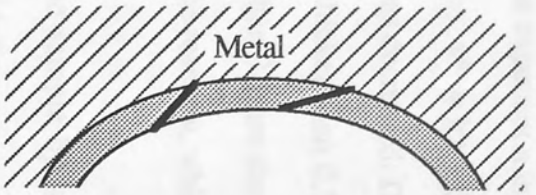

c) Concave surfaces - tensile stresses at the metal/oxide interface place the oxide/atmosphere interface under tension, leading to shear cracking.

Figure 2.13. Effects of surface geometry on an oxide scale growing under a tensile stress.

Romanski [44] found that the exponent n in the parabolic equation,

$$x^n = k't + C \qquad \text{Eq. 2.44}$$

increased as the thickness was decreased. Discs 0.25mm thick had an average exponent of n = 2.5, whereas discs thicker than 0.5mm had an average exponent of n = 2.1. However, the discs thicker than 0.5mm showed some deviation from parabolic kinetics during the initial stages of the reaction, which Romanski attributed to the establishment of thermal equilibrium.

The superheating of the sample by heat generated by the reaction can have a significant effect on the oxidation rate constant (see Section 2.6). Assuming that the sample forms a closed system (i.e. there is no heat transfer between the sample and its surroundings) and that it is at thermal equilibrium, the superheating, ΔT, can be approximated from the heat of the reaction at temperature T. Hence

$$\Delta T = \frac{-\Delta H_T M_M m_O}{C_{p\,(M)} M_O m_M} \qquad \text{Eq. 2.45}$$

where M is the atomic mass, m the the mass of reactant and the subscripts M and O indicate the metal and oxygen respectively. ΔH_T is the heat of formation of MO, and $C_{p(M)}$ is the heat capacity of M.

2.11.4 Core Shrinkage

As metal is consumed by oxidation, the volume and surface area of metal in the sample decrease. Gravimetric studies of oxidation reactions are commonly presented as the ratio of directly measured changes in sample mass (Δm) to original surface area (A_0), so that the parabolic law takes the form

$$\left(\frac{\Delta m}{A_0}\right)^n = k'_p t + C \qquad \text{Eq. 2.46}$$

However, since the effective surface area decreases as the reaction progresses, this approach will lead to (i) an apparent decrease in the rate constant k'_p, and (ii) an apparent deviation from parabolic kinetics towards values of the exponent $n > 2$.

Furthermore, the final surface area cannot be used, because in the limiting case of complete oxidation of the core, A = 0.

The increase in sample mass, Δm, due to the adsorption of oxidant, is proportional to the decrease of the volume of the metallic core, ΔV_M, hence

$$\Delta m = \kappa \Delta V_M \qquad \text{Eq. 2.47}$$

where k is some constant. ΔV_M is a function of the sample's dimensions, which themselves will be a function of time during oxidation. The ratio ($\Delta m/A$), where A is the instantaneous metal surface area, can then be evaluated in terms of the volume change. For example, for a cylindrical metal core of radius r and height h, neglecting the flat end surfaces,

$$\frac{\Delta m}{A} = \kappa \frac{\left(\frac{dV_M}{dr}\right)dr}{A} = \kappa \frac{\left(\frac{d(\pi r^2 h)}{dr}\right)dr}{2\pi r h} = \kappa\, dr \qquad \text{Eq. 2.48}$$

Thus for a cylindrical geometry the ratio ($\Delta m/A$) depends on the change in radius, dr, rather than the instantaneous radius, r [44].

The constant κ can be approximately determined from the stoichiometric composition of the oxide MO,

$$\Delta m = \Delta V_M \rho_M \frac{M_O}{M_M} \Rightarrow \kappa = \rho_M \frac{M_O}{M_M} \qquad \text{Eq. 2.49 (a), (b)}$$

where ρ_M is the density of the metal.

2.11.5 Shape and Size

Romanski [44] experimented with the sulphidation of iron samples of several commonly used geometries: discs, cylinders and parallelepipeds. Generally,

(i) the effects of core shrinkage increase as the specific surface area (ie. the ratio of surface area to volume) increases;

(ii) parabolic kinetics (ie. exponent n = 2) are more closely approached by samples with a large surface area;

(iii) the reproducibility of results decreases with increasing sample mass; and

(iv) of the three basic sample geometries, cylinders give the least reproducible results.

Romanski concluded that the ideal sample geometry was that of the flat disc, because specific surface area could be maximised with minimal effect from edges and curved surfaces.

2.11.6 Reduced Pressures and Dilute Atmospheres

Two factors dependent on the oxygen pressure have already been discussed: flux of oxygen molecules at the oxide/atmosphere interface (Section 2.1), and point defect formation (Section 2.2).

When the oxidising gas is diluted by inert or inactive gases, the gas layers immediately adjacent to the oxide surface are rapidly depleted of the active species. Subsequent oxidation will then depend on the diffusion of molecules of the oxidising gas through the depleted layer. If p_{O_2} is the oxygen partial pressure in the atmosphere, and p'_{O_2} is the partial pressure at the oxide/atmosphere interface, then the flux of oxygen molecules at the oxide surface will be

$$j_{O_2} = -D_{O_2}\frac{p_{O_2} - p'_{O_2}}{\delta} \qquad \text{Eq. 2.50}$$

where D_{O_2} is the diffusion coefficient of oxygen in the atmosphere, and for a binary gas is independent of concentration [10]. j_{O_2} is inversely proportional to δ, the thickness of the boundary layer, and represents the maximum possible reaction rate under these circumstances. The magnitude of δ can be influenced to some extent by controlling the flow rate of the atmosphere [5].

2.12 ALLOYS

Many different factors are involved in the oxidation of alloys, rendering any fundamental approach to the subject highly complex. The addition of alloy elements to a pure metal complicates the understanding of oxidation mechanisms because:

(i) The alloy components will have different affinities for oxygen, so that the oxide scale may not contain the same relative amounts of the alloy components as the alloy itself;

(ii) Solution of oxygen in the alloy may lead to internal oxidation of alloy components;

(iii) Different atomic and ionic species will diffuse at different rates in the alloy and oxides;

(iv) Ternary and higher oxides may be formed. The oxides may be able to combine as a solid solution, or they may be partly or wholly immiscible, producing simple or multi-phase scales; and

(v) Compositional changes in the alloy surface and oxide scale may occur as oxidation progresses.

Wallwork [6] has suggested that some of the complexities arising out of the erratic behaviour of some alloy systems can be ignored, since such unpredictable alloys are of little industrial consequence.

Alloys are thermodynamically unstable in an oxidising atmosphere, and in practical terms good oxidation resistance means that the rate of reaction must be sufficiently low under service conditions to provide a useful working life. The specific goal of alloying in this context is to protect against attack by a hostile environment, in order to preserve the structural integrity of the parent metal or alloy [4, 47]. This may require several steps:

(i) Protection of the alloy during the initial phase of oxidation, before the protective oxide barrier has formed. This may include the creation of a temporary oxide film by one of the alloy components, with lesser stability than the final scale but a

faster rate of formation, and preventing the solution of oxygen in the alloy;

(ii) Formation of a stable, passive, compact scale with low rates of diffusion for the active species;

(iii) Limitation of structural damage to the scale resulting from growth and thermal stresses, and mechanical action associated with service conditions, by the addition of elements that improve scale adherence;

(iv) Adequate concentration of the selectively oxidised element(s) in the surface layers of the alloy to enable ruptured scales to heal by subsequent protective oxide growth.

Steps (ii) and (iv) are the most significant in the long-term protection of the substrate. Repeated loss of the scale, for example as a result of spalling during cyclic oxidation, can lead to the protective barrier becoming progressively less effective through depletion of alloy components.

Optimising the oxidation resistance of an alloy can have serious consequences for other properties such as strength, and therefore many alloys represent a balance between the competing requirements. Many high temperature alloys (eg. gas turbine alloys etc.) consist of seven or eight, and in extreme cases as many as fourteen individual alloying elements, each with a definable role to play in the performance of the alloy [6].

As discussed previously (Section 2.4), the most protective oxide films are usually strongly stoichiometric, but must also be practically free of pores, cracks and other paths for short-circuit diffusion, and must have a very low vapourisation rate. Theory cannot be used to make practical predictions, but thermodynamic studies can help to indicate the possible reactions occurring during oxidation of simple systems, and ternary equilibrium studies associated with two metallic elements and oxygen are useful in assessing reactants and products [6].

2.12.1 Internal Oxidation

The internal oxidation of an alloy AB, in which B is the more noble alloy base, and A the less noble alloying addition, occurs through the dissolution of atomic oxygen into the base metal at the external surface (in the absence of an external oxide scale) or at the alloy/oxide interface. The dissolved oxygen diffuses inwards through the matrix of metal B which will contain a number of previously precipitated oxide particles. At an advancing reaction front, which remains essentially parallel to the external surface, the counter-current diffusion of oxygen and the alloying element A continuously produces concentrations of the solute oxide, AO, in excess to the solubility limits of the solvent matrix. The nucleation and growth of particles of AO results, and the reaction front advances inwards. The rate of advance of the internal oxidation front decreases as the length of the diffusion path for oxygen increases (Figure 2.14) [48].

If the outward flux of A is greater than the concentration of solute consumed by the formation of internal oxide particles, a layer of AO will be formed at the external surface of the alloy (Figure 2.15).

2.12.2 External Oxidation

Exposure of an alloy AB to an oxidising gas is expected to produce nuclei of the oxides AO and BO on the alloy surface. During the initial period of oxidation these oxide nuclei grow laterally and impinge upon each other, until eventually the transport and thermodynamic properties of the oxides and alloy determine a steady state configuration of the phases. This steady state situation can be analysed using methods originally developed by Wagner [49] and, although the whole system is not at thermodynamic equilibrium, it is assumed that each component can be assigned a chemical potential which is a function of position relative to the surface. Assuming that a local thermodynamic equilibrium is attained in a volume that is small compared to the volume of the scale, these chemical potentials can be used to predict the phases which exist at any particular point. Since the flux of each component is a function of the phase

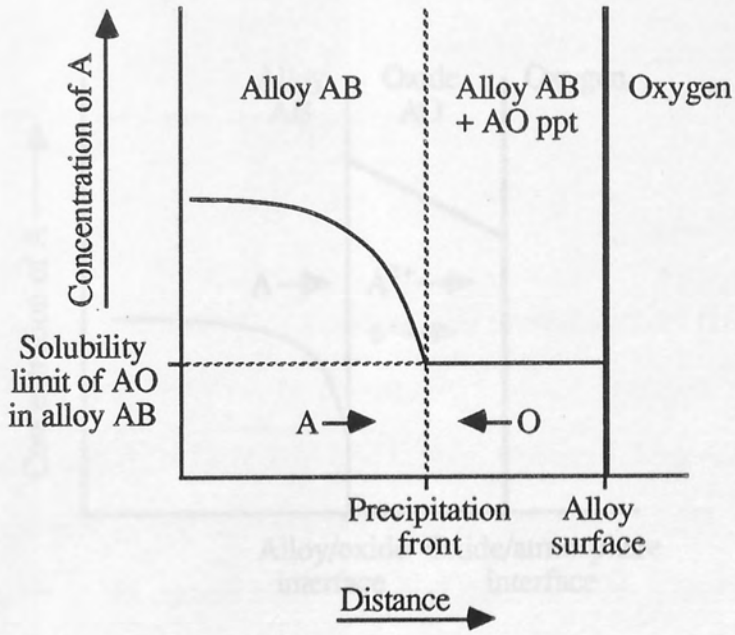

Figure 2.14. Internal oxidation, of less-noble solute element A in alloy AB.

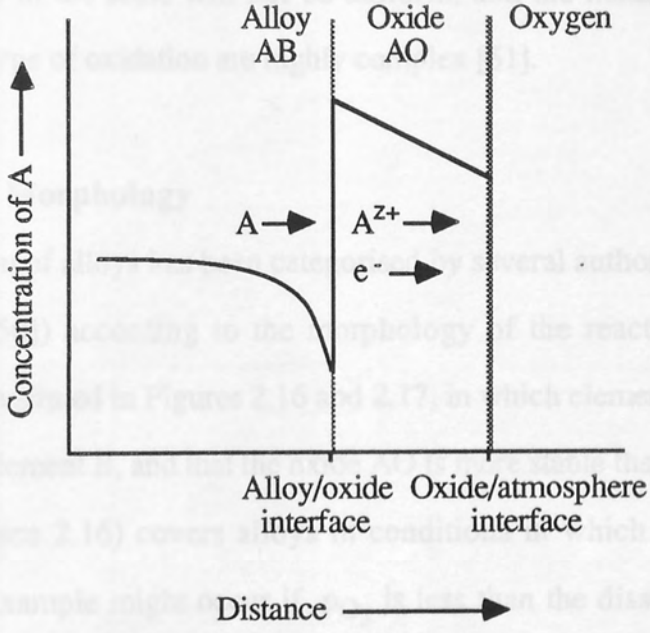

Figure 2.15. External oxidation of less-noble solute element A in alloy AB.

which is formed, the chemical potentials, as a function of position, in turn depend on the phases. Thus the steady state configuration has to be arrived at by an iterative process [50].

If both metals oxidise to form a single solid solution with oxygen, the ratio of the concentrations of metals A and B in the scale will not be equal to the ratio in the alloy, since the less noble metal will tend to enter the scale preferentially. Further, because of the different diffusivities of the cations of metals A and B, the ratio of metals A and B in the scale will vary with distance from the alloy/oxide interface. Thus the distribution of A and B cations in the scale will not be uniform, and the mathematics required for analysis of this type of oxidation are highly complex [51].

2.12.3 Oxide Morphology

The oxidation of alloys has been categorised by several authors (see Wallwork [6], and Atkinson [50]) according to the morphology of the reaction products. These categories are illustrated in Figures 2.16 and 2.17, in which element A is assumed to be less noble than element B, and that the oxide AO is more stable than BO.

Class I (Figure 2.16) covers alloys in conditions in which element B does not oxidise, as for example might occur if p_{O_2} is less than the dissociation pressure for BO. In Figure 2.16a, the outward flux of A is insufficient for the growth of an external oxide layer. Class I oxide scales (Figures 2.16b, 2.16c and 2.16d) may contain a dispersed particulate phase of pure metal B precipitate, or the alloy immediately below the alloy/oxide interface may be enriched with element B. If the concentration of A is greater than B, a continuous external layer of AO should be formed without any internal oxidation [6].

Class II (Figure 2.17) represents the more common alloys, of industrial importance, in which the addition A may be intended to improve the oxidation resistance of the pure metal B. Figures 2.17a and 2.17b represent alloys in which the concentration of A is insufficient to form a protective layer of AO, and is therefore unable to suppress the

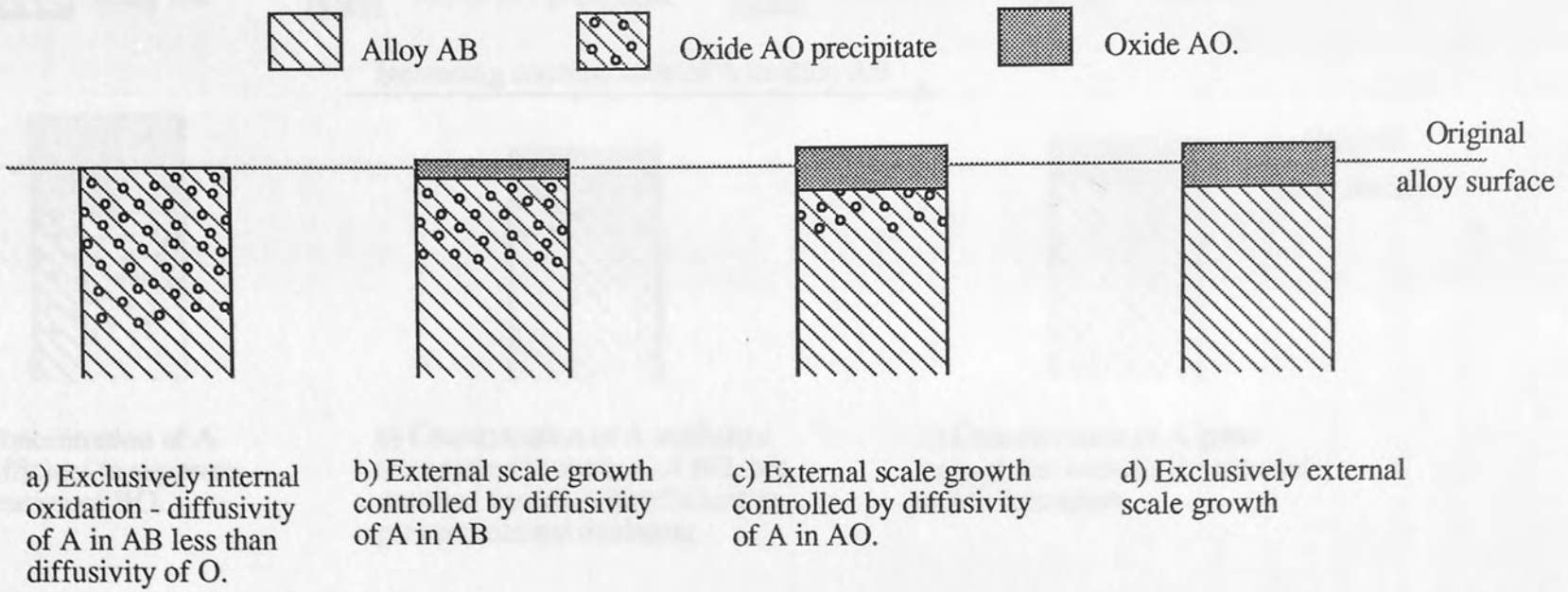

Figure 2.16. Class I oxide morphologies (after Wood [179] and Atkinson [50]). Alloy component A in alloy AB selectively oxidised, alloy component B relatively noble.

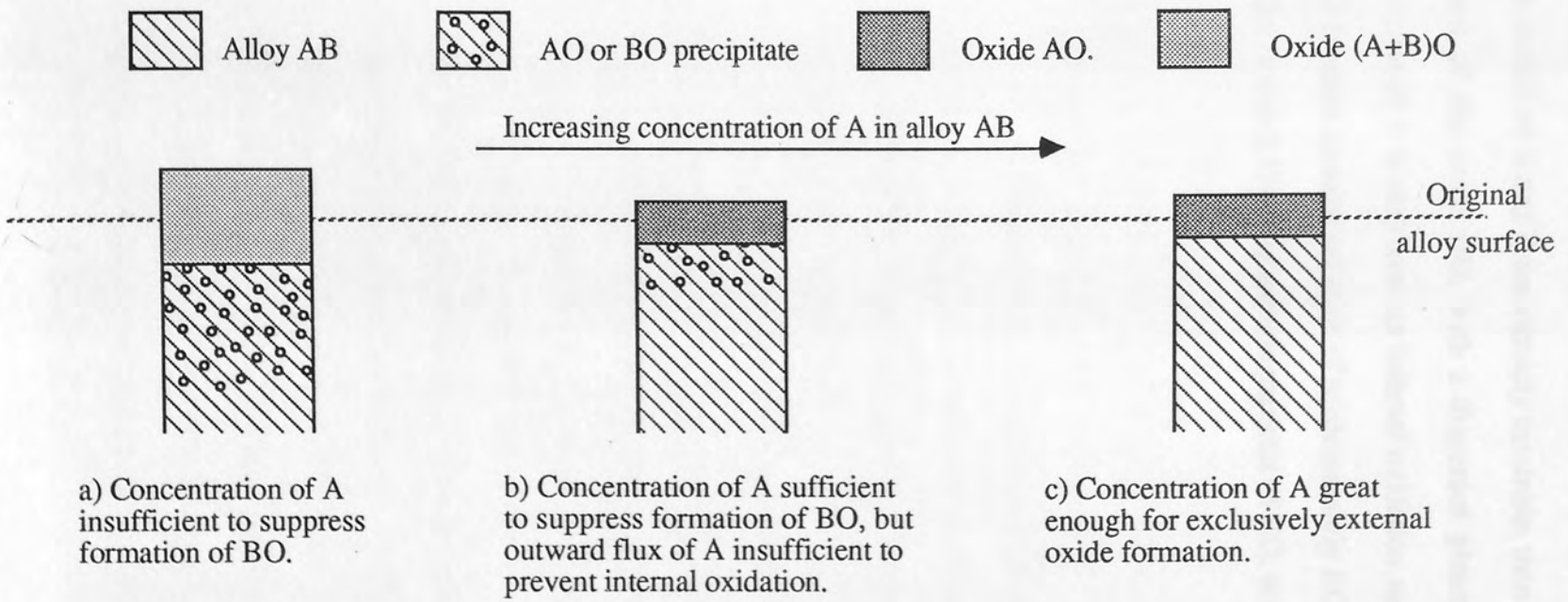

Figure 2.17. Class II oxide morphologies (after Wood [179] and Atkinson [50]). Alloy component A added to matrix B to prevent formation of oxide BO.

formation of the oxide BO.

If AO and BO can react to form a compound, then (AO+BO) may be a single solid solution, or a double oxide (eg. a spinel), which may form a continuous layer of variable composition, or particles in a matrix of BO.

If the oxides of A and B are virtually insoluble, then the scale matrix will probably be formed of the oxide BO, with a dispersed phase of AO particles [6]. If the concentration of A is very low, an internal oxidation zone of AO precipitates may be produced beneath an external scale of predominantly BO [50]. The oxide precipitate in Figures 2.17a and 2.17b may include particles of BO, or (AO+BO).

Section 3

THE OXIDATION OF IRON

Literature Review

3.1 THE IRON-OXYGEN SYSTEM

The Fe-O system (Figure 3.1a) has three independent phases: wüstite ('FeO'), magnetite (Fe_3O_4) and haematite (Fe_2O_3). The solid solubility of oxygen in haematite is negligible, and it may be considered in terms of its stoichiometric compositions (30.06wt% O). There has been some disagreement about the stable range of the magnetite phase field over the years [52, 53]. Darken and Gurry [54] concluded that magnetite is very slightly metal deficient at all but the lowest oxygen partial pressures; at very low values of p_{O_2}, Fe_3O_4 becomes stoichiometric and may even contain a slight metal excess when in equilibrium with wüstite. Above 750°C magnetite is able to dissolve a small amount of oxygen in excess to stoichiometry (up to 0.72 wt% O at its melting point, 1597°C) [54].Magnetite is generally treated in terms of the stoichiometric composition, Fe_3O_4, at all temperatures.

Wüstite is only stable at temperatures above 570°C, below which it will decompose eutectoidally, under equilibrium conditions, into Fe_3O_4 and metallic Fe. Most workers [54 - 56] agree that the wüstite region does not include the composition corresponding to the stoichiometric composition FeO (22.27 wt% O), but is an intermediate phase with excess oxygen. However, Bénard [57] places the low oxygen boundary practically coincident with stoichiometric FeO (22.27 wt% O) at low temperatures, and suggests that the phase field may expand to include it at high temperatures (>800°C). A comparison of published versions of the wüstite phase field has been made by Jette and Foote ([55], their Figure 2), and shows the considerable disagreement on its range and shape. The terms 'wüstite' and 'FeO' are interchangeable in most published work.

From consideration of the formulae, it is apparent that 'FeO' is composed of

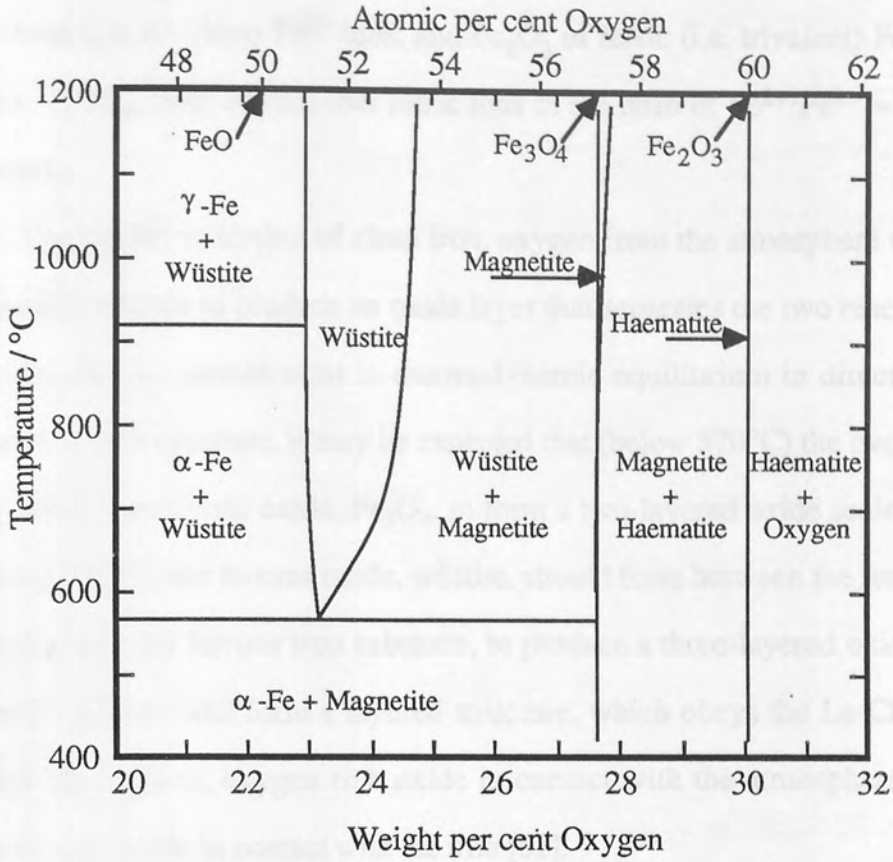

Figure 3.1a

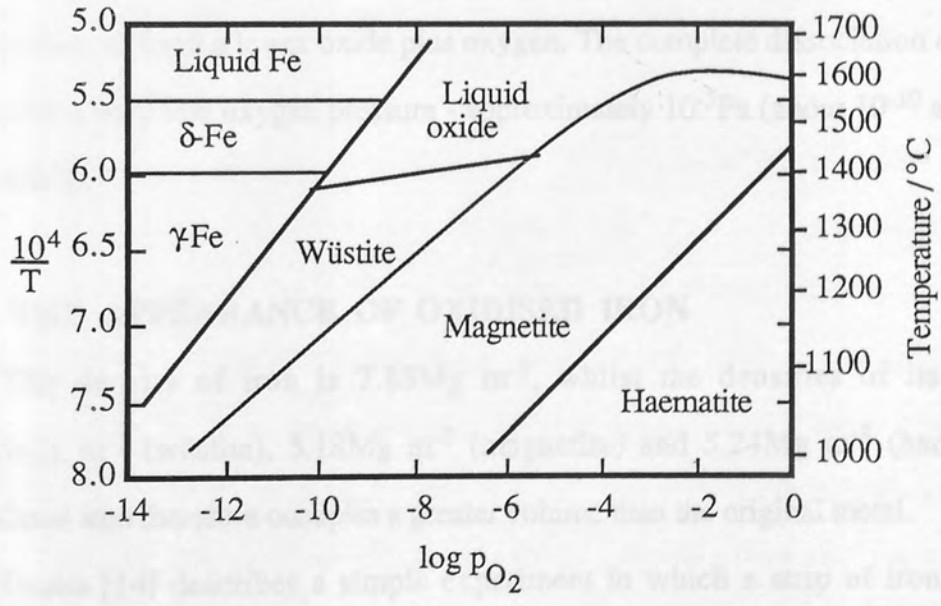

Figure 3.1b

Figure 3.1. The iron oxygen system (after Darken and Gurry [54])

ferrous (i.e. divalent) Fe^{2+} ions, and Fe_2O_3 of ferric (i.e. trivalent) Fe^{3+} ions, with O^{2-} ions. Fe_3O_4, with ferrous and ferric ions in the ratio of Fe^{2+}:Fe^{3+} = 1:2, is an inverse spinel.

During the oxidation of clean iron, oxygen from the atmosphere will react with the metallic surface to produce an oxide layer that separates the two reactants. Since ferric oxide, Fe_2O_3, cannot exist in thermodynamic equilibrium in direct contact with the metallic iron substrate, it may be expected that (below 570°C) the two will be separated by the ferroso-ferric oxide, Fe_3O_4, to form a two-layered oxide scale. At temperatures above 570°C, the ferrous oxide, wüstite, should form between the ferroso-ferric oxide, Fe_3O_4, and the ferrous iron substrate, to produce a three-layered oxide scale. Thus the oxides of iron will form a layered structure, which obeys the Le Chatelier principle, with the highest, oxygen rich oxide in contact with the atmosphere, and the lowest, metal rich oxide in contact with the iron [52].

Figure 3.1b shows the temperature-pressure diagram for iron at unit activity. For a given temperature, reducing the partial pressure of oxygen will cause a higher oxide to dissociate, to form a lower oxide plus oxygen. The complete dissociation of iron oxide requires a very low oxygen pressure - approximately 10^{-5}Pa (about 10^{-10} atmospheres) at 1400°C.

3.2 THE APPEARANCE OF OXIDISED IRON

The density of iron is 7.85Mg m^{-3}, whilst the densities of its oxides are 5.25Mg m^{-3} (wüstite), 5.18Mg m^{-3} (magnetite) and 5.24Mg m^{-3} (haematite) [2]. Oxidised iron therefore occupies a greater volume than the original metal.

Evans [14] describes a simple experiment in which a strip of iron, previously cleaned by abrasion, is strongly heated by a flame at one end, to produce a wedge-shaped oxide film that gets thicker towards the heated end. The thin film of haematite formed at the low-temperature end is transparent, so that incident light is reflected by both the oxide and the underlying metallic surfaces. Interference between the reflected

light rays will, for certain thicknesses of oxide film, cause the partial extinction of particular wavelengths of light, so that the oxide appears to progress through a series of colours as it thickens (see Figure 3.2). However, the thickness of the oxide film cannot be determined from the interference colour alone; destructive interference in thin films occurs when

$$2x = n\lambda \qquad \text{Eq. 3.1}$$

where x is the film thickness, λ is the wavelength of light, and n integer (n = 1, 2, 3...) that cannot be determined from the interference colour. Evans [58] found that the thickness of oxide films producing interference colours is affected by the presence of impurities in the iron, and Mehl and McCandless [59] have noted that the surface preparation before oxidation also has an effect.

The interference colours become fainter as the thickness of semi-transparent oxide increases. Towards the heated end of the strip, a layer of magnetite is formed between the iron and haematite. This under-growth of nearly opaque oxide reduces the thickness of transparent oxide, and a second series of interference colours is created by reflections at the interface of the two oxide layers. Thicker oxide films are opaque, and take on the blue-grey hue of the bulk oxide.

Scales formed by the oxidation of annealed iron between 400°C and 600°C may spall during oxidation, because of cavities formed by vacancy condensation at the metal/oxide interface. The provision of vacancy sinks, for example by prior cold work to increase the number of dislocations in the metal, can make the scale more adherent [32]. Above 600°C, oxide scales usually have enough plasticity to enable them to subside into pores at the metal/oxide interface, maintaining contact with the substrate [32], although plastic flow of oxide can be prevented by unfavourable surface geometries. The differences in the degree contraction of the parent metal and the oxide scale is a frequent cause of spalling during cooling.

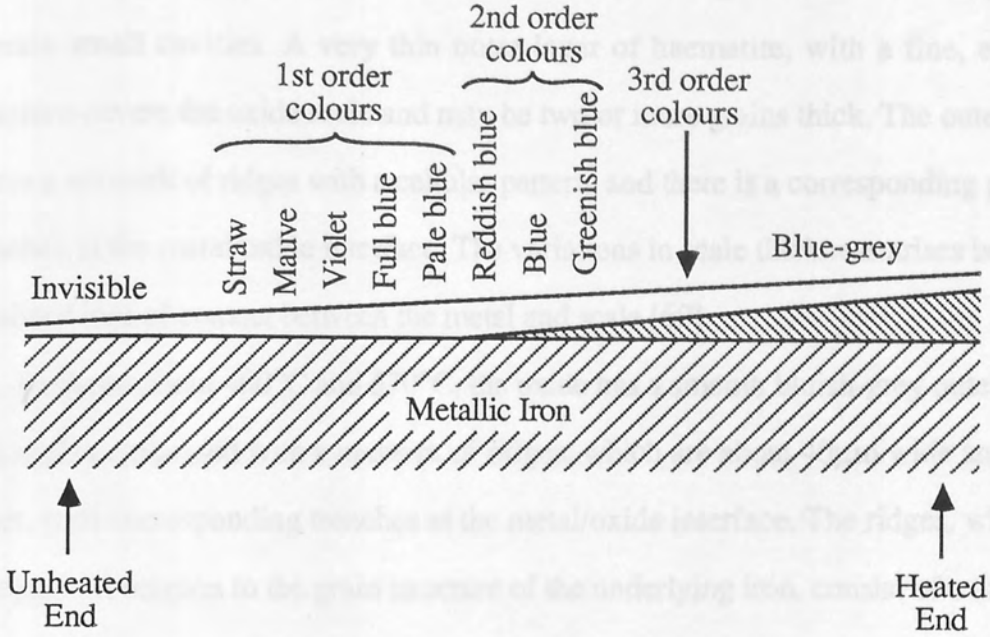

Figure 3.2. Interference colours on an oxidised iron strip (after [14]).

3.3 MICROSTRUCTURE OF IRON OXIDE SCALES

Oxide scales formed at high temperatures (>650°C) generally consist of a coarse columnar-grained layer of wüstite, one grain thick, covered by magnetite, which forms in a much thinner layer, but is also columnar and one grain thick. Both layers may contain small cavities. A very thin outer layer of haematite, with a fine, equi-axed structure covers the oxide scale and may be two or more grains thick. The outer surface forms a network of ridges with a cellular pattern, and there is a corresponding pattern of trenches at the metal/oxide interface. The variations in scale thickness arises because of localised loss of contact between the metal and scale [60].

Between about 400°C and 570°C, the oxide has a smooth bluish-grey outer surface, and is also embossed with a network of ridges, which are about 40μm wide and 200μm apart, with corresponding trenches at the metal/oxide interface. The ridges, which bear no apparent relation to the grain structure of the underlying iron, consist of a thick layer of magnetite, covered by a thin layer of haematite. The intervening depressions are areas of oxide that have become separated from the metal during growth, so that the iron ions required for continued growth have to diffuse from the ridge areas, where contact has been maintained. The curtailed iron supply reduces oxide growth, and leads to the oxidation of the magnetite by the overlying haematite, which becomes the thickest layer in the separated areas. In silhouette, at high magnification, Fe_2O_3 whiskers are detectable on the outer surface [61].

The magnetite layer formed in this temperature range often has a duplex structure, with an porous inner layer of fine equi-axed grains, and an outer layer of coarse columnar grains. The outer layer contains larger cavities, which form at grain boundaries and within the columnar grains. These large oval voids appear to be arranged around common centres in rosette-like clusters. The porosity found in this layer does not form an interconnecting network and is not connected to the oxide/atmosphere interface. The haematite layer is imporous [62].

The surfaces of stress ruptures in the scale are oxidised by the ingress of the

atmosphere, so that a higher oxide may be found beneath a lower oxide [33, 63]. Such a structure may be used to differentiate between growth cracks, due to oxidation, and thermal stress cracks, arising from shrinkage of the metal and oxide during cooling [33].

3.4 COMPOSITION OF SCALES

Above the eutectoid temperature, iron develops three oxide layers which correspond to wüstite (next to the metal), magnetite, and haematite (in contact with the atmosphere) [38, 56]. However the composition of each layer changes continuously, with the metal content highest at the interface closest to the metallic base, and discontinuities in composition at the interfaces [38]; the formulae FeO, Fe_3O_4 and Fe_2O_3 can at best represent the exact composition at only certain particular levels within the scale.

Over a long period of oxidation at high temperatures (>600°C) the three layers will (provided the oxide scale maintains contact with the metallic base) form relative thicknesses in the approximate ratio [19, 52, 60, 64, 65]:

$$\text{wüstite : magnetite : haematite} = 95 : 4 : 1 \qquad \text{Eq. 3.2}$$

The haematite layer is very thin relative to the other oxides, and is sometimes overlooked, as seems probable in the work of Pilling and Bedworth [22], or is ignored: for example, Shaw and Rolls [19] consider the thickness of haematite to have a negligible effect on oxidation, which enabled them to use a theoretical treatment [66] to predict the relative thicknesses of wüstite and magnetite.

Oxide scales formed between 225°C and 570°C usually consist of magnetite with an over-growth of haematite [61, 62, 67 - 72]. The initial oxide may consist of only Fe_3O_4, but after some incubation period has elapsed, a layer of α-Fe_2O_3 nucleates and grows laterally across the surface. The magnetite layer is thickest on attached scales formed at the high end of this temperature range, and over long periods may account for up to 90% of the scale [61], but at around 225°C the oxide layers are likely to be of about equal thickness [67].

The initial oxide formed below 225°C usually has a cubic structure intermediate between Fe_3O_4 and γ-Fe_2O_3, although many workers have observed a single layer of α-Fe_2O_3. After some period of time, α-Fe_2O_3 nucleates and grows across the surface of the cubic oxide, whilst the inner layer becomes resolved into Fe_3O_4 next to the iron and γ-Fe_2O_3 next to the α-Fe_2O_3, with a continuous change of structure and composition in between [67, 68, 73 - 75].

At room temperature in an unpolluted atmosphere, a clean iron surface rapidly forms a very thin passive oxide film [73, 76, 77]. This film is transparent so that the iron appears to retain the original bright surface exposed to the atmosphere, and in this condition can remain stable for long periods (at least 20 years [76]). The film has a composition and structure intermediate between Fe_3O_4 and γ-Fe_2O_3, and may form a covering layer of α-Fe_2O_3. These observations are summarised schematically in Figure 3.3.

3.5 IRON OXIDATION KINETICS

As would be expected from theoretical considerations, the oxidation of iron commences with an initial linear [78, 79], or possibly logarithmic [70, 71, 79], phase, and then progresses to logarithmic kinetics at low temperatures, or parabolic kinetics at high temperatures (see also references [67, 69, 80, 81]). The transition between logarithmic and parabolic kinetics occurs between 200°C and 400°C, depending on the composition and preparation of the iron, and the oxidising atmosphere [67, 71, 80, 81].

The temperature dependence of the parabolic scaling constant obeys the Arrhenius equation (Figure 3.4). There is a discontinuity at around 600°C which is probably associated with the appearance of wüstite in the scale [52]. Another discontinuity occurs between 910°C and 950°C, which is thought to be associated with the α-Fe$\rightarrow\gamma$-Fe phase transformation at 910°C, although it has been suggested that it is due to the delamination of the scale by growth stresses [82].

The observed parabolic scaling constant may vary with time because of the

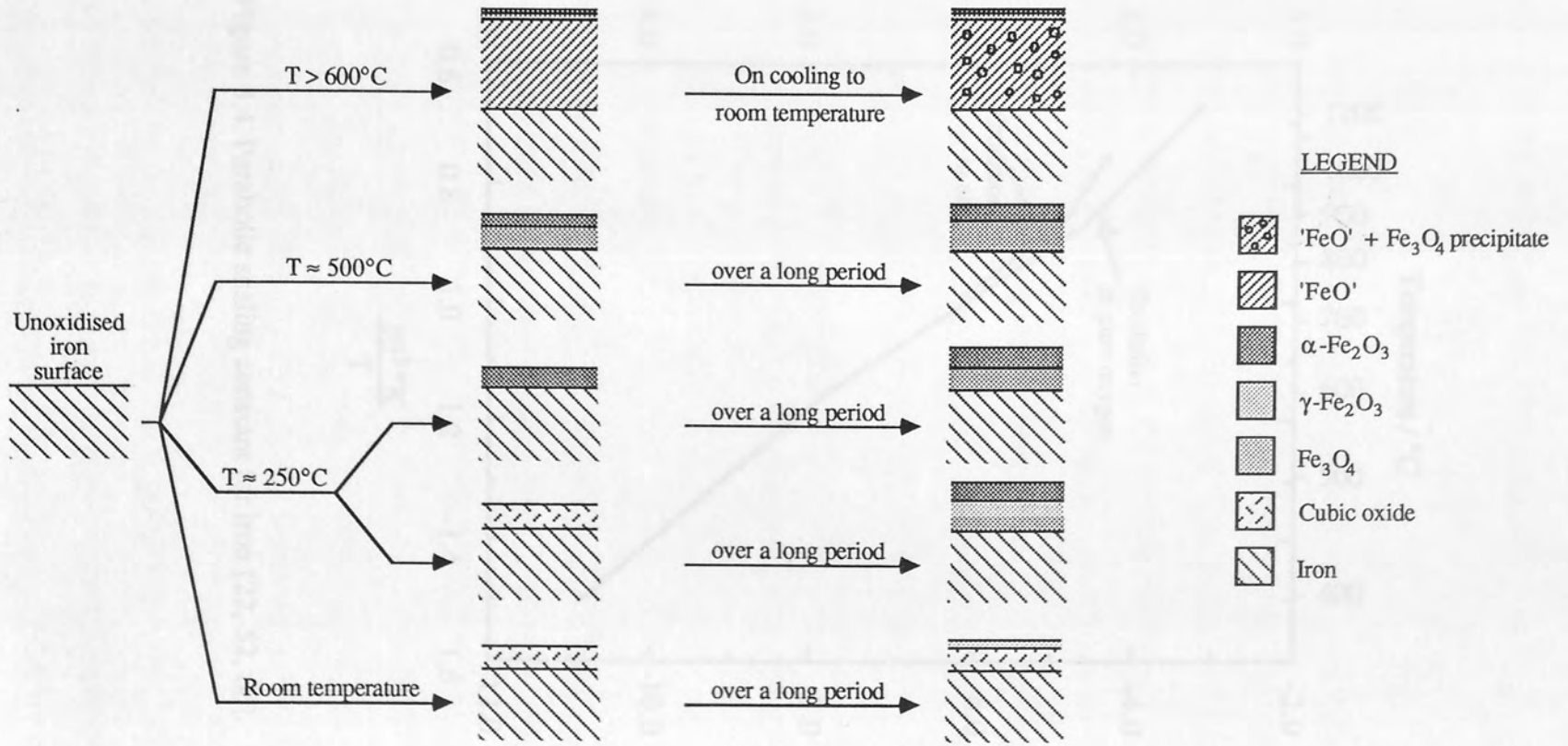

Figure 3.3. Structure of iron oxide scales formed at different temperatures.

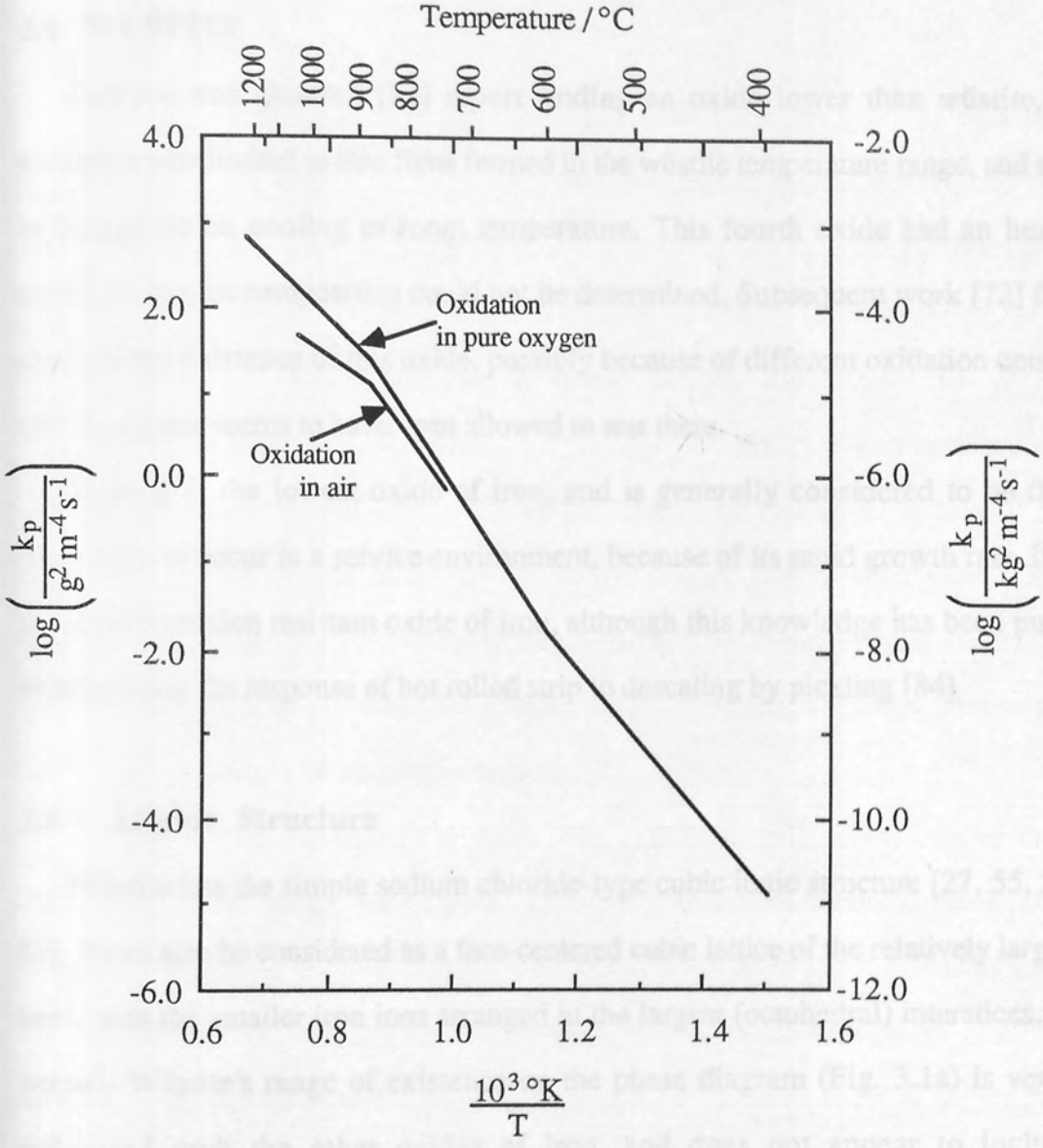

Figure 3.4. Parabolic scaling constant for iron [22, 52, 60].

formation, and healing, of defects at the metal/scale interface and within the scale itself [61]. Discrepancies between published results arise because of the different purities and preparations of materials (e.g. see [32, 60, 67, 70, 72]).

3.6 WÜSTITE

Jackson and Quarrell [83] report finding an oxide lower than wüstite, whose existence was limited to thin films formed in the wüstite temperature range, and reverted to magnetite on cooling to room temperature. This fourth oxide had an hexagonal structure, but its composition could not be determined. Subsequent work [72] failed to confirm the existence of this oxide, possibly because of different oxidation conditions, and the matter seems to have been allowed to rest there.

Wüstite is the lowest oxide of iron, and is generally considered to be the least desireable to occur in a service environment, because of its rapid growth rate. It is also the least corrosion resistant oxide of iron, although this knowledge has been put to use in improving the response of hot rolled strip to descaling by pickling [84].

3.6.1 Atomic Structure

Wüstite has the simple sodium chloride-type cubic ionic structure [27, 55, 59, 85 - 89]. It can also be considered as a face-centered cubic lattice of the relatively large oxide ions, with the smaller iron ions arranged in the largest (octohedral) interstices, or *vice versa*[1]. Wüstite's range of existence on the phase diagram (Fig. 3.1a) is very wide compared with the other oxides of iron, and does not appear to include the stoichiometric composition FeO implied by its NaCl-type structure (see Section 3.1).

The excess oxygen appears to be entirely due to vacancies in the iron sub-lattice [55, 86 - 88], whilst the oxygen sub-lattice is thought to be perfect (at equilibrium) [53]. The formula for wüstite is therefore more accurately expressed as $Fe_{1-\delta}O$, in which δ represents the iron deficiency, expressed as the ratio of vacant cation sites to

1 The radii of ionic species in iron oxides are 132pm (O^{2-}), 74pm (Fe^{2+}) and 64pm (Fe^{3+}) [2].

the total number of cation sites, hence

$$\delta = 1 - \left(\frac{m_{Fe}}{M_{Fe}} \frac{M_O}{m_O} \right) \qquad \text{Eq. 3.3}$$

where m_{Fe}, m_O are the masses of iron and oxygen in the oxide, and M_{Fe}, M_O are their atomic masses respectively. At 1000°C, wüstite has a range of compositions varying between $Fe_{0.876}O$ and $Fe_{0.956}O$.

The vacancies in the iron sub-lattice are distributed in a linear concentration gradient, which increases towards the wüstite/magnetite interface [88], and many of them form clusters with resulting poor mobility [90]. The number of 'free vacancies' increases as a function of temperature and the iron deficiency of the oxide [90], but their mobility appears to be independent of the overall vacancy concentration [88, 90].

To maintain the electrical neutrality of the oxide, the deficiency of iron ions calls for the presence of both Fe^{2+} and Fe^{3+} in the structure. The number of Fe^{3+} ions is determined by the degree of deficiency, so that $Fe_{1-\delta}O$ will contain 2δ Fe^{3+} ions per formula unit. With the reduction in size brought about by the removal of an electron, the ferric ions are able to move into the smaller tetrahedral sites, whilst the ferrous ions are confined to the larger octohedral interstices [86].

Neutron diffraction studies by Roth [87], and X-ray diffraction studies by Smuts [86], have shown that the vacancy concentration is about double the number calculated from the iron deficit, and that iron ion interstitials are present in concentrations of about half that of the total vacancy concentration. It seems, therefore, that for each vacancy created as a result of non-stoichiometry, an equal number of Frenkel defect pairs are formed simultaneously in the iron sub-lattice. The interstitial ferric ions do not occupy tetrahedral sites in a systematic manner [86], although Roth [87] suggests that if they did, they might act as the nuclei for the magnetite crystals formed during the decomposition of wüstite below 570°C (see Section 3.7.3).

The absence of some of relatively large ferrous ions and the substitution of others by smaller ferric ions reduces the atomic volume of wüstite. The lattice parameter of wüstite, $a_{'FeO'}$, is therefore dependent on the iron content, and Jette and Foote [91] have

found that there is a nearly linear relationship between the two (Figure 3.5a). Goldschmidt [85] has confirmed that this applies to wüstite layers on iron, so that $a_{'FeO'}$ decreases with increasing distance from the metallic substrate. The range of values of the wüstite lattice parameter (between the Fe/'FeO' and 'FeO'/Fe_3O_4 interfaces) increases as the oxidation temperature increases [92] (Figure 3.5b) because of the increasing composition range of the wüstite phase.

3.6.2 Epitaxy of Iron and Wüstite

Goldschmidt [85] suggests that the results of Jette and Foote [91] may indicate some simple relationship between the structures of α-Fe and wüstite, based on the fact that

$$2a_{'FeO'} \approx 3a_{\alpha\text{-}Fe} \qquad \text{Eq. 3.4}$$

and that this approximation becomes increasingly accurate as the iron-rich boundary of the wüstite phase field is approached. In other words, 2^3 unit cells of 'FeO' occupy the same volume as 3^3 unit cells of α-Fe, and might be derived from the latter, in some way, by the removal of iron, the addition of oxygen and some rearrangement of the ions.

Wüstite layers grown on different planes of α-Fe single crystals all show the same crystallographic orientation relationship [59] (Figure 3.6c):

$$(100)_{\alpha\text{-}Fe} \parallel (100)_{'FeO'} \qquad \text{Eq. 3.5}$$

$$[100]_{\alpha\text{-}Fe} \parallel [110]_{'FeO'} \qquad \text{Eq. 3.6}$$

The epitaxy of this relationship places the 'FeO' lattice under some strain, which is apparent in X-ray diffraction patterns [59]. Calculation shows that the strain is compressive, and at most 6%, although this would probably be reduced slightly by expansion of the metal lattice [27].

The continuity between the two lattices suggests a possible atomic-crystallographic mechanism for the formation of the 'FeO' from α-Fe [59]. The body-centred cubic

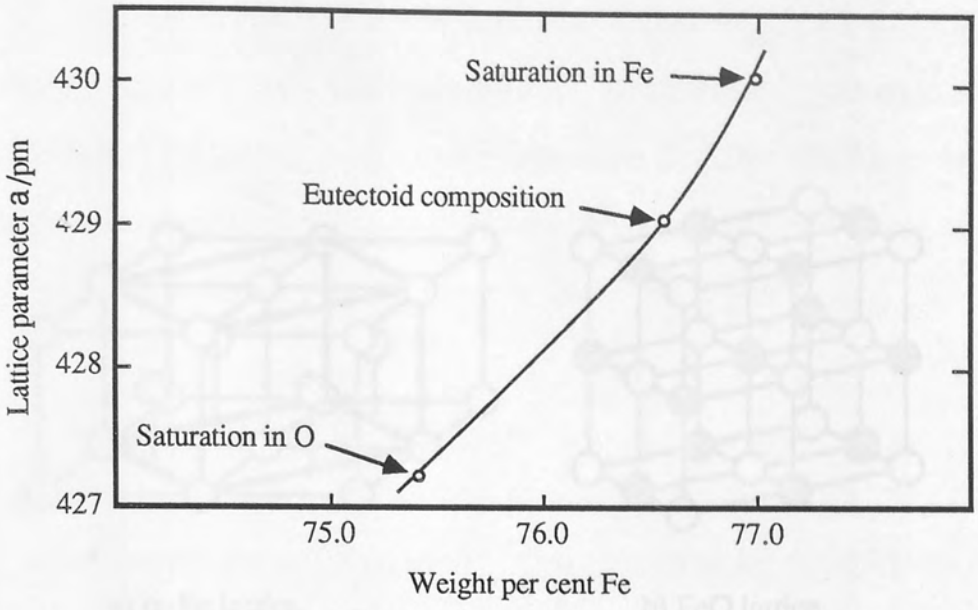

Figure 3.5a. Wüstite lattice constant as a function of iron content (after Jette and Foote [91]).

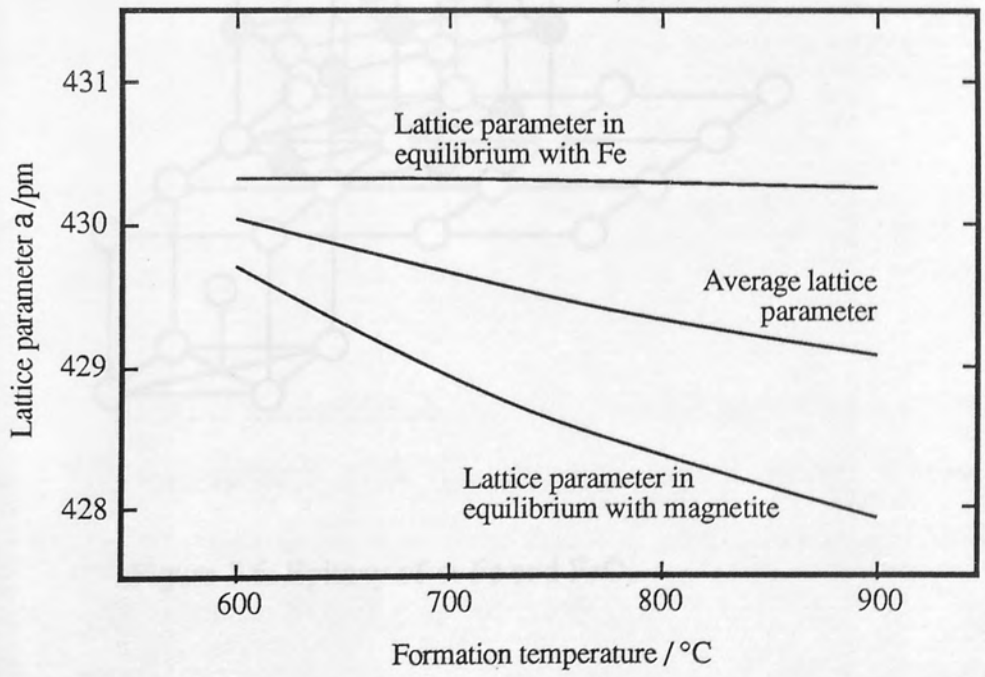

Figure 3.5b. Lattice parameter of wüstite as a function of temperature (after Pinder [92]).

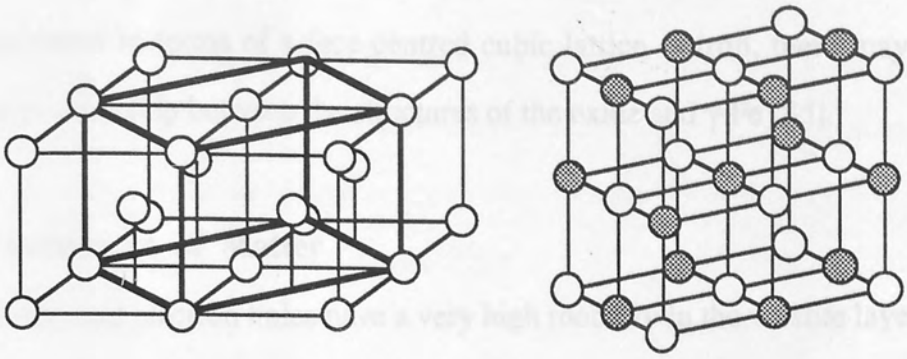

a) α-Fe lattice. b) FeO lattice.

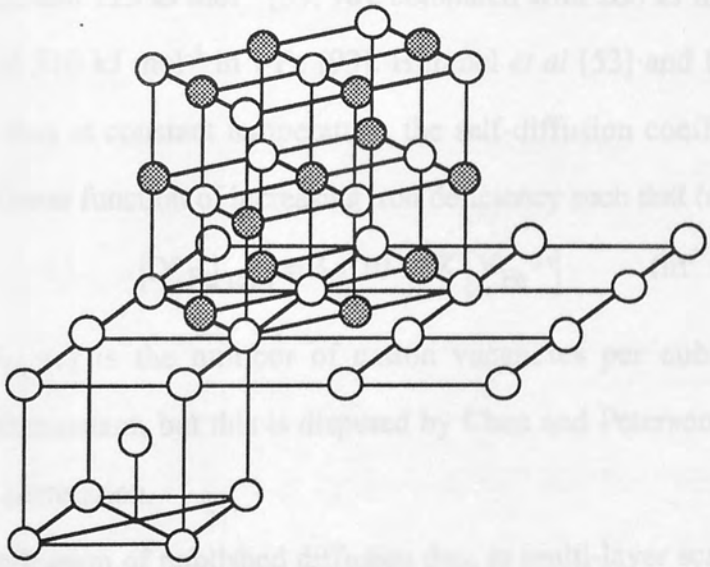

Figure 3.6. Epitaxy of α-Fe and FeO.

lattice of α-Fe contains a face-centred tetragonal lattice with an axial ratio c:a equal to 1:√2 (Figure 3.6a). At the moment of formation of 'FeO' this face-centred tetragonal lattice could expand to form a face-centred cubic lattice of iron (with an axial ratio of unity), with oxygen ions at the octohedral interstices (Figure 3.6b). Since wüstite can be considered in terms of a face-centred cubic lattice of iron, there may be an even simpler relationship between the structures of the oxide and γ-Fe [85].

3.6.3 Transport of Matter

Cations and electron holes have a very high mobility in the wüstite layer because of the high concentration of cation vacancies. Measurements of the self-diffusion of iron in wüstite, using radioactive Fe^{55} tracers, show that diffusion requires an activation energy of around 123 kJ mol^{-1} [53, 90], compared with 280 kJ mol^{-1} for self-diffusion in α-Fe, and 310 kJ mol^{-1} in γ-Fe [93]. Himmel *et al* [53] and Hembree and Wagner [94] found that at constant temperature, the self-diffusion coefficient increases as an essentially linear function of increasing iron deficiency such that (at 1100°C)

$$\left(D^*_{Fe}\right)_{'FeO'} = 3 \times 10^{-25} K \left[V_{Fe}^{2+}\right] \qquad (m^2\ s^{-1}) \qquad \text{Eq. 3.7}$$

where $[V_{Fe^{2+}}]$ is the number of cation vacancies per cubic metre and K is a dimensional constant, but this is disputed by Chen and Peterson [90], who could find no specific correlation.

The application of published diffusion data to multi-layer scaling theories (eg. due to [20, 66]) of the oxidation of iron, and comparison with experimental evidence [19, 65, 95], show that wüstite grows at a rate that is in fairly good agreement with that predicted by the classical Wagner oxidation theory [41].

According to Engell [88], the diffusion coefficient of the mobile defects (ie. vacancies) in wüstite is somewhat greater than the self-diffusion coefficient of iron at high temperatures, which, it is suggested, may be due to the participation of oxygen in the transport of matter through the oxide. Marker experiments (eg. [37, 38, 52, 53,

96]) intended to determine the contributions made by ionic species to the growth of wüstite seem only to have confused the matter. Some experiments have indicated that the extent of diffusion of anions in wüstite is negligible, so that the Fe/'FeO' interface and oxide ions added at the outer face of the phase remain essentially fixed in space [33, 37, 52, 53].

Juenker *et al* [37] found that markers in adherent scales were always found at the metal/oxide interface, whereas with detached scales they were found buried within the separated oxide. Since the former observation precludes the inward diffusion of anions, the formation of oxide on the internal surface of the detached scale (necessary to cover the marker, which has stuck to the oxide during separation) must be due to the adsorption of gaseous oxygen. Pfeil [38] reports that clean iron heated in a vacuum, in the neighbourhood of oxygen-rich wüstite, aquires a wüstite scale, and Juenker *et al* [37] suggest that this dissociation mechanism would account for oxide growth at the void/oxide interface. However, the oxygen content at the void/oxide interface is not very high, and because of the very low dissociation pressure, such a mechanism is improbable (as discussed in Section 2.9.2); gaseous oxygen is much more likely to enter the void through micro-channels in the scale.

Sachs [96] has shown that the results of marker experiments are influenced to a considerable extent by the nature of the marker. For example, Sachs suggests that the radioactive silver markers used by Davies *et al* [52] may have been forced into solution in the wüstite, and after diffusing through the oxide, was finally deposited at the metal/oxide interface, leading to the incorrect conclusion that there is negligible anion diffusion. Sachs' own conclusion, based on several different types of marker, was that there is a minor, though not unimportant, contribution made by the inward diffusion of oxygen, counter-current to the outward diffusion of iron.

An experiment conducted by Mackenzie and Birchenall [97] has some bearing on this discussion. Whilst trying to prepare solid specimens of wüstite by the oxidation of iron in pure oxygen, they found that the result was a 'box' of wüstite. At 800°C, the internal dimensions of this box, which had sharp corners and good surface definition,

exactly corresponded to the original dimensions of the iron specimen. At higher temperatures, the dimensions of the void decreased, probably because the scale was more plastic, and able to follow the retreating metal surface. These observations indicate that at 800°C there is no (or negligible) inward growth of oxide, suggesting that there is no diffusion of anions.

The diffusion of oxygen through the lattice appears to be improbable under equilibrium conditions, because of the apparent perfection of the oxygen sub-lattice [53], and the small size of the interstitial sites relative to the oxide ions. It seems therefore, that the transport of oxygen through the wüstite layer must depend on short-circuit diffusion, and the direct oxidation of metallic iron (or metal-rich wüstite) by molecular oxygen penetrating cracks in the scale, or possibly formed by dissociation in cavities.

Possible pathways through the oxide, which could effectively short circuit lattice diffusion, are interconnected porosity, grain boundaries and dislocations [41]. Cavities in wüstite generally form by the condensation of vacancies [33, 37], so it is unlikely that they could form an interconnected network (rather they would grow in size and coalesce). Grain size has very little effect on the growth rate of wüstite [60], which implies that grain boundary transport makes only a small contribution to short circuit diffusion. The most probable short circuit pathways are therefore dislocations, which may arise from the deformation of the oxide.

3.6.4 Plasticity and Creep

The plasticity of wüstite, which increases rapidly above 800°C [98], is a major factor in the oxidation of iron. Without adequate vacancy sinks, the large number of vacancies created at the metal/oxide interface (by the departure of iron ions from the metal, into the oxide) will coalesce to form voids [33, 37]; the separation of metal and oxide should drastically reduce the oxidation rate, but this is not always observed because the plasticity of wüstite enables it to flow into the voids, maintaining contact

with the retreating metal surface [32, 37, 97].

Deformation of the wüstite layer is driven by the compressive stresses generated by the growth of the oxide scale, although the strain rate during isothermal oxidation is so low that creep data has to be used for modelling exercises, rather than compression or tensile data [21].

When the extent of plastic flow is insufficient for the wüstite to maintain contact with the metal (for example, below 800°C [98]), the oxide scale is suspended above the metal surface by the more rigid layers of magnetite and haematite (which have fewer slip systems in their spinel and rhombohedral structures, and are therefore less prone to plastic deformation [97]). The scale is supported by any parts of its structure that remain in contact with the metal surface.

3.6.5 Formation

Wüstite does not, in normal conditions, grow in direct contact with the atmosphere: the transfer of electrons to adsorbed oxygen atoms in the outer layers of the oxide scale results in the creation of ferric ions, and thus the formation of ferroso-ferric oxide (Fe_3O_4), or ferric oxide (Fe_2O_3). Therefore, the formation of the ferrous oxide, wüstite, must occur by the reduction of the outer layers of the oxide, as cations diffuse outwards from the metal.

In very thin oxide films wüstite is found to form at temperatures as low as 400°C [83], and its existence depends essentially on the extent of initial oxidation; it reverts to Fe_3O_4 if the film is allowed to thicken, and it is not found at all in thick oxide films below 570°C [72]. The initial magnetite film formed on iron is found to be in a strained state because of the difference between the lattice parameters of the oxide and iron, and Gulbransen and Ruka [100] suggest that the strain energy in the film is sufficient to activate the reduction of Fe_3O_4 to 'FeO' by ferrous ions,

$$Fe_3O_4 + Fe^{2+} + 2e^- = 4FeO \qquad \text{Eq. 3.8}$$

an event which is otherwise unlikely to occur below 570°C, based on thermodynamic

data.

The reduction of magnetite (Equation 3.5) in thin oxide films proceeds rapidly above 570°C, but much more slowly for thick films. Gulbransen and Ruka [100] attribute this to the length of the diffusion path for iron ions migrating through wüstite that has already formed.

3.6.6 Decomposition

The decomposition of a bulk sample of wüstite free from the metal has been studied by Chaudron, Bénard and co-workers. Chaudron [101] determined that decomposition below 570°C occurs by dissociation,

$$4\,FeO = Fe_3O_4 + Fe^{2+} + 2e^- \qquad \text{Eq. 3.9}$$

rather than by oxidation,

$$3\,FeO + O^{2-} = Fe_3O_4 + 2e^- \qquad \text{Eq. 3.10}$$

Chaudron and Forestier [102] have shown that the rate of isothermal decomposition is greatest at 480°C (Figure 3.7). It is clearly able to exist as a metastable phase at room temperature for very long periods (*viz* the work of Wingrove [103] on oxides in Roman slags). An X-ray diffraction study by Bénard and Chaudron [104] indicated that, between 350°C and 500°C, the iron which is first liberated dissolves in the remaining wüstite, increasing the lattice parameter. Later work [105] showed that the stability of wüstite depends upon the temperature of formation of the bulk oxide and its composition, and that the oxides richest in iron are the most stable.

Decomposition of wüstite scales on iron starts in the outer, oxygen rich region, with iron precipitating most readily along grain boundaries of the newly formed magnetite. The size of the precipitate particles tends to increase with increasing distance from the iron substrate [33], which is in accordance with the observations of Chaudron and Bénard [105].

The effects of wüstite decomposition, on the analysis of scale microstructures, were first noted by Jackson and Quarrell [83], who studied iron oxides both at high temperature and after cooling to room temperature. Bruce and Hancock [64] have

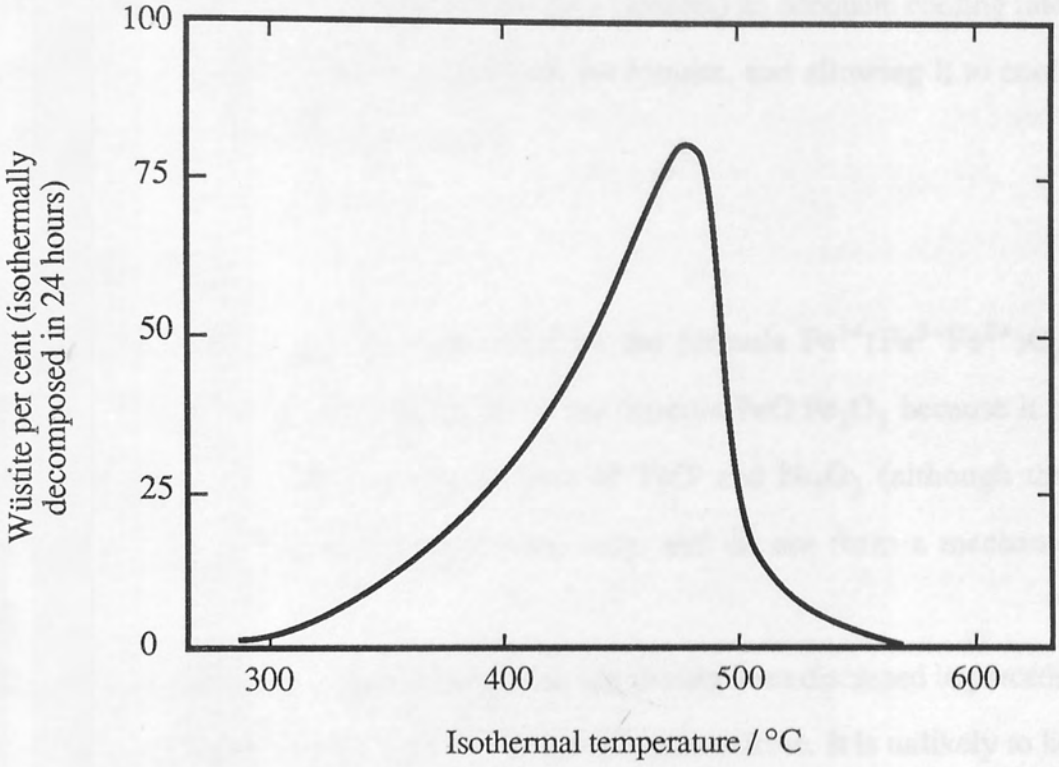

Figure 3.7. Isothermal decomposition of wüstite below 570°C (after Chaudron and Forestier [102]).

estimated that over 50% of the magnetite found in furnace-cooled oxide scales, formed at 800°C, may be due to the decomposition of wüstite. Therefore, the preservation of an oxide scale structure formed above 570°C (eg. for laboratory analysis) requires rapid cooling, although the effects of cooling stresses must also be considered. In general, it would appear that (in the case of small laboratory samples) an adequate cooling rate is achieved by removing the oxidised iron from the furnace, and allowing it to cool to room temperature in dry air (eg. see [106]).

3.7 MAGNETITE

Magnetite, Fe_3O_4, may be represented by the formula $Fe^{3+}(Fe^{3+}Fe^{2+})O_4$to emphasise that it is an inverse spinel, or by the formula $FeO.Fe_2O_3$ because it is a composite oxide, i.e. it behaves as a mixture of 'FeO' and Fe_2O_3 (although these oxides are present in molecular proportions only, and do not form a mechanical mixture).

Much that applies to the nature of magnetite has already been discussed in preceding sections, but it is worth repeating that it less ductile than wüstite. It is unlikely to heal cavities by creep, and if the magnetite layer is sufficiently thick it can provide the structural support necessary to prevent the scale following the retreating iron surface, thereby creating cavities at the metal/scale interface.

3.7.1 Atomic Structure

Goldschmidt [85] derived a simple relationship between the lattice parameters of metallic iron, wüstite and magnetite[2], using the work of Jette and Foote [91] (Figure 3.5). This was based on the following approximations:

$$a_{\alpha\text{-Fe}}:a_{\text{'FeO'}} \approx 3:2 \Rightarrow 2/3\ a_{\text{'FeO'}} \approx a_{\alpha\text{-Fe}} \qquad \text{Eq.3.11}$$

$$a_{\text{'FeO'}}:a_{Fe_3O_4} \rightarrow 2:1 \Rightarrow 1/3\ a_{Fe_3O_4} \approx a_{\alpha\text{-Fe}} \qquad \text{Eq.3.12}$$

2 The lattice parameters at 20°C are a(α-Fe) = 286pm, and a(Fe_3O_4) = 839pm [2, 87, 89, 92, 107, 108]

Equation 3.11 applies to iron-rich wüstite, and Equation 3.12 is based on an extrapolation of a_{FeO} to the oxygen content of Fe_3O_4. A plot of these approximations, against oxide oxygen content (Figure 3.8), suggests that some simple relationship exists between the ionic structures of wüstite and magnetite. Goldschmidt proposed that magnetite could be derived from wüstite by the removal of iron ions, and some rearrangement of oxygen ions, but without the need for a structural transformation.

The unit cell of magnetite is constructed of 32 oxygen ions and 24 iron ions (ie. $Fe_{24}O_{32}$, with 8 Fe^{2+} and 16 Fe^{3+} ions) [87, 92, 107, 108]. The arrangement of the ions has been interpreted in several ways, all with the aim of maintaining the cubic symmetry of the unit cell. Most workers advocate a cubic close-packing arrangement of the oxygen ions to form eight, face centred cubic cells, with iron ions at the interstices (Figure 3.9c) [68, 87, 107 - 109]. This construction contains 64 tetrahedral interstices (surrounded by four oxygen ions) and 32 larger octahedral interstices (surrounded by six oxygen ions). The eight relatively large ferrous ions are confined to octahedral sites, and the smaller ferric ions appear to be divided equally between the octohedral and tetrahedral sites.

Magnetite has the inverse spinel structure below room temperature, but at higher temperatures the the cation distribution is not so clear [109]. According to Roth [87] the Fe_3O_4 structure of is obtained by alternating layers shown in Figures 3.9a and 3.9b. Based on magnetite's relatively high electrical conductivity, Verwey and Haayman [107] have suggested that iron ions occupy the octohedral sites at random, and that their distribution fluctuates (and might be described statistically).

The homogeneity range of magnetite is much narrower than that for wüstite, and expands with increasing temperature and increasing oxygen pressure [54]. Verwey and Haayman [107] have shown, from X-ray lattice parameter measurements, that the deviation from stoichiometry is due to vacant cation sites, rather than interstitial oxide ions. These vacancies are most likely to occur at octohedral sites [68, 75], and Dieckmann and Schmalzried [110] have determined that the dependence of tetrahedral (V_{Tet}) and octohedral (V_{Oct}) vacancies on the partial pressure of oxygen is given by

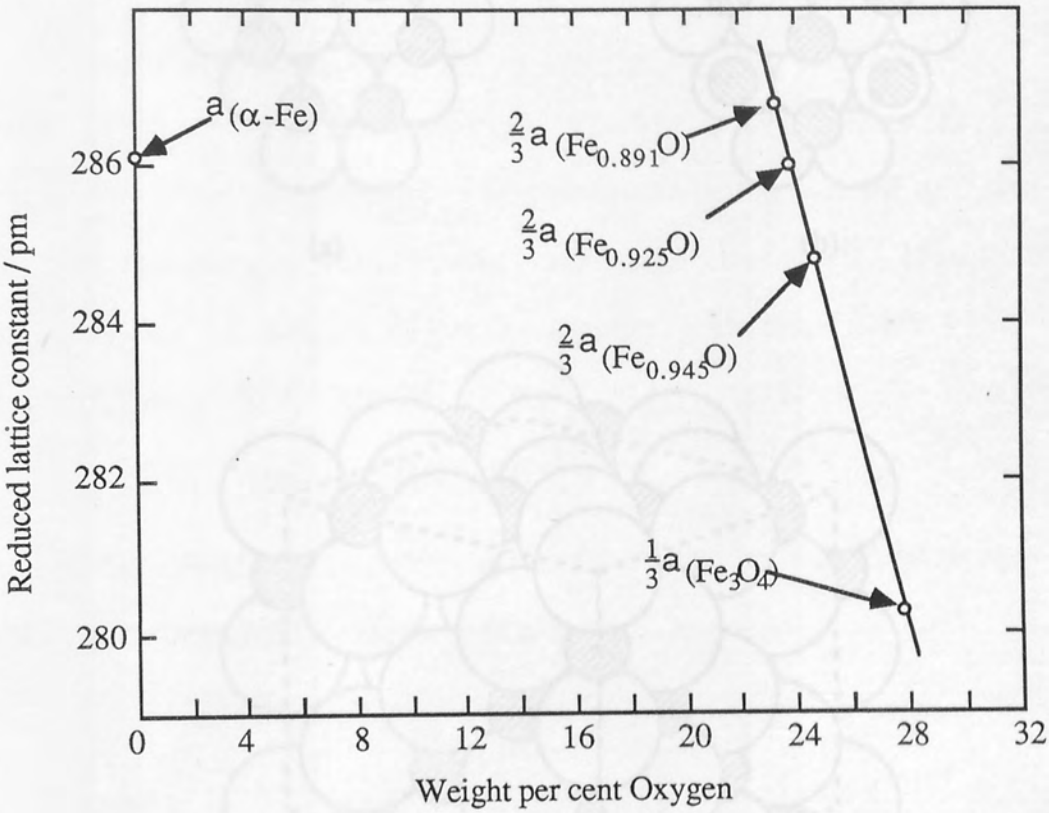

Figure 3.8. Lattice constants of 'FeO' and Fe_3O_4, as a function of oxygen content (after Goldschmidt [85]).

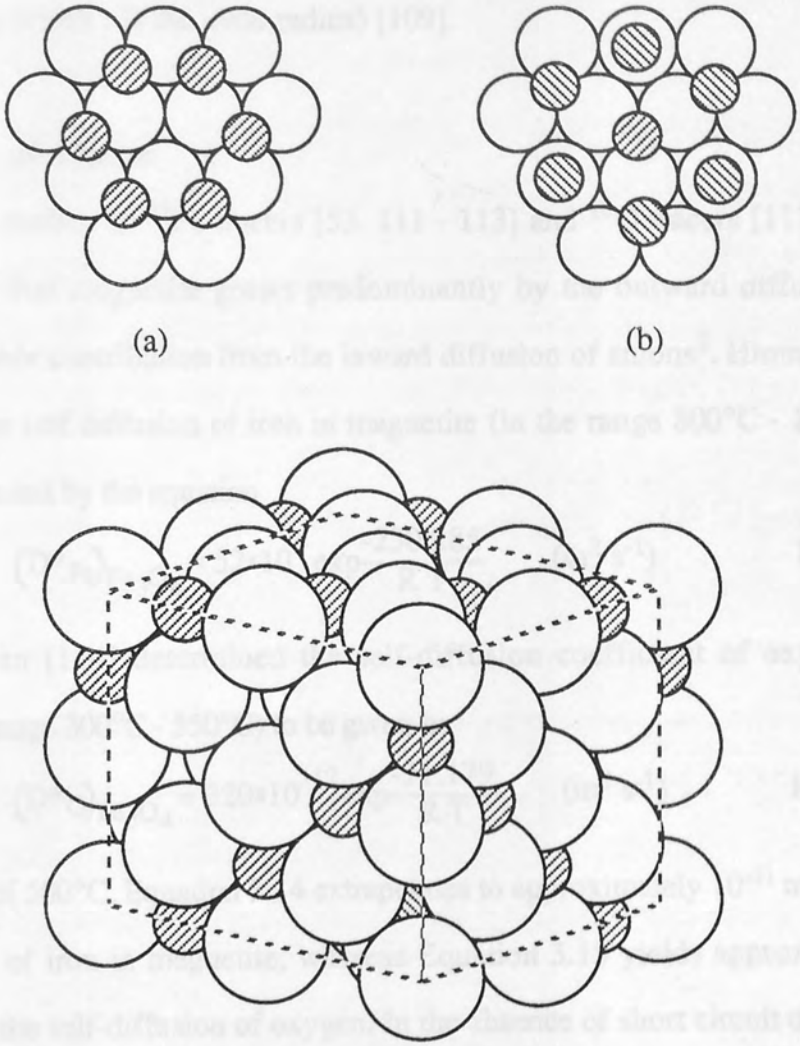

Figure 3.9. Ionic structure of magnetite. (a) and (b) show an arrangment of iron ions in successive close-packed planes of oxygen ions (after Roth [87]). (c) Magnetite unit cell (after Jette and Foote [91]).

$$V_{Tet} \alpha V_{Oct} \alpha (p_{O_2})^{2/3} \qquad \text{Eq.3.13}$$

The oxygen sub-lattice is nearly perfect compared to the iron sub-lattice, which may be concluded from the dense packing and the relatively large size of the oxide ions ($r_{O^{2-}} \approx 2\, r_{Fe^{2+}} \approx 2\, r_{Fe^{3+}}$, where r is the ionic radius) [109].

3.7.2 Transport of Matter

Self-diffusion studies of ^{55}Fe tracers [53, 111 - 113] and ^{18}O tracers [111, 113 - 115] have shown that magnetite grows predominantly by the outward diffusion of cations, with a minor contribution from the inward diffusion of anions[3]. Himmel *et al* [53] found that the self diffusion of iron in magnetite (in the range 800°C - 1000°C) could be approximated by the equation

$$(D^*_{Fe})_{Fe_3O_4} = 52 \times 10^{3} \exp\frac{-230{,}285}{R\,T} \qquad (m^2\ s^{-1}) \qquad \text{Eq.3.14}$$

Castle and Surman [114] determined the self-diffusion coefficient of oxygen in magnetite (in the range 300°C - 550°C) to be given by

$$(D^*_{O})_{Fe_3O_4} = 320 \times 10^{-12} \exp\frac{-71{,}179}{R\,T} \qquad (m^2\ s^{-1}) \qquad \text{Eq. 3.15}$$

At a temperature of 500°C, Equation 3.14 extrapolates to approximately 10^{-11} $m^2\ s^{-1}$ for the self-diffusion of iron in magnetite, whereas Equation 3.15 yields approximately 5×10^{-15} $m^2\ s^{-1}$ for the self-diffusion of oxygen. In the absence of short circuit diffusion pathways, therefore, it would appear that oxygen diffusion plays a very small role in the growth of magnetite.

The oxygen partial pressure, which Darken and Gurry [54] found to affect the composition of magnetite, has also been found to determine the predominant cation

---

3 Early work in this field, by Davies, Simnad and Birchenall [r42], indicated that magnetite grows largely by the diffusion of oxide ions, though with a sizeable contribution (about 20%) from iron ion diffusion. This interpretation of their results was later found to be in error (see footnote on page 828 of Himmel, Mehl and Birchenall [r104]). The inward diffusion of oxygen may be observed under certain conditions, but this is most probably *via* the gas phase through micro-channels in the oxide [113].

transport mechanism [109, 112, 113]. At low values of p_{O_2}, when Fe_3O_4 is stoichiometric, the intrinsic defects are Frenkel pairs in the iron sub-lattice, and cation diffusion is dominated by the more mobile iron interstitials. As the value of p_{O_2} increases, the number of iron interstitials decreases, which reduces the self-diffusion coefficient for iron, $(D^*_{Fe})_{Fe_3O_4}$. However, as the oxygen partial pressure continues to increase, vacancies are formed in the iron sub-lattice, and a minimum point is reached beyond which the contribution of vacancy diffusion exceeds that of interstitial diffusion, and from that point on, $(D^*_{Fe})_{Fe_3O_4}$ increases with increasing p_{O_2}. The partial pressure of oxygen at which the minimum in the self-diffusion coefficient occurs increases with increasing temperature, from about 10^{-20}Pa at 500°C, to 1Pa at 1200°C [109].

Below 700°C, observed parabolic growth rates for magnetite tend to be greater than predicted by Wagner's theory [12]. The distribution of ^{55}Fe and ^{18}O tracers in scales formed at 500°C indicate that the oxidation mechanism is rate controlled by the outward diffusion of iron along short circuit pathways, with no appreciable contribution to scale growth from 'through-scale' oxygen transport [111]. Atkinson and Taylor [111] identified Fe_3O_4 grain boundaries as the short circuit pathway, although Atkinson [12] later remarks that the results were qualitative and that it was not possible to distinguish between different short circuits.

In addition to the P-type semi-conduction made possible by the creation of point defects in magnetite, Verwey and Haayman [107] have observed a degree of intrinsic P-type semi-conduction, which they attribute to the transfer of electrons between ferrous and ferric ions in neighbouring octahedral interstices.

3.7.3 Formation

With cation diffusion being the major transport mechanism in magnetite, Fe_3O_4 is most likely to form by the reduction of the overlying Fe_2O_3 layer,

$$4Fe_2O_3 + Fe^{n+} + ne^- = 3Fe_3O_4 \qquad \text{Eq.3.16}$$

where n represents the valency of the cation. Above 570°C, the supply of iron ions to

the Fe_3O_4/Fe_2O_3 interface is reduced by the combination of Fe and Fe_3O_4 at the 'FeO'/Fe_3O_4 interface to form wüstite (Equation 3.17). Calculations of the parabolic rate constant for the growth of magnetite, show that it grows eighteen time faster on a wüstite substrate than it does when both oxides are growing simultaneously on an iron substrate [65].

Observed rates of growth of magnetite during the oxidation of iron above 700°C are within an order of magnitude of the rate predicted by inserting the self-diffusion coefficient for Fe in Fe_3O_4 into the equation based on Wagner's theory [19, 65, 95]. Below 700°C, observed growth rates are greater than predicted and tend to be widely scattered [12]. Channing and Graham [116] found that the activation energy for the growth of magnetite at 450-550°C was of the order of 130kJmol^{-1}, and Szlarska-Smialowska and Jurek [71] report a value of only 100kJmol^{-1} (for the combined growth of magnetite and haematite) in the range 250-300°C, both of which are very much lower than the energy required purely for lattice diffusion. Furthermore, magnetite formed below 570°C often exhibits duplex growth [41], so it would appear that short circuit diffusion makes a considerable contribution to ionic transport in this temperature range. The wide scatter of observed growth rates could be due to the unpredictable concentrations of short circuit pathways [12].

Magnetite growth rates are also modified by the presence of an overlying layer of haematite [117]. During the early stages of oxidation, surface coverage of the iron by a magnetite layer is often completed before the haematite layer has nucleated, and so outward growth of Fe_3O_4 will commence at the ambient oxygen partial pressure. However, the completion of the Fe_2O_3 layer reduces the oxygen partial pressure at the Fe_3O_4 surface to the dissociation pressure of Fe_2O_3, and the magnetite growth rate will decrease as the cation vacancy concentration adjusts to the lower equilibrium value. Thus an initially rapid oxidation rate is reduced by the completion of an overlying haematite layer; according to Boggs *et al* [117] this layer may be so thin that it cannot be detected by X-ray diffraction techniques.

As described in Section 3.6.6, magnetite can also form by the decomposition of 'FeO' below 570°C, by the reaction [101]

$$4FeO = Fe_3O_4 + Fe^{2+} + 2e^- \qquad \text{Eq. 3.17}$$

Magnetite nuclei form in the oxygen-rich outer layer of wüstite near the 'FeO'/ Fe_3O_4 interface, possibly by the systematic arrangement of iron ions in the tetrahedral interstices of the 'FeO' lattice, as suggested by Roth [87]. For this to occur the system must be maintained very close to equilibrium during cooling below 570°C, and would consequently be very slow. However, the dissolution of the metallic iron in the remaining 'FeO' during slow cooling increases the stability of the lower oxide [104, 105], so that complete decomposition of wüstite into a eutectoid phase of Fe plus Fe_3O_4 is unlikely to occur.

3.7.4 Substrate Epitaxy

X-ray studies of wüstite grown on magnetite by Mehl and McCandless [59] have shown that the lattices of the two oxides are parallel, that is

$$(100)_{'FeO'} \parallel (100)_{Fe_3O_4} \qquad \text{Eq. 3.18}$$

$$[100]_{'FeO'} \parallel [100]_{Fe_3O_4} \qquad \text{Eq. 3.19}$$

This relationship is shown in Figure 3.10, and also it may be noted that

$$2\, a_{'FeO'} \approx a_{Fe_3O_4} \qquad \text{Eq. 3.20}$$

which requires a 2% tensile strain in the Fe_3O_4 lattice for perfect epitaxy.

Mehl and McCandless [59] did not attempt to solve the relationship between α-Fe and Fe_3O_4, because of the possibility that there would be an intervening, non-equilibrium, transitional layer of 'FeO'. Layers of wüstite have been observed below thin films of magnetite at temperatures as low as 400°C [100], but there is no evidence that this is a transitional layer; Gulbransen and Ruka's [100] interpretation was that the wüstite was the non-equilibrium product of the strain energy in the thin magnetite (see Section 3.6.5).

If a piece of iron is oxidised first below and then above 570°C, the magnetite layer

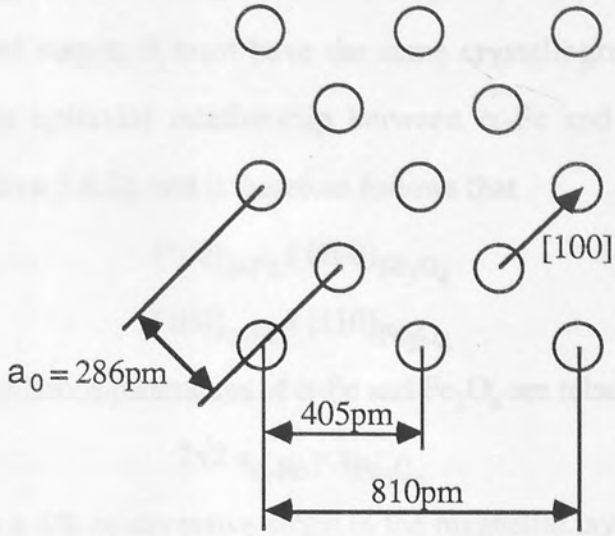

(a) Pattern of iron atoms on (100) plane of α -Fe.

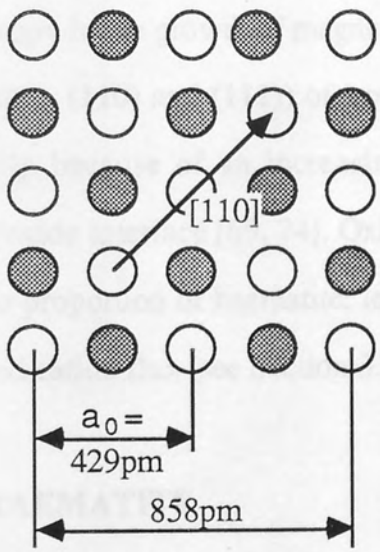

(b) Pattern of iron and oxygen ions on (100) plane of wüstite.

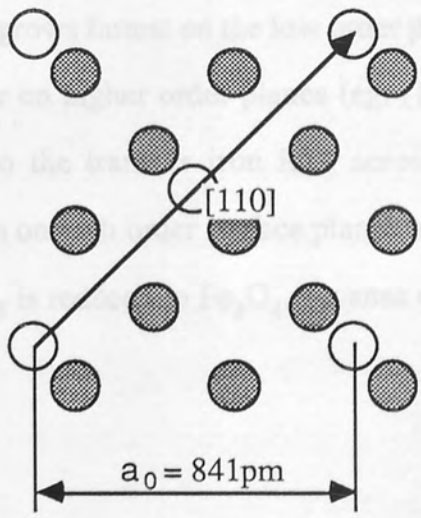

(c) Pattern of iron and oxygen ions on (100) plane of magnetite.

Figure 3.10. Substrate epitaxy of magnetite (after Mehl and McCandless [59]).

formed in the first stage will remain attached as a layer of wüstite forms between it and the metal during the second stage. Since the magnetite cannot recrystallise between the first and second stages, it must have the same crystallographic orientation to both substrates. The epitaxial relationship between α-Fe and 'FeO' has already been discussed (Section 3.6.2), and it therefore follows that

$$(100)_{\alpha\text{-Fe}} \parallel (100)_{Fe_3O_4} \qquad \text{Eq. 3.21}$$

$$[100]_{\alpha\text{-Fe}} \parallel [110]_{Fe_3O_4} \qquad \text{Eq. 3.22}$$

Furthermore the lattice parameters of α-Fe and Fe_3O_4 are related by

$$2\sqrt{2}\, a_{\alpha\text{-Fe}} \approx a_{Fe_3O_4} \qquad \text{Eq. 3.23}$$

which requires a 4% compressive strain in the magnetite layer for perfect epitaxy (by way of comparison, the epitaxy of α-Fe and FeO requires a 6% tensile strain in the oxide).

The difficulty of maintaining this epitaxial relationship produces a marked anisotropy in the growth of magnetite. The oxide grows fastest on the low order planes (ie. (100), (110) and (111)) of iron, but is slower on higher order planes (eg. (112)), possibly because of an increasing resistance to the transfer iron ions across the metal/oxide interface [69, 74]. Oxide films grown on high order surface planes have a greater proportion of haematite; less of the Fe_2O_3 is reduced to Fe_3O_4, because of the reduced cation flux (see Section 3.8.1).

3.8 HAEMATITE

The highest oxide of iron has four phases, of which the β and δ phases are unstable [11], and do not appear to have required any attention in published work on the oxidation of iron. On the whole, haematite has not received the attention given to the two lower oxides of iron, largely because it grows slowly and tends to exist only in small amounts [12]; at temperatures greater than about 600°C, Fe_2O_3 may account for less than 1% of the oxide [60]. However, as has been discussed in Section 3.7.3, its presence, even in very thin films, greatly reduces the growth rate of magnetite, and thus

it can be very protective to iron in an oxidising environment [117]. Haematite always forms the outer layer of iron oxide scales and should not, at equilibrium, be in contact with metallic iron, since its Fe^{3+} ions would capture electrons from the substrate and thereby become Fe^{2+}.

The nucleation of haematite on magnetite growing on iron, occurs after an incubation period, which appears to be dependent on the cation flux through the oxide film. Simmons *et al* [68] found that after 1000 minutes at 225°C in pure oxygen, the oxide composition was approximately $Fe_{2.91}O_4$ (too cation deficient to be either Fe_3O_4 or Fe_2O_3), which they attributed to the low cation flux at that temperature. However, after only 10 minutes at 450°C there was a single oxide layer of Fe_3O_4; the absence of an Fe_2O_3 layer was thought to be due to the much higher cation flux, which maintained a high iron content in the oxide film, and that haematite would only nucleate once the cation flux had fallen below some critical level, as the film thickened. When seeking an intermediate case, 5 minutes at 350°C was found to be adequate time for a two-layered oxide film of Fe_2O_3 on Fe_3O_4 to form.

There is much published work that supports the observation that (over short periods of time) the haematite layer may be absent on films formed below about 225°C, and between about 400-570°C (eg. see [67, 71, 72]). Of particular interest is the work of Szlarska-Smialowska and Jurek [71], whose ellipsometric studies of films formed at 250-350°C revealed that haematite does not form a single, homogeneous layer, but consists of several layers with different optical properties. There appears to have been no subsequent research on what other properties these layers might have.

At temperatures below 350°C, the rate of nucleation of haematite is reduced by decreasing the partial pressure of oxygen, although this effect seems to be negligible at 450°C and higher temperatures [117]. The major consequence of this is the rapid growth of magnetite, which is in direct contact with the atmosphere, and initial oxidation rates are therefore higher than those observed over longer periods. The oxidation rate decreases as the proportion of Fe_2O_3 in the scale increases [117].

The growth mechanism of haematite is not at all clear, since it has not been determined whether the diffusion of oxygen or iron is the rate controlling process [12]. The two limiting cases are (a) oxygen transport only, leading to a reaction at the Fe_3O_4/Fe_2O_3 interface,

$$2\,Fe_3O_4 + O^{2-} = 3\,Fe_2O_3 + 2\,e^- \qquad \text{Eq. 3.24}$$

or (b) iron transport only, leading to a reaction at the oxide/atmosphere interface,

$$2\,Fe^{3+} + {}^3/_2\,O_2 + 6\,e^- = Fe_2O_3 \qquad \text{Eq. 3.25}$$

3.8.1 Alpha Haematite

This is the stable phase of haematite, and has a rhombohedral structure, with the oxygen ions in a nearly close-packed hexagonal arrangement, with iron ions at the interstices [52, 67, 118, 119].

Alpha haematite is apparently stoichiometric at all temperatures [54], but exhibits N-type semi-conduction [120] which indicates an oxygen deficiency, although it is not certain whether this is due to oxygen vacancies or iron interstitials [121]. Bevan *et al* [120] have found that the resistivity of α-Fe_2O_3 increases with decreasing oxygen partial pressure; they interpret the falling conductivity as the result of 'free' electrons being trapped by oxygen vacancies, the concentrations of which would be expected to increase at low oxygen pressures. The resistivity also increases with increasing temperature [120], but above 1000°C conduction becomes independent of the oxygen partial pressure and there is a degree of P-type semi-conduction [121], implying that there are vacancies or interstitials on both iron and oxygen sub-lattices.

The lattice diffusion rates of iron and oxygen in α-Fe_2O_3 are of comparable magnitude, and apparently identical at around 1100°C, as shown in Figure 3.11. The diffusion coefficients are given by the Arrhenius-type equations

$$\left(D^*_{Fe}\right)_{\alpha\text{-}Fe_2O_3} = 4\times10^{9}\exp\left(\frac{-468{,}944}{R\,T}\right) \quad (m^2\,s^{-1}) \qquad \text{Eq. 3.26}$$

for iron in the range $900°C \le T \le 1300°C$ [53], and

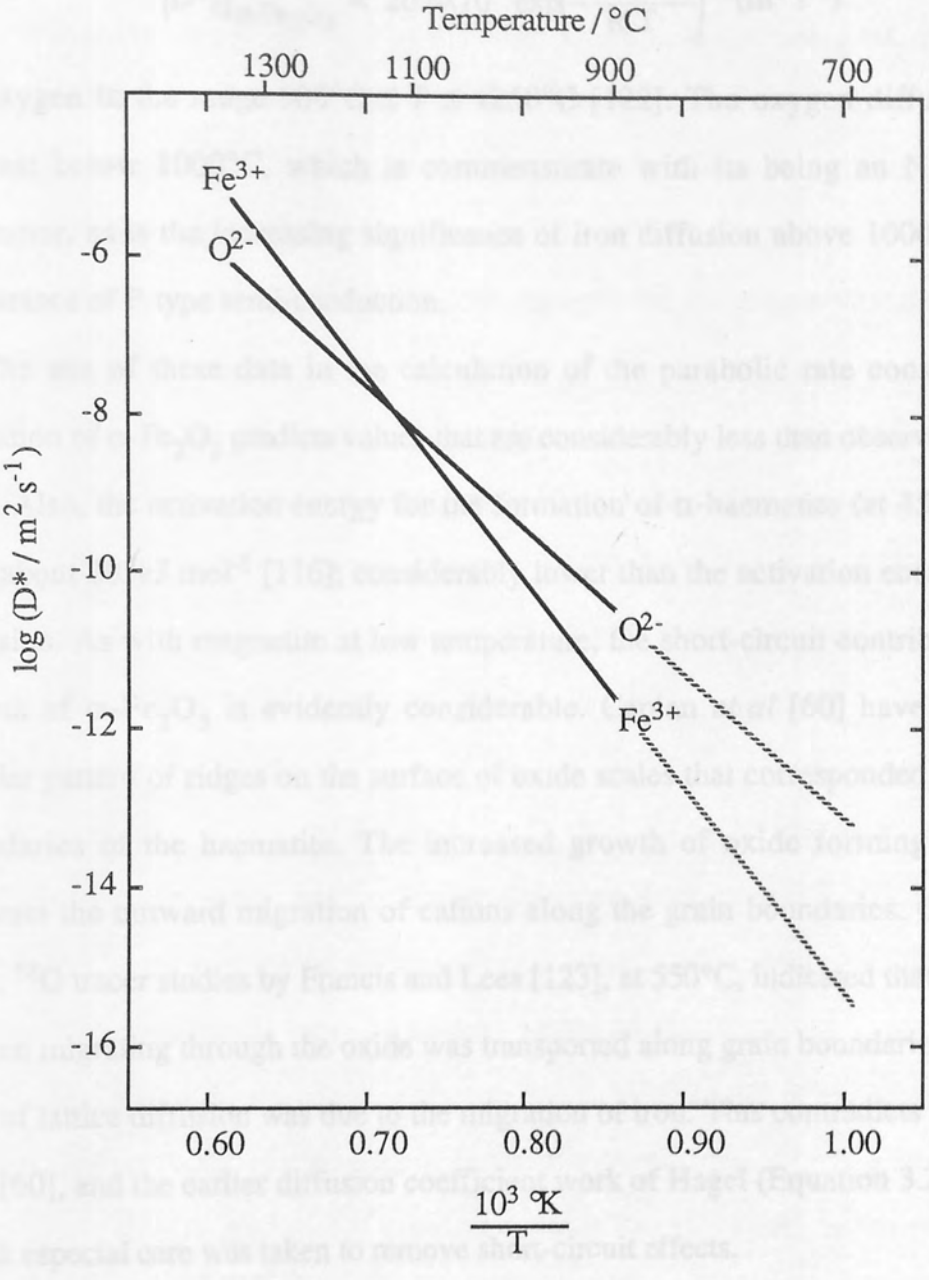

Figure 3.11. Temperature dependence of iron and oxygen self diffusion coefficients in α -Fe_2O_3 (after Himmel et al [53], and Hagel [122]).

$$(D^*_O)_{\alpha\text{-}Fe_2O_3} = 20.4\times10^{3}\exp\left(\frac{-326{,}167}{RT}\right) \quad (m^2\,s^{-1}) \qquad \text{Eq. 3.27}$$

for oxygen in the range 900°C ≤ T ≤ 1250°C [122]. The oxygen diffusion rate is greatest below 1000°C, which is commensurate with its being an N-type semi-conductor, as is the increasing significance of iron diffusion above 1000°C with the appearance of P-type semi-conduction.

The use of these data in the calculation of the parabolic rate constant for the formation of α-Fe_2O_3 predicts values that are considerably less than observed rates [41, 122]. Also, the activation energy for the formation of α-haematite (at 450-550°C) is only about 205kJ mol^{-1} [116]; considerably lower than the activation energy for self-diffusion. As with magnetite at low temperature, the short-circuit contribution to the growth of α-Fe_2O_3 is evidently considerable. Caplan *et al* [60] have observed a cellular pattern of ridges on the surface of oxide scales that corresponded to the grain boundaries of the haematite. The increased growth of oxide forming the ridges, suggests the outward migration of cations along the grain boundaries. On the other hand, ^{18}O tracer studies by Francis and Lees [123], at 550°C, indicated that most of the oxygen migrating through the oxide was transported along grain boundaries, whilst the bulk of lattice diffusion was due to the migration of iron. This contradicts both Caplan *et al* [60], and the earlier diffusion coefficient work of Hagel (Equation 3.27) [122], in which especial care was taken to remove short-circuit effects.

Bruckman and Simkovich [124] have conducted experiments in which markers were placed on a magnetite substrate, which was then oxidised at 1100°C. The markers were found to be buried in the haematite, at a depth of approximately one ninth of the total thickness of the Fe_2O_3 layer below the surface. Bruckman and Simkovich were able to explain these findings without the need for any oxygen transport in the α-Fe_2O_3 layer. They suggest that Fe_3O_4 transforms directly to α-Fe_2O_3 at the magnetite/haematite interface by the reaction

$$6\,Fe_3O_4 - 2\,Fe = 8\,Fe_2O_3 \qquad \text{Eq. 3.28}$$

(*sic*), with the excess iron diffusing to the oxide surface to combine with oxygen from the atmosphere, according to Equation 3.25. Note that, for every six molecules of Fe_3O_4 transformed, Equation 3.28 yields eight molecules of Fe_2O_3 below the marker, whilst Equation 3.25 yields one molecule of Fe_2O_3 above the marker; this would explain the position of the marker, at one ninth of the α-Fe_2O_3 thickness below the surface. Other authors (eg. [75, 125]) have reported the direct transformation of Fe_3O_4 to α-Fe_2O_3.

The oxygen ions of the Fe_3O_4 (111) plane and the basal plane of the α-Fe_2O_3 rhombohedral structure form a very close epitaxial relationship, although the iron ions in each oxide show no agreement whatsoever [59]. Dunnington *et al* [33] have noted the precipitation of α-Fe_2O_3 platelets on {111} planes in slowly cooled magnetite.

3.8.2 Gamma Haematite

Gamma haematite is more akin to Fe_3O_4 than α-Fe_2O_3; it is ferro-magnetic (α-Fe_2O_3 is para-magnetic), and has a cubic spinel-type structure [67, 108, 118, 126]. In fact it was because of its spinel-like structure that in 1931, Thewlis [108] gave this phase of haematite the 'γ' label, by analogy with γ-Al_2O_3.

Gamma haematite therefore appears to be a modified form of magnetite, and since the unit cell of Fe_3O_4 can be represented by the formula $Fe_{24}O_{32}$ (see Section 3.7.1), the unit cell of γ-Fe_2O_3 should have the formula $Fe_{24}O_{36}$ [108], ie. four O^{2-} ions are added to the basic spinel-type structure. However, David and Welch [126] have found that the preparation of γ-Fe_2O_3 from 'wet' Fe_3O_4 (prepared by aqueous precipitation) cannot be repeated in anhydrous conditions; the oxidation of rigorously dried Fe_3O_4 in dry oxygen always yields α-Fe_2O_3. Thus γ-Fe_2O_3 is stabilised by the adsorption of moisture from the atmosphere [77, 126], although the exact nature of this is the matter of some debate [127]; the electro-neutrality of the γ-Fe_2O_3 structure could be be maintained by the substitution of some oxygen ions by hydroxyl ions (eg. producing molecules of FeOOH) [126], or the substitution of some iron ions by protons (eg.

HFe_5O_8) [127, 77]. The latter mechanism seems the more probable, since the reduction of α-Fe_2O_3 in dry hydrogen has been shown [77] to proceed according to the reaction

$$8\ (\alpha\text{-}Fe_2O_3) + H_2 = 2\ HFe_5O_8 + 2\ Fe_3O_4 \qquad \text{Eq. 3.29}$$

Bloom and Goldenberg [77] have interpreted the results of Kruger and Yolken [78] as implying that the minimum partial pressure of water in the atmosphere required for the formation of γ-Fe_2O_3 is of the order of 10^{-5} Pa.

The retained moisture cannot be removed without transforming γ-Fe_2O_3 to some other oxide, and the rate of this transformation increases with rising temperature [52, 67, 118, 126]: γ-Fe_2O_3 is entirely transformed to α-Fe_2O_3 when heated above 225°C in air [67, 72], and above 200°C *in vacuo* it transforms to Fe_3O_4 [73]. γ-Fe_2O_3 is stabilised by the presence of alumina [118]. The reverse transformation (α-$Fe_2O_3 \rightarrow$ γ-Fe_2O_3) does not occur under normal conditions [52].

The structural similarities of Fe_3O_4 and γ-Fe_2O_3 make it difficult to differentiate the two by X-ray diffraction techniques [127], although their cathodic behaviour during electrochemical reduction is very distinct [128]. γ-Fe_2O_3 appears to be pore-free and non-conducting, so that it has a considerable resistance to electrochemical corrosion [73].

The oxidation of small magnetite crystals has been studied by Gallagher *et al* [75], who found that the structure depended on the concentration of ferrous ions in the film. At Fe^{2+} concentrations greater than 22%, the structure and composition are those of Fe_3O_4, and of γ-Fe_2O_3 at concentrations of less than 8.5% Fe^{2+}. In the band 8.5% - 22% Fe^{2+}, there exists an intermediate composition with a cubic structure similar to that of $LiFe_5O_8$. This work confirmed that it is possible for Fe_3O_4 and γ-Fe_2O_3 to form a single layer, in which the composition and structure change continuously between the iron/oxide and oxide/atmosphere interfaces.

3.9 PASSIVE FILMS ON IRON

The passivity of iron in air, at room temperature, is associated with the presence of a thin surface layer of electrically insulating γ-Fe_2O_3 on a conducting layer of Fe_3O_4 [77]. In fact there may be only a single layer, with the composition and structure changing continuously between the iron/oxide and oxide/atmosphere interfaces [73, 75, 77, 127]. The relatively high cation flux during the initial stages of oxidation of a clean iron surface maintains a high iron content throughout the film, and the film will have a composition corresponding to Fe_3O_4. This unprotective stage of growth may last for several weeks at room temperature [129], though it is important to note that oxidation, including the adsorption of oxygen, is very slow at this temperature, and that the oxide film will probably be less than 5μm thick. The nucleation and growth of γ-Fe_2O_3, and possibly α-Fe_2O_3 later, on top of the Fe_3O_4, greatly reduces oxidation, and the subsequent growth rate may be negligible [76, 78, 129].

The formation of the passive film represents a reaction in the ternary system Fe-O-H_2O. Even in very moist air (over 90% humidity) there will be no corrosion of the iron, provided all the components in the reaction are very pure. Rusting, that is, the formation of dark brown or red deposits on the iron surface, will only occur in the presence of contaminants, which may be present in the form of impurities in the iron, or air-borne pollution such as sulphur dioxide. Once rusting has started, it will continue even if the metal is removed from the polluted atmosphere, because the contaminant already incorporated in the rust deposits will catalyse the reaction [130]

3.10 ALLOYING

There are a number of elements that can be added to iron to improve its oxidation resistance, however, for reasons that will become apparent in Section 4, on powder metallurgy, only aluminium, copper, phosphorus and silicon will be discussed in this review.

3.10.1 Aluminium

Although pure aluminium has a relatively low melting point (660°C), the Fe-Al alloy system (Figure 3.12) exhibits a series of high melting point solid solutions, and intermetallic compounds. The primary phase (α-Fe) can retain up to 10wt% Al in solid solution at room temperature.

Wüstite does not dissolve aluminium to any appreciable extent. The dissolution of aluminium in iron and magnetite, reduces their thermodynamic activity relative to wüstite. Aluminium therefore destabilises wüstite, reducing its growth rate, and a large addition can prevent its formation [131]. The oxidation resistance of Fe-Al alloys increases with increasing aluminium content above 0.1wt% Al, below which level, the oxidation rate is more rapid than that of the pure metal [14]. More than 5wt% Al can cause breakaway oxidation, and at over 10wt% Al, alloys become brittle [11, 14, 131].

With alloy contents as high as 25wt% Al, oxidation below 800°C can produce the oxides Fe_3O_4 and α-Fe_2O_3 only [14], though more usually a layer of the spinel oxide $FeO.Al_2O_3$ is found between the alloy and the Fe_3O_4 layer [14]. The interposition of the spinel phase, which may contain a greater concentration of aluminium than the alloy [11, 132], obstructs the passage of metal ions into the oxide, reducing the oxidation rate. Above 570°C the oxide γ-Al_2O_3 starts to appear, and above 800°C the oxide film is almost pure alumina, and oxidation rates are consequently very slow [14]. γ-Al_2O_3 can dissolve considerable amounts of Fe_2O_3 [131].

3.10.2 Copper

Copper has a lower affinity for oxygen than iron, and it plays no part in the formation of an oxide scale. However, as iron diffuses outwards into the oxide the alloy next to the alloy/oxide interface becomes enriched with copper, and when the copper solubility limit in the iron is exceeded, a copper-rich phase will precipitate. This second phase has a very low solubility for iron (Figure 3.13), and provided the oxidation temperature is below the melting point of copper (1085°C), it will act as a

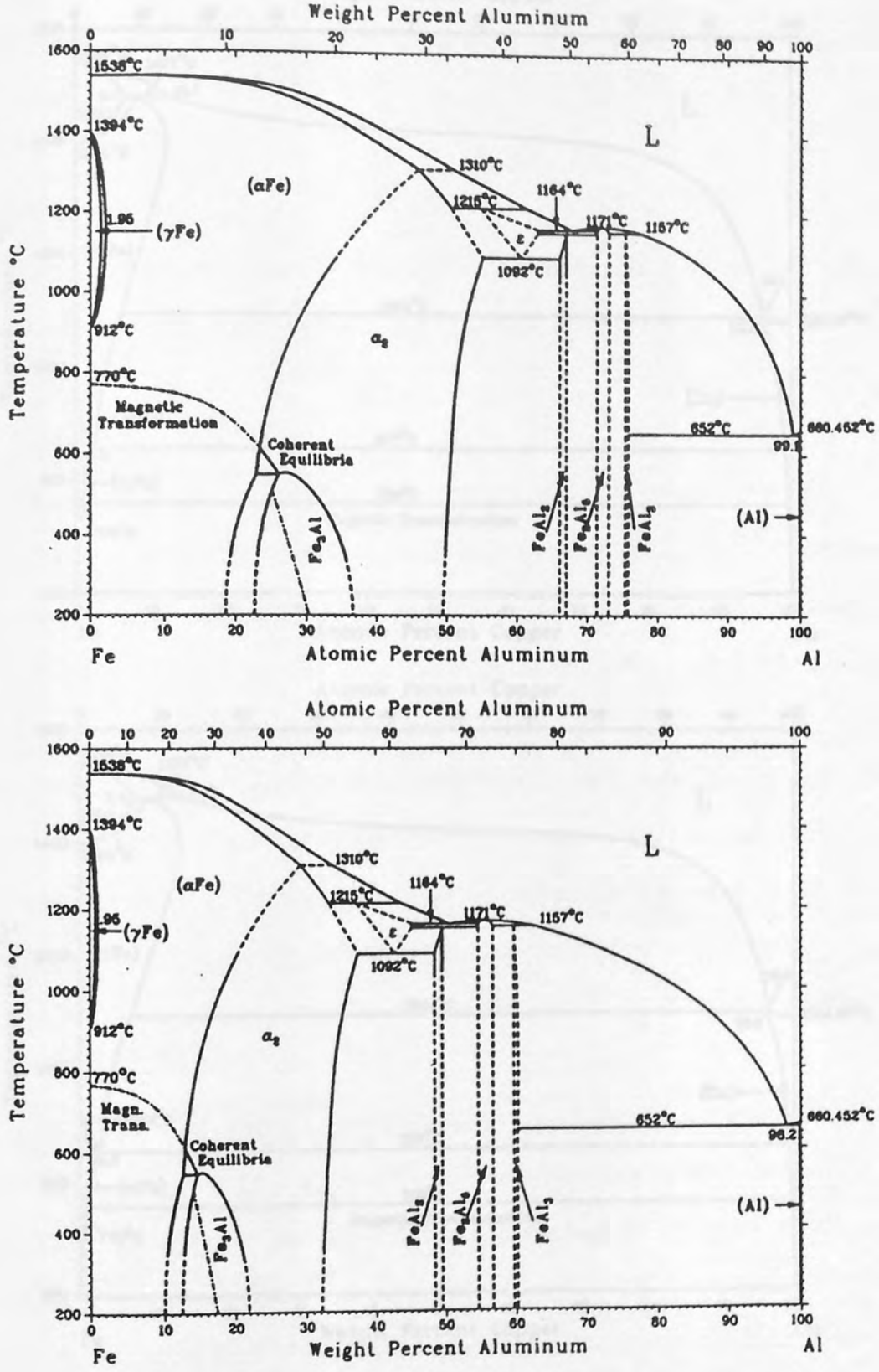

Figure 3.12. The iron - aluminium phase diagram [179].

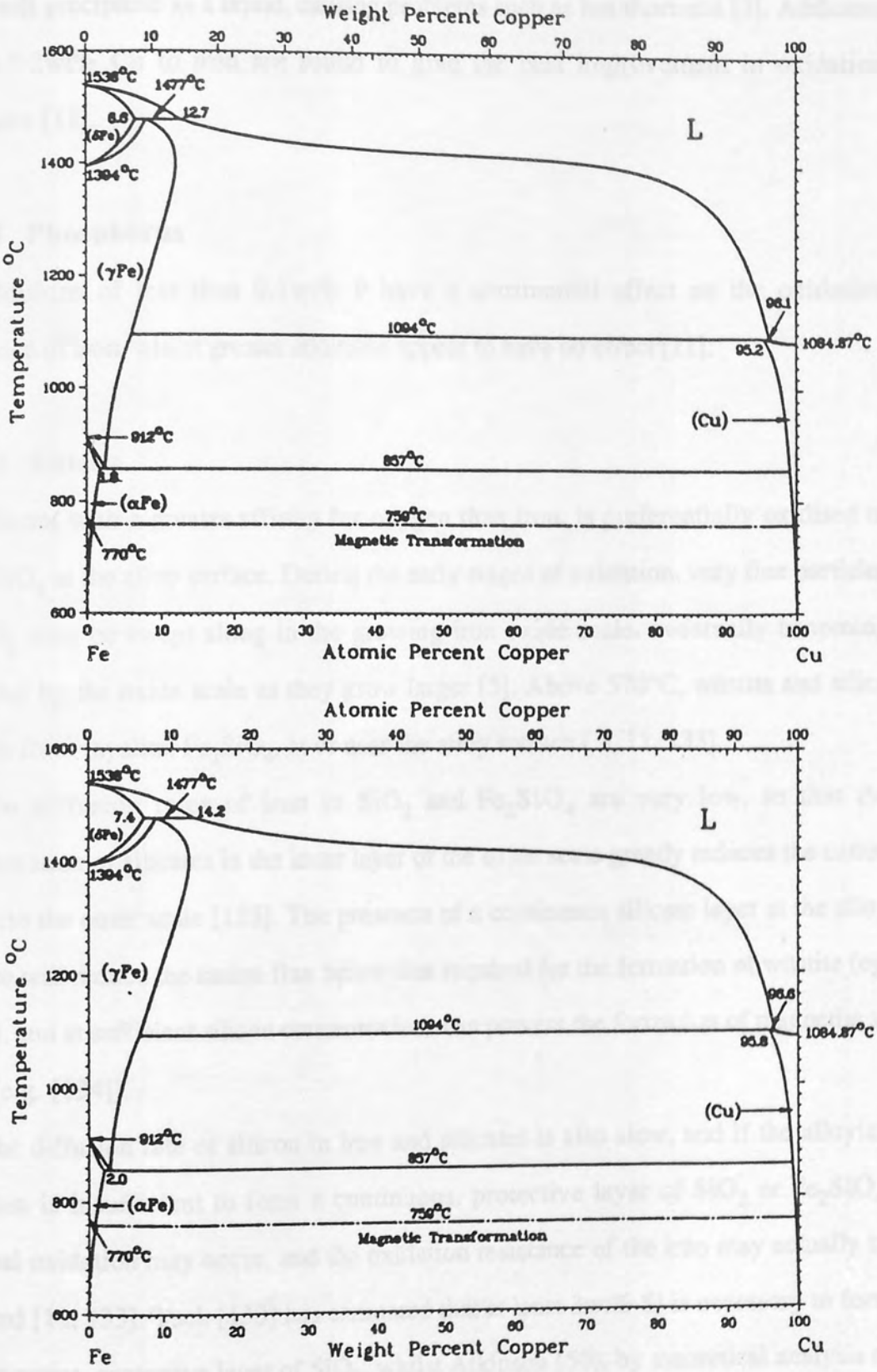

Figure 3.13. The iron - copper phase diagram [179].

solid barrier to the diffusion of iron into the scale. At higher temperatures the second phase will precipitate as a liquid, causing problems such as hot shortness [5]. Additions of 0.8-2.2wt% Cu to iron are found to give the best improvement in oxidation resistance [11].

3.10.3 Phosphorus

Additions of less than 0.1wt% P have a detrimental effect on the oxidation resistance of iron, whilst greater additions appear to have no effect [11].

3.10.4 Silicon

Silicon, with a greater affinity for oxygen than iron, is preferentially oxidised to form SiO_2 at the alloy surface. During the early stages of oxidation, very fine particles of SiO_2 may be swept along in the growing iron oxide scale, eventually becoming engulfed by the oxide scale as they grow larger [5]. Above 570°C, wüstite and silica react to form fayalite, Fe_2SiO_4, at or near the alloy surface [5, 11, 133].

The diffusion rates of iron in SiO_2 and Fe_2SiO_4 are very low, so that the concentration of silicates in the inner layer of the oxide scale greatly reduces the cation flux into the outer scale [133]. The presence of a continuous silicate layer at the alloy surface will reduce the cation flux below that required for the formation of wüstite (eg. [133]), and at sufficient silicon concentrations can prevent the formation of magnetite as well (e.g. [134]).

The diffusion rate of silicon in iron and silicates is also slow, and if the alloying addition is insufficient to form a continuous, protective layer of SiO_2 or Fe_2SiO_4, internal oxidation may occur, and the oxidation resistance of the iron may actually be reduced [11, 133]. Tuck [133] has estimated that at least 3wt% Si is necessary to form a continuous, protective layer of SiO_2, whilst Atkinson [50], by theoretical analysis of the oxidation of Fe-Si alloys, has predicted 2.6wt% Si as the minimum requirement. Generally the oxidation resistance of the alloy increases with increasing silicon content,

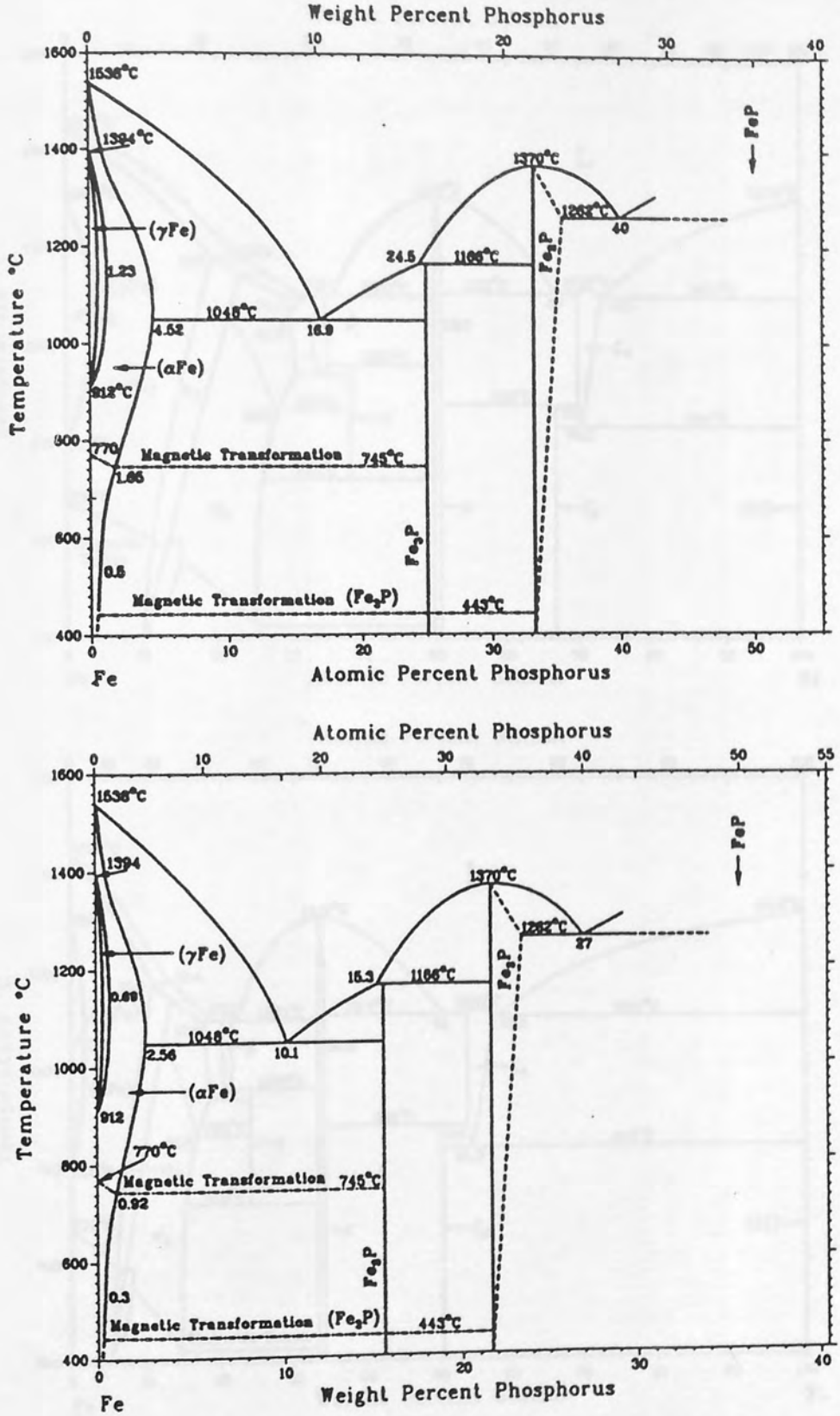

Figure 3.14. The iron - phosphorus phase diagram [179].

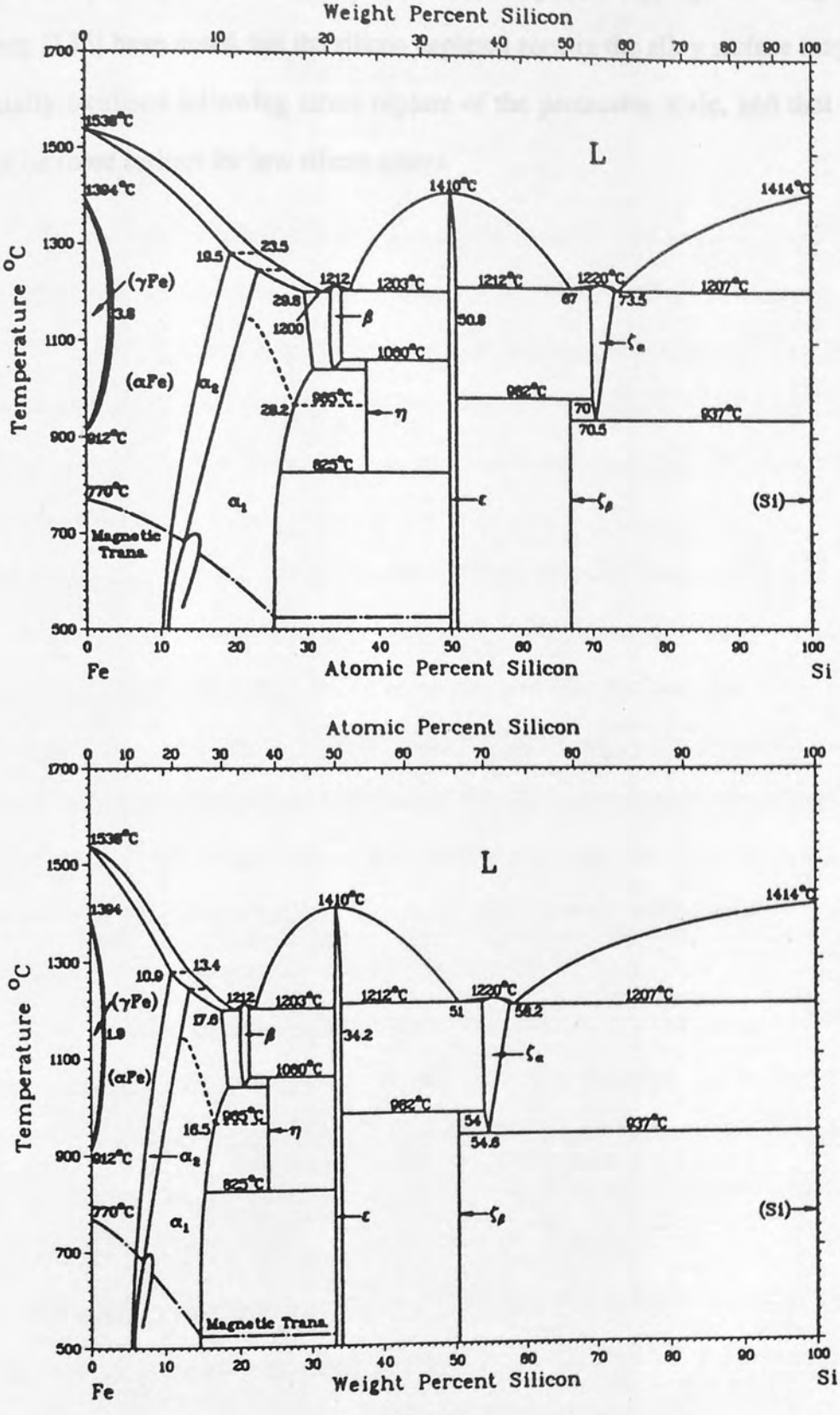

Figure 3.15. The iron - silicon phase diagram [179].

although at concentrations greater than about 10wt% the scales are often mechanically unstable, and spalling and breakaway oxidation may occur [134]. Svedung and Vannerberg [135] have noted that the silicon depleted zone in the alloy surface may be preferentially oxidised following stress-rupture of the protective scale, and that this effect will be more serious for low silicon alloys.

Section 4

RELEVANT ASPECTS OF POWDER METALLURGY

Literature Review

4.1 METAL POWDERS

Methods for manufacturing powders are can be divided into three main groups: chemical, chemical-mechanical and mechanical [136]. Chemically reduced powders, produced from metal oxides, tend to be very fine and irregularly shaped. The large surface area associated with such fine powders can lead to partial sintering during the reduction process, to form a porous sponge that may require subsequent comminution to render it into a useable form.

Powders can also be prepared by electrolysis from solution. Electrolysis generally produces very pure powders, either as a brittle mass (which has to be comminuted, to yield angular or acicular particles), or as a loose tangle of dendritic particles.

Comminution is generally performed by the milling of coarse powders. Machining (to produce turnings, chips, filings etc. from a metallic mass) tends to be expensive, and few pure metals are brittle enough to be broken down by crushing. Particle shape and size depends on the method and extent of comminution, whilst purity (or alloy uniformity) depends on the condition of the original metallic mass.

Atomisation, by the physical disintegration of a stream of liquid metal in gas jets or water jets, generally yields irregularly shaped particles, although the molten metal droplets will tend to become more spherical if solidification rates are slow. Since these powders are formed directly from the melt they tend to be of uniform composition and free of inclusions.

The carbonyl process for iron produces a powder of fine spherical particles by the decomposition of gaseous iron pentacarbonyl, $Fe(CO)_5$, which is produced by the reaction of crude iron powder with carbon monoxide under pressure.

Powders used for powder metallurgy broadly fall into three groups: elemental

(pure) metal, partially pre-alloyed and fully pre-alloyed. Alloy additions tend to cause hardening, which reduces compressibility [137]. Fully pre-alloyed powders may therefore be difficult to compact, and powders prepared from cast alloys, by mechanical methods, may be segregated [138].

This difficulty can be minimised by the use of elemental, or partially pre-alloyed powders. The partially pre-alloyed powder may contain alloy elements that are difficult to render or use as elemental powders. Besides improving compressibility, this approach also reduces die wear, increases the toughness and ductility of the sintered component, and there is greater alloying flexibility. The major disadvantage of this approach is that the unsintered alloy is always highly segregated, with discrete particles of the alloy components, and homogenisation may require prolonged sintering [137, 139, 140].

4.2 PROCESS ROUTE

The normal process route for producing PM parts has three main stages, namely mixing, compaction and sintering. The general aim is to produce the net shaped, or near-net shaped component in these three stages, to reduce the number of subsequent finishing operations (such as machining to the final shape).

4.2.1 Mixing

The first stage in the PM process route is to produce a powder with a uniform distribution of particles (in terms of both size and composition). Additions may be made to a base powder, which can include other metal powders (to produce an alloy), and a lubricant (to reduce friction at tooling contact faces, and to aid powder flow, during compaction,).

The method, and duration of mixing has a marked effect on the distribution of particles in the compacted powder [141]. Mixing is best performed by a tumbling action, and the optimum mixing time, which can be determined from changes in the

bulk density of the powder, depends on the characteristics of the powders. Insufficient mixing results in powders remaining segregated by size and composition. Excessive mixing can cause agglomeration of particles, and even the re-segregation of the powder. The optimum mixing time achieves the most efficient packing of the powder particles, and is characterised by a minimum in a plot of powder's bulk density, against mixing time (Figure 4.1).

4.2.2 Compaction

The most widely used method for compacting metal powders is the punch and die technique. The die cavity is charged with the loose powder, which occupies a volume characteristic of it bulk density. The punch is then inserted into the die, and pressure is applied to compact the powder charge.

Compaction occurs in three stages (Figure 4.2). Firstly, the movement of the punch takes up the looseness of the powder charge, causing a rearrangement of the powder particles and reducing their packing density. Interparticle movement abrades the oxide films on particle surfaces, allowing metal-to-metal contact, and in the second stage of compaction, pressure welding occurs at these contact areas. Further application of pressure leads to the third stage of compaction, in which particles deform plastically and work harden. Each stage of compaction requires a greater compaction pressure for less densification (Figure 4.2d), and it is unlikely that the true density of the powder will be realised [136]. The limiting factors for densification during compaction are the strength of the tooling, and the entrapment of gas.

In the case of multi-component systems, the most abundant powder forms a matrix, within which the minor components are embedded. The microstructure of the compact depends on the relative hardnesses of the different powders, with the softer particles being plastically deformed by the harder ones. The voids between particles are interconnected by a network of capillaries, which may extend contiguously from the external surface to the core of the compact [139].

It has been established for some time that the density of a compact decreases with

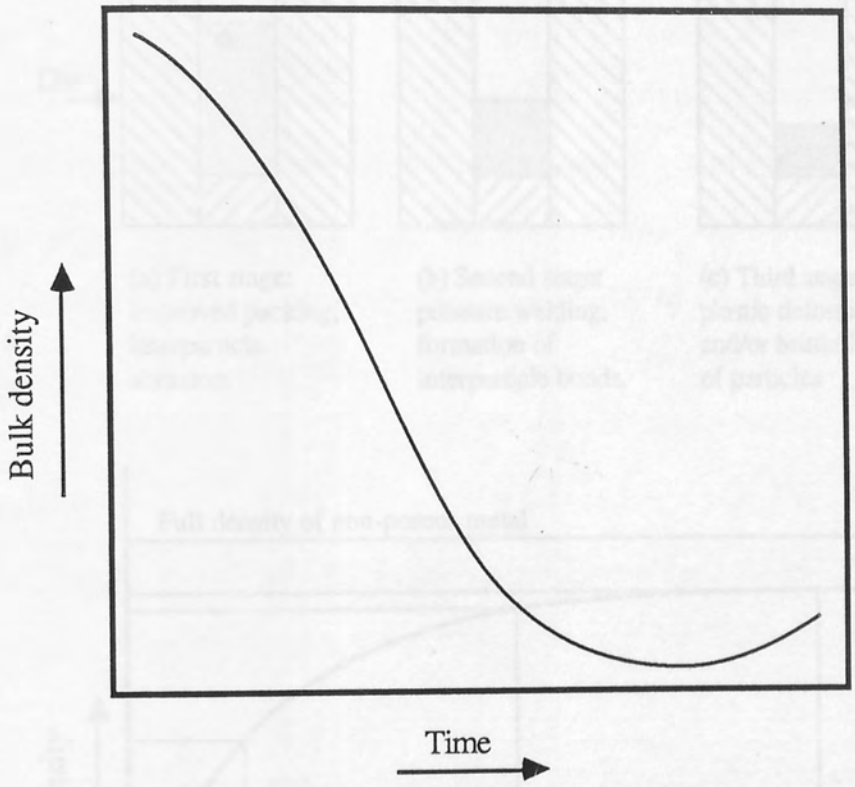

Figure 4.1. Variation of bulk density of powder with time, during the mixing of powders (after [141]).

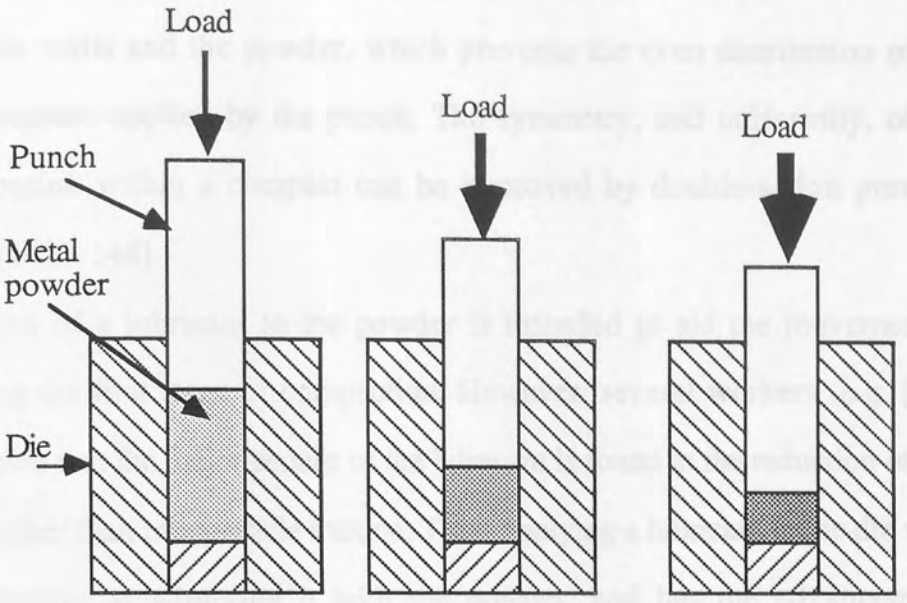

(a) First stage: improved packing, interparticle abrasion.

(b) Second stage: pressure welding, formation of interparticle bonds.

(c) Third stage: plastic deformation and/or brittle fracture of particles

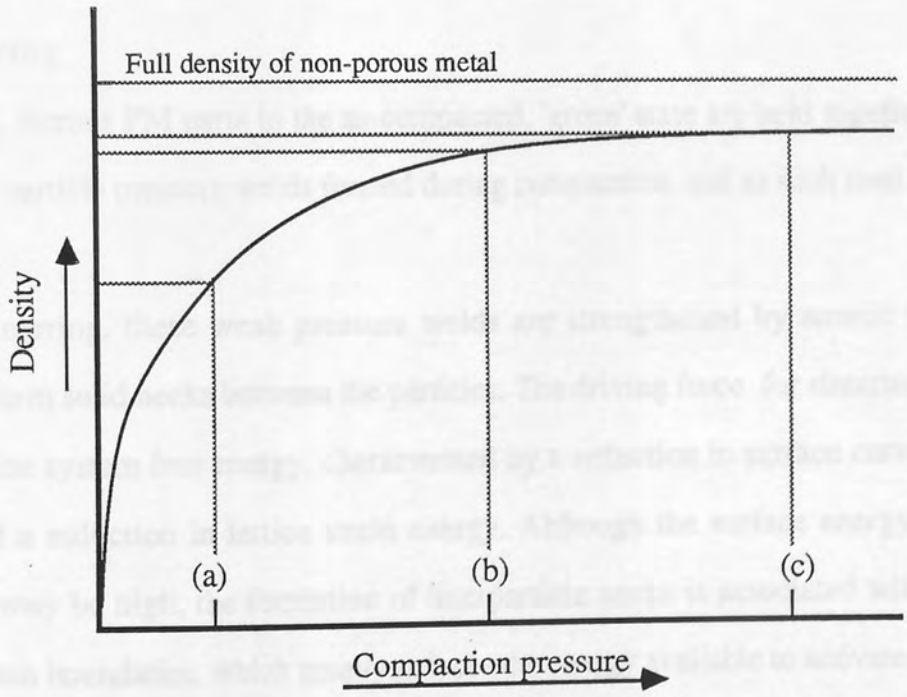

(d) Typical pressure-density curve.

Figure 4.2. Die pressing of powders.

increasing distance from the punch surface (see Figure 4.3a). This is due to the friction between the die walls and the powder, which prevents the even distribution of the compaction pressure applied by the punch. The symmetry, and uniformity, of the density distribution within a compact can be improved by double-action pressing (Figure 4.3b) [142 - 144].

The addition of a lubricant to the powder is intended to aid the movement of particles during the first stage of compaction. However, several workers (e.g. [145, 146]) have shown that the major benefit of the lubricant is found in the reduction of die-wall friction, rather than interparticle friction. Thus, applying a lubricant to the die walls can be as effective as admixing it with the powder, and has the advantages of eliminating the need for a lubricant burn-off treatment prior to sintering, and reducing contamination of the furnace atmosphere during sintering [147].

4.2.3 Sintering

Generally, ferrous PM parts in the as-compacted, 'green' state are held together by the weak interparticle pressure welds formed during compaction, and as such tend to be friable.

During sintering, these weak pressure welds are strengthened by atomic mass transport, to form solid necks between the particles. The driving force for sintering is a reduction in the system free energy, characterised by a reduction in surface curvature and area, and a reduction in lattice strain energy. Although the surface energy of a porous body may be high, the formation of interparticle necks is associated with the creation of grain boundaries, which greatly reduces the energy available to activate mass transport [140].

To enable sintering to proceed it is necessary that the atoms have sufficient mobility to move to new positions. Atomic mobility is a function of temperature, and thus sintering is markedly temperature dependent [136]. Typically sintering occurs at temperatures between $0.5T_M$ and T_M, the absolute melting point of the metal (or of the

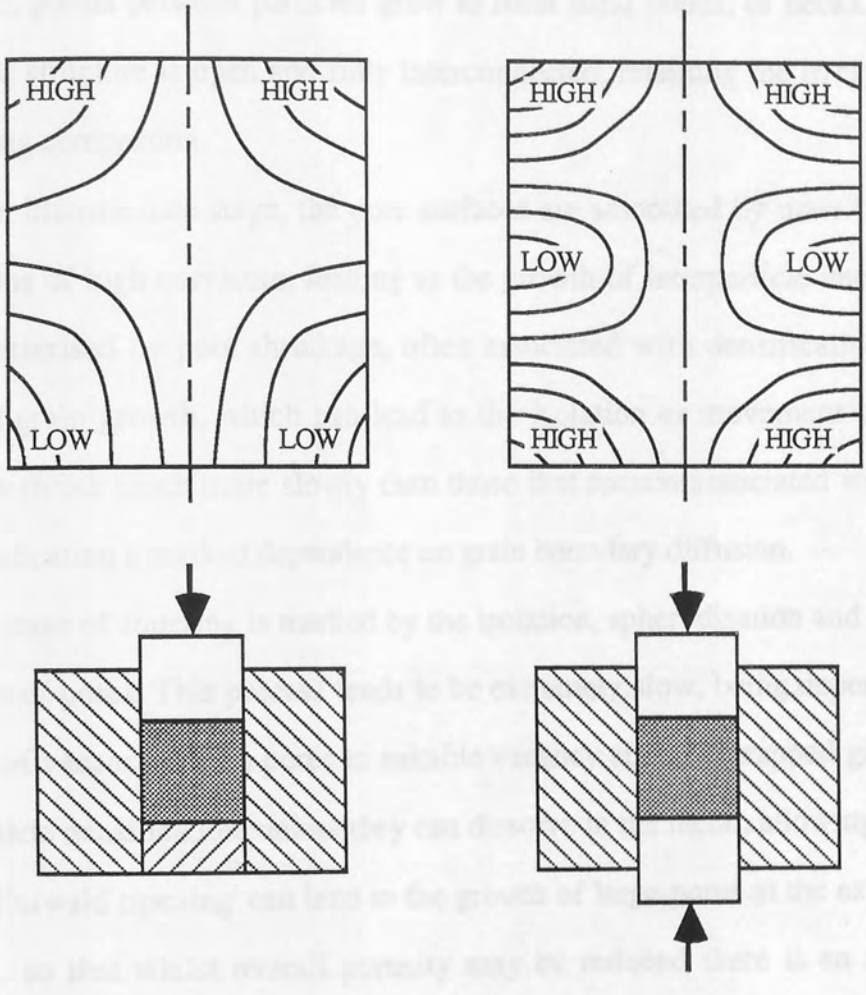

(a) Single-action pressing.

(b) Double-action pressing.

Figure 4.3. Density distribution obtained with (a) single-action pressing, and (b) double-action pressing (after Thompson [142]).

base metal of an alloy). The transport mechanisms are diffusion over surfaces, along grain boundary and dislocation pathways [140], and possibly also by a vapour phase mechanism [136].

Three stages of sintering can be identified, which are illustrated in Figure 4.4 [140]. Firstly, contact points between particles grow to form solid bonds, or necks. At this stage, the pore structure is open and fully interconnected, retaining the irregularities produced during compaction.

During the intermediate stage, the pore surfaces are smoothed by mass transport towards regions of high curvature, leading to the growth of interparticle necks. This stage is characterised by pore shrinkage, often associated with densification of the compact, and grain growth, which can lead to the isolation or movement of pores. Isolated pores shrink much more slowly than those that remain associated with grain boundaries, indicating a marked dependence on grain boundary diffusion.

The final stage of sintering is marked by the isolation, spherodisation and ultimate disappearance of pores. This process tends to be extremely slow, being dependent on the diffusion of vacancies from pores to suitable vacancy sinks. Entrapped gases will prevent complete densification, unless they can dissolve in the metal, allowing closure of the pore. 'Ostwald ripening' can lead to the growth of large pores at the expense of smaller ones, so that whilst overall porosity may be reduced there is an apparent coarsening of the pore structure [140].

Work on the sintering of copper powders [148] has shown that, whilst inter-connected porosity is eliminated at an almost constant rate throughout sintering, the proportion of closed porosity remains almost constant (Figure 4.5). This is because the rate of creation of closed porosity, by the isolation of interconnected pores, is approximately equal to the rate of annihilation of closed pores.

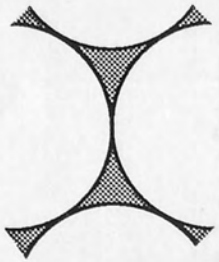

Initial state:
Powder particles bonded by pressure welds during compaction.

First stage:
Formation of inter-particle necks by atomic mass transport.

Second stage:
Pore rounding and smoothing.

Third stage:
Pore isolation and elimination.

Figure 4.4. Micrsostructural changes during sintering.

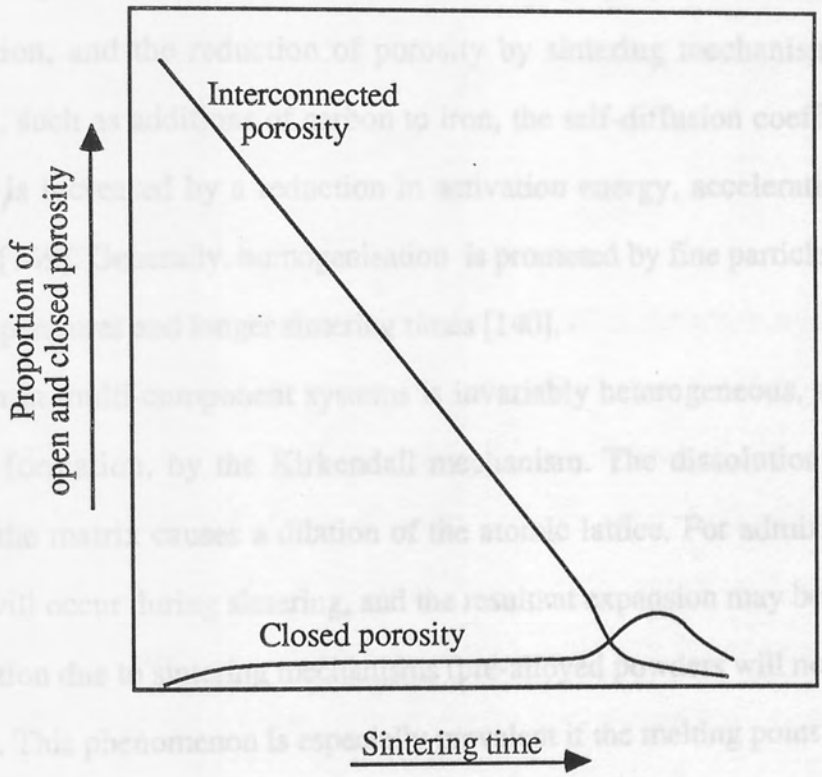

Figure 4.5. Interconnected and closed porosity, as a function of time, during sintering (after Arthur [148]).

4.2.4 Homogenisation

The sintering of mixed phase systems, such as alloys prepared from elemental and partially pre-alloyed powders, is complicated by the introduction of chemical concentration gradients. The effect of these on diffusion processes are generally greater than the driving force for sintering mechanisms, and will dominate mass transport until interdiffusion has reduced the gradients below some critical level [140]. Concentration-activated diffusion causes material interchange between particles, and may therefore result in bonding, but the ultimate realisation of an alloy's properties will depend on its homogenisation, and the reduction of porosity by sintering mechanisms [136]. In certain cases, such as additions of carbon to iron, the self-diffusion coefficient of the major phase is increased by a reduction in activation energy, accelerating sintering mechanisms [149]. Generally, homogenisation is promoted by fine particle size, higher sintering temperatures and longer sintering times [140].

Diffusion in multi-component systems is invariably heterogeneous, and can give rise to pore formation, by the Kirkendall mechanism. The dissolution of alloying elements in the matrix causes a dilation of the atomic lattice. For admixed powders, dissolution will occur during sintering, and the resultant expansion may be greater than the densification due to sintering mechanisms (pre-alloyed powders will not exhibit this effect) [150]. This phenomenon is especially prevalent if the melting point of the minor phase is much lower than that of the major phase, as for example occurs with additions of aluminium to iron melt during sintering [140]. Compact swelling is caused by the penetration of the liquid phase at grain boundaries (eg. see [150 - 152]). The formation of a liquid phase is often observed in multi-component systems, and rapid diffusion in it generally enhances sintering mechanisms [136]. The amount of alloying addition required to create an effective liquid phase depends on the nature (eg. particle size, shape and morphology) of the base powder [153].

Sintering temperatures used for ferrous-based PM materials usually lie in the austenite temperature range, at which the iron has a face-centred cubic structure.

However, the diffusivities of some dissolved elements in the body-centred cubic ferrite phase, α-Fe, are more than two times their diffusivity in γ-Fe. Thus elements that can stabilise α-Fe up to and above the sintering temperature, such as silicon (Figure 3.17), will increase sintering and homogenisation rates, and their effectiveness increases with decreasing initial particle size [153 - 155].

Phase diagrams can be used as a guide to the phases likely to form during the sintering of multi-component systems [172]. However, it is important to recognise that the high concentrations of alloy components at particle/particle interfaces, especially in the early stages of sintering, may lead to the formation of transient phases, and possibly the formation of insoluble intermetallics [140].

4.3 OXIDATION OF POROUS SINTERED IRON

The presence of interconnected porosity greatly increases the active surface area of a body, and reactive species may be able to penetrate to the core of a PM compact. Thus reactions that affect the properties of the porous metal (mechanical and electrical) can occur throughout a PM part, and may affect its performance under service conditions. Untreated PM parts are generally considered unsuitable for use in such conditions (eg. see [156, 157]), and most of the work published in this field has concentrated on sealing external surfaces, in order to isolate porosity from the ambient atmosphere.

Methods for sealing external surfaces can be divided into those that use the metal matrix, and those that introduce some other material. In the first group, there are mechanical methods, which deform the surface, smearing the metal matrix into surface porosity (eg. shot peening), and chemical methods, such as steam treatment, in which pores are sealed by oxide growth. In the second group are impregnation (eg. with an oil, a plastic, or a solder-type alloy), and coating (eg. electroplating, hot dipping in molten metal, metal spray) [156]. Some of these methods, such as impregnation, are unsuitable for high temperature applications. The effectiveness of methods that seal surface porosity only, is dependent on the contiguity of the treated surface, and its

resistance to oxidative attack. A paper by Fedorchenko *et al* [158], published in 1963, appears to be the only major study of the oxidation of sintered metals, as opposed to the protection of PM parts in oxidising conditions.

The oxidation of a porous body depends to a considerable extent on the permeability of the pores, which can be substantially reduced as the reaction progresses, as a result of the closure of capillaries by oxide scale. In addition, the diffusion of oxygen through the atmosphere pervading the porosity may be a rate-controlling factor.

Fedorchenko's experiments [158], with the oxidation of porous nickel, to form NiO, demonstrated these effects (Figure 4.6). Below some critical temperature, compacts were oxidised throughout. Above the critical temperature, the rate of removal of oxygen from the atmosphere exceeded the rate at which it could permeate through the sample, and consequently an increasing amount of core porosity remained unoxidised. Thus, despite the formation of a thicker oxide scale, the overall weight gain was reduced above the critical temperature. The value of the critical temperature decreases with decreasing sample porosity, reflecting the importance of pore size on the permeability of the compact. This experiment was repeated for porous sintered iron, for which it was found that the critical temperature lay below 600°C (Figure 4.7).

Fedorchenko *et al* [158] also considered the exothermic nature of the oxidation reaction. They found that, because of the large surface area of a porous body, the heat evolved during the early stages of oxidation could raise a sample's temperature significantly above the ambient furnace temperature. For iron (Figure 4.8), a double peak in sample temperature was observed below 600°C. Fedorchenko and his co-workers do not appear to have been familiar with the oxides of iron, and do not comment on the multi-layer nature of iron oxide scales.

The effects of alloy powder homogeneity on the formation of protective oxide films, especially in service conditions that allow galvanic corrosion, are very important [157]. For example, nickel and copper additions to iron powders may produce relatively noble alloy phases during sintering, which will accelerate corrosion.

One approach to this problem is the use of fully pre-alloyed powders. Searson and

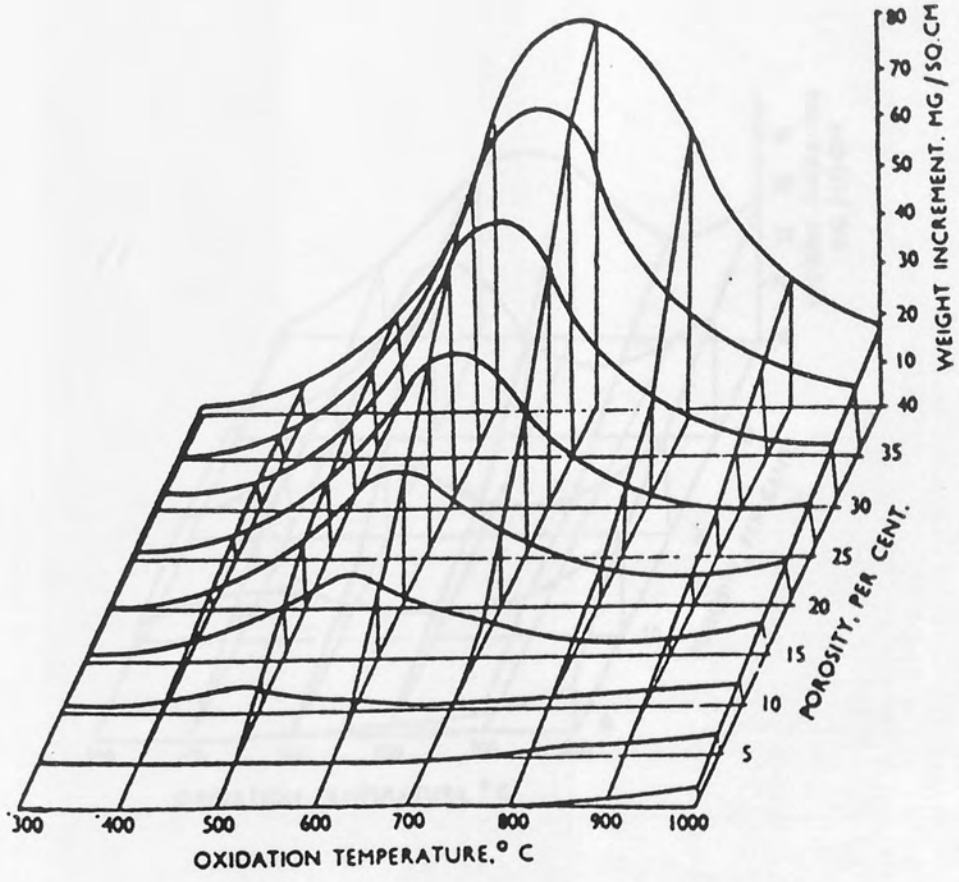

Figure 4.6. Weight change of sintered nickel powder compacts, as a function of oxidation temperature and porosity [158].

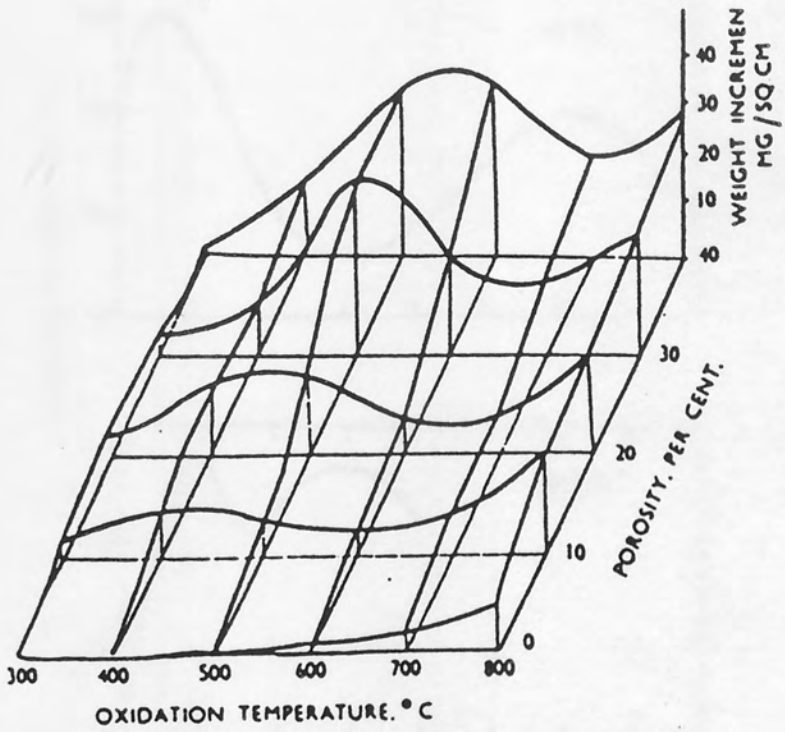

Figure 4.7. Weight change of sintered iron powder compacts, as a function of oxidation temperature and porosity [158].

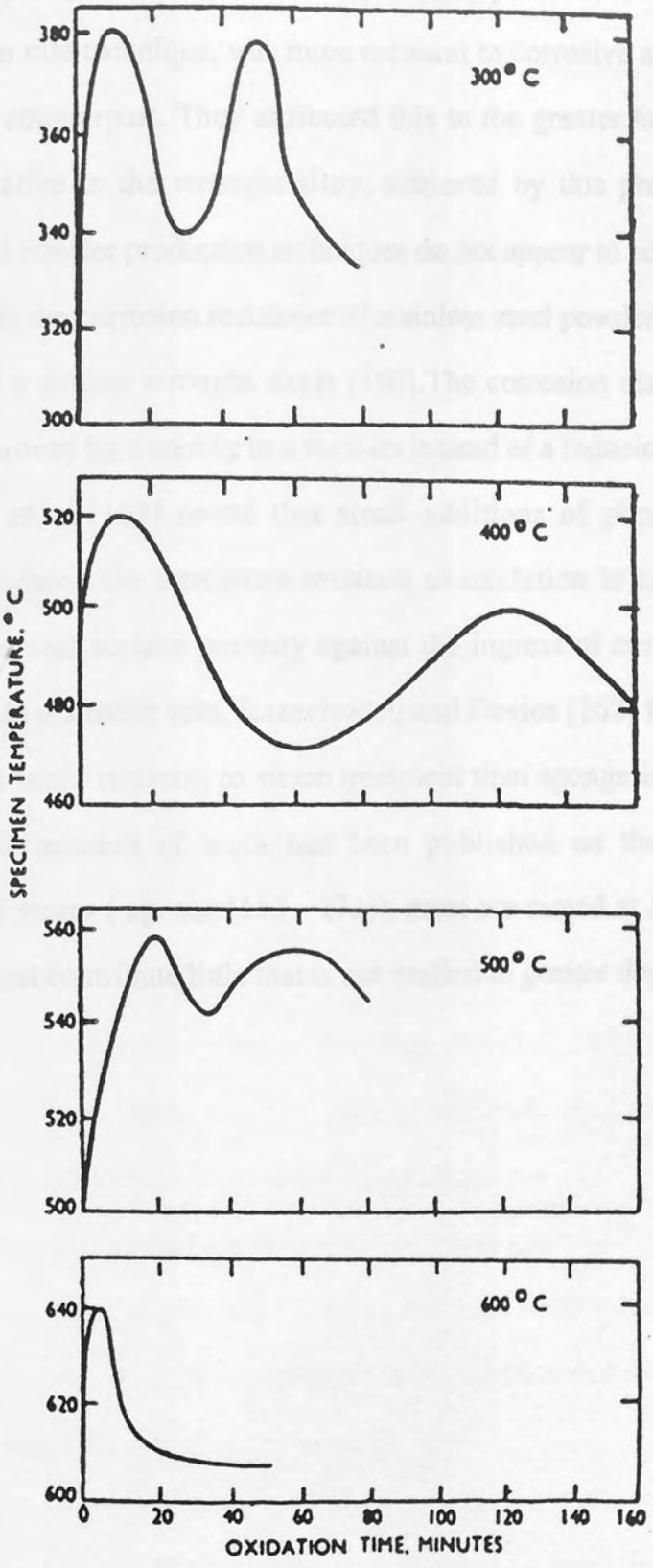

Figure 4.8. Core temperature of sintered iron powder compacts during oxidation [158].

Latanision [159] found that a stainless steel powder, manufactured by a rapid solidification rate technique, was more resistant to corrosive and oxidative attack than its wrought counterpart. They attributed this to the greater homogeneity of the alloy powder, relative to the wrought alloy, achieved by this production method. More conventional powder production techniques do not appear to achieve this improvement, and generally the corrosion resistance of stainless steel powders does not compare well with that of a similar wrought steels [160].The corrosion resistance of PM stainless steels is improved by sintering in a vacuum instead of a reducing atmosphere [160].

Siddiqi *et al* [161] found that small additions of phosphorus in pre-alloyed powders rendered the iron more resistant to oxidation in steam, a treatment often employed to seal surface porosity against the ingress of corrosive media in service conditions. In a similar vein, Razavizadeh and Davies [162] found that atomised iron powder was more resistant to steam treatment than sponge iron powder. Although a considerable amount of work has been published on the oxidation of iron by superheated steam (eg. see [163 - 171]), most are aimed at improving the industrial technique, and contribute little that is not studied in greater depth by Fedorchenko *et al* [158].

Section 5
EXPERIMENTAL METHOD

5.1 OBJECTIVES

The aim of this research was to determine the effects of subjecting porous sintered iron to oxidising conditions, and then to study how alloying might alter its oxidation behaviour.

The long term goal of the research is to identify an iron-based PM alloy composition with an oxidation resistance comparable to (or better than) that of wrought pure iron at elevated temperatures (300°C to 700°C). To be of practical value, this alloy has to be simple, cheap, have good compressibility and reasonable dimensional stability during sintering and subsequent elevated temperature service.

5.2 EXPERIMENTAL DESIGN

The oxidation behaviour of sintered porous iron was studied by selecting a range of values for sample compaction pressure, oxidation time and temperature. Controlling the oxidation of the sintered porous iron was approached by studying the effects of admixing small additions of other readily available elemental metal powders. The outline experimental plan is shown in Figure 5.1.

Oxidation was studied by thermo-gravimetric analysis (TGA), that is, in terms of the increase in mass of samples resulting from the formation of oxide films or scales, by exposure to an oxidising atmosphere at high temperatures. TGA experiments were performed with a Stanton Thermobalance.

A literature review (see Section 4) indicated that the relationship between compaction pressure, oxidation time and temperature was complex. A large number of tests would therefore have to be conducted in order to obtain any degree of statistical confidence in the results. However, the critical resource for experiments was the TGA, which limited the number of oxidation tests that could be performed, thus making a

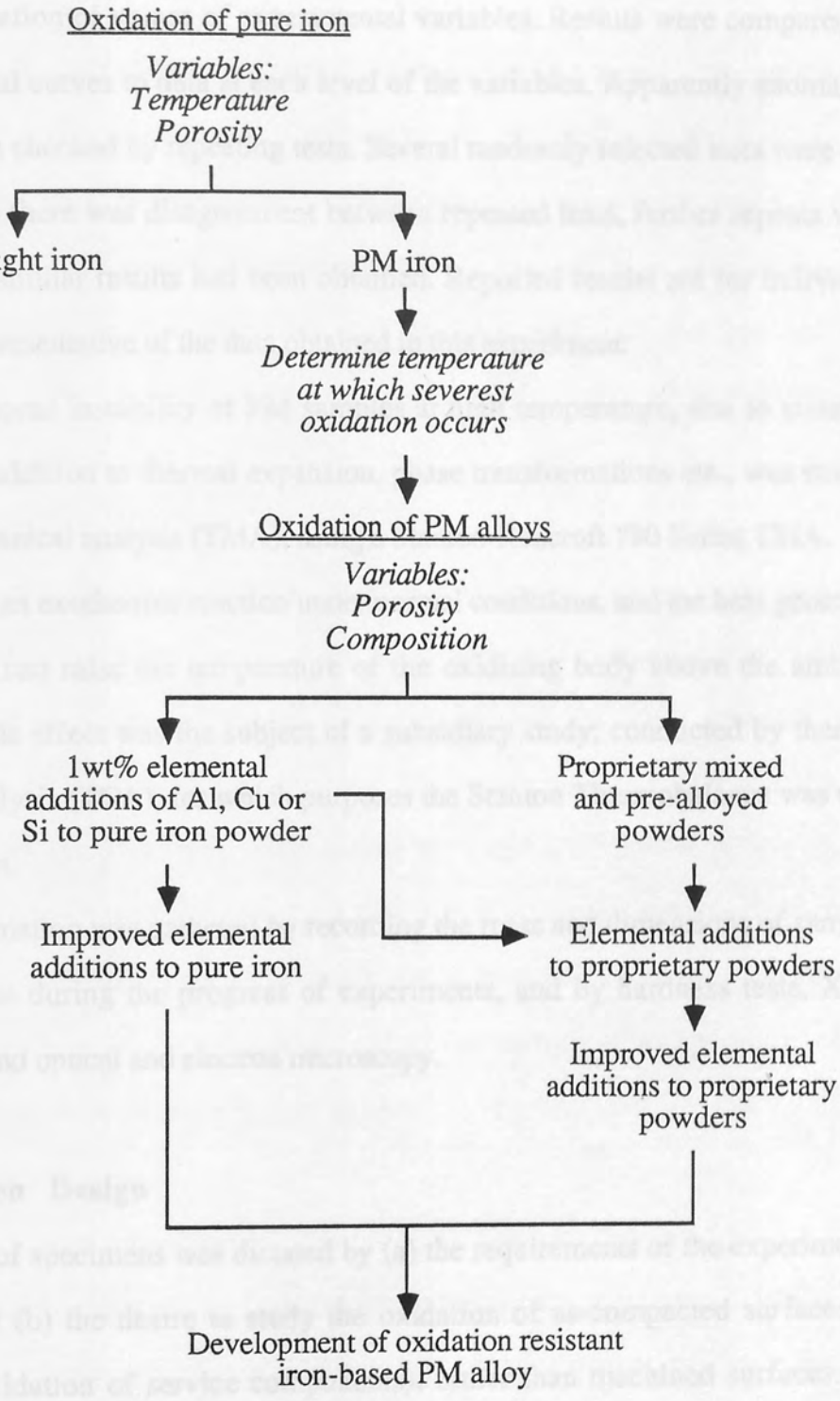

Figure 5.1. Outline of experimental plan.

statistical design of experiments impractical. Therefore, one experiment was conducted for each combination of values of experimental variables. Results were compared by fitting polynomial curves to data at each level of the variables. Apparently anomalous results were then checked by repeating tests. Several randomly selected tests were also repeated. Where there was disagreement between repeated tests, further repeats were made until two similar results had been obtained. Reported results are for individual tests, and are representative of the data obtained in this experiment.

The dimensional instability of PM samples at high temperature, due to sintering mechanisms in addition to thermal expansion, phase transformations etc., was studied by thermo-mechanical analysis (TMA), using a Stanton-Redcroft 790 Series TMA.

Oxidation is an exothermic reaction under normal conditions, and the heat generated by the reaction can raise the temperature of the oxidising body above the ambient temperature. This effect was the subject of a subsidiary study, conducted by thermo-calorimetric analysis (TCA), for which purposes the Stanton Thermobalance was used in modified form.

Other information was gathered by recording the mass and dimensions of samples at various stages during the progress of experiments, and by hardness tests, X-ray diffractometry and optical and electron microscopy.

5.2.1 Specimen Design

The design of specimens was dictated by (a) the requirements of the experimental equipment, and (b) the desire to study the oxidation of as-compacted surfaces (to simulate the oxidation of service components), rather than machined surfaces. For example, finishing operations, such as cutting-up a PM bar into sample lengths, tend to close surface porosity by smearing the metal matrix into neighbouring cavities. This would prevent the penetration of the oxidising gas into interconnected porosity, which is a major difference between the oxidation of porous and fully dense materials. Whenever possible, therefore, PM samples had to be compacted to the required

experimental specimen geometry.

Ideally, specimens for oxidation studies should take the form of large flat disks, of sufficient thickness to avoid the complete oxidation of the metal core during the experimental period [44]. However, bearing in mind the probability of the oxidising gas penetrating to the core of PM samples through interconnecting porosity, it was decided to use cylindrical specimens, which could be considered as very thick discs. Although Romanski [44] observed that the cylindrical geometry produces the least reliable oxidation results, it does have some of the advantages of the disc geometry (two flat surfaces and the minimum number of edges), but the disadvantage of a large curved surface.

The limitations of the Stanton Thermobalance were (a) the vertical tube furnace has a diameter of 30mm, and a hot zone of about 30mm long, and (b) the balance assembly could accommodate a sample weight of not more than 20g. PM samples were compacted with a 12.7mm diameter punch and die set, to a height of 12.5±0.5mm, and wrought pure iron samples were machined to the same dimensions, which gave a maximum possible sample weight of about 13g. The height tolerance was imposed so that individual results could be directly compared, without the need to adjust data by some factor dependent on the ratio of curved to flat surface area. The value of the tolerance, ±0.5mm, was to some extent dictated by the practical limitations of the compaction technique.

Samples for Stanton-Redcroft 790 Series TMA were compacted with a 7.6mm diameter cylindrical punch and die set, this being the maximum sample diameter that would fit into the dilatometer sample tube (see Section 5.7.1). Since the linear thermal expansion of a body is directly proportional to its length, the accuracy of dilatometry experiments is increased with increasing sample length. The maximum practical compact height (i.e. sample length) that could be produced with the die set was 10.0±1.0mm.

5.2.2 Compaction Pressure Range

Compaction pressure, rather than compact porosity, was chosen as an experimental variable since the latter varies with the nature of the powder and densification during sintering, and is therefore to a large extent unpredictable without considerable study.

A compaction pressure range of 150-550MPa was chosen because it bracketed the range of pressures used in industry. The upper limit, 550MPa, was the maximum safe working pressure for the powder compaction die-set used for manufacturing TGA samples.

5.2.3 Atmosphere

The Stanton Thermobalance furnace tube could not be sealed against the ingress of the laboratory atmosphere. Since it was desirable to conduct oxidation experiments in a controlled atmosphere, a flowing gas mixture of 80% N_2, 20% O_2 was used for all thermobalance tests. This has approximately the same oxygen partial pressure as air, but is free from corrosive pollutants such as SO_2. The flow rate had to be sufficient for there to be a slightly positive gas pressure in the furnace tube.

The design of the Stanton Redcroft TMA did not allow for the sintering of samples in a vacuum, and therefore an inert atmosphere of flowing argon was used for the dilatometry experiment.

5.3 EXPERIMENTAL VARIABLES

5.3.1 Thermo-Gravimetric Analysis Experiment

The variables studied for TGA experiments on pure iron were compaction pressure, oxidation temperature and time. To extend the experimental range, wrought pure iron was used to represent fully-dense iron, which could not be prepared by powder compaction. The range of values are shown in Table 5.1. The constants for these tests were sample composition and size, and oxidative atmosphere (composition and flow rate).

Compaction pressure (MPa)	Oxidation temperature (degrees C)	Time
150 250 350 450 550 (wrought iron)	300 400 500 600 700	Continous 24 hour record of tests
6 values	5 values	
30 TESTS		

Table 5.1. Variables for thermo-gravimetry experiments with pure iron.

For TGA tests on alloys, the variables studied were composition, compaction pressure and time, the ranges of which are shown in Table 5.2. The constants for these tests were sample size, and oxidation temperature (500°C) and atmosphere (composition and flow rate). A very few tests were done with different oxidation temperatures.

5.3.2 Thermo-Mechanical Analysis (Dilatometry) Experiment

TMA tests were all done according to a preset temperature programme (described in Section 5.8), with constant sample size and density, and atmosphere (composition and flow rate). The only variable in these tests was the sample composition, which were the same as for TGA tests (Table 5.2).

5.3.3 Thermo-Calorimetric Analysis Experiment

The variables for TCA tests on pure iron were compaction pressure, oxidation temperature and time. Wrought pure iron was used to represent fully-dense iron. The range of values is shown in Table 5.3. The constants for these tests were sample composition and size, and oxidative atmosphere (composition and flow rate).

For TCA tests on alloys, the only variables were sample composition and time. The constants were sample size and compaction pressure (150MPa), oxidation temperature (550°C) and atmosphere (composition and flow rate).

5.4 POWDER METALLURGY SAMPLES

The metal powders used in experiments are described in Table 5.4. Plates 5.1 to 5.5 are photo-micrographs of the powders, taken with a scanning electron microscope (see Section 5.13).

5.4.1 Powder Mixes

The powder mixes are described in Table 5.5. The ASC100.29 and PNC60 powders were used as the base powders for elemental alloy mixes.

Alloy composition balance Fe (weight percent)	Compaction pressure (MPa)	Time
0.6P 0.1Si 1.0Si 3.0Si 1.0Cu 1.0 Al 0.6P, 1.0Si 0.6P, 3.0Si 0.6P, 1.0Cu 1.0Si, 1.0Cu 0.6P, 1.0Si, 1.0Cu 1.75Ni, 1.50Cu, 0.50Mo 4.00Ni, 1.50Cu, 0.50Mo	150 350 550	Continous 24 hour record of tests
13 values	3 values	
39 TESTS		

Table 5.2. Variables for thermo-gravimetric analysis experiments on iron alloy powders.

Compaction pressure (MPa)	Oxidation temperature (degrees C)	Time
150 350 550 (wrought iron)	450 500 550 600 650	Continuous 60 minute record of tests
4 values	5 values	
20 TESTS		

Table 5.3. Variables for thermo-calorimetry experiments with pure iron.

Source	Powder	Nominal composition (wt%)	Other information
Hoganas	ASC100.29	Fe (<0.01 C)	Atomised, high compressibility pure iron powder
Hoganas	PNC60	0.60 P, balance Fe	NC100.24 (pure sponge iron powder) admixed with ferro-phosphorus powder
Hoganas	Distaloy AB	1.75 Ni, 1.50 Cu, 0.50 Mo, <0.01 C, balance Fe	Diffusion alloyed powder based on ASC100.29
Hoganas	Distaloy AE	4.00 Ni, 1.50 Cu, 0.50 Mo, <0.01 C, balance Fe	Diffusion alloyed powder based on ASC100.29
Metco	aluminium	Al	-90μm powder
Makin	copper	Cu	-45μm powder
Aldrich Chemical Co.	silicon	99 Si	-45μm powder

Table 5.4. Powders used for experimental alloys.

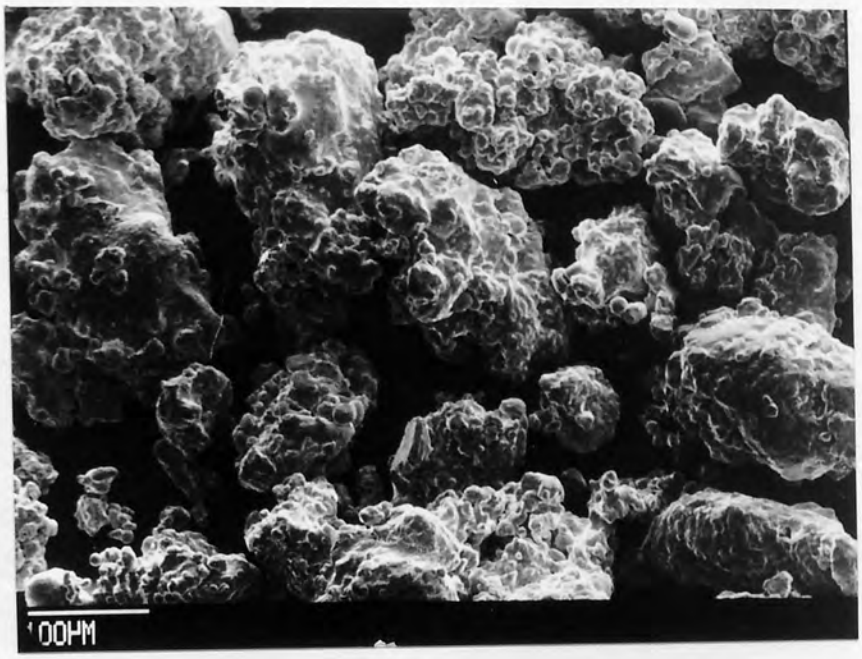

Plate 5.1. Höganäs ASC100.29, atomised pure iron powder.

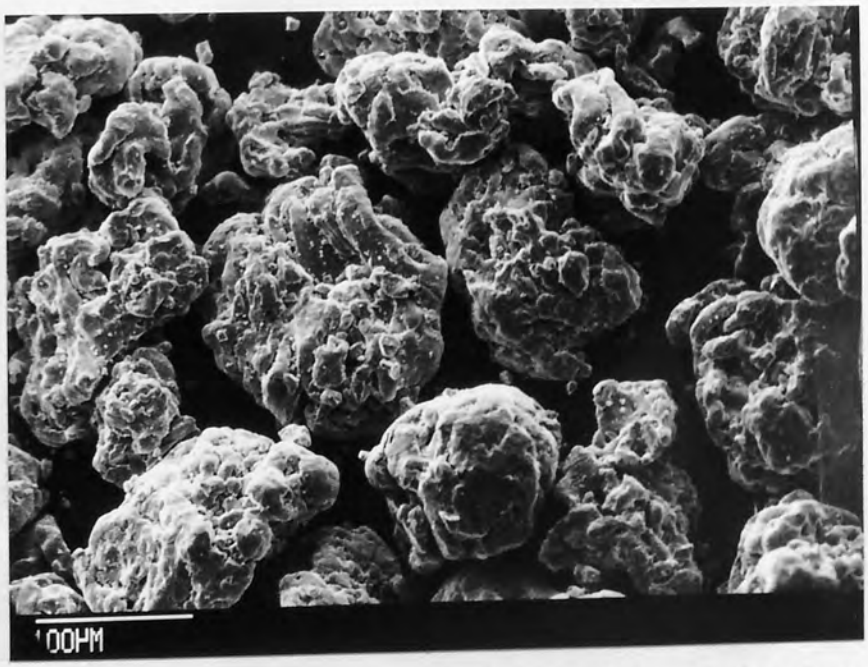

Plate 5.2. Höganäs PNC60, sponge pure iron powder with 0.60wt% phosphorus, admixed as ferro-phosphorus powder.

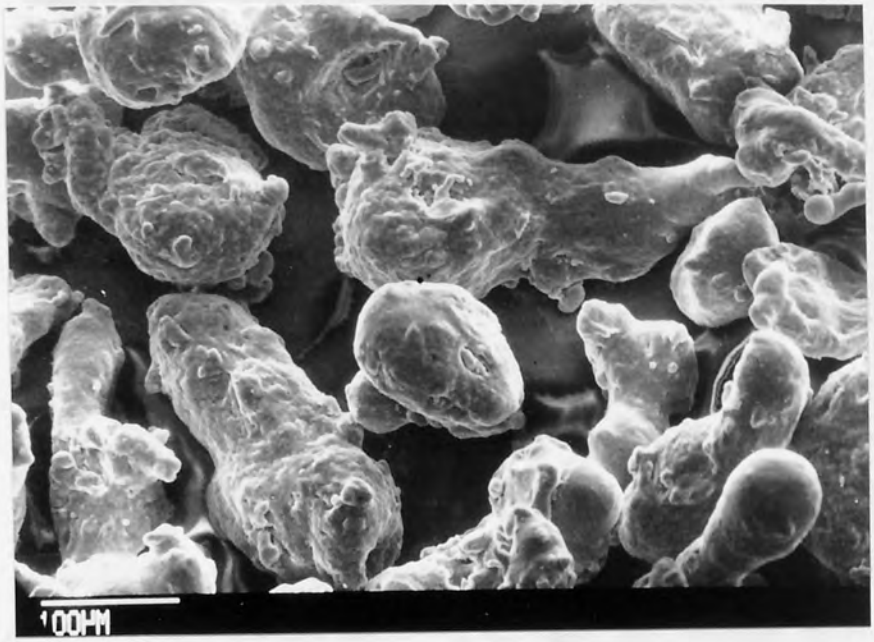

Plate 5.3. Aluminium powder.

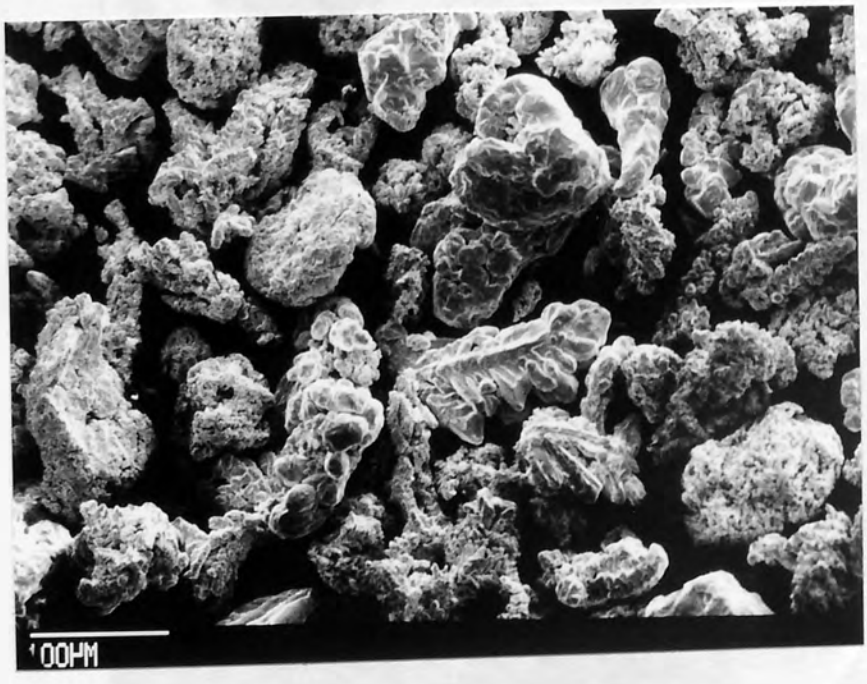

Plate 5.4. Copper powder.

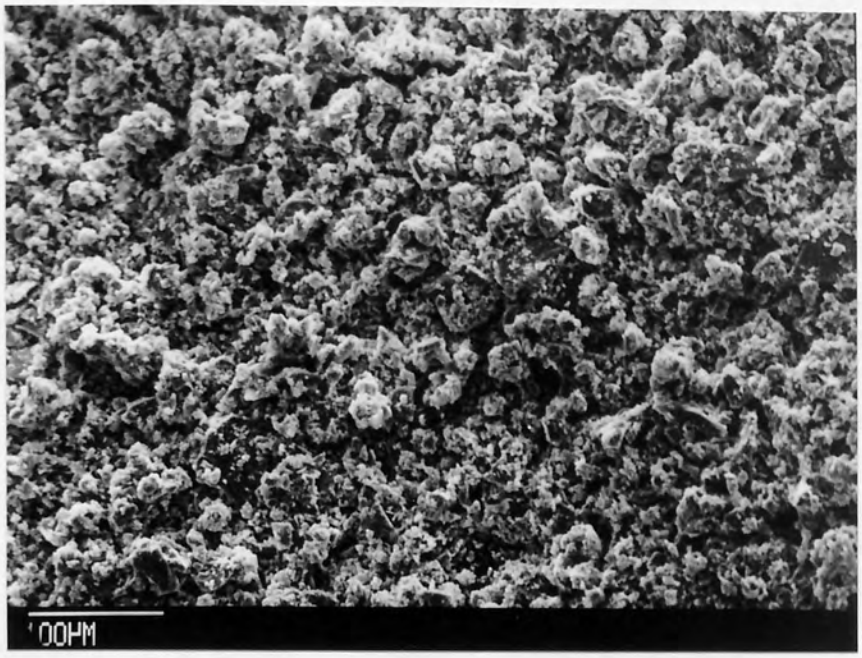

Plate 5.5. Silicon powder.

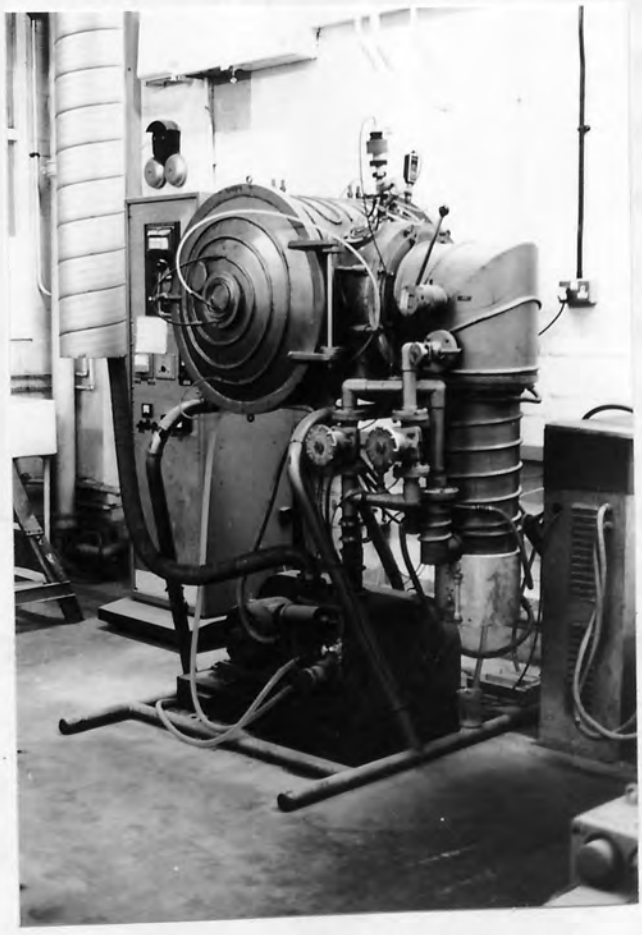

Plate 5.6. Vacuum sintering furnace.

Code	Composition (wt%, balance Fe)	Component powders
A	pure Fe	ASC100.29
B	1.0 Si	ASC100.29, Si
C	1.0 Cu	ASC100.29, Cu
D	1.0 Al	ASC100.29, Al
E	0.60 P	PNC60
F	1.75 Ni, 1.50 Cu, 0.50 Mo	Distaloy AB
G	4.00 Ni, 1.50 Cu, 0.50 Mo	Distaloy AE
H	0.1 Si	ACS100.29, Si
J	3.0 Si	ASC100.29, Si
K	0.60 P, 1.0 Si	PNC60, Si
L	0.60 P, 3.0 Si	PNC60, Si
M	1.0 Cu, 1.0 Si	ASC100.29, Cu, Si
N	0.60 P, 1.0 Cu	PNC60, Cu
R	0.60 P, 1.0 Cu, 1.0 Si	PNC60, Cu, Si

Table 5.5. Powder mixes, and identification codes.

5.4.1.1 Development of Powder Alloys

The following are some brief notes to explain the basic line of development of powder mixes. See the Discussion, Section 7, for more detail.

Powder A (pure Fe, ASC100.29): Basic data for comparison with subsequent developments.

Powders B (Fe-Si), C (Fe-Cu) and D (Fe-Al): 1wt% additions of elemental powders to determine effects on oxidation resistance.

Powders E (PNC60), F (Distaloy AB) and G (Distaloy AE): Comparison of oxidation resistance of partially pre-alloyed powders with pure Fe.

Powders H (Fe, 0.1Si) and J (Fe, 3.0Si): Determine effects of varying silicon additions on oxidation resistance of pure Fe powder.

Powders K (Fe, 0.6P, 1.0Si) and L (Fe, 0.6P, 3.0Si): Determine whether silicon additions have same effect on oxidation for pre-alloyed Fe, 0.6P powder (PNC60), as for pure Fe powder (ASC100.29).

Powders M (Fe, 1.0Cu, 1.0Si), N (Fe, 0.6P, 1.0Cu) and R (Fe, 0.6P, 1.0Cu, 1.0Si): Determine whether addition of copper could be used to counteract sintering shrinkage in Fe, 1.0Si alloy (powder B), pre-alloyed Fe, 0.6P alloy (powder E, PNC60) and Fe, 0.6P, 1.0Si alloy (powder K).

5.4.1.2 Mixing

Component powders for the alloys were weighed out on an analytical balance, to make up 300g batches. The batches were mixed in storage jars, which were approximately one-third filled with the 300g of powder. The storage jars were mounted in a powder blender, and rotated end over end, at a constant 38 revolutions-per-minute for 30 minutes. Mixed powders were visually inspected for signs of segregation and coalescence of particles. If found, the powder was sieved, to break up coalesced particles, and then remixed. This procedure has been shown to be effective by several specific short term projects at this university, circa 1975 [141].

5.4.2 Powder Compaction

PM samples were made with cylindrical, double-ended, punch and floating die tool sets, with stearic acid die-wall lubrication, using a 50 tonne capacity Avery-Dennison tension-compression machine.

Oxidation (TGA and TCA) samples were compacted in a 12.7mm diameter die set, to a height of 12.5±0.5mm.

Pure iron samples were compacted at 150, 250, 350, 450 and 550MPa, and alloy samples were compacted at 150, 350 and 550 MPa.

Dilatometry (TMA) samples were compacted in a 7.6mm diameter die set, to a height of 10.0±1.0mm, and were compacted at approximately 350MPa, the actual pressure being varied to obtain green densities similar to those of the TGA samples.

Thermo-calorimetric tests on pure iron showed that the heat of oxidation was greatest for samples compacted at 150MPa. Alloy powders were compacted at 150MPa only for these tests.

The compaction process was the same for all types of PM samples, and is illustrated in Figure 5.2.The punch faces and die wall were painted with a saturated solution of stearic acid dissolved in diethyl ether. The diethyl ether evaporated, leaving the die and punch surfaces coated with stearic acid. The bottom punch and die were assembled, with a metal chock supporting the die above the punch base (Figure 5.2a). The mass of powder required to make a compact of the required height was calculated, and then weighed out on a balance. This powder charge was poured into the die cavity, and the die was tapped to make the powder settle. The top punch was inserted into the die orifice, and the whole assembly placed between the compression platens of the tension/compression machine. When a load of about 2kN had been applied to the punches, the friction between the compressed powder in the die cavity and the die wall was sufficient to support the weight of the die, and the chock between the die and bottom punch was removed, leaving the die 'floating' (Figure 5.2b). The full

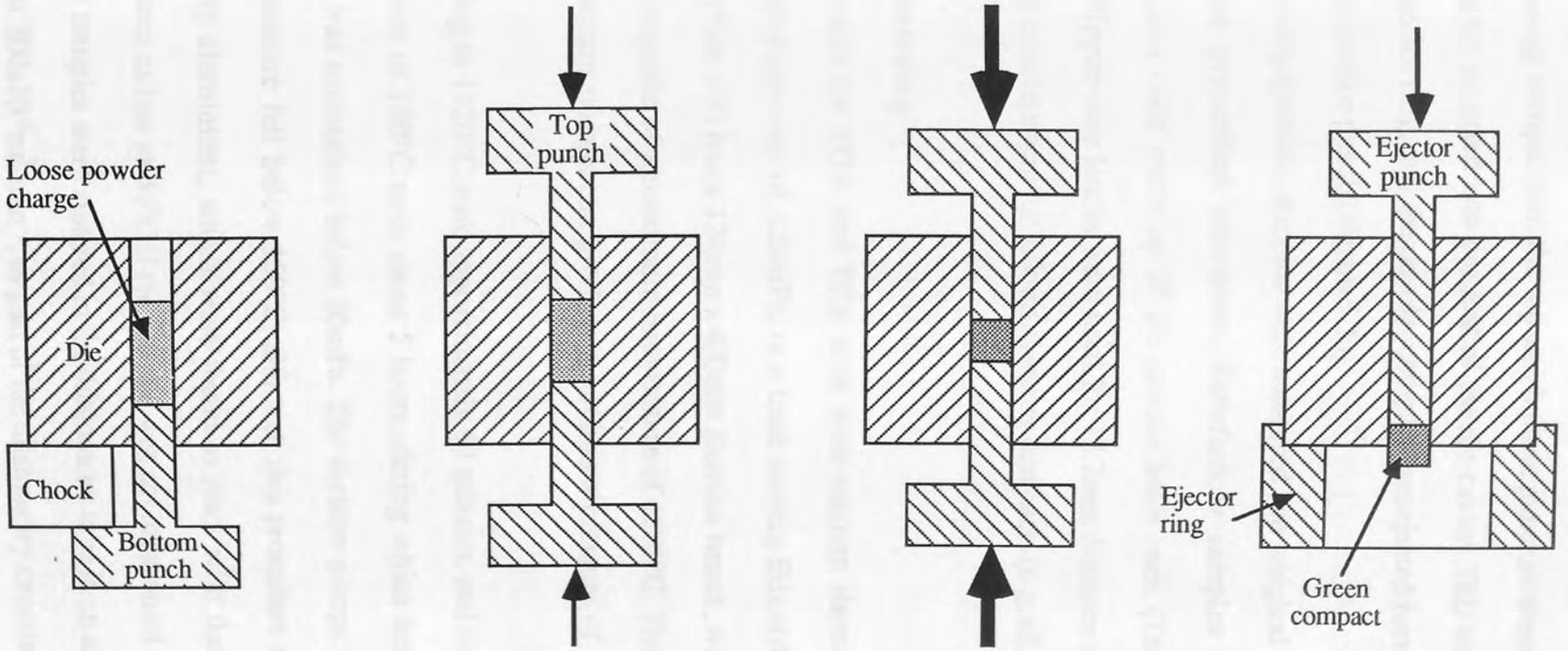

(a) Assembly of bottom punch and die with chock to produce die cavity.

(b) Light compression of powder charge allows removal of chock, to leave die 'floating.'

(c) Compaction.

(d) Ejection.

Figure 5.2 Powder compaction procedure.

compaction load was then applied and maintained for 5 seconds (Figure 5.2c).

Following compaction, the top and bottom punches were removed, and a special ejector punch inserted into one end of the die cavity. This assembly was then placed onto an ejector ring, and the powder compact was ejected into the cavity by applying a load to the ejector punch (Figure 5.2d).

Following ejection, samples were measured and weighed to ensure that they were within the prescribed tolerances. Satisfactory samples were marked with an identification code made up of the powder letter code (Table 5.5) and a compact number. Upper case letters were used for 12.7mm diameter compacts (e.g. A1, H4), and lower case letterers for 7.6mm diameter compacts (e.g. a3, k2).

5.4.3 Sintering

Compacts for TGA and TCA tests were vacuum sintered at 1120±5°C for 60 minutes at a pressure of <20mPa, in a front loading Edwards vacuum furnace. This furnace (Plate 5.6) has a 120mm x 400mm alumina hearth, with molybdenum heating elements capable of a maximum temperature of 1300°C. The Edwards diffusion and rotary vacuum pumps can produce a minimum pressure of <10mPa in the vacuum chamber.

Heating to 1120°C took approximately 60 minutes, and cooling from the sintering temperature to 150°C took about 5 hours, during which time the vacuum chamber pressure was maintained below 20mPa. The vacuum pumps were switched off when the temperature fell below 150°C, although this procedure was modified for alloys containing aluminium, which were found to react with the furnace atmosphere at temperatures as low as 50°C if the vacuum was not maintained at <20mPa.

TMA samples were sintered in the dilatometer tube in an atmosphere of inert argon flowing at $200 \times 10^{-6} m^3.min^{-1}$, as part of the dilatometry experiment.

5.5 WROUGHT PURE IRON SAMPLES

Since the oxidation resistance of sintered metals varies with compact density [158], it was desireable to make a comparison with the oxidation of fully dense iron. However, because of the retention of residual porosity it is not possible to achieve the absolute density of iron ($7.87 Mg.m^{-3}$) by the PM production route, and so fully dense samples had to be made from wrought iron.

The composition of the wrought iron had to be comparable to that of the ASC100.29 iron powder, which is exceptionally pure for a commercial product (<0.01wt% impurities). The purest commercial wrought iron available is Armco Iron (<0.1wt% impurities), made by the American Rolling Mill Company.

Armco bar was machined to a diameter of 12.7±0.1mm, and cut into 12.5±0.5mm lengths for thermobalance samples. For dilatometer samples, Armco bar was machined to a diameter of 7.6±0.1mm, and cut into 10.0±1.0mm lengths. Machining marks were removed by hand grinding with 1200 grit silicon carbide paper, taking care to maintain the definition of the edges of sample.

Samples were then marked with an identification code, made up of the letter 'A' (12.7mm diameter samples) or 'a' (7.6mm diameter samples), to denote pure iron, and a number (distinct differences between PM samples of ASC100.29, also denoted by the letters 'A' and 'a', and Armco samples precluded any confusion). Samples were degreased by ultrasonic cleaning in methylated spirits, and were then vacuum annealed at 920°C for 20 minutes at a pressure of <20MPa.

5.6 STORAGE AND HANDLING OF SAMPLES

When not being studied, samples were stored in a dessicator to minimise the contamination of surfaces with moisture, grease and dust. Following sintering or vacuum annealing, samples were kept clean by handling with clean metal tongs only.

5.7 THERMO-GRAVIMETRY EXPERIMENT

Thermo-gravimetric experiments were performed with the Stanton Thermobalance, and lasted for 24 hours at a constant temperature of 300, 400, 500, 600 or 700°C, in an atmosphere of 80% N_2, 20% O_2 gas flowing at $200x10^{-6}m^3.min^{-1}$.

5.7.1 Stanton Thermobalance Specification

Furnace: Platinum-rhodium bifilar wound vertical tube furnace, maximum temperature 1400°C (minimum controllable temperature 180°C). Controlled by electro-mechanical contact switch linked to platinum/platinum-13%rhodium thermocouple. 30mm diameter alumina furnace tube with vent to atmosphere at top.

Balance: Range 100mg, extended to ±1000mg by automated loading mechanism. Maximum sample weight 20g.

Chart recorder: Dedicated (built-in) two-pen recorder:

(1) Sample mass-change: Range 100mg, resolution 1mg.

(2) Furnace temperature: Range 0-1400°C. Resolution 20°C at 0-500°C, and 10°C at 500-1400°C.

5.7.2 Description of the Stanton Thermobalance

The thermobalance (Plate 5.7 and Figure 5.3) essentially consists of three linked units: a vertical tube furnace, a two-pen chart recorder and a modified analytical balance. The furnace is situated behind the chart recorder, and together these are mounted on the roof of the balance cabinet.

An alumina sample support rod is mounted on gimbals at one end of the balance beam, and extends up into the furnace tube through a hole in the balance chamber roof. At the top of the support rod is an alumina platform for the oxidation sample. The sample support rod and platform are maintained vertical by the balance loading pan,

Figure 5.3. Schematic diagram of thermobalance.

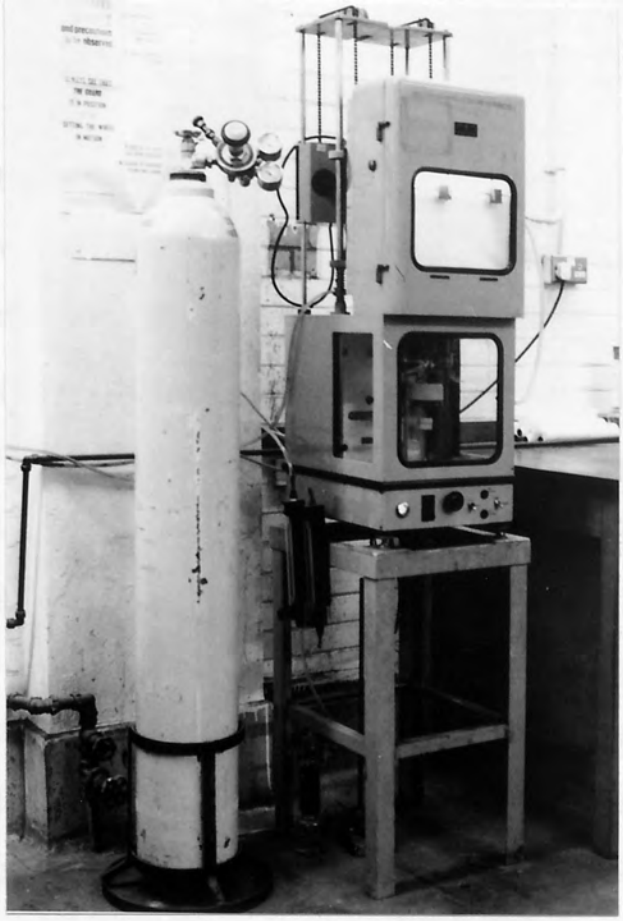

Plate 5.7. Stanton Thermobalance TGA.

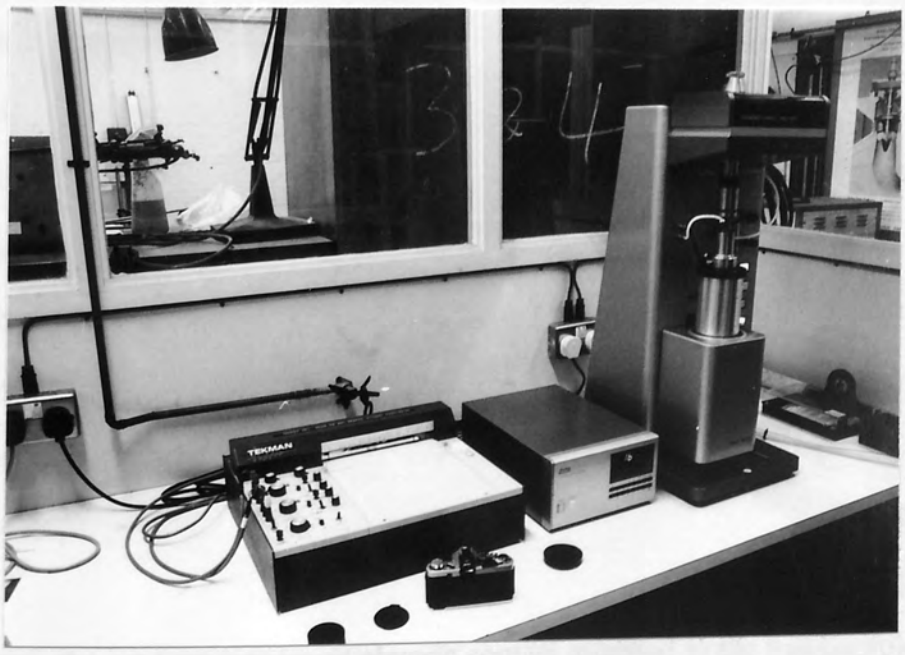

Plate 5.8. Stanton Redcroft TMA (dilatometer).

which hangs rigidly below the gimbals.

The furnace moves on vertical columns, its position being maintained by the weight of the electric power supply transformer, which is similarly mounted behind it in a counterbalance arrangement. The furnace can be raised up the columns to gain access to the sample platform. In the lowered position, the furnace tube locates in a closely fitting water cooling jacket. Gases for controlled atmospheres can be introduced through the gas distribution ring below the water jacket, and are exhausted to the atmosphere through a vent at the top of the furnace tube. In the absence of a controlled atmosphere, air will be drawn in through the sample support rod hole at the bottom of the furnace.

At the other end of the balance beam, above the counterbalance pan, is fixed a capacitance plate, above which is a follower plate. The follower plate is supported at one end by knife edges that are co-axial with the balance beam knife edge, and suspended at the other end by a pick-up arm, which can be moved up or down by a servo motor. The servo motor is operated by an electronic circuit that monitors the charge between the capacitance and follower plates. The charge, and hence the separation, between the plates is kept constant by raising or lowering the pick-up arm. The servo motor also moves the mass-change pen on the chart recorder, so that changes in the attitude of the balance beam, due to changes in the sample mass in the furnace, are accurately recorded on the chart.

When the mass-change pen reaches either extreme of its travel, it operates a micro-switch to activate an automatic weight loading mechanism. This mechanism adds or removes weights from the loading pan, counteracting sample mass changes greater than 100mg, to a limit of ±1000mg.

The furnace temperature is controlled by an electric circuit, in which the furnace temperature pen of the chart recorder forms a circuit breaker switch. The chart pen is driven by a servo-motor controlled by the furnace thermocouple. When the temperature is at, or above, the set temperature an electric contact attached to the pen completes the control circuit, and the furnace power supply is switched to a low output setting. The

furnace power supply is automatically switched to a high output setting when the control circuit is broken by the pen moving to indicate a temperature below the set level.

The balance is designed to operate unattended, and to prevent the balance mechanism becoming stuck because of long periods of inactivity during experiments (e.g. because the sample mass does not change significantly, or the settling of dust on the knife edges), an automatic mechanism periodically arrests the balance beam. This mechanism works simply by lifting the balance beam clear of the knife edge fulcrum (the arrest position), and then lowering it back again (the action position). The arrests last for a few seconds of every 5 minute period during automatic operation, and are recorded by the mass-change pen of the chart recorder as a small flick towards the middle of the chart.

5.7.3 TGA Experimental Procedure

Preliminary tests established the accuracy of the balance to be better than ±0.5mg and that furnace temperature control was within ±10°C of set temperatures of 300, 400, 500, 600 and 700°C. The periodic balance arrest mechanism was found to gain ≤5 seconds in every 24 hours. Experiments showed that the optimum flow rate for the 80% N_2, 20% O_2 gas lay between $150x10^{-6}$ and $300x10^{-6} m^3.min^{-1}$. The gas was dried by passing through silica gel before admitting to the furnace .

TGA tests on pure iron samples were conducted at 300, 400, 500, 600 and 700°C, and established that the oxidation rate of PM samples in this temperature range was greatest at 500°C. Thus it was decided to conduct TGA tests on alloy samples at 500°C, with a very few tests conducted at 400°C and 600°C.

Before the start of each test, the vertical tube furnace was raised clear of the sample platform, and allowed to stabilise at the experimental temperature. The oxidation sample was placed on the platform with a suitable counterweight mass on the counterbalance pan, and the thermobalance was set to operate automatically. After a steady gas flow rate of $200x10^{-6} m^3.min^{-1}$ had been established, the oxidation test was started by

lowering the furnace at the next automatic balance arrest.

It should be noted that each test started with the sample at room temperature in the ambient laboratory atmosphere. Initial conditions were therefore affected by thermal equalisation and the purging of laboratory air from the furnace tube by the 80% N_2, 20% O_2 gas mixture.

Each test lasted for 24 hours, after which the furnace was raised at the next balance arrest, and the sample allowed to cool to room temperature whilst its mass-change continued to be recorded.

The dimensions and masses of samples were recorded before and, when practical, after oxidation tests. Dimensions were measured with a micrometer screw guage to ±0.005mm, and masses determined on an analytical balance to ±0.1mg.

5.8 THERMO-MECHANICAL (DILATOMETRY) EXPERIMENT

Dilatometry experiments were performed with a Stanton-Redcroft 790 Series TMA, controlled by a Stanton-Redcroft 706 Temperature Programmer unit (Plate 5.8). Output from the dilatometer transducer and the furnace thermocouple were recorded by a two channel chart recorder.

The control unit was programmed with the cycle shown in Figure 5.4, which was designed to represent sintering (at 1120°C) followed by a period at an elevated temperature typical of oxidation tests (500°C). Tests were conducted in a controlled atmosphere of argon gas flowing at $200 \times 10^{-6} m^3.min^{-1}$, which was passed through a drying and purifying train before entering the furnace.

5.8.1 TMA Specification

Furnace: Platinum-rhodium bifilar wound vertical tube furnace, maximum temperature 1500°C. Platinum/platinum-13%rhodium thermocouple.

Dilatometer transducer: LVDT sensitivity 1V mm^{-1}.

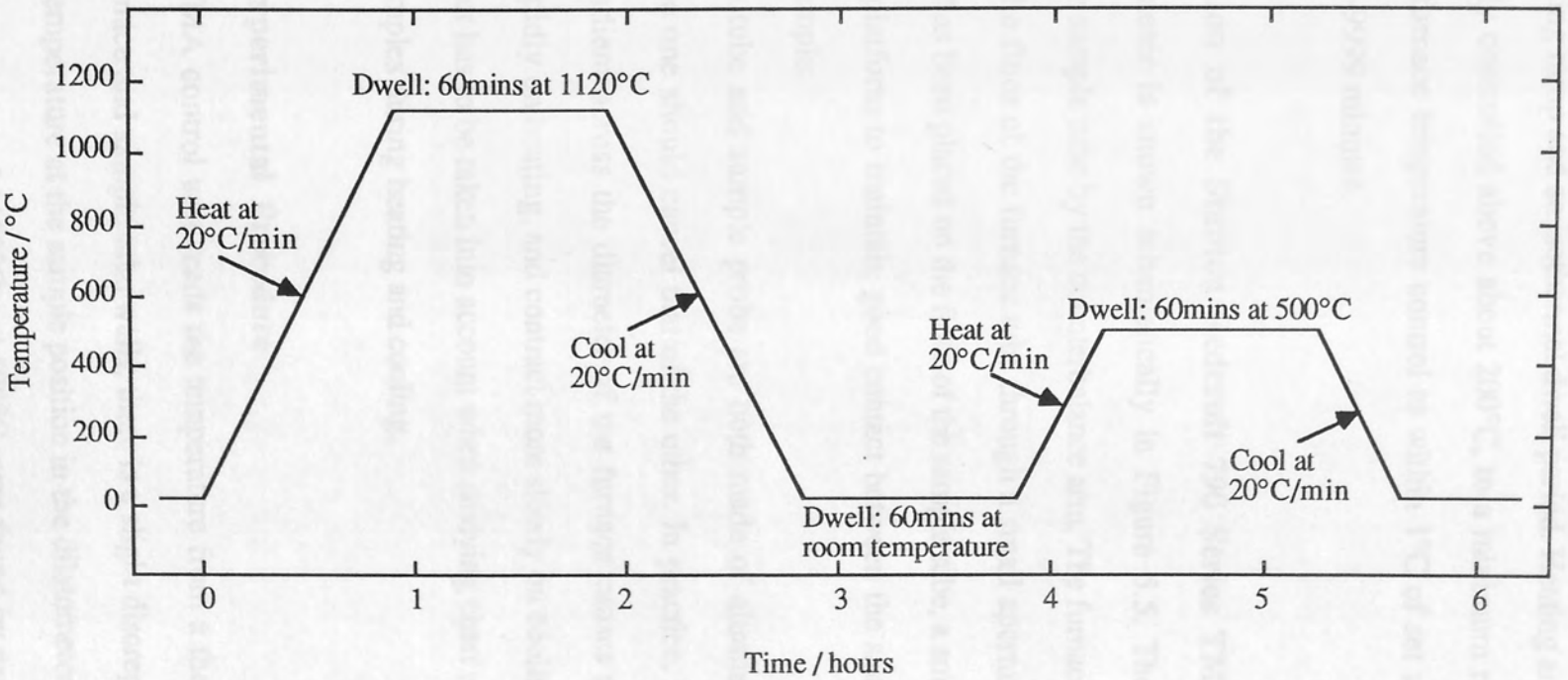

Figure 5.4. Thermal cycle for TMA experiment.

Controller: 4 stage programmable microprocessor. Each stage consists of a heating/cooling ramp and an isothermal dwell period. Heating and cooling rates can be accurately controlled above about 200°C, to a minimum rate of 10°C min^{-1}. Isothermal furnace temperature control to within 1°C of set temperature. Dwell periods of 1-9999 minutes.

5.8.2 Description of the Stanton Redcroft 790 Series TMA

The dilatometer is shown schematically in Figure 5.5. The sample probe is suspended in the sample tube by the counterbalance arm. The furnace can be lowered to gain access to the floor of the furnace tube through a small aperture in the tube wall. When a sample has been placed on the floor of the sample tube, a small weight is placed on the loading platform to maintain good contact between the sample probe and top surface of the sample.

The sample tube and sample probe are both made of alumina, so that thermal expansion of the one should cancel that of the other. In practice, it is found that the temperature gradient across the diameter of the furnace causes the sample tube to expand more rapidly on heating, and contract more slowly on cooling, than the sample probe. This effect has to be taken into account when studying chart records of the linear expansion of samples during heating and cooling.

5.8.3 TMA Experimental Procedure

Since the TMA control unit reads the temperature from a thermocouple placed between the furnace and sample tube walls, there is a slight discrepancy between that and the actual temperature at the sample position in the dilatometer tube. The settings required for temperatures of 1120°C and 500°C were found by experimentation, and due to the microprocessor control were precisely reproducible. Similarly, the internal clock of the microprocessor made the timing of the temperature programme very

Figure 5.5. Schematic diagram of dilatometer.

accurate.

An initial experiment was performed on the TMA to establish the thermal instability of the dilatometer. The test programme (Figure 5.4) was run without a sample several times, and average values taken. These values were used to correct the data aquired in subsequent TMA tests, thereby eliminating the effects of dilatometer thermal instability from the apparent thermal instability of the sample.

7.6mm diameter samples were placed in the sample tube, and a 2g weight placed on the sample probe loading platform to ensure good sample/probe contact. The furnace was raised to surround the sample tube, and the programme shown in Figure 5.4 was run. The height of samples was measured to an accuracy of ±0.005mm with a micrometer screwgauge before and after the test.

5.9 THERMO-CALORIMETRY EXPERIMENT

TCA tests were performed with the modified Stanton Thermobalance, in an atmosphere of 80% N_2, 20% O_2 gas flowing at $200 \times 10^{-6} m^3.min^{-1}$. Each test lasted for about 60 minutes, during which time the core temperature of the oxidation sample was measured and recorded with a chart recorder, with an accuracy of ±2°C.

5.9.1 Description of TCA Equipment

The modifications to the thermobalance consisted of replacing the sample support rod and sample platform with a double-bore 4.5mm diameter alumina support tube (Figure 5.6). The bead of a platinum/platinum-13%rhodium thermocouple was seated at the top end of this tube, at the centre of the furnace hot zone. The thermocouple wires passed down the bores in the tube, and re-emerged through holes in the tube wall just above the balance beam, where they were connected to compensation wires leading to the chart recorder. The thermobalance could not be used for weighing operations in this configuration, because of the relatively heavy leads connected to the thermocouple wires.

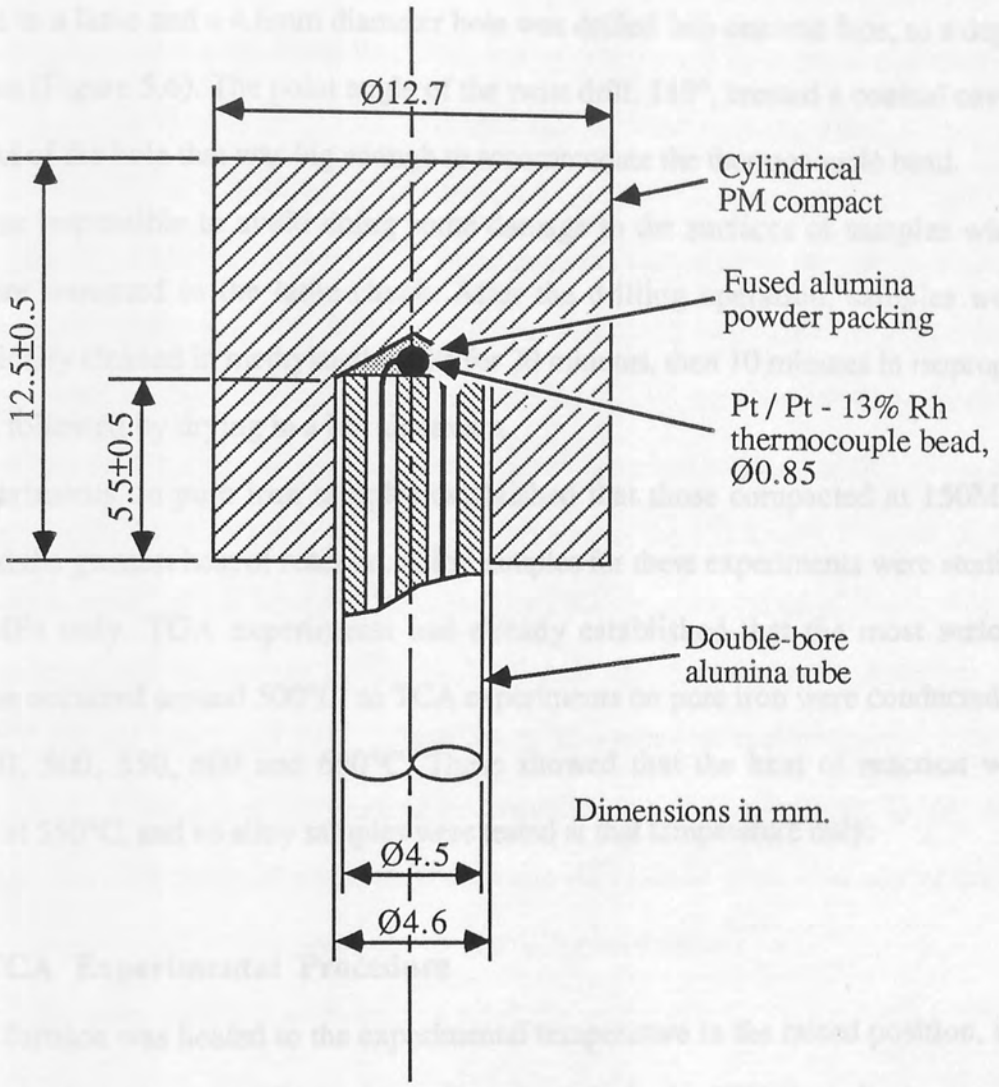

Figure 5.6. TCA test sample and thermocouple position.

5.9.2 TCA Sample Preparation

Samples for TCA experiments were compacted to the same dimensions as TGA samples (diameter 12.7mm, height 12.5±0.5mm). After sintering, samples were mounted in a lathe and a 4.6mm diameter hole was drilled into one end face, to a depth of 5.5mm (Figure 5.6). The point angle of the twist drill, 118°, created a conical cavity at the end of the hole that was big enough to accommodate the thermocouple bead.

It was impossible to avoid doing some damage to the surfaces of samples when they were mounted in the lathe chuck. After the drilling operation, samples were ultrasonically cleaned in methylated spirits for 20 minutes, then 10 minutes in isopropyl alcohol, followed by drying in a hot air stream.

Experiments on pure iron samples established that those compacted at 150MPa exhibited the greatest heat of reaction. Alloy samples for these experiments were studied at 150MPa only. TGA experiments had already established that the most serious oxidation occurred around 500°C, so TCA experiments on pure iron were conducted at 400, 450, 500, 550, 600 and 650°C. These showed that the heat of reaction was greatest at 550°C, and so alloy samples were tested at that temperature only.

5.9.3 TCA Experimental Procedure

The furnace was heated to the experimental temperature in the raised position, i.e. clear of the thermocouple. The 4.6mm diameter hole in the TCA sample was partly filled with fused alumina powder. The sample was then carefully placed on the thermocouple tube so that the powder surrounded the thermocouple bead in the conical drill-point cavity (Figure 5.6). This was intended to protect the thermocouple bead in the event of oxide scale growth in the hole.

When the furnace reached the experimental temperature, the 80% N_2, 20% O_2 gas flow rate was set at $200 \times 10^{-6} m^3.min^{-1}$, and the chart recorder started. The furnace was then lowered, and a continuous record of the specimen's core temperature was made, including the initial heating-up period. Each test was continued until it appeared certain

that the core temperature had stabilised with that of the furnace.

5.10 HARDNESS TESTS

Following each oxidation experiment, the surface hardness of one end face of the sample was tested with a Rockwell hardness testing machine. The average and standard error of ten tests made with the 1/16th inch steel ball indenter were recorded.

The irregularity of the oxide scale surface, and the presence of surface porosity, made the use of the 1/16th inch steel ball indenter preferable, since it spread the indenter load over more of the surface than the pointed Rockwell brale indenter. The large impression made by the indenter made it impossible to take accurate readings from the curved surface of the sides of samples, so hardness tests had to be confined to the end faces of samples. Most of the hardness tests fell within the Rockwell 'F' scale (60kgf load), though some of the harder oxides required the 'B' scale (100kgf load). For the softest oxides it was necessary to use the Rockwell superficial surface hardness test scales '45T' (45kgf load) and '30T' (30kgf load). The range of results obtained on the 'F' scale allowed for some samples to be retested on the overlapping 'B' or '45T' scales, and likewise some samples tested on the '45T' scale were also tested on the '30T' scale, providing comparative data for the different scales.

During the early stages of experiments, attempts were made to use the more accurate Vickers hardness test. However, measuring the diagonals of the Vickers pyramid impressions (with a micrometer scale viewed through a microscope, with incident-light illumination) on the irregular, dark grey, non-reflecting porous oxide scales was very difficult, and consequently the results showed a large standard error, were not reproducible and generally appeared unreliable. The Rockwell test has the advantage of giving a direct reading of hardness on a dial gauge.

5.11 X-RAY DIFFRACTION (XRD) TESTS

The XRD equipment consists of a Phillips PW1050 goniometer controlled by a microcomputer. Samples were irradiated with a beam of monochromatic cobalt K_α X-rays, and the reflection intensity was recorded by a chart recorder. The recorded intensity peaks correspond to the angle 2θ in the Bragg equation

$$n\lambda = 2\,d\,\sin\theta \qquad (5.1)$$

where n is an integer, λ the wavelength of the incident radiation, and d is the interplanar spacing of the crystal structure. The crystal can be identified by comparing calculated values of d and the relative intensity of peaks with standard reference patterns [178].

Alloy samples were analysed to determine the alloy phases produced by sintering compacts of mixed elemental powders. 12.7mm diameter compacts were sectioned along the longitudinal axis, and the flat face ground on silicon-carbide paper to 1200 grit size. This section was then mounted in the XRD goniometer with the flat face facing the X-ray source.

Oxidised samples were analysed, to determine the oxides present in the surface scale. These samples were placed whole in the XRD goniometer, so that the X-radiation was incident on the oxide scale on the flat end surface.

5.12 METALLOGRAPHY

The preparation of metallographic samples by grinding and polishing was made very difficult by the presence of porosity and the oxide scales. There was a tendency for the metal and oxide to smear into cavities, and for the oxide to be torn out by the grinding and polishing action. Numerous authors have written about the difficulty of preparing oxide scales [173] and porous metals [174] for microscopical examination, but none appear to have tackled these two features combined.

The eventual process developed for this present work is outlined in Figure 5.7, and discussed in the following subsections.

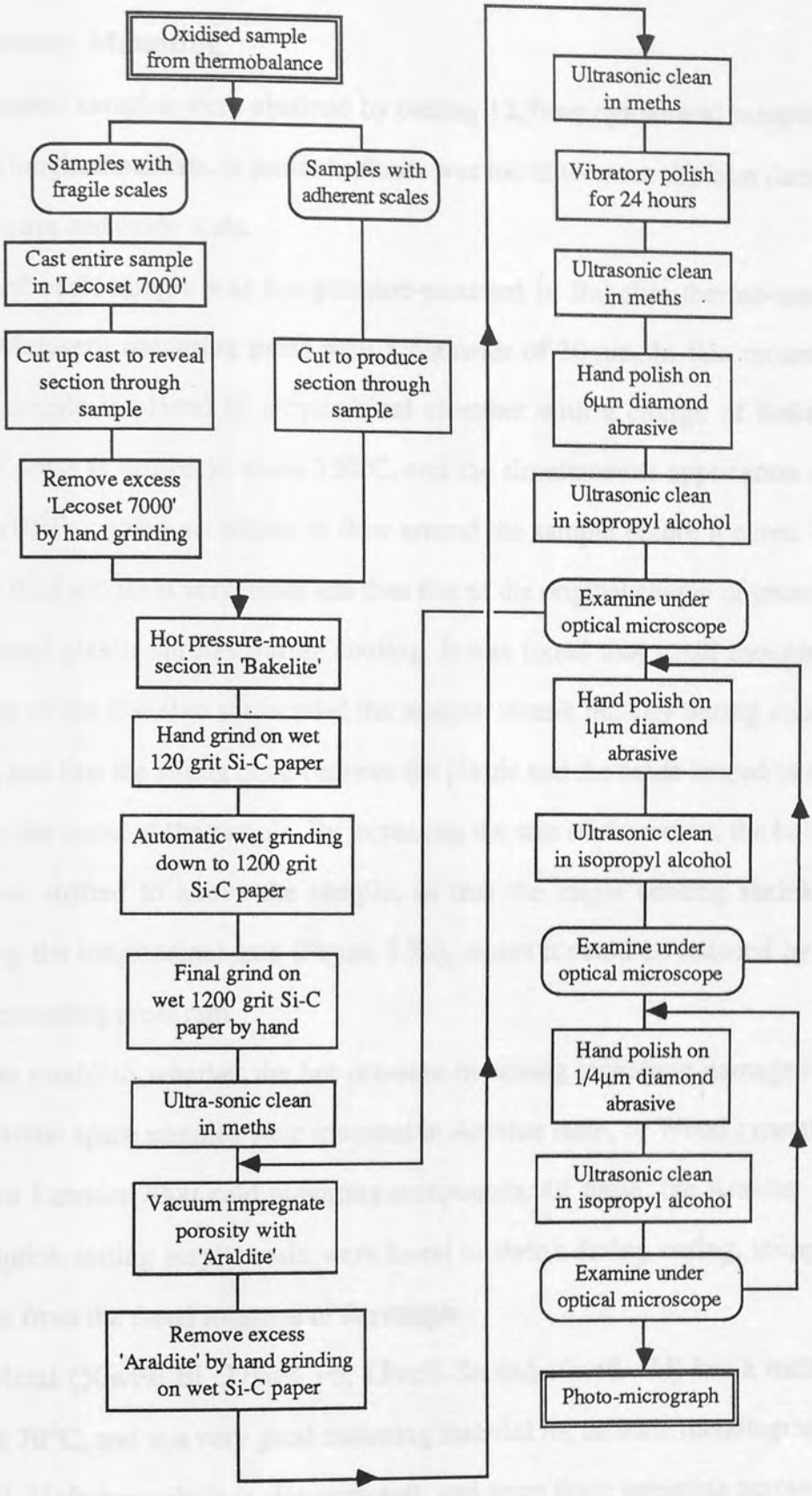

Figure 5.7. Metallographic preparation procedure.

5.12.1 Specimen Mounting

Metallographic samples were obtained by cutting 12.7mm cylindrical samples in half along the longitudinal axis. A junior hacksaw was found to cause the least damage to the metal matrix and oxide scale.

One half of each sample was hot pressure-mounted in Bakelite thermo-setting plastic, in a Metaserv mounting press with a diameter of 30mm. In this mounting process, the sample is placed in a cylindrical chamber with a charge of Bakelite granules. The press is heated to about 150°C, and the simultaneous application of a pressure of $3x10^5$Pa causes the plastic to flow around the sample before it cures. The volume of the final mount is very much less than that of the original charge of granules, and the hardened plastic shrinks during cooling. It was found that small mounts, in which the bulk of the Bakelite surrounded the sample, shrank radially during cooling (Figure 5.8a), and that the strong bond between the plastic and the oxide tended to strip the scale from the metal of the sample. By increasing the size of the mount, the bulk of the plastic was shifted to above the sample, so that the major cooling shrinkage occurred along the longitudinal axis (Figure 5.8b), where it could be reduced by the action of the mounting press ram.

In order to establish whether the hot pressure-mounting technique damaged the oxide scales, some spare samples were mounted in Araldite resin, or Wood's metal, or Howmedica or Lecoset 7000 cold mounting compounds. Of these, the Araldite and Howmedica quick-setting acrylic resin were found to shrink during curing, stripping the oxide scale from the metal substrate of the sample.

Wood's Metal (50wt% Bi, 27wt% Pb, 13wt% Sn and 10wt% Cd) has a melting point of about 70°C, and is a very good mounting material for delicate metallographic samples [174]. Unfortunately it is also very soft, and apart from smearing across the PM sample surface and filling up pores, it also irretrievably contaminated polishing cloths.

Lecoset 7000 is a cold curing polymer, formulated to have very low shrinkage; only

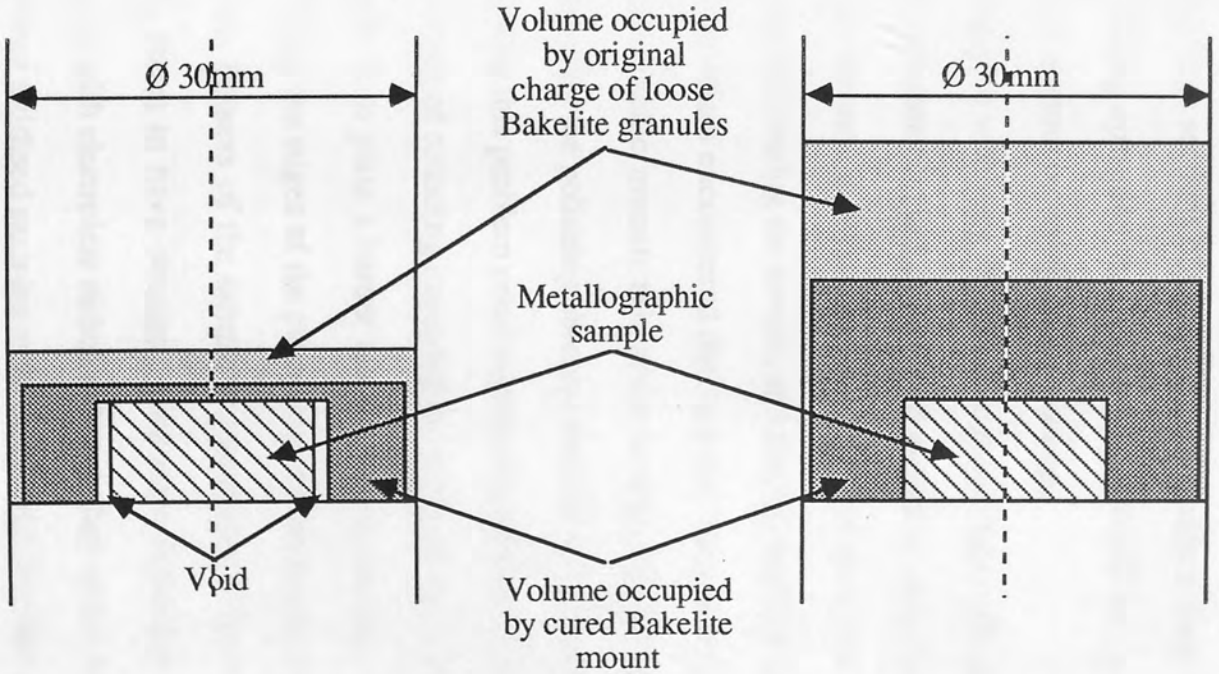

a) Short mount: considerable radial shrinkage during curing.

b) Tall mount: mainly longitudinal shrinkage during curing.

Figure 5.8. Shrinkage of Bakelite thermo-setting plastic during mounting of metallographic specimens.

0.1 - 0.2%, according to the manufacturer. Although it lived up to these claims quite admirably, it turned out to be a little too soft for manual metallographic preparation techniques, often leading to unintentionally bevelled mounts.

Comparative samples prepared by mounting in Bakelite and Lecoset 7000 indicated that the former process did not damage oxide scales. In fact, the most detrimental part of the preparation process was found to be the cutting with a hacksaw, which often caused large sections of poorly attached oxide scale to flake off samples. Unfortunately this cutting operation was necessary and could not be replaced by any other available method without incurring greater damage.

Samples with very friable oxide scales (especially those oxidised at 600°C or 700°C) were therefore cast in Lecoset 7000 mounting compound before sectioning. After being cut up, the mounts were hand ground until there was about a 3mm thick layer of the Lecoset left coating the sample, and this was then mounted in Bakelite.

A problem encountered during polishing was the rounding of sample edges in the metallographic mount; this arose because the mounting medium was more easily removed by the polishing abrasive than the harder metal matrix (Figure 5.9a). Samples exhibiting this problem could not be photographed with an optical microscope, because the degree of rounding exceeded the depth of focus of the optics. One frequently used remedy is to plate a harder metal onto the sample surface before mounting; during polishing, the edges of the plated coating are rounded instead of the sample's edges, so that the flatness of the sample is maintained (Figure 5.9b) [174]. Guruswamy *et al* [175] claim to have obtained good edge definition by plating oxidised iron alloy samples with electroless nickel, although they do not describe their technique.

Some oxidised samples were plated with Buehler Edgmet electroless nickel to test out these claims. It would appear that successful plating requires the complete removal of the passive haematite layer (eg. by electrolytic cleaning in NaOH solution), which casts some doubt over the metallography of Guruswamy *et al* [175]. The electroless nickel was found to form a good hard coating on magnetite, but since the aim of the

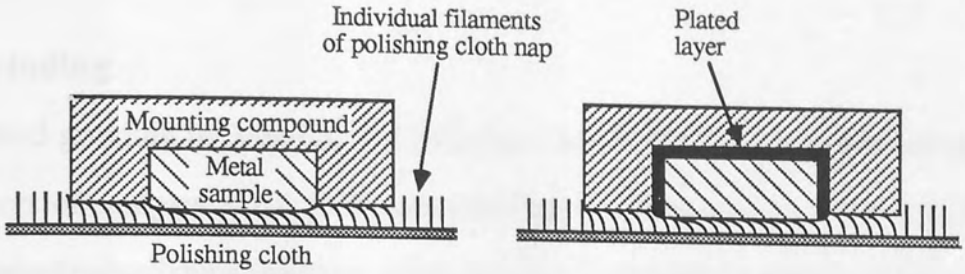

(a) Rounding of sample's edges due to preferential removal of soft mounting compound during polishing.

(b) Hard plated layer on sample prevents rounding of sample's edges.

Figure 5.9. Development of surface relief during polishing.

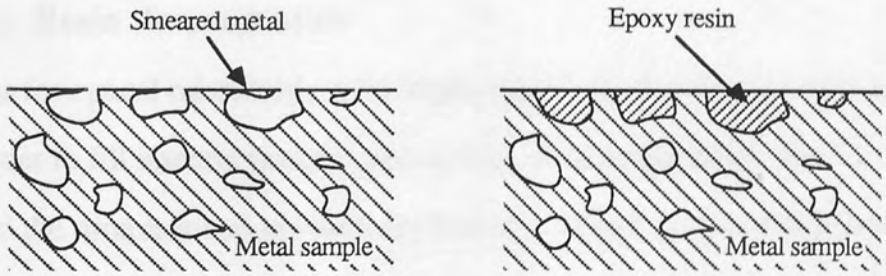

a) Unimpregnated surface: polishing smears unsupported pore edges across surface.

b) Impregnated surface: epoxy resin supports edges of pores at polished surface, preventing smearing.

Figure 5.10. Smearing of the metal matrix during the polishing of PM metallographic specimens.

plating process had been to retain the edge definition of the haematite layer, this result was of little practical value. Good edge definition was eventually achieved with improved grinding and polishing techniques.

5.12.2 Grinding

After hand grinding on wet 120 grit SiC paper to remove the hacksaw-damaged surface layers of samples, subsequent wet grinding was done with a Leco Vari/Pol automatic grinding/polishing machine, producing flat, unbevelled specimens. Samples were ground six at a time in a special mounting jig, at a pressure of about 42kPa (ie. a load of 275.8kPa (40psi) distributed evenly over six 30mm diameter samples) on 120, 480, 600 and 1200 grit papers. Three fresh papers of each grit size were used for 3 minutes at a time, according to the manufacturer's recommended procedure. A final hand-grinding on wet 1200 grit Si-C paper was necessary to reveal the porosity in the sample.

5.12.3 Epoxy Resin Impregnation

All samples for optical microscopy were impregnated with Araldite epoxy resin after grinding, in order to fill internal porosity and cavities at the metal/oxide interface. This greatly reduced the time required to obtain the true microscopic structure of samples by polishing. Without impregnation, the metal matrix was smeared into surface porosity (Figure 5.10), and the oxide scale sometimes broke out of the mounting. As a further benefit, impregnation sealed open porosity against the ingress of polishing compounds and lubricants during polishing. Samples were almost impossible to clean if their surfaces were not sealed, as the polishing media continuously oozed out of the porosity. Although the shrinkage of Araldite precludes its use as a metallographic mounting medium, the quantities of the resin present in sample porosity are so small as to make the effect negligible in this situation.

A common preparatory step during the impregnation of PM samples is to strongly

etch the metal for several minutes (for example in 4vol% HNO_3 in alcohol). This dissolves the thin films of metal smeared across surface pores, and improves the penetration of the epoxy resin. However, this etching was found to severely damage the oxide scales on samples, and was therefore excluded from the metallographic preparation procedure. It was very difficult to open up all the surface porosity by only grinding and polishing, so impregnation was not always successful, especially for samples with small pores, which sometimes had to be re-impregnated several times to obtain a satisfactory result. Samples requiring re-impregnation were polished with 6μm diamond abrasive, in an attempt to open-up more surface porosity.

After ultrasonic cleaning in methylated spirits, samples were dried in a hot air stream, and then placed in a vacuum dessicator for at least fifteen minutes, to evaporate residual moisture.

Araldite MY778 epoxy resin was mixed in the ratio 1 part hardener to 8 parts resin, by volume, and then warmed for about 5 minutes in an oven at 50°C to reduce its viscosity. The resin was then poured onto the metal surface of dried samples, which were placed in the vacuum dessicator. The dessicator was evacuated to allow the air trapped in pores to bubble through the epoxy resin. After 5 minutes, the dessicator was re-opened, and the resin was forced into the evacuated pores by atmospheric pressure. Araldite-impregnated samples were cured for a minimum of sixteen hours in an oven at 40°C.

When the Araldite had cured, the excess was removed by hand-grinding with wet 1200 grit Si-C paper, taking care not to remove the impregnated metal surface.

5.12.4 Polishing

The nap of polishing cloths has a tendency to deform under pressure, and follow the surface relief of the specimen being polished, leading to the increased removal of relatively soft phases in the microstructure (in much the same way as occurs with the mounting compound - see Figure 5.9). Napless cloths cannot retain very much

polishing compound, and so tend to polish very slowly [176]. For these reasons, the next stage after impregnation was vibratory polishing for 24 hours, using a Nashton MI4 metallurgical vibratory polisher, using napless terylene cloth impregnated with 1μm diamond abrasive suspended in Microfin oil. At the end of this period, samples were ultrasonically cleaned in methylated spirits.

Supporting the metal matrix by impregnation gave very good results with vibratory polishing. However, previous experience had shown that the vibratory polishing of unimpregnated porous samples produced smeared surfaces, no matter how short or long the polishing period. Therefore, since at this stage it was not known whether the impregnation process had been entirely successful, each vibratory-polished sample was hand polished for 5 minutes with 6μm diamond abrasive, suspended in Microfin oil on Leco Pan K cloth, which has a very short nap (and should, therefore, not produce very much surface relief on the sample). This did no significant damage to the sample, but did reveal any unimpregnated porosity sealed by smearing of the metal matrix. Badly smeared samples were returned to the impregnation stage of preparation. The same treatment was accorded to samples that continued to ooze lubricating oil from their surfaces after cleaning.

Successfully impregnated and polished samples were next ultrasonically cleaned in isopropyl alcohol for 10-15 minutes. Isopropyl alcohol leaves less residue than methylated spirits when the sample surface is dried [177].

Samples were then polished with 1μm diamond abrasive in Microfin oil, on Metaserv Metron (synthetic velvet) cloth. Polishing was done by hand with only light pressure (to minimise distortion of the polishing cloth nap) and for short periods. Each polishing period lasted 3 minutes, after which samples were ultrasonically cleaned in isopropyl alcohol for 3 minutes. For final polishing, 1/4μm diamond abrasive, suspended in Microfin oil on Metaserv Metron cloth, was used, with the same procedure as for the 1μm polish. This was repeated until examination with an optical microscope showed no improvement in sample microstructure between polishing

stages.

5.12.5 Etching

Oxidised samples with a large proportion of wüstite in their oxide scale (those oxidised at 600°C and 700°C) were etched in 20.0 vol% HCl in alcohol, to reveal the wüstite grain boundaries and the wüstite/magnetite interface. Thin oxide scales were rapidly damaged by exposure (either by immersion or swabbing) to either etchant, so all specimens oxidised at 500°C or below were examined in the unetched condition.

5.12.6 Micro-Examination

Metallographic specimens were examined by optical microscopy, and the micro-structures were recorded with photo-micrographs, taken with a Polyvar metallurgical microscope.

Specimens prepared by the method described above were unsuitable for examination in the scanning electron microscope (SEM). The Araldite would have evaporated under the heating effect of the electron beam, and subsequent condensation would have damaged to the electron optics. Samples prepared without impregnation were badly smeared and tended to be difficult to clean and dry sufficiently for examination in the SEM.

5.13 SCANNING ELECTRON MICROSCOPY

The surface morphologies and compositions of oxide scales, alloys and powders were studied with a Cambridge Instruments Stereoscan 150 scanning electron microscope, in conjunction with a Link Systems energy dispersive X-ray analyser and a Link Systems 860 Series 2 minicomputer. The characteristic X-rays of light elements, below sodium in the periodic table, cannot penetrate the beryllium window of the analyser. Consequently, elements such as carbon and oxygen cannot be detected by this equipment.

5.13.1 Energy Dispersive X-Ray Micro-Analysis

The interaction of the electron beam with the sample produces X-rays, in addition to the secondary electrons and back-scattered electrons used for imaging. The X-rays consist of a continuous energy spectrum (white radiation), and sharp peaks at certain energies that are characteristic of the elements present in the sample. The Link system identifies and counts these X-rays, and after a suitable period (eg. 100 seconds), will have gathered enough data to produce an analysis of the sample's composition. This analysis will contain some errors due to the interaction of X-rays from different elements, and is therefore semi-quantitative.

An accurate, quantitative analysis depends on the computer being able to make corrections for inter-element effects, such as ionisation and back-scatter (Z), absorbtion (A) and fluorescence (F). This task is accomplished by a software programme, ZAF4, which compares the sample X-ray spectrum with that of a standard of known purity (usually cobalt). The ZAF4 software is designed for the analysis of flat, polished samples, and a later version, ZAF.PB, is designed for the analysis of irregular surfaces, such as fractures and powders.

5.13.2 Oxide Scales

Oxide scale specimens for SEM work were taken from the remaining halves of samples cut up for metallographic examination. These half-cylinders were further cut up to provide a sample of the oxide on the flat top surface, and another from the curved side surface. After ultrasonic cleaning in methylated spirits, these two samples were mounted on a aluminium base with double-sided adhesive tape. Samples of the metal powders were also stuck to aluminium mounts with the double-sided adhesive tape.

The specimen in an electron microscope is 'illuminated' by a beam of electrons, which must be able to flow to earth to prevent it (the specimen) becoming electrically charged. However, iron oxides are only semi-conductors, so it was necessary to give samples a very thin conductive coating of carbon or gold before examining them in the

SEM. Since it was desired to analyse the composition of the oxides, samples were first coated with carbon (which is not detected by the X-ray analyser) in a Nanotech sputter coater. The analyses were initially made with the ZAF.PB software, because of the irregular sample surfaces, but doubts about their accuracy lead to them being repeated semi-quantitatively, without ZAF corrections.

The electrical conduction of the carbon coating was not adequate for high resolution photography of the oxide surfaces. Following composition analysis, samples were gold coated in an Emscope SC500 sputter coater, and then replaced in the SEM for the recording of photo-micrographs.

5.13.3 Porous Sintered Alloy Composition Analysis

Small samples of PM alloys were mounted in electrically conductive Bakelite, and then hand ground and polished to a 6μm diamond abrasive finish. These samples were not impregnated with Araldite, but were heavily smeared in order to seal surface porosity. These samples were then analysed with the SEM, using the ZAF4 software.

Section 6
RESULTS and OBSERVATIONS

6.1 POWDER MIXES

All the alloy additions to base powders appeared (on visual inspection) thoroughly mixed by the method described in Section 5.4.1. There were no signs of particle agglomeration or segregation.

6.2 COMPACTION

6.2.1 TGA (12.7mm Diameter) Compacts

Figure 6.1 shows the mean compressibility curves for the Höganäs powders ASC100.29 and PNC60, which were used as the bases for alloys. Only two PNC60 samples were compacted at each pressure level, so it is not practical to indicate the confidence interval for these results.

PNC60 is a pre-mixed powder based on Höganäs NC100.24, a sponge pure iron powder, made from iron ore. Sponge iron powders tend to have poorer compressiblity than atomised iron powders, because the thermo-chemical production process does not remove the trace impurities that increase hardness.

Distaloy AB (Fe, 1.75Ni, 1.5Cu, 0.50Mo) and Distaloy AE (Fe, 4.00Ni, 1.5Cu, 0.50Mo) are diffusion-alloyed powders, based on ASC100.29. The compressibilities of these two powders and ASC100.29, over the range 150MPa to 550MPa, are virtually identical.

The compressibilities of ASC100.29 and PNC60 were affected only slightly by the small additions of alloy powders. Table 6.1 shows these effects on the relative green densities of compacts produced over the compaction pressure range 150MPa to 550MPa.

The 1wt% Cu, and 1wt% Al additions slightly improved the compressibility of ASC100.29. Both metals are relatively soft, and during compaction, plastic flow into

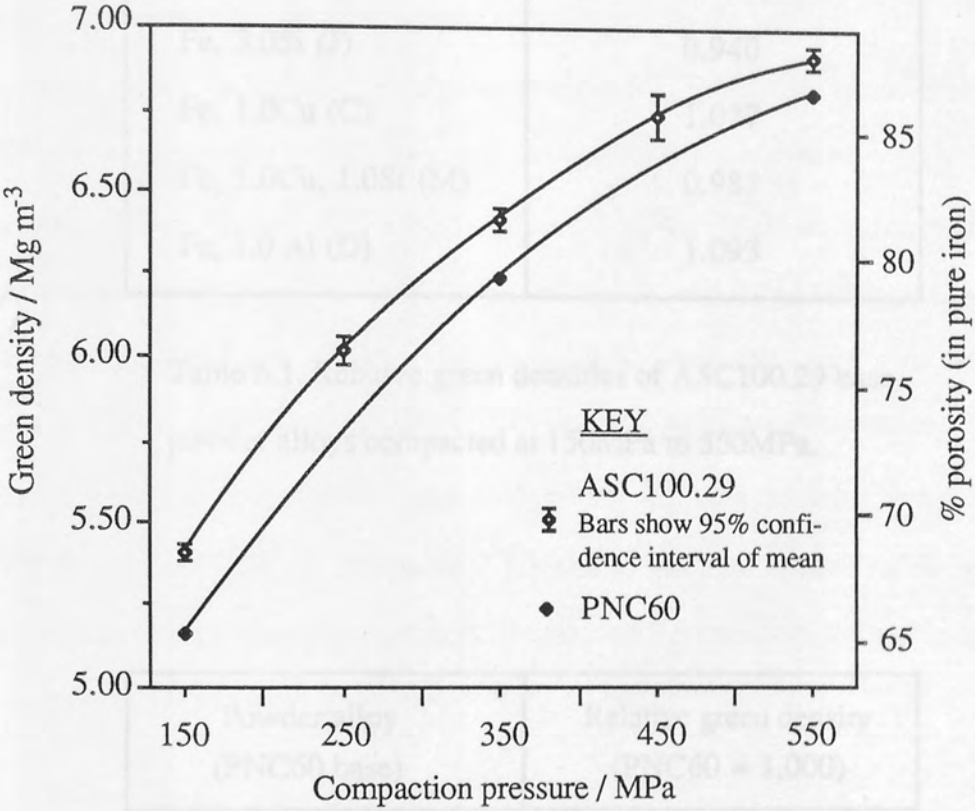

Figure 6.1. Compressibility curves for Höganäs ASC100.29 (pure iron) and PNC60 (Fe, 0.60P) powders. (Data from compaction of cylindrical samples for TGA and TCA tests.)

Powder alloy (ASC100.29 base)	Relative green density (ASC100.29 = 1.000)
Fe, 0.1Si (H)	1.004
Fe, 1.0Si (B)	0.999
Fe, 3.0Si (J)	0.940
Fe, 1.0Cu (C)	1.027
Fe, 1.0Cu, 1.0Si (M)	0.987
Fe, 1.0 Al (D)	1.093

Table 6.1. Relative green densities of ASC100.29 base powder alloys compacted at 150MPa to 550MPa.

Powder alloy (PNC60 base)	Relative green density (PNC60 = 1.000)
Fe, 0.6P, 1.0Si (K)	0.974
Fe, 0.6P, 3.0Si (L)	0.927
Fe, 0.6P, 1.0Cu (N)	0.995
Fe, 0.6P, 1.0Si, 1.0Cu (R)	0.972

Table 6.2. Relative green densities of PNC60 base powder alloys compacted at 150MPa to 550MPa.

the voids between the harder iron particles would occur, reducing the green porosity. This small improvement did not occur with the copper addition to PNC60 (Table 6.2), possibly because the more irregular shape of the sponge NC100.24 base powder reduced the effect of the plastic flow of the added powder.

The Fe, 1.0Al compacts had bright smears on their top surfaces. This was caused by the gravity separation of the iron and aluminium particles during the charging of the die cavity, and appeared to be unavoidable.

The effect of silicon additions on the compressibility of ASC100.29 and PNC60 are probably due to the packing of the small silicon particles in a matrix of relatively large iron particles. The 0.1% and 1.0% silicon additions to ASC100.24 had almost no effect on the compressibility of ASC100.29 (Figure 6.2), so it seems probable that the silicon particles occupied packing positions in the voids between the larger iron particles. However, a 1% Si addition does reduce the compressibility of PNC60 (Figure 6.3), possibly because the voids between the sponge iron particles are more irregular than those found in the ASC100.29 compacts. Additions of 3% silicon significantly reduced the compressibility of both the ASC100.29 and PNC60 powders, probably because larger number of silicon particles were trapped between iron particles.

6.3.2 TMA (7.62mm Diameter) Compacts

Samples for TMA tests were compacted at 362MPa. This pressure was determined by experimentation, to produce the same green density as the larger 12.7mm diameter TGA samples compacted at 350MPa. TMA tests were intended to provide data on the dimensional behaviour of compacts during sintering, rather than their oxidation resistance, so pore structure was not the primary concern.

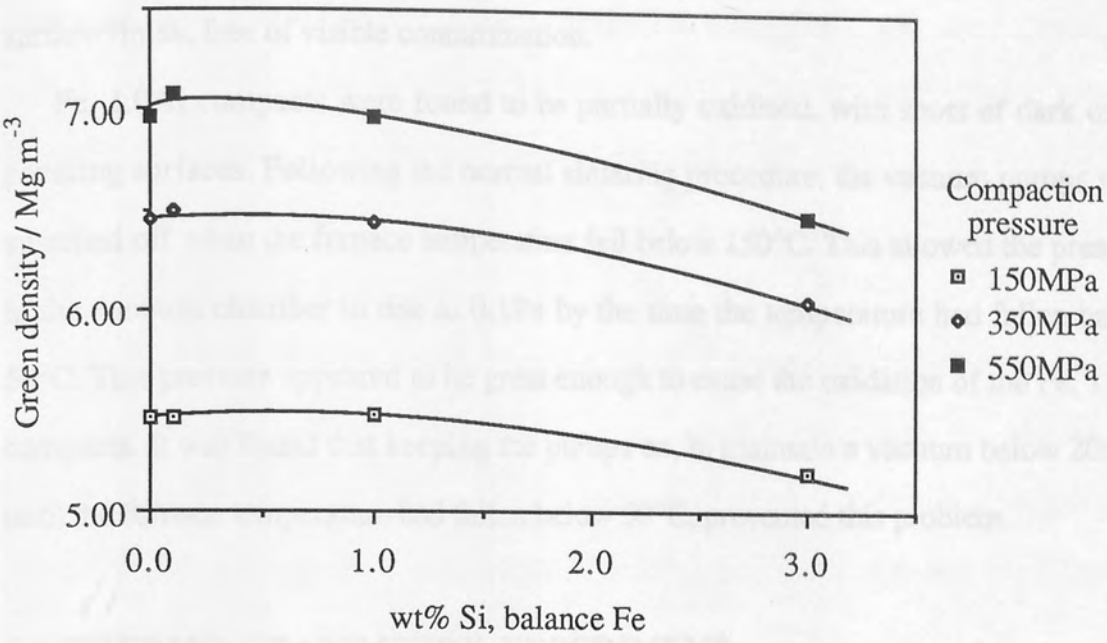

Figure 6.2. Effect of Si additions on the compressibility of pure iron (ASC100.29) powder.

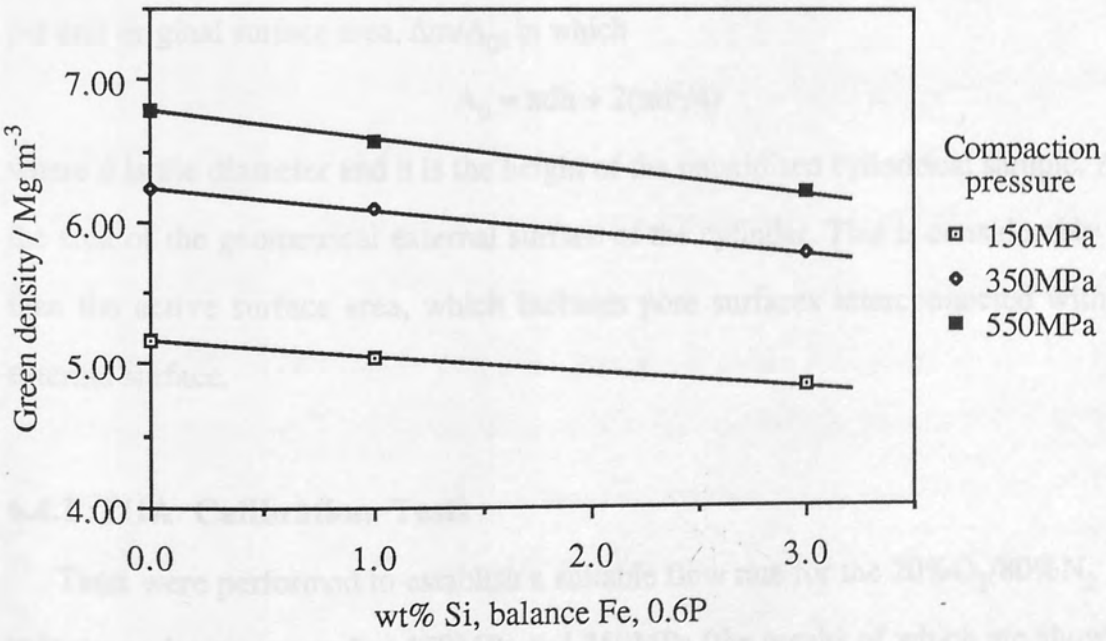

Figure 6.3. Effect of Si additions on the compressibility of Fe, 0.6P (PNC60) powder.

6.3 SINTERING

Generally, all compacts removed from the vacuum sintering furnace had a bright surface finish, free of visible contamination.

Fe, 1.0Al compacts were found to be partially oxidised, with spots of dark oxide covering surfaces. Following the normal sintering procedure, the vacuum pumps were switched off when the furnace temperature fell below 150°C. This allowed the pressure in the vacuum chamber to rise to 0.1Pa by the time the temperature had fallen below 50°C. This pressure appeared to be great enough to cause the oxidation of the Fe, 1.0Al compacts. It was found that keeping the pumps on, to maintain a vacuum below 20mPa until the furnace temperature had fallen below 50°C, prevented this problem.

6.4 THERMO-GRAVIMETRY EXPERIMENT

The oxidation curves obtained from TGA tests are reproduced in Appendix A. The periodic arrests of the Thermobalance provided convenient points for taking data from TGA chart records. These data, in the form of sample weight increase, were entered into spreadsheet software on a micro-computer, and then processed to yield weight gain per unit original surface area, $\Delta m/A_0$, in which

$$A_0 = \pi dh + 2(\pi d^2/4)$$

where d is the diameter and h is the height of the unoxidised cylindrical sample. A_0 is the area of the geometrical external surface of the cylinder. This is considerably less than the active surface area, which includes pore surfaces interconnected with the external surface.

6.4.1 TGA Calibration Tests

Tests were performed to establish a suitable flow rate for the $20\%O_2/80\%N_2$ gas, using samples compacted at 150MPa and 350MPa (the results of which are shown in Figures A.1 and A.2, Appendix A). With no gas flow, samples were oxidised in laboratory air, which was drawn in through the sample support rod aperture at the

bottom of the furnace. Increasing the gas flow rate steadily reduced the oxidation rate, with a significant reduction occurring at $150 \times 10^{-6} m^3 min^{-1}$. At $400 \times 10^{-6} m^3 min^{-1}$ and above the gas current began to disturb the balance, causing apparent oscillations in sample mass. A flow rate of $200 \times 10^{-6} m^3 min^{-1}$ was selected as a compromise between excluding the laboratory atmosphere from experiments, and disturbing the balance.

6.4.2 Oxidation of Pure Iron

The mass gain of pure iron after oxidation for 24 hours, as a function of porosity and temperature, is shown in Figure 6.4. For a given temperature, the weight gain during oxidation increases with increasing porosity. However, for a given porosity, the weight gain increases to a maximum at around 500°C, within the experimental temperature range.

Figure 6.5 shows the mass gain as a function of time, for the oxidation of cylinders compacted at 350MPa. The same general form was shown by cylinders compacted at other pressures, and are reproduced in Appendix A. Individual results, which take the form of continuous curves, are identified by symbols, placed every five hours along each curve.

Figure 6.6 shows the rate of oxidation, as a function of time (ie. $d(\Delta m/A_0)/dt$), for the results shown in Figure 6.5. In order to smooth the data used in Figure 6.6, gradients were determined as the slope of a straight line between points 1.5 hours before and after the datum. Thus the gradients for the first and last 1.5 hours of the test period could not be calculated.

Oxidation at 300°C (Fig. A.3, Appendix A) resulted in weight gains of about $30 gm^{-2}$ or less over 24 hours. The rate of oxidation (Fig. 6.6) is relatively low throughout the 24 hour test period, and decreases very little. The oxide films were thin enough to produce a range of refraction colours, mostly yellows, greens and blues. Most samples showed two or more colours, and there was no apparent pattern to their distribution, indicating uneven film growth. The weight gain of the Armco sample

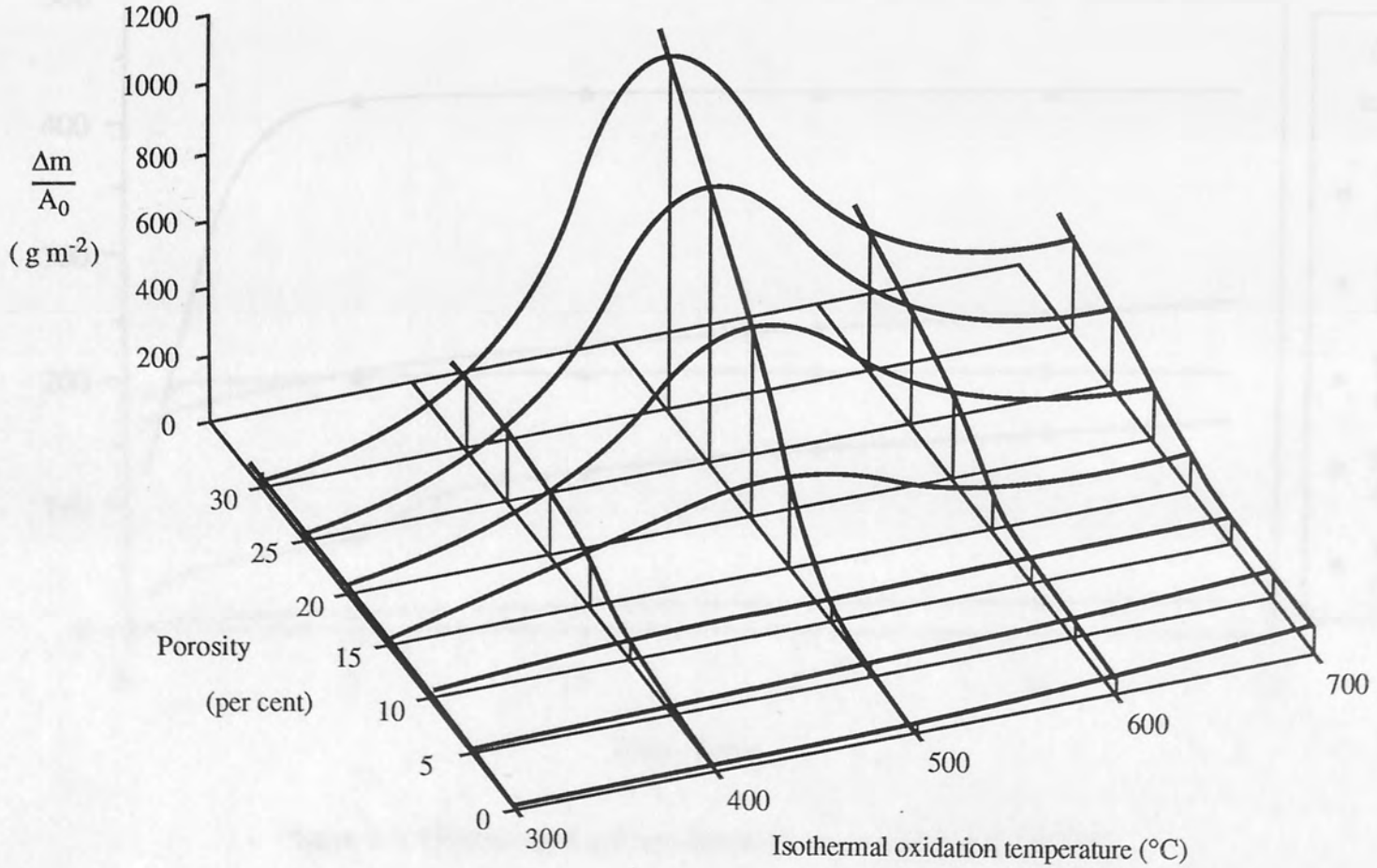

Figure 6.4. Mass gain due to isothermal oxidation of PM pure iron (ASC100.29), in 20%O_2 /80%N_2 , for 24 hours.

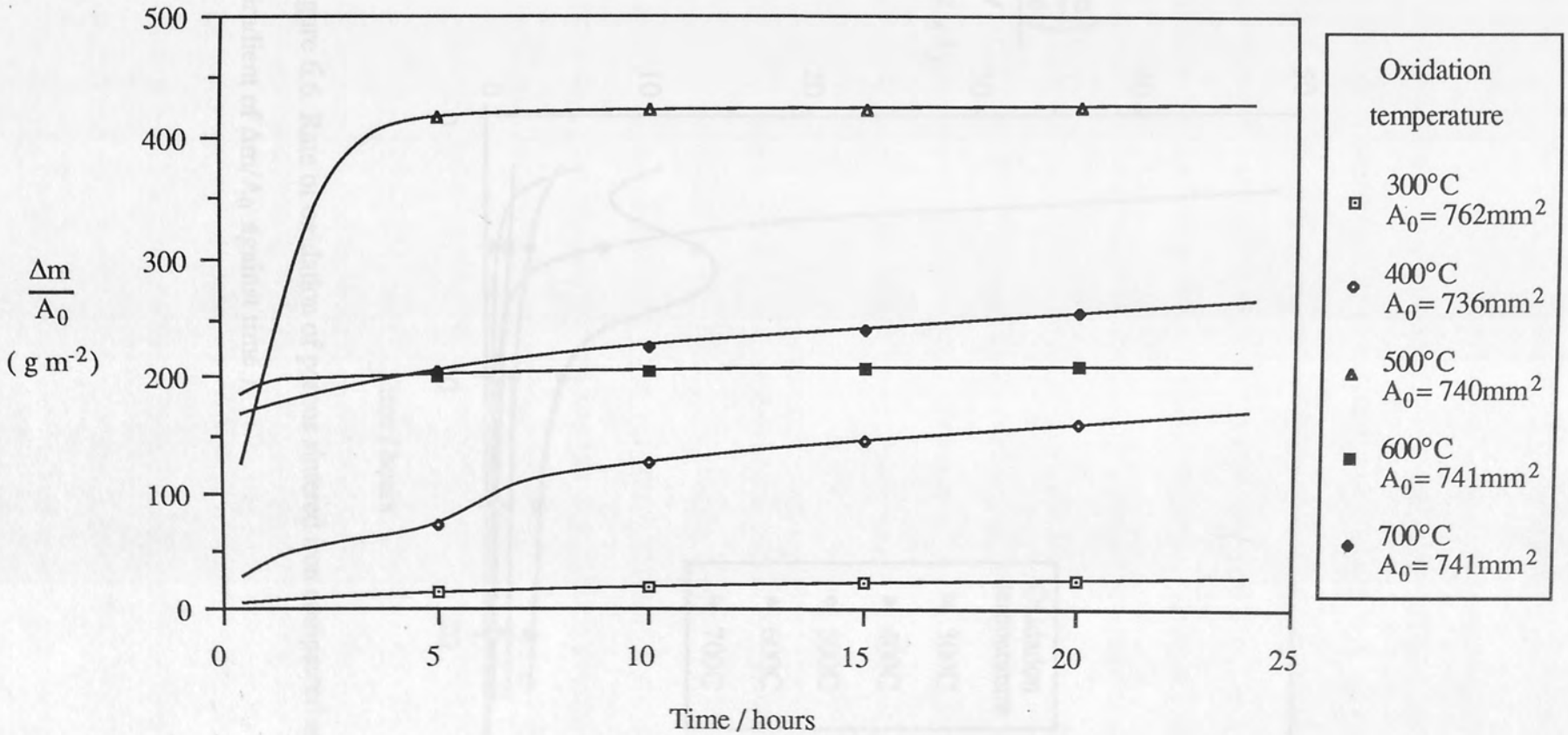

Figure 6.5. Oxidation of porous sintered iron compacted at 350MPa.

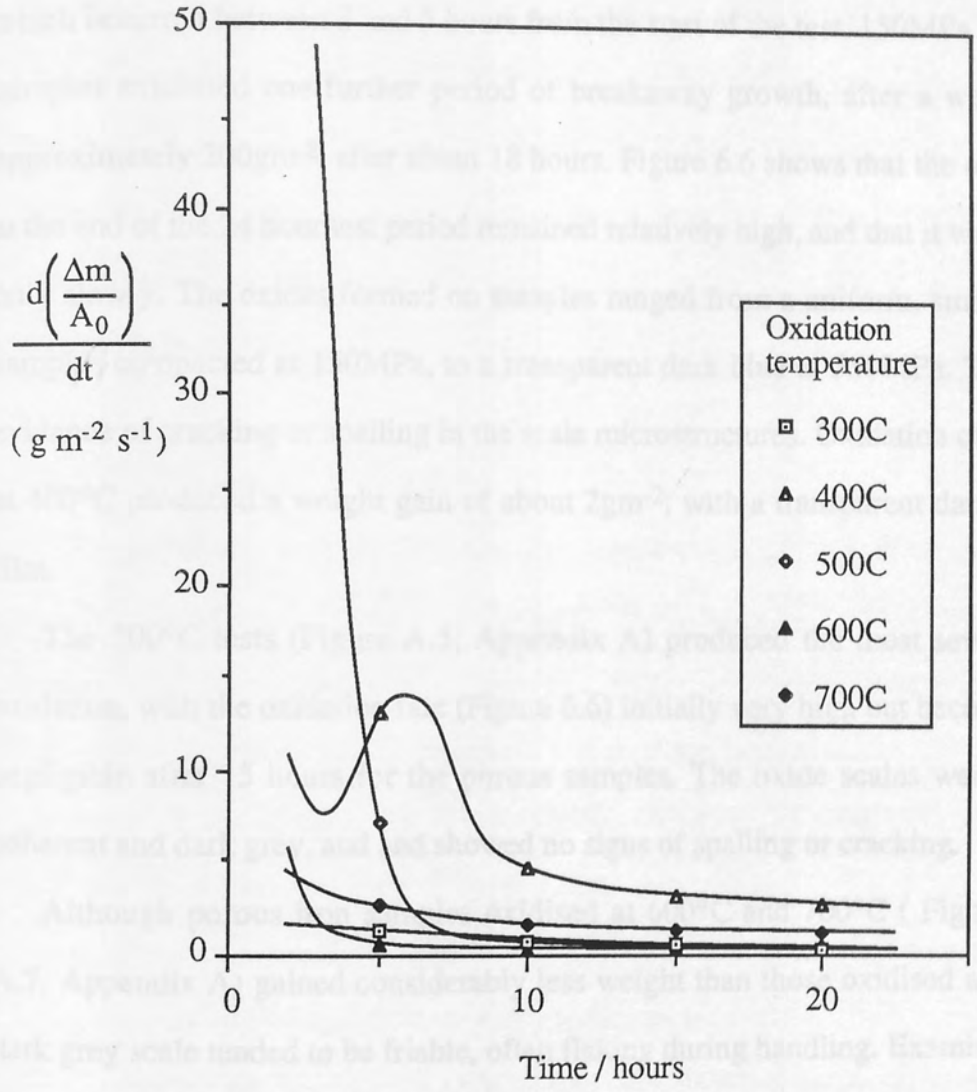

Figure 6.6. Rate of oxidation of porous sintered iron compacted at 350MPa. (Gradient of $\Delta m/A_0$ against time.)

oxidised at 300°C was less than 0.1mg (or less than 1.3g m^{-2}), and could not be measured by either the TGA balance or the analytical balance.

All porous iron samples oxidised at 400°C (Fig. A.4, Appendix A) exhibited an oxidation mechanism somewhat similar to classical parabolic breakaway oxidation. In all cases there was an increase in the oxidation rate after a weight gain of about $70gm^{-2}$, which occurred between 3 and 5 hours from the start of the test. 150MPa and 250MPa samples exhibited one further period of breakaway growth, after a weight gain of approximately $200gm^{-2}$, after about 18 hours. Figure 6.6 shows that the oxidation rate at the end of the 24 hour test period remained relatively high, and that it was decreasing only slowly. The oxides formed on samples ranged from a uniform, smooth grey for samples compacted at 150MPa, to a transparent dark blue at 550MPa. There was no evidence of cracking or spalling in the scale microstructures. Oxidation of Armco iron at 400°C produced a weight gain of about $2gm^{-2}$, with a transparent dark blue oxide film.

The 500°C tests (Figure A.5, Appendix A) produced the most severe cases of oxidation, with the oxidation rate (Figure 6.6) initially very high but becoming almost negligible after 15 hours for the porous samples. The oxide scales were all tightly adherent and dark grey, and and showed no signs of spalling or cracking.

Although porous iron samples oxidised at 600°C and 700°C (Figures A.6 and A.7, Appendix A) gained considerably less weight than those oxidised at 500°C, the dark grey scale tended to be friable, often flaking during handling. Examination of the TGA chart records showed there were no occurrences of spalling during the tests. The friability of scales increased with density, and was most pronounced on the curved surfaces of the cylinders. The 150MPa samples had adherent scales at both 600°C and 700°C, whilst the 550MPa and Armco samples lost large portions of their oxide scales as they were removed from the TGA. Samples compacted at 350MPa exhibited an intermediate state of friability, with adherent scales on their end faces, but very loose scale on their curved sides. The adherent scales could not be chipped away with a metal

scribe, indicating that they were strongly bonded to the metal. Samples oxidised at 700°C, and some samples oxidised at 600°C, were bonded to the TGA sample platform by the growth of the oxide scale.

Armco Iron (with 0% porosity) was generally the least oxidised at all temperatures, and showed a continuous increase in weight gain with oxidation temperature, without the peak at around 500°C exhibited by the porous samples. At 600°C and 700°C, Armco iron samples gained more weight over 24 hours than the corresponding 550MPa ASC100.29 samples. This may be due to the different compositions and levels of impurities in the wrought and powdered irons. Samples oxidised at 500°C and below had adherent, dark grey scales. Samples oxidised at 600°C or 700°C had non-adherent, dark grey scales.

6.4.3 Oxidation of PM Alloys

Following the tests on the pure iron powder, ASC100.29, three other Höganäs powders were tested (Figure 6.7). Distaloy AB, Distaloy AE and PNC60 all exhibited greater resistance to oxidation than the ASC100.29. The increased Ni content in Distaloy AE (4.00wt% Ni) produces a significant improvement on the oxidation resistance of the Distaloy AB (1.75wt% Ni). However, PNC60, made by admixing 0.6P (as Fe_3P powder) with a sponge pure iron powder (NC100.24) had the best oxidation resistance of the powders tested, and so was chosen as a suitable base powder for extending the alloy range for oxidation tests.

Simple binary alloys of Fe-Cu, Fe-Al and Fe-Si were tested at 500°C, using 1.0wt% additions of the elemental powders to ASC100.29. The oxidation curves of samples compacted at 350MPa are shown in Figure 6.8.

Oxidation of Fe, 1.0Al at 500°C produced a dark grey adherent oxide scale, covered by dispersed light grey 'pimples', about 0.5mm in diameter, and standing a little proud of the surrounding scale. The presence of this particulate phase indicated that the sintered alloy had retained some of the inhomogeneity of the green compact.

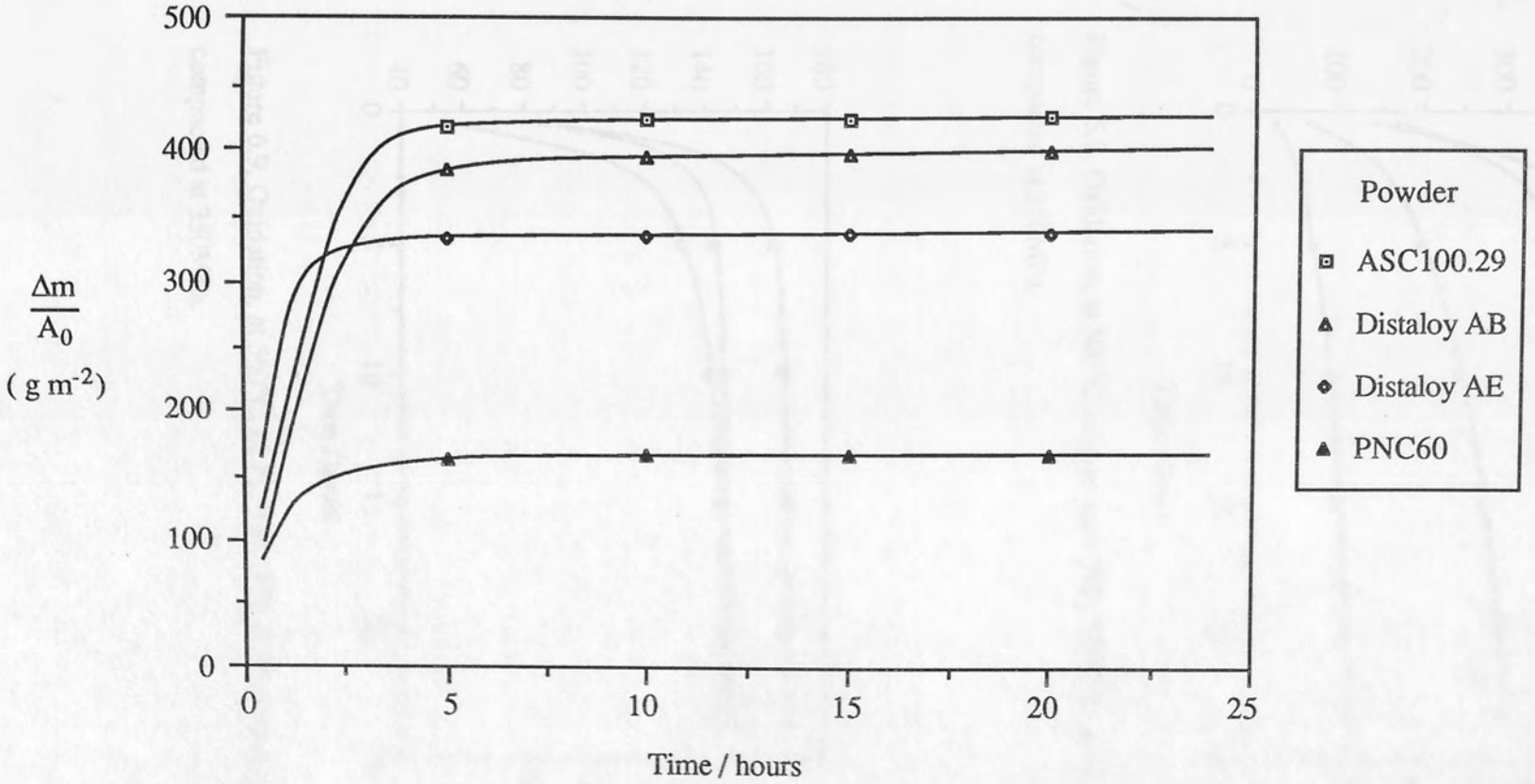

Figure 6.7. Oxidation, at 500°C, of partially pre-alloyed powders compacted at 350MPa.

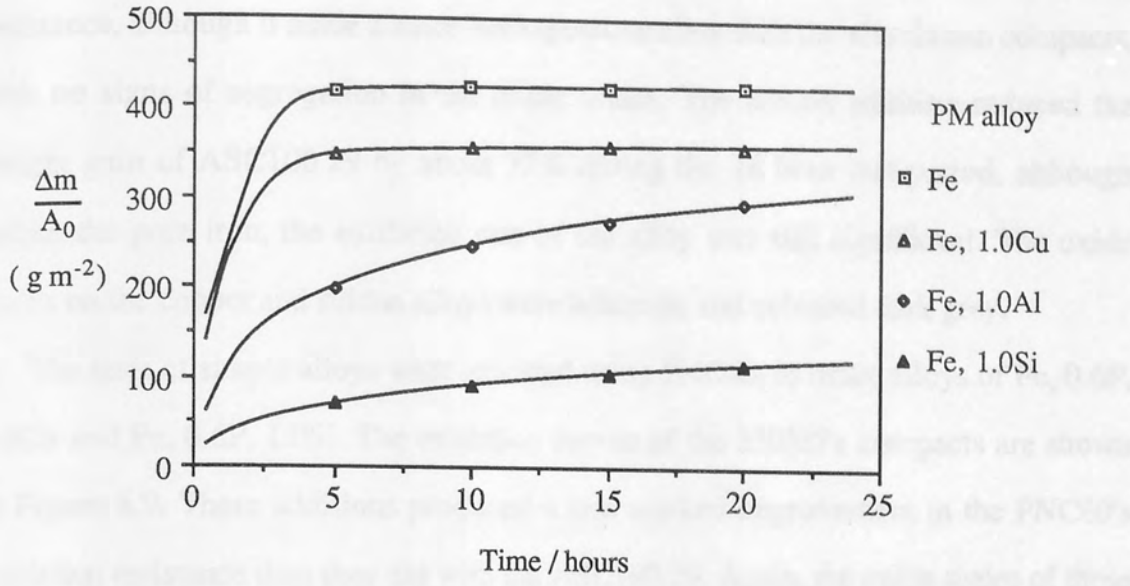

Figure 6.8. Oxidation, at 500°C, of pure iron (ASC100.29) based alloys, compacted at 350MPa.

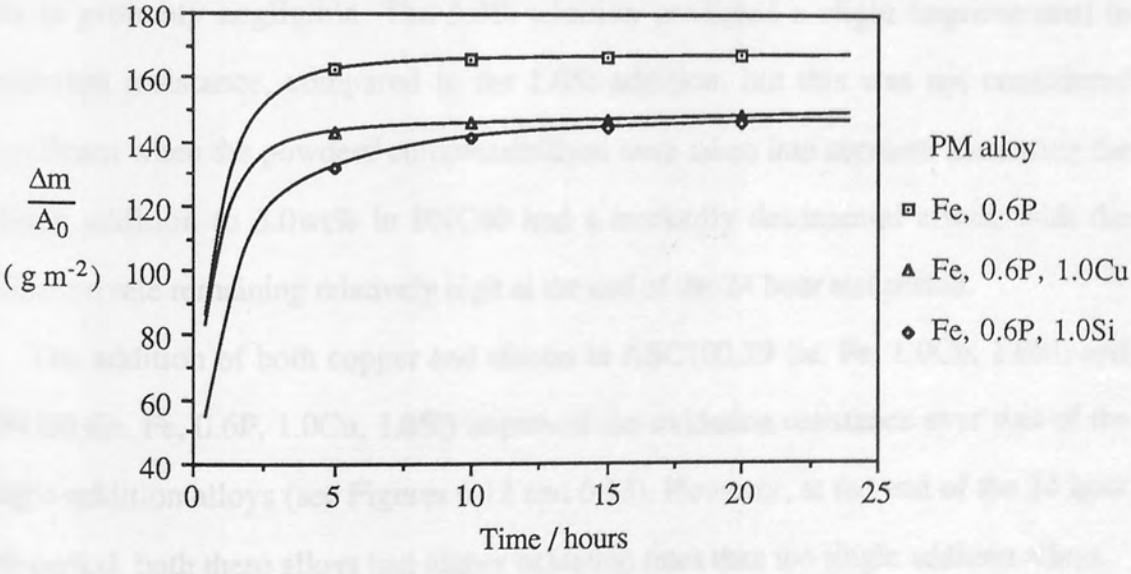

Figure 6.9. Oxidation, at 500°C, of Fe, 0.6P (PNC60) based alloys, compacted at 350MPa.

The use of aluminium as an alloying addition was not taken further.

Copper had the least effect of the three alloy additions on improving oxidation resistance, although it made a more homogeneous alloy than the aluminium compacts, with no signs of segregation in the oxide scales. The silicon addition reduced the weight gain of ASC100.29 by about 75% during the 24 hour test period, although unlike the pure iron, the oxidation rate of the alloy was still significant. The oxide scales on the copper and silicon alloys were adherent, and coloured dark grey.

The tests of simple alloys were repeated using PNC60, to make alloys of Fe, 0.6P, 1.0Cu and Fe, 0.6P, 1.0Si. The oxidation curves of the 350MPa compacts are shown in Figure 6.9. These additions produced a less marked improvement in the PNC60's oxidation resistance than they did with the ASC100.29. Again, the oxide scales of these alloys were adherent, and coloured dark grey.

The effects of varying the silicon addition to ASC100.29 and PNC60 are shown in Figures 6.10 and 6.11 respectively. For the ASC100.29, an addition of 0.1Si had a slightly detrimental effect, although allowing for some natural variation between tests, this is probably negligible. The 3.0Si addition produced a slight improvement in oxidation resistance, compared to the 1.0Si addition, but this was not considered significant when the powders' compressibilities were taken into account. Increasing the silicon addition to 3.0wt% in PNC60 had a markedly detrimental effect, with the oxidation rate remaining relatively high at the end of the 24 hour test period.

The addition of both copper and silicon to ASC100.29 (ie. Fe, 1.0Cu, 1.0Si) and PNC60 (ie. Fe, 0.6P, 1.0Cu, 1.0Si) improved the oxidation resistance over that of the single-addition alloys (see Figures 6.12 and 6.13). However, at the end of the 24 hour test period, both these alloys had higher oxidation rates than the single addition alloys.

All the samples oxidised at 500°C, except for the Fe, 1.0Al mentioned earlier, had adherent, dark grey oxide scales. Samples of PNC60 (Fe, 0.6P) and Fe, 1.0Si (ASC100.29 base) were also oxidised at 400°C and 600°C (Figures A.11 and A.14, Appendix A, respectively). At 400°C they had adherent, dark grey oxide scales, similar

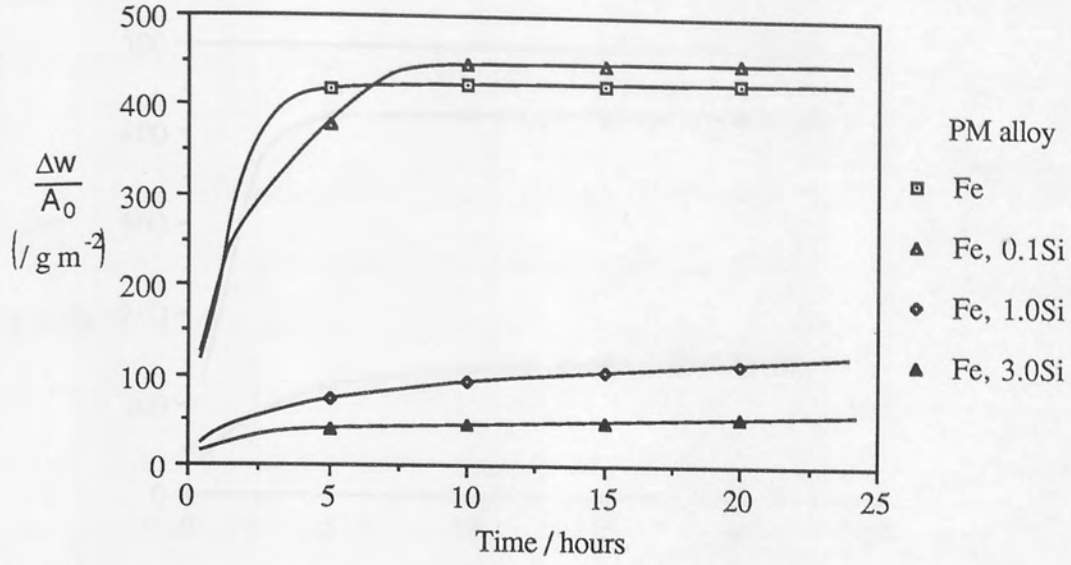

Figure 6.10. Effect of Si on the oxidation, at 500°C, of pure iron (ASC100.29), compacted at 350MPa.

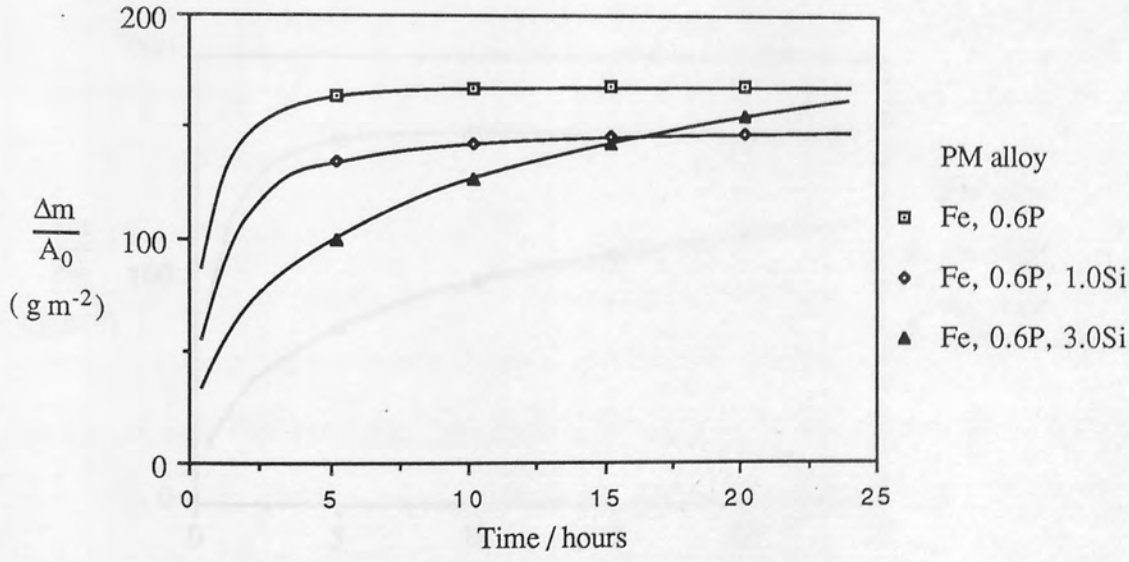

Figure 6.11. Effect of Si additions on the oxidation, at 500°C, of Fe, 0.6P (PNC60), compacted at 350MPa.

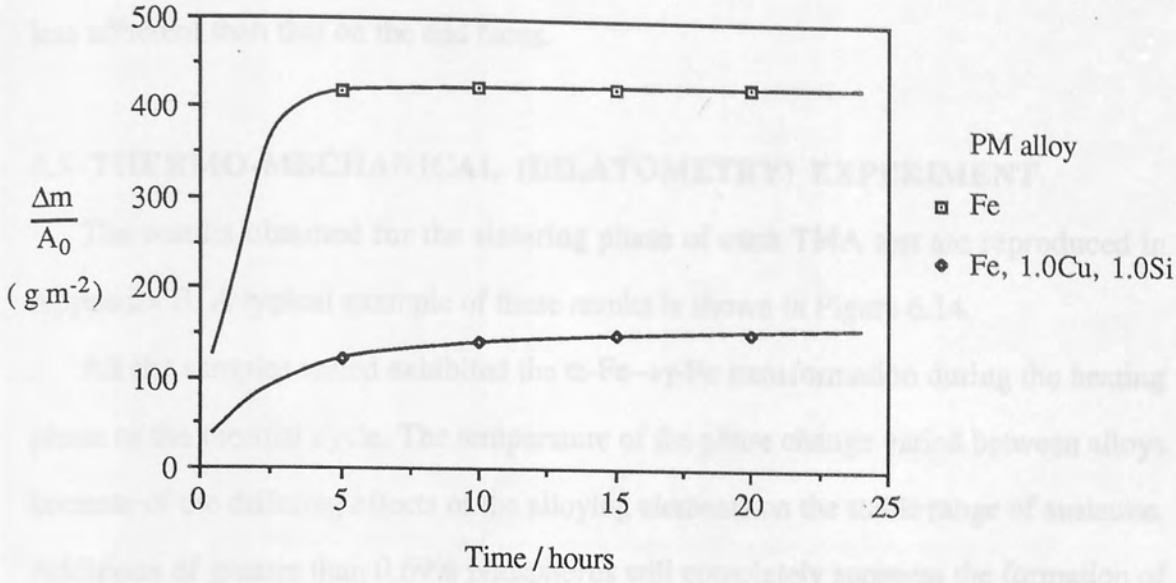

Figure 6.12.Effect of 1.0Cu, 1.0Si addition on the oxidation, at 500°C, of pure iron (ASC100.29), compacted at 350MPa.

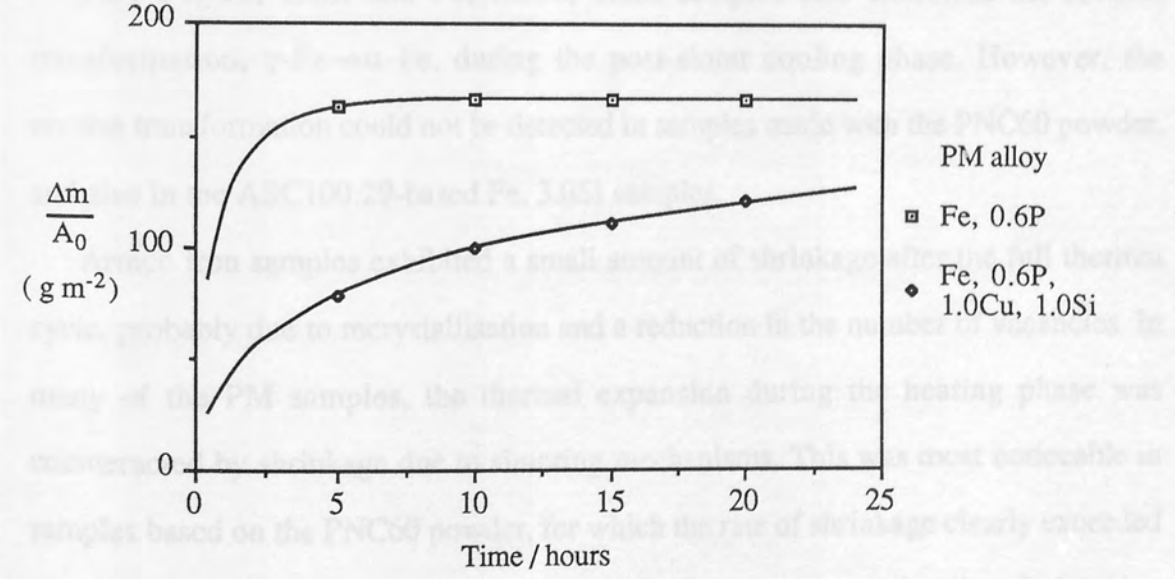

Figure 6.12.Effect of 1.0Cu, 1.0Si addition on the oxidation, at 500°C, of Fe, 0.6P (PNC60), compacted at 350MPa.

to those observed on the samples oxidised at 500°C. The samples oxidised at 600°C also had dark grey scales, but they were slightly friable, the side surface oxide being less adherent than that on the end faces.

6.5 THERMO-MECHANICAL (DILATOMETRY) EXPERIMENT

The results obtained for the sintering phase of each TMA test are reproduced in Appendix B. A typical example of these results is shown in Figure 6.14.

All the samples tested exhibited the α-Fe→γ-Fe transformation during the heating phase of the thermal cycle. The temperature of the phase change varied between alloys because of the differing effects of the alloying elements on the stable range of austenite. Additions of greater than 0.69% phosphorus will completely suppress the formation of γ-Fe under equilibrium conditions (see phase diagram, Fig. 3.14). The PNC60-based compacts exhibited only a very small change in height during the α-Fe→γ-Fe transformation, which occurred at around 1000°C; the extent of the dimensional change due to the transformation is difficult to separate from the shrinkage due to sintering.

Pure Fe, Fe, 1.0Si and Fe, 1.0Cu, 1.0Si samples also exhibited the reverse transformation, γ-Fe→α-Fe, during the post-sinter cooling phase. However, the reverse transformation could not be detected in samples made with the PNC60 powder, and also in the ASC100.29-based Fe, 3.0Si samples.

Armco iron samples exhibited a small amount of shrinkage after the full thermal cycle, probably due to recrystallisation and a reduction in the number of vacancies. In many of the PM samples, the thermal expansion during the heating phase was counteracted by shrinkage due to sintering mechanisms. This was most noticeable in samples based on the PNC60 powder, for which the rate of shrinkage clearly exceeded thermal expansion above 800°C. Table 6.3 gives summary details of sintering shrinkage of samples. Note that in many cases the rate of shrinkage was still high at the end of the sintering period, and presumably shrinkage continued as samples cooled. However, it is difficult to separate thermal contraction and sintering-mechanism

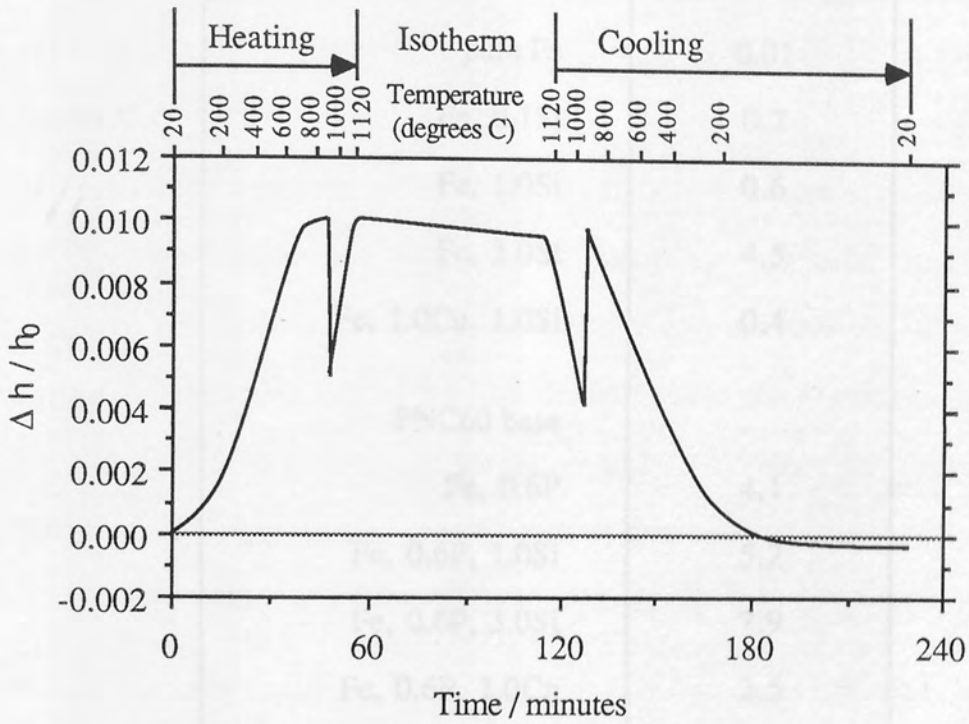

Figure 6.14. Dimensional changes in pure iron (ASC100.29) compact during sintering thermal cycle.

Alloy	Shrinkage %
Armco Iron	0.1
ASC100.29 base	
pure Fe	0.01
Fe, 0.1Si	0.2
Fe, 1.0Si	0.6
Fe, 3.0Si	4.5
Fe, 1.0Cu, 1.0Si	0.4
PNC60 base	
Fe, 0.6P	4.1
Fe, 0.6P, 1.0Si	5.2
Fe, 0.6P, 3.0Si	7.9
Fe, 0.6P, 1.0Cu	2.5
Fe, 0.6P, 1.0Cu, 1.0Si	4.7

Table 6.3. Sintering shrinkage of TMA samples.

induced shrinkage at this stage.

The second heating phase, to 500°C, did not induce any detectable shrinkage in any of the samples. Presumably the sintering mechanisms that cause shrinkage did not operate at this temperature.

6.6 THERMO-CALORIMETRY EXPERIMENT

The Thermobalance was modified, as described in Section 5.9, so that the sample core temperatures could be measured during oxidation. Some examples of the test records are shown in Figure 6.15, whilst the bulk of the results are reproduced in Appendix C.

All the samples were introduced into the preheated furnace at room temperature. The times taken for the core temperature of pure iron samples to reach the furnace temperature are shown in Tables 6.4 to 6.6. The core temperature of most samples continued to rise above that of the furnace, because of the exothermic effect of the oxidation reaction. As the reaction proceeded, and the oxidation rate subsided from its initially high value, sample core temperatures gradually equalised with the furnace temperature. In most cases, this temperature equalisation took less than 60 minutes.

6.6.1 Oxidation of Pure Iron

Samples compacted at 150MPa, and oxidised at 500°C to 550°C exhibited the double-peak in core temperature (Table 6.4), first observed by Fedorchenko *et al* [158]. The apparent trend of these results (Fig. C.1, Appendix C) is for the second peak to grow in magnitude, and occur closer to the first, with increasing temperature. Thus at 450°C the absence of a second peak may be explained by its being too small to be detected, whilst at 600°C the two peaks are presumably too close together to be separated.

Samples compacted at 350MPa show only one, small peak (Table 6.5), whilst for those compacted at 550MPa the presence of a peak is barely discernible (Table 6.6).

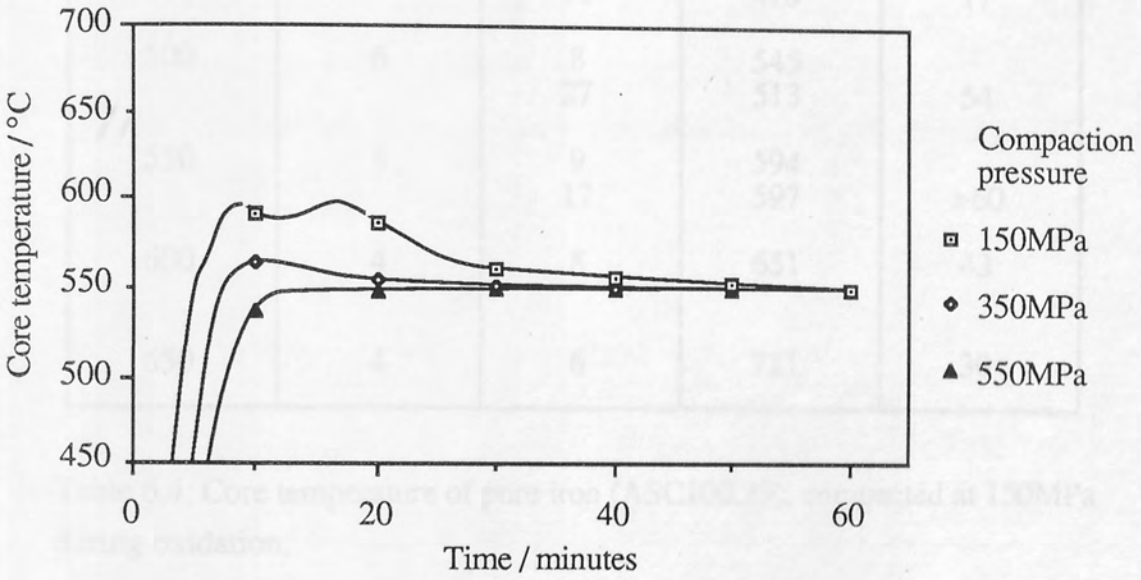

Figure 6.15. Core temperatures of pure iron (ASC100.29) compacts during oxidation at 500°C

Furnace temperature (°C)	Time to temperature (minutes)	Peak		Time to stabilise (minutes)
		Time (minutes)	Temperature (°C)	
450	7	11	475	17
500	6	8	545	
		27	513	54
550	5	9	594	
		17	597	>60
600	4	8	651	43
650	4	6	711	30

Table 6.4. Core temperature of pure iron (ASC100.29), compacted at 150MPa during oxidation.

Furnace temperature (°C)	Time to temperature (minutes)	Peak		Time to stabilise (minutes)
		Time (minutes)	Temperature (°C)	
450	11	14	468	31
500	10	13	516	37
550	8	11	565	59
600	6	9	621	38
650	7	9	665	22

Table 6.5. Core temperature of pure iron (ASC100.29), compacted at 350MPa, during oxidation.

Furnace temperature (°C)	Time to temperature (minutes)	Peak		Time to stabilise (minutes)
		Time (minutes)	Temperature (°C)	
450	13	18	456	35
500	12	17	502	36
550	13	†	†	13
600	14	16	604	>60
650	17	†	†	17

Table 6.6. Core temperature of pure iron (ASC100.29), compacted at 550MPa, during oxidation.

† No peak was detected in these tests.

The exothermic effect increases the heating rate of samples, when they are introduced into the furnace. Samples compacted at 150MPa were heated to the furnace temperature in 4 to 7 minutes, whilst those compacted at 550MPa took 12 to 17 minutes.

6.6.2 Oxidation of PM Alloys

TCA tests on pure iron showed that the 'double-peak' effect was greatest for samples compacted at 150MPa, and oxidised at 550°C, and therefore these conditions were chosen for experiments with alloys.

All of the alloys exhibited a single peak in core temperature, though they were of differing magnitudes, as shown in Table 6.7.

6.7 HARDNESS TESTS

Reported hardness values, in Table 6.8, are the means of at least ten Rockwell hardness tests. The tolerances on these values represent the 95% confidence interval for the means. Hardness tests were done on one end face of each oxidised TGA sample, taking care that individual ball indentations were well separated. The distribution of hardness values for each sample generally had a standard error of less than one, so that the 95% confidence interval for the means is better than ±2.3.

The hardnesses of oxidised surfaces of pure iron (ASC100.29) are compared in Figures 6.16 and 6.17. In the compaction range 150MPa to 550MPa, oxidation at 500°C produces the hardest surfaces, although the hardness decreases with decreasing porosity. This trend continues in samples oxidised at 600°C, although it is not so pronounced, and is the opposite to that observed in samples oxidised at 300°C, 400°C and 700°C.

The effects of silicon additions to ASC100.29 and PNC60, oxidised at 500°C, are shown in Figures 6.18 and 6.19. For low density compacts, small alloy additions of silicon to ASC100.29 results in a considerable softening of the oxidised surfaces. The addition of 3.0Si has the opposite effect, with the oxidised alloy almost as hard as the

Alloy	Time to temperature (minutes)	Peak		Time to stabilise (minutes)
		Time (minutes)	Temperature (°C)	
ASC100.29 base				
Fe, 1.0Si	10	16	555	33
Fe, 3.0Si	11	17	554	35
Fe, 1.0Cu	5	8	588	33
Fe, 1.0Al	6	13	594	>60
Fe, 1.0Cu, 1.0Si	10	15	552	23
PNC60 base				
Fe, 0.6P	4	6	593	28
Fe, 0.6P, 1.0Si	6	9	576	40
Fe, 0.6P, 3.0Si	9	12	560	41
Fe, 0.6P, 1.0Cu	5	7	597	29
Fe, 0.6P, 1.0Cu, 1.0Si	7	10	574	36

Table 6.7. Core temperature of alloy powder compacts, compacted at 150MPa, during oxidation at 550°C.

Alloy powder	Unoxidised Compacted at 350MPa	Oxidised at 500°C for 24 hours Compaction pressure		
		150MPa	350MPa	550MPa
ASC100.29 base				
pure Fe (ASC100.29)	51.9 ± 1.8	97.2 ± 2.1	78.6 ± 1.6	60.4 ± 1.8
Fe, 1.75 Ni, 1.50Cu, 0.50Mo (Distaloy AB)	-	†102.9 ± 1.7	97.5 ± 0.4	†96.8 ± 0.7
Fe, 4.00Ni, 1.50Cu, 0.50Mo (Distaloy AE)	-	†104.7 ± 1.1	100.4 ± 1.8	97.7 ± 1.9
Fe, 0.1Si	22.2 ± 1.5	90.8 ± 0.9	70.1 ± 1.6	59.6 ± 2.1
Fe, 1.0Si	47.1 ± 1.4	39.7 ± 2.3	59.1 ± 1.8	67.2 ± 2.1
Fe, 3.0Si	88.5 ± 1.1	61.9 ± 1.8	86.1 ± 0.5	94.4 ± 0.9
Fe, 1.0Cu	54.4 ± 3.6	†99.5 ± 0.4	76.8 ± 0.6	84.5 ± 1.7
Fe, 1.0Si, 1.0Cu	61.5 ± 1.5	†31.7 ± 1.2	73.8 ± 1.4	82.1 ± 1.4
Fe, 1.0 Al	46.8 ± 1.7	33.5 ± 4.4	66.3 ± 2.0	71.3 ± 2.5
PNC60 base				
Fe, 0.P (PNC60)	89.4 ± 1.7	90.3 ± 0.9	94.8 ± 0.9	94.4 ± 0.0.7
Fe, 0.6P, 1.0Si	95.3 ± 0.8	88.3 ± 0.9	98.0 ± 0.5	97.9 ± 0.9
Fe, 0.6P, 3.0Si	†104.7 ± 1.4	88.1 ± 1.4	101.9 ± 0.9	†102.6 ± 1.6
Fe, 0.6P, 1.0Cu	93.3 ± 0.9	90.3 ± 1.8	99.9 ± 0.5	99.4 ± 1.8
Fe, 0.6P, 1.0Si, 1.0Cu	95.0 ± 1.5	82.9 ± 0.9	99.9 ± 1.2	100.4 ± 1.5

Table 6.8. Surface hardnesses of TGA samples.
(Entries marked † are estimated from data obtained on the Rockwell B scale or 45T superficial hardness scale.)

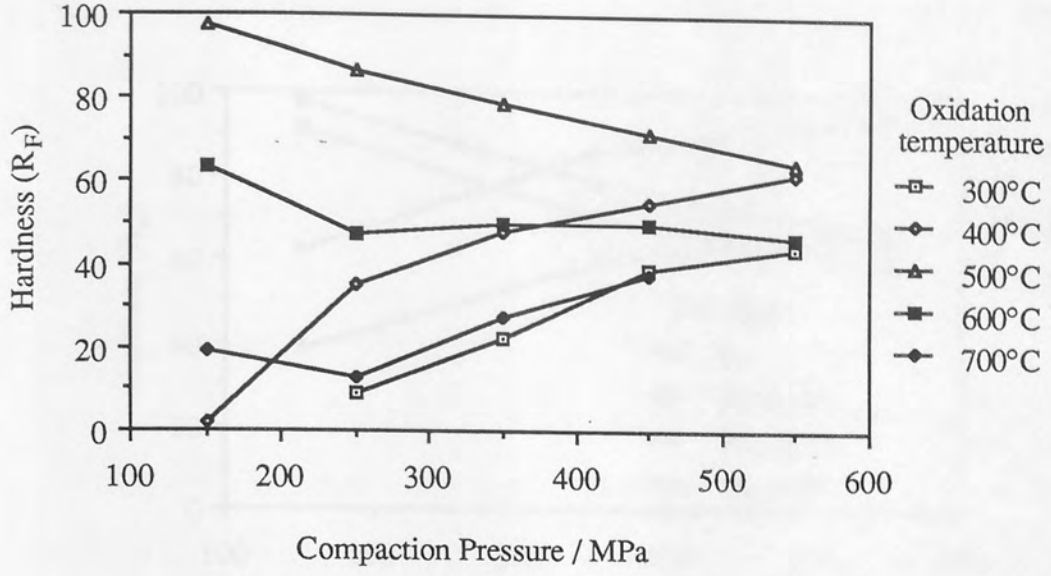

Figure 6.16. Oxidised surface hardness of pure iron (ASC100.29), as a function of compaction pressure.

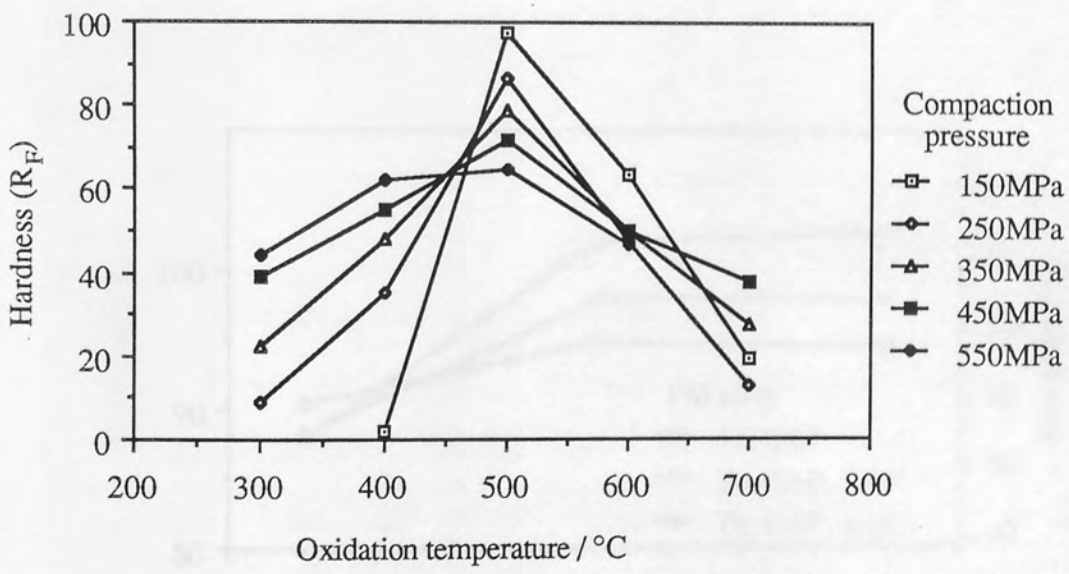

Figure 6.17. Oxidised surface hardness of pure iron (ASC100.29), as a function of oxidation temperature.

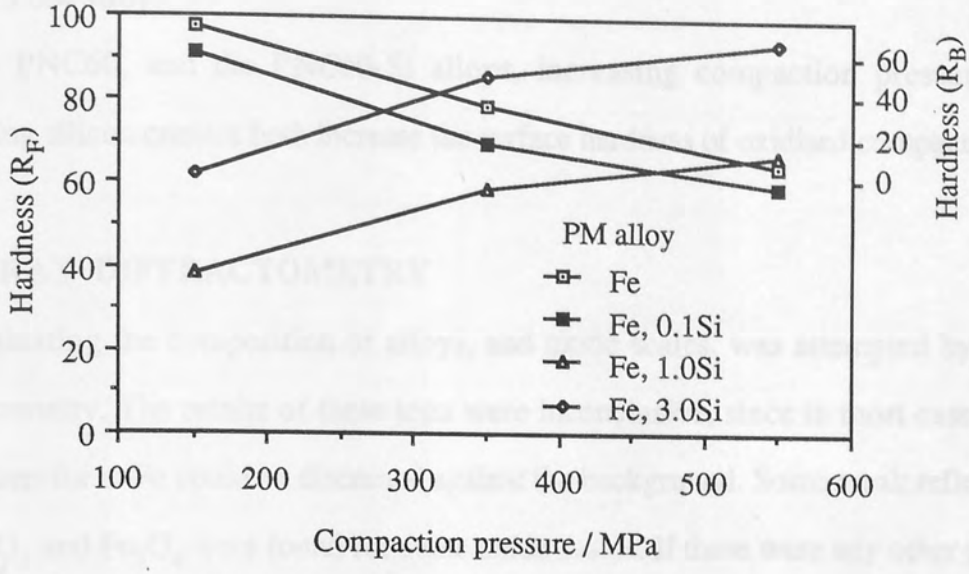

Figure 6.18. Effect of Si on the oxidised surface hardness of pure iron (ASC100.29), compacted at 350MPa, and oxidised at 500°C.

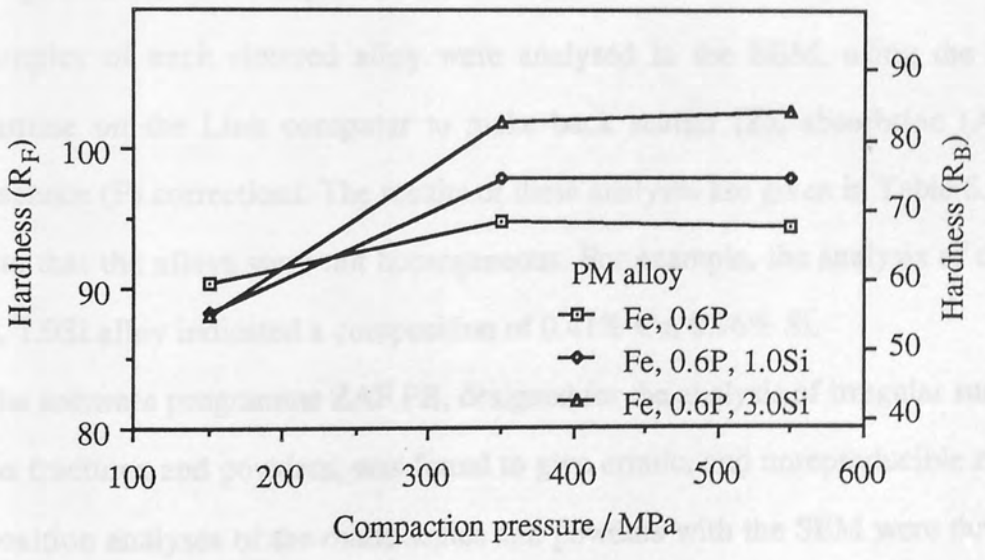

Figure 6.19. Effect of Si additions on the oxidised surface hardness of Fe, 0.6P (PNC60), compacted at 350MPa, and oxidised at 500°C.

oxidised pure iron. Increasing the compaction pressure for the low silicon alloys increases their oxidised surface hardness, whilst it causes softening in the pure iron and the Fe, 3.0Si alloy.

For PNC60, and the PNC60-Si alloys, increasing compaction pressure and increasing silicon content both increase the surface hardness of oxidised compacts.

6.7 X-RAY DIFFRACTOMETRY

Evaluating the composition of alloys, and oxide scales, was attempted by x-ray diffractometry. The results of these tests were inconclusive, since in most cases only reflections for α-Fe could be discerned against the background. Some weak reflections for Fe_2O_3 and Fe_3O_4 were found for some oxide scales. If there were any other phases present, the intensity peaks for their characteristic x-ray reflections could not be reliably separated from the background noise on the chart records.

6.8 ELECTRON MICROSCOPY

6.8.1 Quantitative Analyses

Samples of each sintered alloy were analysed in the SEM, using the ZAF4 programme on the Link computer to make back scatter (Z), absorbtion (A) and flourescence (F) corrections. The results of these analyses are given in Table 6.9, and indicate that the alloys were not homogeneous. For example, the analysis of the Fe, 1.0Cu, 1.0Si alloy indicated a composition of 0.41% Cu, 0.96% Si.

The software programme ZAF.PB, designed for the analysis of irregular surfaces, such as fractures and powders, was found to give erratic, and unreproducible results. Composition analyses of the oxide scales and powders with the SEM were therefore made semi-quantitatively.

6.8.2 Semi-Quantitative Analyses

The energy-dispersive x-ray analyser on the SEM was used to make semi-

Nominal Composition	Analysed Composition (balance Fe)
ASC100.29 base	
Fe, 1.0Si	1.1±0.1 Si
Fe, 3.0Si	2.6±0.1 Si
Fe, 1.0Cu	1.0±0.3 Cu
Fe, 1.0Al	0.1±0.1 Al
Fe, 1.0Cu, 1.0Si	0.4±0.3 Cu 1.0±0.1 Si
PNC60 base	
Fe, 0.6P, 1.0Si	0.6±0.1 P 0.8±0.1 Si
Fe, 0.6P, 3.0Si	0.4±0.1 P 2.5±0.1 Si
Fe, 0.6P, 1.0Cu	0.6±0.1 P 1.0±0.3 Cu
Fe, 0.6P, 1.0Cu, 1.0Si	0.5±0.1 P 1.2±0.3 Cu 1.2±0.1 Si

Table 6.9. Quantitative SEM analyses of PM alloys.

quantitative analyses of the powders (Table 6.10) and oxide scale compositions (Table 6.11). These do not include corrections for ZAF effects, and should therefore only be taken as a guide to the elements present. Also, the beryllium window of the Link analyser adsorbs the characteristic x-rays of elements lighter than sodium, so that it is not possible to measure oxygen concentrations with this equipment.

6.9 MICROGRAPHY

Samples were studied on a microscopic scale using optical and SEM techniques. As described in Section 5.12, preparation of samples for optical microscopy was laborious due to the combination of porous and oxidised structures. Despite every effort, the removal of pieces of oxide scale, by the tearing action of grinding and polishing media, could not be prevented.

6.9.1 Oxidation of Pure Iron

6.9.1.1 Unoxidised Microstructure

Plates 6.1 to 6.4 compare the end and side surfaces of a sample of (unoxidised) pure iron (ASC100.29) compacted at 350MPa. The end surface is broken by open pores, whilst that of the side has a fairly continuous smeared surface, to a depth of about 20μm. Compaction at 150MPa left the end surface very open, with pores penetrating into the bulk of the compact clearly discernible with the SEM. The side surface of the 150MPa sample did not have a smeared layer, and was only slightly less open than the end face of the 350MPa sample (Plate 6.1).

Compaction at 550MPa produced an almost continuous, smeared side surface to a depth of about 40μm. The edges of the metal smeared over pore openings in this surface could be detected with the SEM, as can be seen in parts of the corresponding area of the 350MPa sample (Plate 6.3). The presence of these edges suggests that the surface was not completely sealed by the smearing action associated with ejection from the compaction die.

Powder	Semi-Quantitative Analysis (wt%)
ASC100.29	100.0 Fe
PNC60	0.4 P 0.1 Si 98.0 Fe 1.2 others
Copper	1.5 Si 0.5 Ti 98.0 Cu
Aluminium	100.0 Al
Silicon	100.0 Si

Table 6.10. Semi-quantitative SEM analyses of powders.

Alloy	Oxide scale composition (balance Fe)	
	150MPa compacts	550MPa compacts
ASC100.29 base		
Fe, 1.0Si	0.8 Si	1.3 Si
Fe, 3.0Si	0.9 Si	1.4 Si
Fe, 1.0Cu	Fe only	Fe only
Fe, 1.0Al	8.5 Al 0.9 Si 0.4 W	11.8 Al 3.2 Si 1.1 W
Fe, 1.0Cu, 1.0Si	0.3 Si	0.2 Si
PNC60 base		
Fe, 0.6P	0.7 Si	0.6 P 0.5 Si
Fe, 0.6P, 1.0Si	0.1 P 0.8 Si	0.6 P
Fe, 0.6P, 3.0Si	0.6 Si	0.3 P 0.5 Si
Fe, 0.6P, 1.0Cu	0.8 Si	0.5 Si
Fe, 0.6P, 1.0Cu, 1.0Si	0.5 Si	0.5 Si

Table 6.11. SEM semi-quantitative analyses of alloy oxide scales.

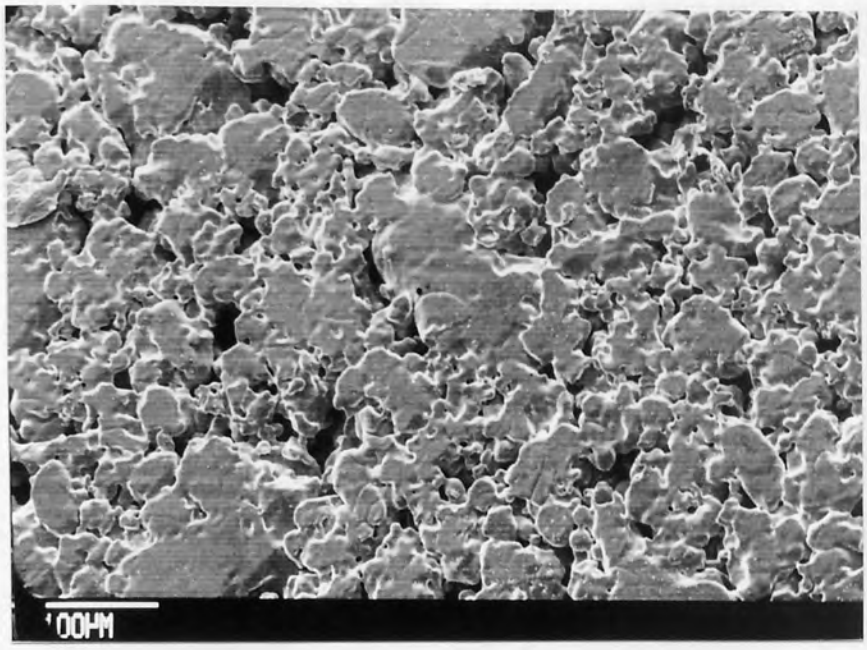

Plate 6.1. Electron micrograph of (unoxidised) end surface of pure iron (ASC100.29) compact, compacted at 350MPa.

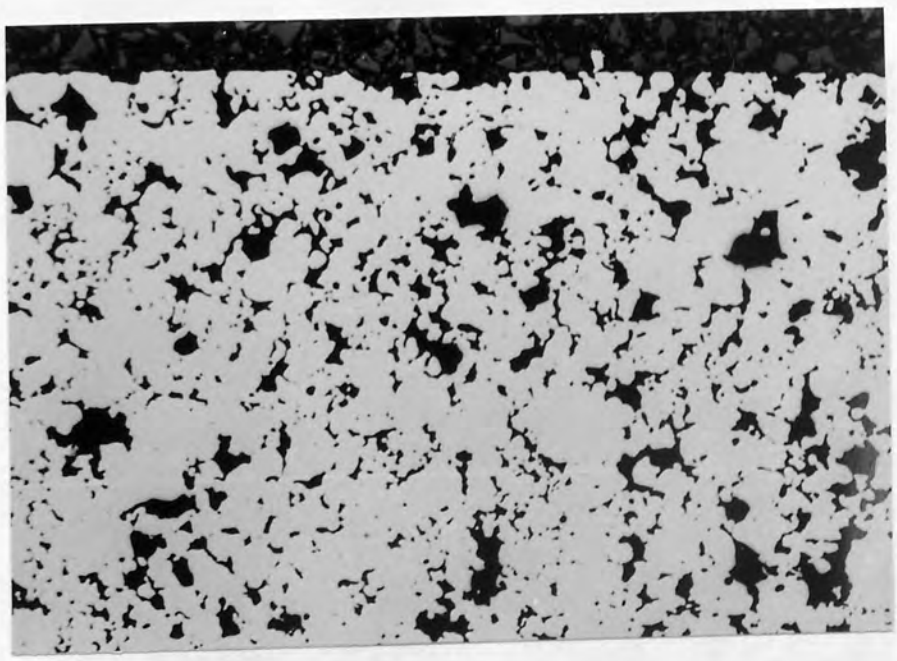

Plate 6.2. Microstructure of (unoxidised) end face of pure iron (ASC100.29) compact, compacted at 350MPa. Magnification x100.

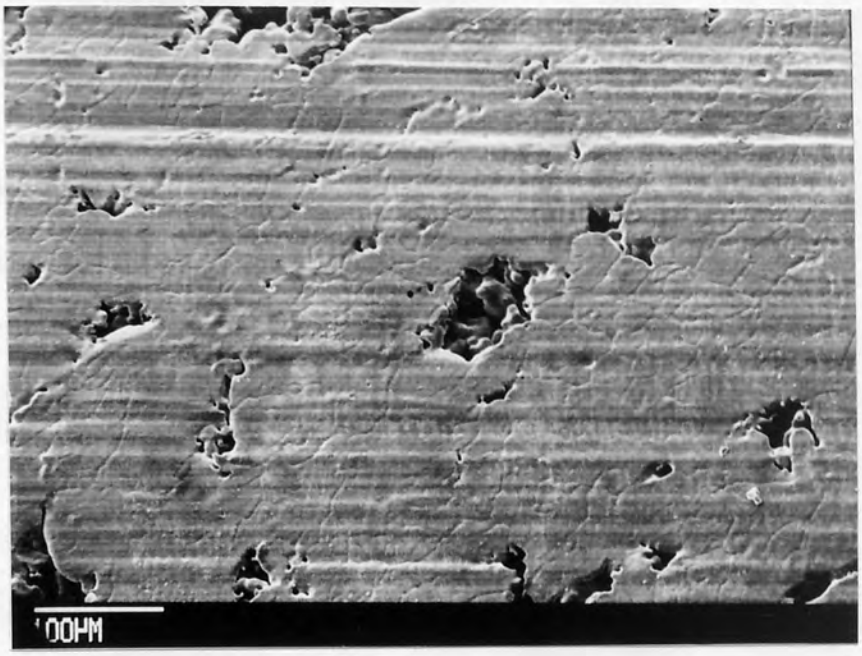

Plate 6.3. Electron micrograph of (unoxidised) side surface of pure iron (ASC100.29) compact, compacted at 350MPa.

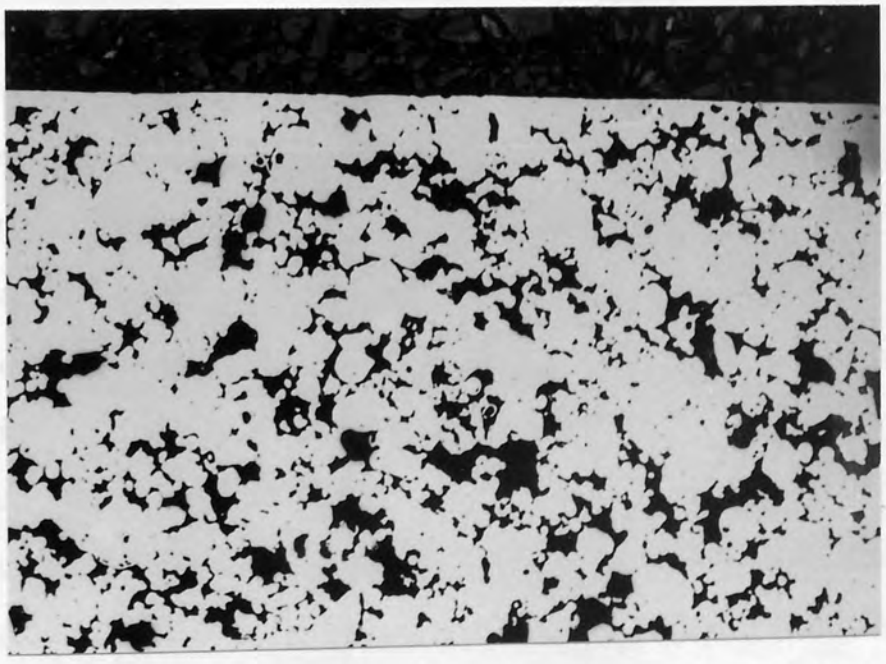

Plate 6.4. Microstructure of (unoxidised) side surface of pure iron (ASC100.29) compact, compacted at 350MPa. Magnification x100.

6.9.1.2 Oxidation of Porous Iron at 300°C to 500°C

Plate 6.5 is a photo-macrograph of a typical metallographic section along the axis of the cylindrical sample, in this case ASC100.29 compacted at 350MPa, and oxidised at 500°C for 24 hours (the flat end faces are at the top and bottom). The plate shows an oxidised surface zone, which has a fairly uniform depth of 3.7mm on both the end and side faces, decreasing towards the corners of the sample, and an unoxidised core. This effect, revealing the depth of oxidation, occurred in many oxidised samples, but was extremely difficult to record, being totally dependent on lighting conditions. In fact, Plate 6.5 was the only successful photograph of this type.

Plates 6.6, 6.8 and 6.9 are sections through an end surface of samples of ASC100.29 compacted at 150MPa, 350MPa and 550MPa respectively, and oxidised at 500°C for 24 hours. The two layer structure of the scale can be clearly seen in all three plates, with the light grey Fe_2O_3 layer only slightly thinner than the darker Fe_3O_4. The thicknesses of the scales, measured from photo-micrographs, are listed in Table 6.12.

The thickness of the oxide scale on the 150MPa sample (Plate 6.6) varies considerably across the micrograph, because of the irregularity of the original metallic surface. The greater pressure used in the compaction of the 350MPa and 550MPa samples Plates 6.8 and 6.9) has created flatter substrates. The thicknesses of the scales on the end surface of these (measured from the micrographs) are approximately 5μm (350MPa sample) and 4μm (550MPa sample). In both cases there are approximately equal thicknesses of magnetite and haematite.

Plate 6.7 is an SEM micrograph of the surface of oxide surface on the 150MPa sample, showing a rounded but uneven relief. In general, the oxide scale follows the contours of the original metal surface, so that under inspection at fairly coarse magnifications (say x200) oxidised and unoxidised surfaces would appear identical.

Plates 6.10 to 6.13 compare the surface and core zones of samples oxidised at 500°C for 24 hours. Plates 6.10 and 6.11 show that the oxidation reaction had penetrated to the core of the sample compacted at 150MPa. The sample compacted at

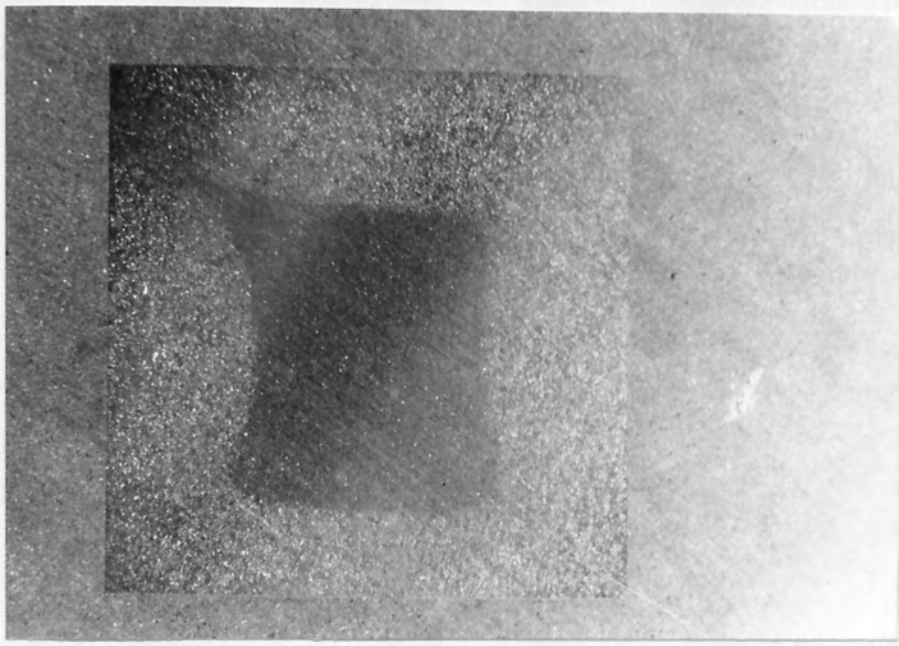

Plate 6.5. Depth of oxidation of pure iron (ASC100.29) compact, compacted at 350MPa, and oxidised at 500°C.

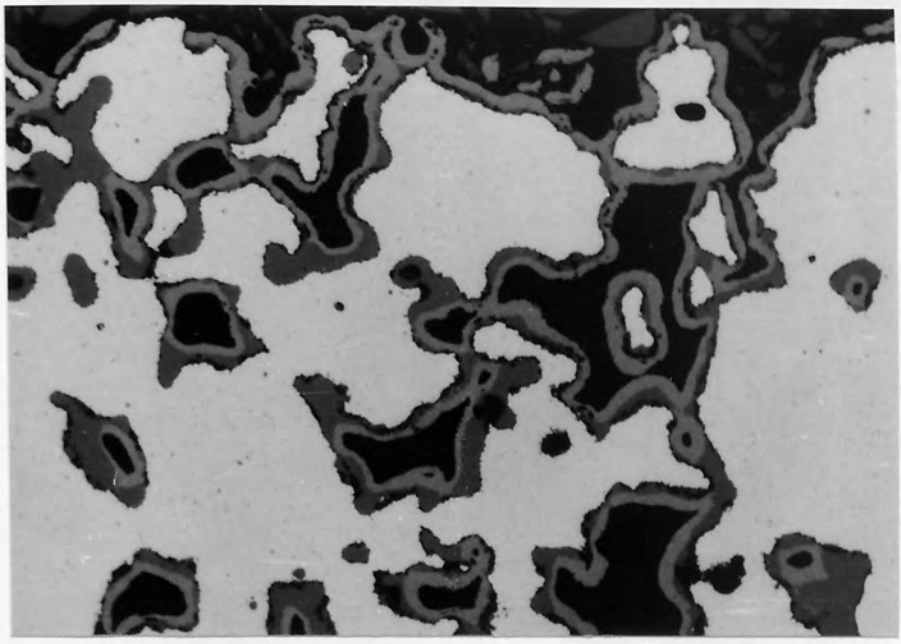

Plate 6.6. Microstructure of end face of pure iron (ASC100.29) compact, compacted at 150MPa, and oxidised at 500°C. Magnification x450.

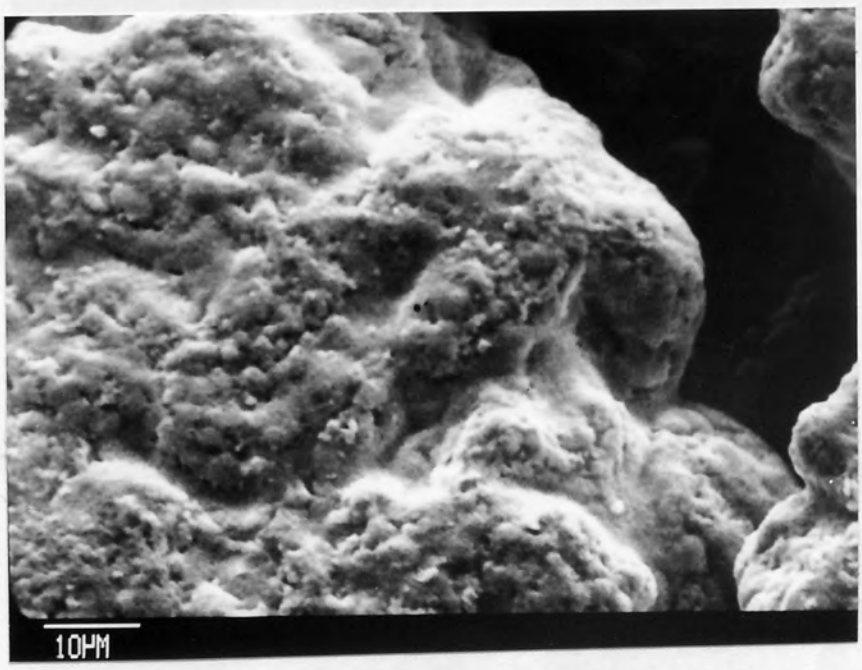

Plate 6.7. Electron micrograph of end surface of pure iron (ASC100.29) compact, compacted at 150MPa, and oxidised at 500°C.

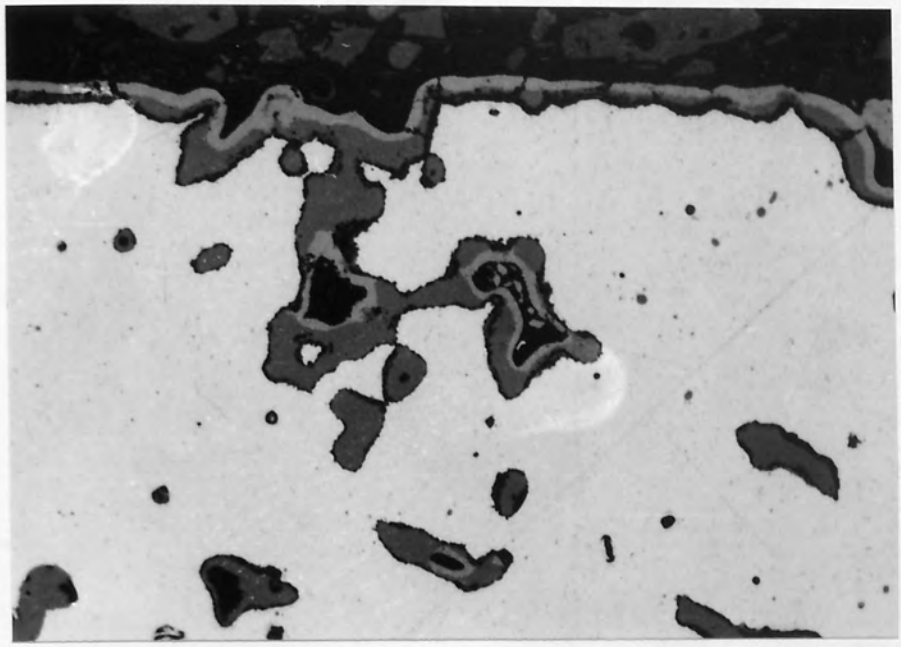

Plate 6.8. Microstructure of end face of pure iron (ASC100.29) compact, compacted at 350MPa, and oxidised at 500°C. Magnification x450.

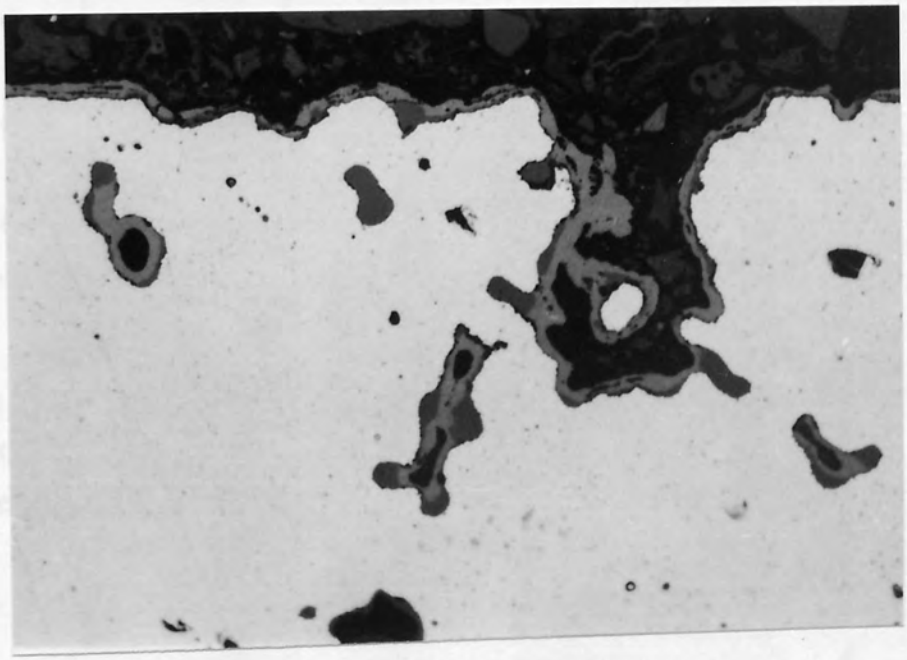

Plate 6.9. Microstructure of end face of pure iron (ASC100.29) compact, compacted at 550MPa, and oxidised at 500°C. Magnification x450.

Oxidation temperature	Oxide scale thickness / μm			
	ASC100.29 Compaction pressure			Armco iron
	150MPa	350MPa	550MPa	
300°C	(#1)	(#1)	(#1)	(#1)
400°C	(#1)	(#1)	(#1)	(#1)
500°C	4 - 6 *	6 - 9 *	4 - 6 *	7
600°C	11 - 35 *	14	11 - 21 *	28
700°C	173	161	143 - 178 *	115

Figure 6.12. Oxide scale thicknesses, measured from photo-micrographs.
(#1 Oxide scale too thin to be resolved.)
* Scale thickness variable.

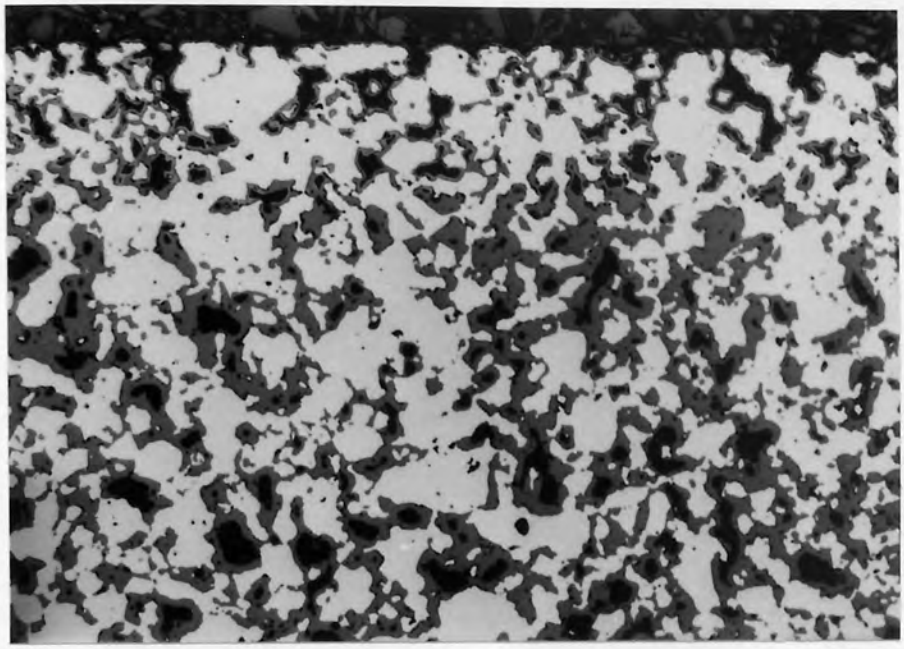

Plate 6.10. Microstructure of end face of pure iron (ASC100.29) compact, compacted at 150MPa, and oxidised at 500°C. Magnification x100.

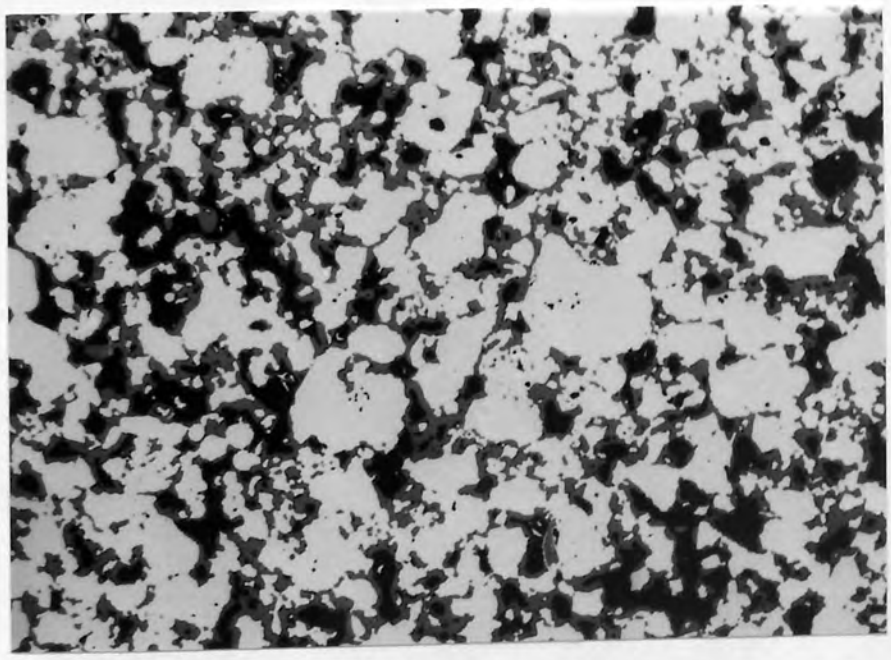

Plate 6.11. Microstructure of core of pure iron (ASC100.29) compact shown in Plate 6.10. Magnification x100.

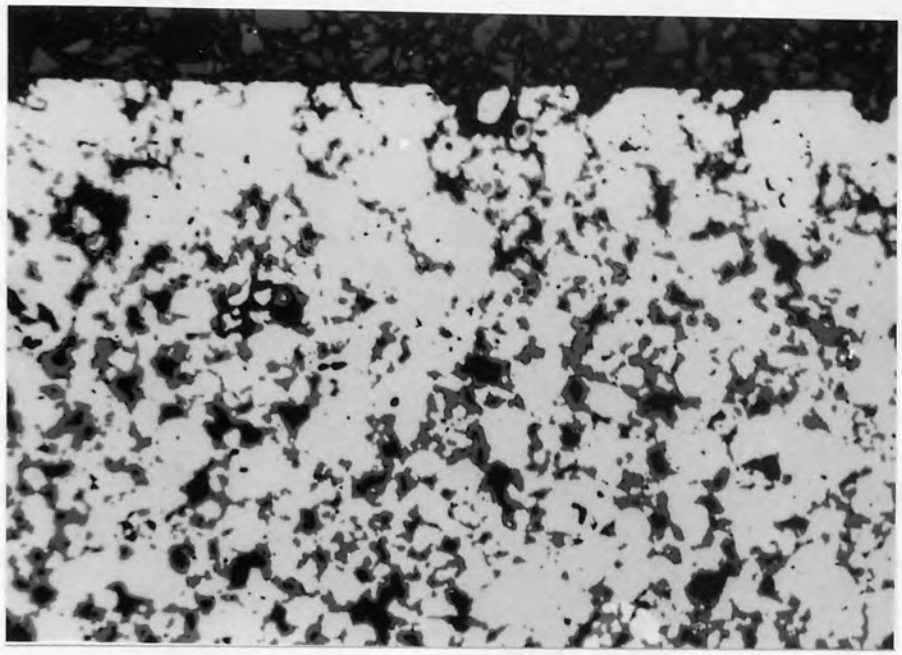

Plate 6.12. Microstructure of end face of pure iron (ASC100.29) compact, compacted at 350MPa, and oxidised at 500°C. Magnification x100.

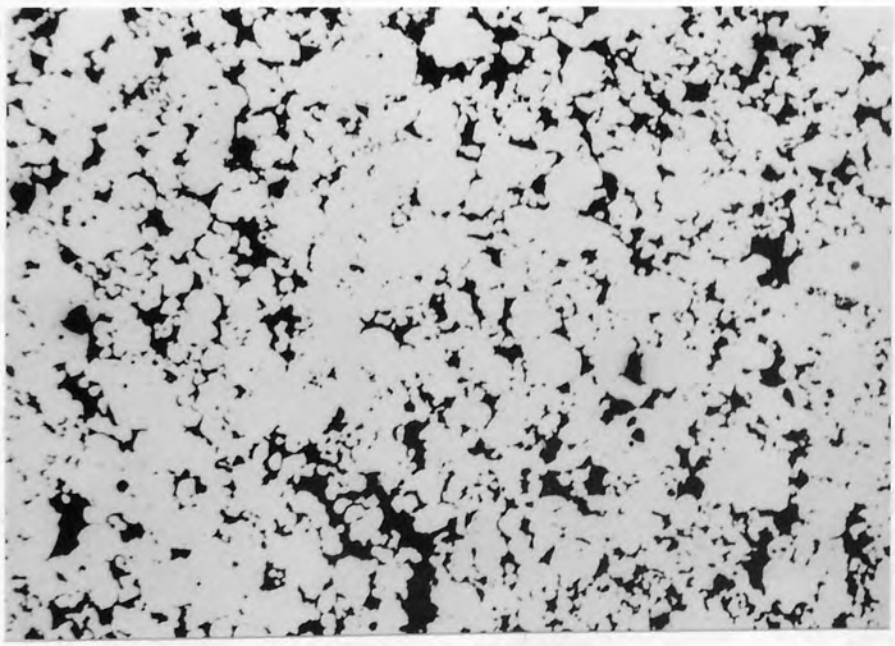

Plate 6.13. Microstructure of core of pure iron (ASC100.29) compact shown in Plate 6.12. Magnification x100.

350MPa (Plates 6.12 and 6.13) had an unoxidised core (which is also shown in Plate 6.5). Similarly, a sample compacted at 550MPa had an unoxidised core.

When oxidised at 400°C, samples compacted at both 150MPa and 350MPa had oxide in the core porosity, whilst the 550MPa sample core was unoxidised. No samples oxidised at 600°C and 700°C had any discernible oxide in their core porosity.

6.9.1.3 Oxidation of Porous Iron at 600°C and 700°C

Samples oxidised at 600°C had either a two-layer (magnetite and haematite), or a three-layer (wüstite, magnetite and haematite) oxide scale. None of the samples exhibited both types of structure. Oxidation at this temperature is very close to the equilibrium formation temperature of wüstite (570°C), and it may be that the temperature control of the thermobalance furnace (to ±10°C) was responsible for the different scales.

Plate 6.14 shows the etched microstructure of pure iron compacted at 150MPa, and oxidised at 700°C for 24 hours. The oxide scale is about 175µm thick (see Table 6.12), and has a three layer structure, with wüstite, magnetite and haematite in the ratio 75:14:11 (compared to reported ratios of 95:4:1 - see Section 3.4). The Fe_3O_4/'FeO' interface is just below the fracture line running across the area of the micrograph. The wüstite in this scale has two layers. The thin outer layer (about 15µm thick) has a uniform structure, whilst the inner layer (125µm thick) has a dense concentration of particles, that appear to be the same shade of grey as the magnetite phase.

Plate 6.15 is an SEM photomicrograph of the oxide scale surface of ASC100.29 compacted at 150MPa, and oxidised at 700°C, as for Plate 6.14. The very irregular surface, caused by localised high growth rates, can also be seen in cross-section in Plate 6.14.

Plate 6.14. Microstructure of three-layered oxide scale formed on pure iron powder (ASC100.29), compacted at 150MPa, and oxidised at 700°C. Magnification x450.

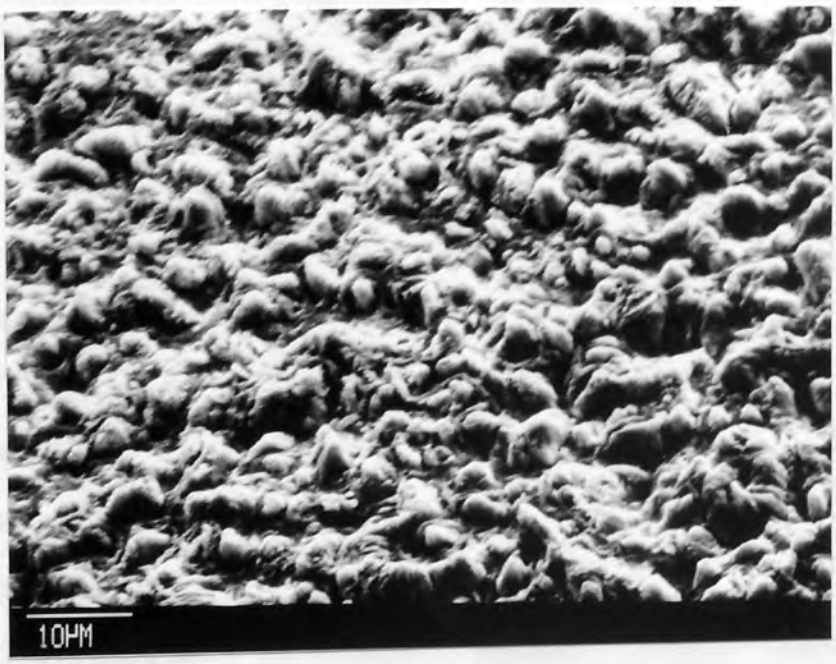

Plate 6.15. Electron micrograph of the surface of an oxide scale formed on pure iron powder (ASC100.29), compacted at 150MPa, and oxidised at 700°C.

6.9.1.4 Oxidation of Wrought Iron

The oxide film grown on Armco iron at 300°C was too thin to be detected by optical metallography, whilst those at 400°C and 500°C were just thick enough to be discerned. The oxide formed at these temperatures could not be seen in sufficient detail to determine the scale structure, and whether both magnetite and haematite were present.

At 600°C (Plate 6.16) and 700°C the oxide scales were considerably thicker, at about 100μm and 200μm thick respectively. The scales formed on Armco iron differ from those formed on ASC100.29 in two respects. Firstly, the thickness ratio of the Armco oxide layers is approximately 1:6:93 (haematite:magnetite:wüstite), which is very close to reported values of 1:4:95 (see Section 3.4). Secondly, the wüstite, which again has two layers, has a thick outer layer (about 85% of the total thickness of wüstite) with an apparently decomposed structure (wüstite and magnetite), and a thin inner layer of uniform structure. This layer arrangement is the opposite of that found on the ASC100.29 compact scales.

6.9.2 Oxidation of PM Alloys

All of the alloy compacts oxidised at 500°C were examined with the optical microscope and SEM. They were all found to have the two-layer scale of haematite on magnetite.

6.9.2.1 Pre-alloyed Powder Compacts

Pores in PNC60 compacts were smaller and more irregular than those seen in ASC100.29 compacts. However, the interparticle necks, and pore surfaces of the PNC60 compacts were more rounded than those of ASC100.29, Distaloy AB and Distaloy AE compacts.

Plates 6.17 and 6.18 show the oxide scale formed on PNC60 compacted at 150MPa. Compared to a similar sample of ASC100.29 (eg. Plates 6.6 and 6.7), the PNC60 has produced an oxide scale of far more variable thickness and variable

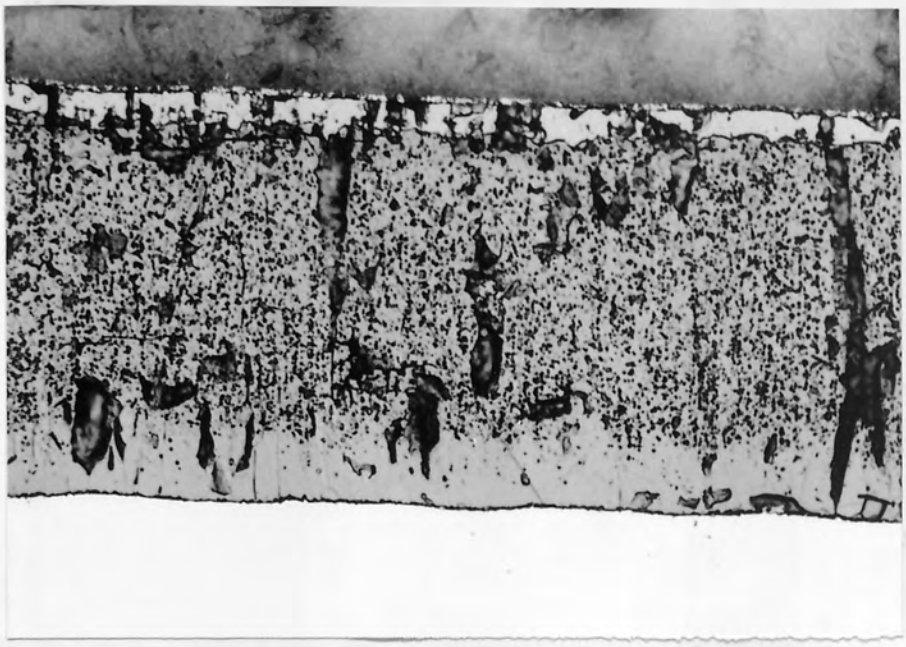

Plate 6.16. Microstructure of three-layered oxide scale formed on wrought pure iron powder (Armco Iron), oxidised at 700°C Magnification x450.

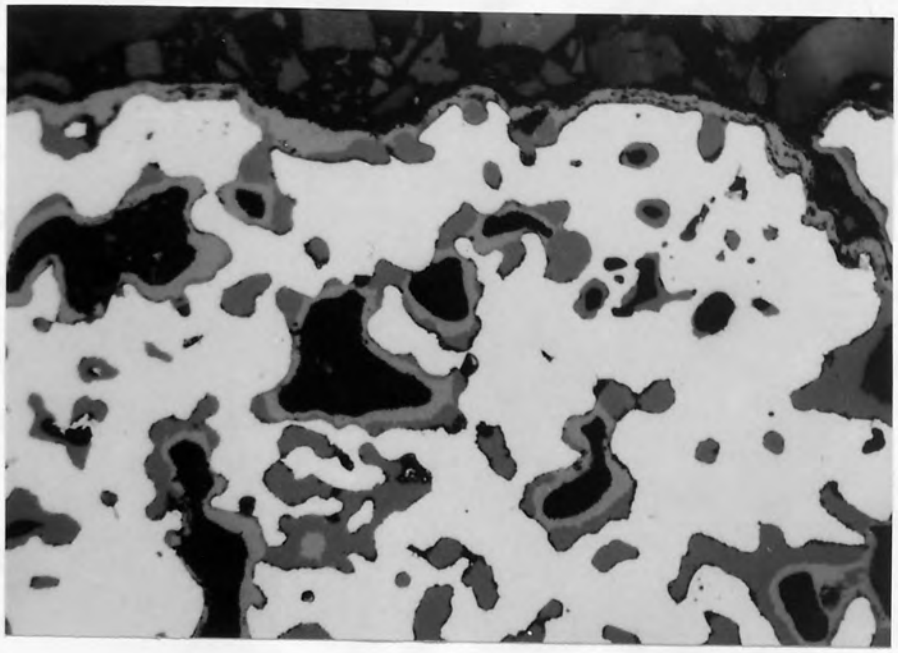

Plate 6.17. Microstructure of end face of Fe, 0.6P (PNC60) powder compact, compacted at 150MPa, and oxidised at 500°C. Magnification x450.

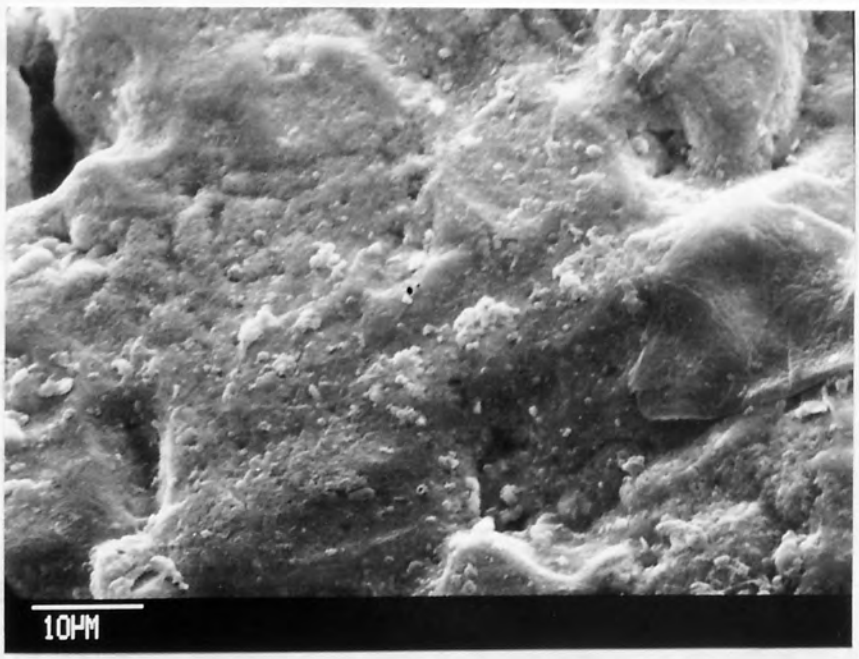

Plate 6.18. Electron micrograph of end surface of Fe, 0.6P (PNC60) powder compact, compacted at 150MPa, and oxidised at 500°C.

proportion of haematite to magnetite. The PNC60 has a greater number of smaller pores than the ASC100.29, and many of them have been completely blocked by the growth of magnetite. The growth of the scale has tended to round the pore surfaces in the PNC60, removing some of the irregularities seen in the unoxidised microstructure.

The oxide scales formed on Distaloy AB and Distaloy AE were very similar to those formed on ASC100.29. The scales are of uniform thickness, and their growth has remained approximately parallel to the metal surface.

6.9.2.2 Effect of Silicon Additions

Additions of 1.0% and 3.0% silicon to ASC100.29 significantly reduced the thickness of the oxide scale formed after 24 hours at 500°C. In the case of the Fe, 3.0Si alloy, the oxide scale could not be detected. The Fe, 0.1Si alloy had an oxide scale similar to that seen on pure ASC100.29.

Plates 6.19 and 6.20 are SEM photomicrographs of oxidised samples of the Fe, 1.0Si and Fe, 3.0Si alloys, both compacted at 150MPa. Compared with a similar sample of pure ASC100.29 (Plate 6.7), the surfaces of the silicon-containing compacts are much smoother. Examination of their microstructures indicates that the silicon addition causes rounding of pore surfaces during sintering. However, the oxide scales shown in Plates 6.19 and 6.20 appear to have been in the process of developing the small 'pits' of reduced growth surrounded by areas of accelerated growth, that may have created the relief observed on the pure ASC100.29 (Plate 6.7).

Additions of silicon to PNC60 (Plates 6.21 and 6.22) had a less noticeable affect, and only reduced the oxide scale thickness slightly.

6.9.2.3 Effect of Copper Additions

Additions of copper to the two alloy base powders produced irregular and uneven oxide scales, after 24 hours at 500°C. The scale on the Fe, 1.0Cu (Plate 6.23) appears to be an exaggerated version of the scale formed on pure ASC100.29 (Plate 6.7), but

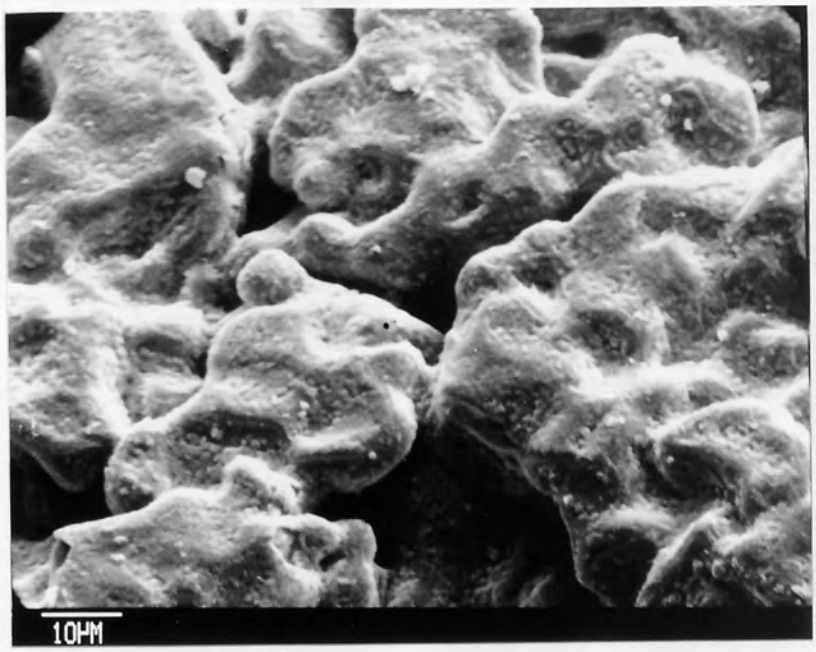

Plate 6.19. Electron micrograph of end surface of Fe, 1.0Si (ASC100.29 base) powder compact, compacted at 150MPa, and oxidised at 500°C.

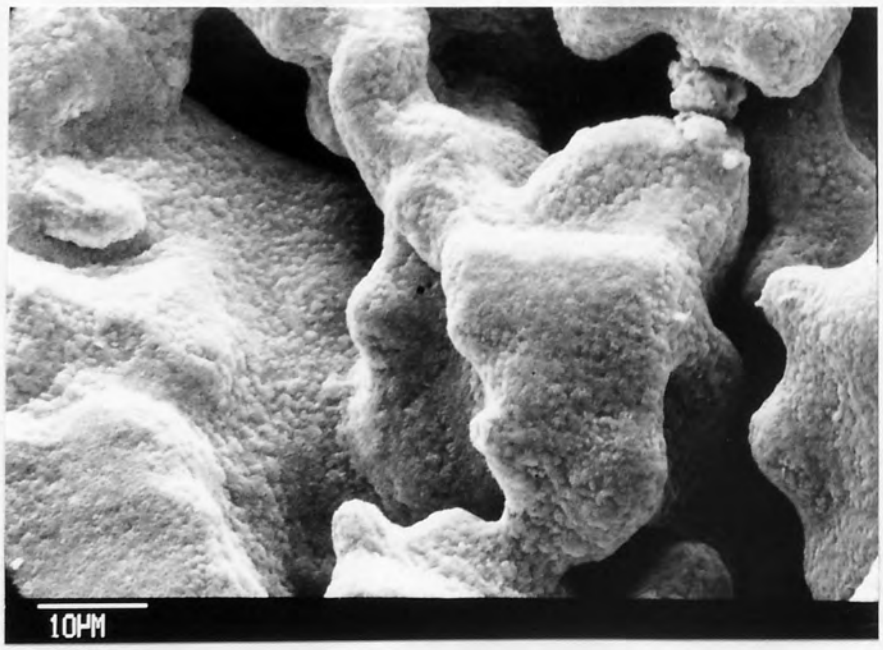

Plate 6.20. Electron micrograph of end surface of Fe, 3.0Si (ASC100.29 base) powder compact, compacted at 150MPa, and oxidised at 500°C.

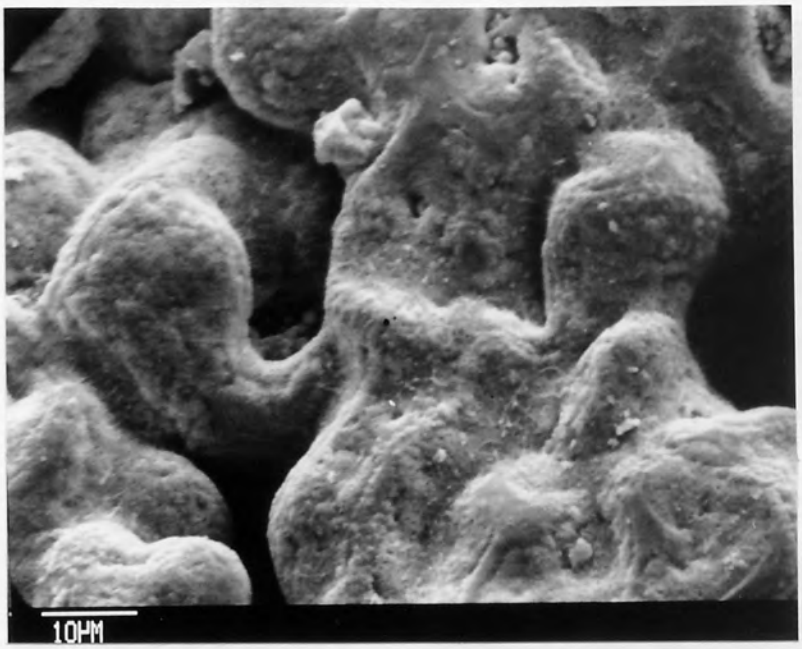

Plate 6.21. Electron micrograph of end surface of Fe, 0.6P, 1.0Si (PNC60 base) powder compact, compacted at 150MPa, and oxidised at 500°C.

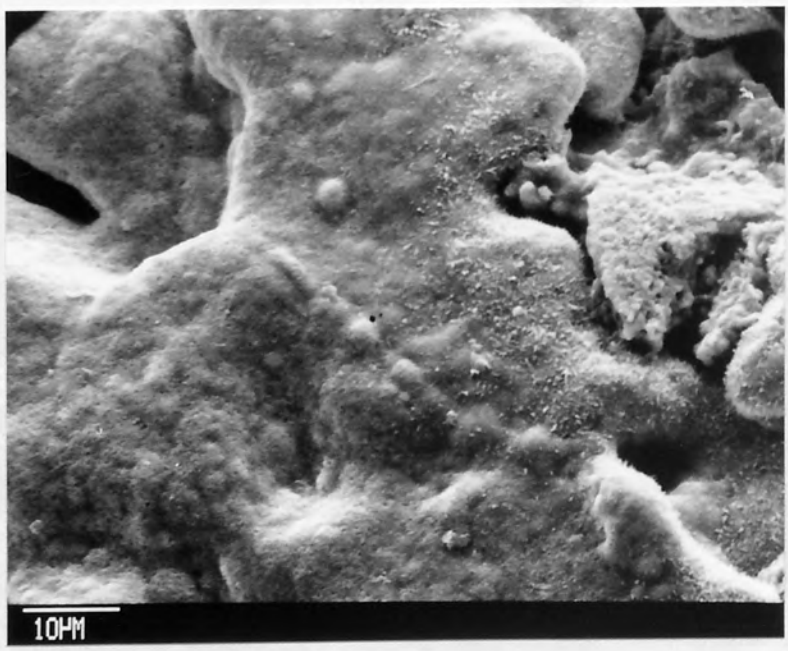

Plate 6.22. Electron micrograph of end surface of Fe, 0.6P, 3.0Si (PNC60 base) powder compact, compacted at 150MPa, and oxidised at 500°C.

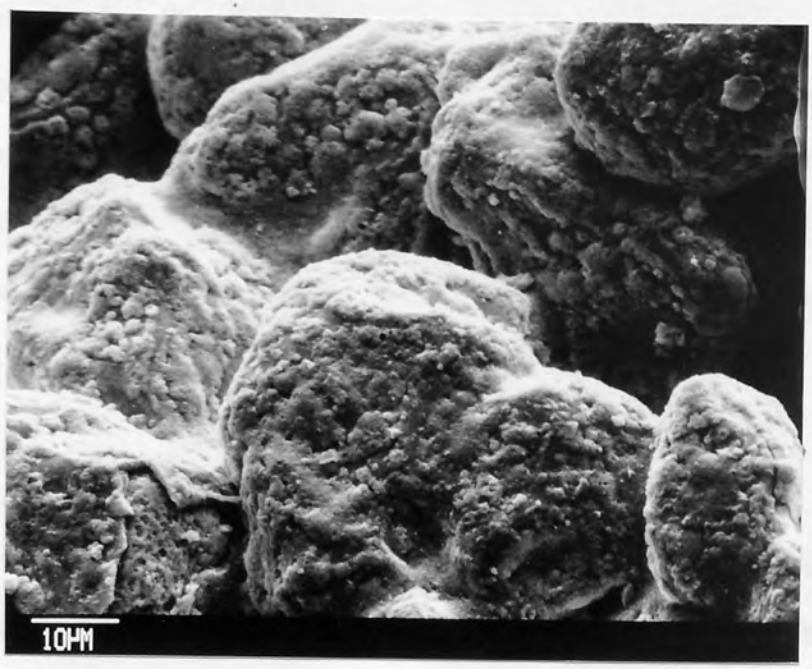

Plate 6.23. Electron micrograph of end surface of Fe, 1.0Cu (ASC100.29 base) powder compact, compacted at 150MPa, and oxidised at 500°C.

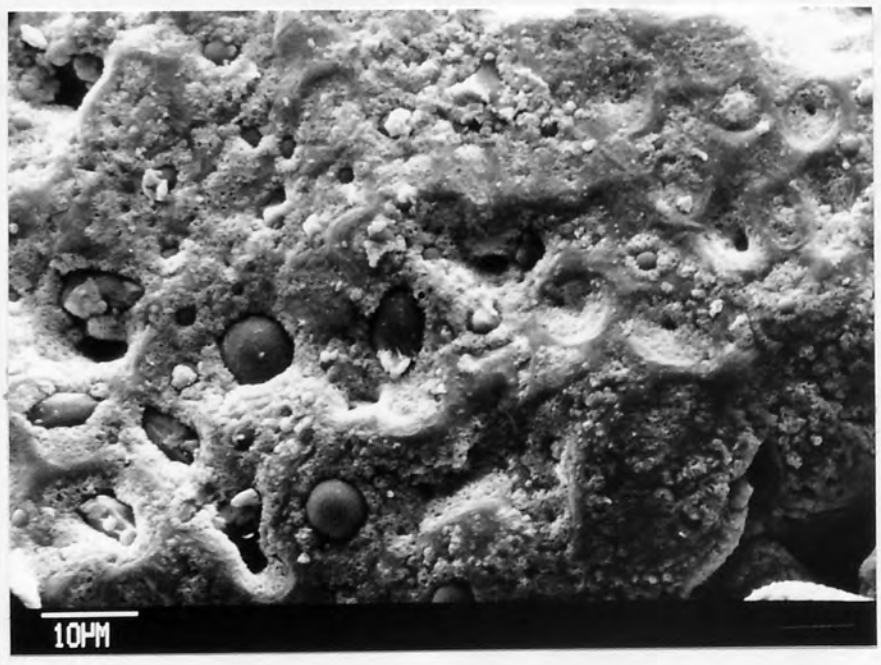

Plate 6.24. Electron micrograph of end surface of Fe, 0.6P, 1.0Cu (PNC60 base) powder compact, compacted at 150MPa, and oxidised at 500°C.

shows some evidence of spalling (in the bottom left corner).

Plate 6.24, of the oxide scale on the PNC60-based Fe, 0.6P, 1.0Cu shows a very irregular and pitted surface. There are what appears to be spherical particles, partially buried in the scale, the largest of these has a diameter of about 7μm.

The pore structures of both of the ASC100.29- and PNC60-based alloys were slightly rounded by the addition of copper.

6.9.2.4 Effects of Cu-Si Additions

The combined additions of copper and silicon (ie. ASC100.29, or PNC60, plus Cu, plus Si) appear to have prevented the pore rounding observed in the single addition alloys (ie. ASC100.29, or PNC60, plus Cu or Si).

The ASC100.29 base alloy (Fe, 1.0Cu, 1.0Si), shown in Plate 6.25, produced a thin oxide scale, of uniform thickness, less than 2μm thick, which could only just be seen with the optical microscope. The scale on the PNC60 base alloy (Fe, 0.6P, 1.0Cu, 1.0Si) has filled surface irregularities, creating the smooth surface seen in Plate 6.26. The thickness of the scale varied from about 10μm on concave surfaces, to less than 2μm on convex surfaces.This alloy does not have the small spherical particles seen seen embedded in the scale of the single addition alloy, Fe, 0.6P, 1.0Cu alloy (Plate 6.24).

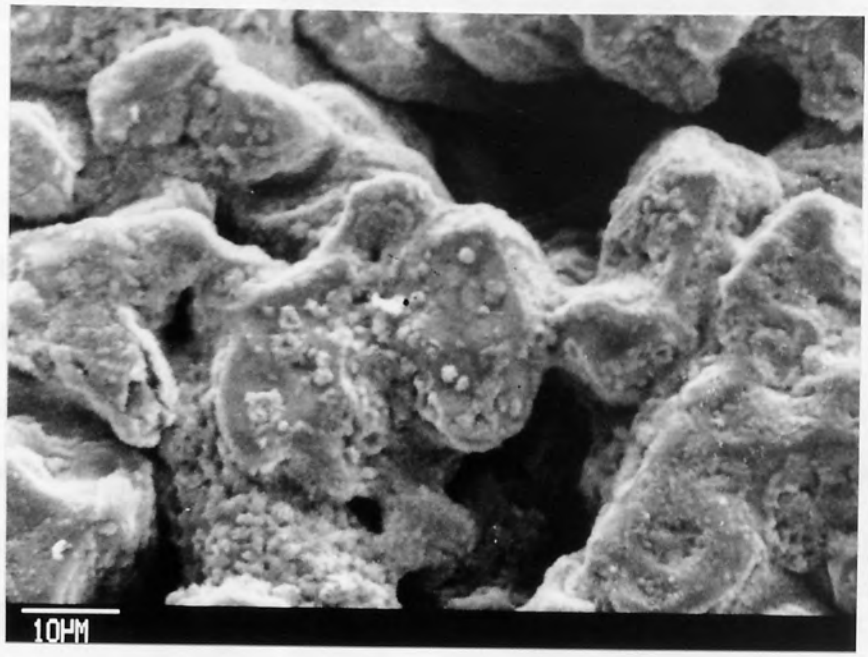

Plate 6.25. Electron micrograph of end surface of Fe, 1.0Cu, 1.0Si (ASC100.29 base) powder compact, compacted at 150MPa, and oxidised at 500°C.

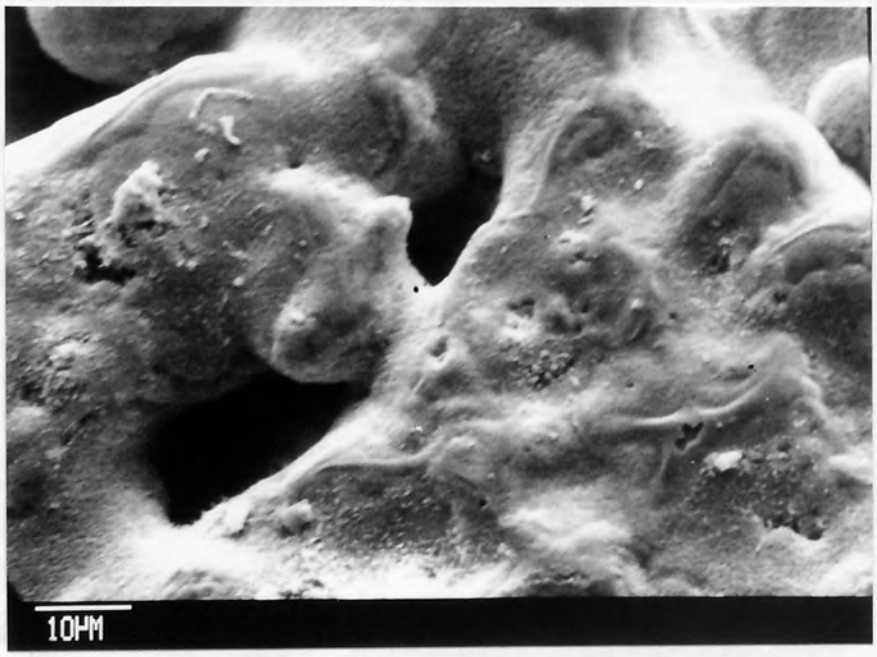

Plate 6.26. Electron micrograph of end surface of Fe, 0.6P, 1.0Cu, 1.0Si (PNC60 base) powder compact, compacted at 150MPa, and oxidised at 500°C.

Section 7
DISCUSSION

7.1 INTERPRETATION OF THERMO-GRAVIMETRY EXPERIMENT

7.1.1 Parabolic Scaling Constants

There are a variety of forms in which the parabolic scaling constant may be expressed, depending on the aspect of oxidation being studied. For this work, the constant applying to mass gain, with the dimensions $[M]^2\ [L]^{-4}\ [T]^{-1}$, is appropriate, and is denoted by the symbol k in the relationship

$$\left(\frac{\Delta m}{A_0}\right)^2 = k\,t \qquad \text{Eq. 7.1}$$

where Δm is the observed mass gain, A_0 the external surface area of the test sample and t is the time.

Values for k used in the text are taken from Figure 3.4. It is assumed in all calculations that the oxidation rate can be calculated with Equation 7.1. The experimental results show that there is a significant difference between the mass gain rate of porous samples, and the oxidation rate. This, it will be shown, is due to large changes in the area of metal being oxidised.

Some aspects of the oxidation of a porous body are dependent on the thickness, x, of oxide formed, such that

$$x^2 = k_x\,t \qquad \text{Eq. 7.2}$$

where k_x is the parabolic scaling constant for oxide thickness, with the dimensions $[L]^2\ [T]^{-1}$.

The parabolic scaling constants for mass gain, k, and for thickness, k_x, are related by

$$k_x = \left(\frac{M_{MO}}{\rho_{MO}\, b\, M_O}\right)^2 k \qquad \text{Eq 7.3}$$

where M_{MO} is the molecular weight of the oxide M_aO_b, ρ_{MO} is the density of the oxide,

and the term (b M_O) is the weight of atomic oxygen in one molecule of oxide.

7.1.2 Units of Oxidation

The accepted way to present the results of thermo-gravimetric oxidation experiments is in terms of mass gain per unit original surface area, ie. $\Delta m/A_0$, and the effects of sample shape are largely ignored. Clearly it is sensible to conform with the practice, although shape effects cannot be ignored for porous samples.

Comparison of the results for porous sintered iron, and for wrought pure iron, show that the presence of porosity significantly increases the mass gain during oxidation. Whilst it is possible to measure the total surface area of a porous sample before oxidation, it is impractical to repeat the measurement during oxidation. The results indicate that the active surface area of porous samples must decrease very rapidly during certain phases of oxidation, as porosity becomes blocked by oxide scale. Therefore, quoting results in terms of the initial active surface area may be just as misleading as quoting them in terms of the initial external surface area.

The approach used here has been to plot results in terms of $\Delta m/A_0$, and to quote the value of A_0, which is calculated as the surface area of a cylinder with the diameter and height of the sample, before oxidation. Results in the form $\Delta m/A_0$ are meaningful only if the sample is sufficiently massive or dense for the core to remain unoxidised. The oxidation of such samples can then be compared with the oxidation of non-porous samples, and conclusions may be drawn about the effects of the porosity.

In the case of porous samples that are oxidised throughout, the mass gain is dependent on the original sample size. Since oxidation is then effectively independent of the external surface area, results in the form $\Delta m/A_0$ are meaningless. For this situation, it may be more appropriate to quote results in terms of the original active surface area, as opposed to the external surface area.

The major problem, however, is how to compare the results for samples with oxidised cores, with the results for samples with unoxidised cores. By using samples

with identical dimensions, to within practical limits, all the samples have similar external surface areas. Hence the results, in the form of sample mass gain, remain in proportion to each other when quoted in terms of $\Delta m/A_0$, and may be compared without adjustment.

7.1.3 Sources of Error

7.1.3.1 Core Shrinkage

The area of the metal/oxide interface will decrease if the consumption of metal by the formation of oxide causes the interfaces at different parts of the sample to retreat towards each other. As oxidation progresses, the true area of the metal/oxide interface decreases from its initial value, A_0, so that the calculation of $\Delta m/A_0$ will result in the underestimation of the oxidation rate.

In 24 hours, the oxidation of a plane surface of iron at 700°C in air will produce an expected mass gain of

$$\frac{\Delta m}{A_0} = \sqrt{k\ t} = \sqrt{10^{-0.52} \times (24 \times 3600)} \approx 161 g\ m^{-2} \qquad \text{Eq 7.4}$$

The mass of metal gained by the oxide, Δm_M is

$$\frac{\Delta m_M}{A_0} = \frac{\Delta m}{A_0} \times \frac{a\ M_M}{b\ M_O} \qquad \text{Eq. 7.5}$$

where the oxide formula is M_aO_b, M is the atomic mass, and the subscripts M and O denote the metal and oxygen respectively. The metal loss is equal to $-\Delta m_M/A_0$, hence the distance moved by the metal/oxide interface (relative to the original metal surface) is

$$x_M = -\frac{m_{MO}}{\rho_M A_0} = -\frac{\Delta m}{\rho_M A_0} \times \frac{a\ M_M}{b\ M_O} \qquad \text{Eq. 7.6}$$

Thus, for the conditions cited (700°C for 24 hours), and assuming that the oxide scale is 100% wüstite,

$$x_M = -\frac{161 \times 10^{-3}}{7.87 \times 10^{3}} \times \frac{1 \times 0.056}{1 \times 0.016} = -72 \times 10^{-6} m \qquad \text{Eq. 7.7}$$

Ignoring the effects of edges and curved surfaces on oxidation kinetics, this result can be used to calculate the theoretical mass gain of a cylindrical sample for the formation of the calculated thickness of oxide scale. Thus, for a cylinder of initial diameter 12.700mm and height 12.500mm, the dimensions of the oxidised core, after 24 hours at 700°C in air, will be diameter 12.556mm and height 12.356mm. This core shrinkage is equivalent to the consumption of 421mg of iron, or the formation of 541mg of wüstite. Hence the mass gain of the cylinder is 160g m^{-2}, which is only 0.6% less than the value calculated for a plane surface (Equation 7.4). From these calculations, it is apparent that core shrinkage should have a negligible effect on oxidation, over a period of 24 hours.

7.1.3.2 Chart Record Accuracy

The resolution of the thermobalance chart record for mass change is 1mg, and for small mass gains, as observed for wrought pure iron samples at 500°C and below, this has a significant affect on the accuracy of results. A mass change of 1mg for a sample with a surface area of about 750mm^2 is equivalent to 1.3g m^{-2}. The actual chart record was a smooth, continuous curve: the resolution problem arose only because of the need to translate the analogue data into numerical data.

At 400°C, the observed mass gain for a sample of Armco iron, with a surface area of 748mm^2 (see Figure A.4, Appendix A), was 2±0.5mg, giving $\Delta m/A_0$ equal to 2.6±0.6g m^{-2}. For large mass gains, as observed for porous samples of pure iron, and at 600°C and above for wrought pure iron, the resolution of the chart record will have a negligible effect.

7.1.3.3 Temperature Control

Above 600°C, the parabolic scaling constant increases rapidly (see Figure 3.4). The thermobalance temperature control was found to be ±10°C above 500°C. At 700°C, this could result in a parabolic scaling constant in air of between $10^{-0.63}g^2m^{-4}s^{-1}$, at 690°C,

and $10^{-0.41}$, at 710°C (see Section 3.5). Thus after 24 hours of oxidation at a nominal temperature of 700°C, the mass gain of a plane wrought pure iron sample in air would, theoretically, be expected to lie in the range 161±22g m^{-2} to Thus the maximum possible error from this source is of the order of ±14% at 700°C.

7.1.3.4 Sample Platform Interaction

Samples oxidised at 700°C, and some of those oxidised at 600°C, were bonded to the sample platform by the growth of oxide. (Plate 6.5 shows that the depth of oxidation at the base of a sample, oxidised at 500°C, is only about two-thirds the depth at the top.) The area of the base of a typical oxidation sample is about 127mm^2, or 17% of the total surface area. Thus for a typical sample, with a surface area of 750mm^2, the observed mass gain after 24 hours at 700°C would theoretically lie between 134g m^{-2} (if the sample platform completely prevents oxidation of the base, and the effective reduction in active surface area is not taken into account during calculations) and 161g m^{-2} (if the sample platform has no effect). The maximum error from this source, at 700°C, is -17%, although the presence of oxide on the bases of samples indicates that the actual error was considerably less (ie. of smaller magnitude) than this.

7.1.3.5 Oxygen Supply

A 20%O_2/80%N_2 gas flow rate of 200x$10^{-6}m^3$ min^{-1} supplies oxygen at a rate of 57mg min^{-1} (at room temperature). The most rapid oxidation observed in any test, occurred for samples of pure iron powder compacted at 150MPa, and oxidised at 700°C (Figure A.7, Appendix A). These had a mass gain of 375mg (equivalent to 500g m^{-2}) during the first 30 minutes of the test, during which time the mass of oxygen supplied to the atmosphere was 1710mg. The oxygen supply in the furnace atmosphere was therefore probably not a constraint on oxidation.

7.1.3.6 Measurement of Sample Dimensions

Samples were measured to an accuracy of 0.01mm, using a micrometer screw gauge. This produces a possible error in calculations of the external surface area of less than ±0.2%.

7.1.3.7 Cumulative Error

Of the six sources of errors discussed here, only two (temperature control, and sample interaction with the sample platform) have a significant effect at high temperatures. For low mass gains, for example for Armco iron oxidised at 400°C or 500°C, a third factor, the accuracy of readings from the mass gain record must also be taken into account.

The theoretical mass gain for pure iron oxidised at 700°C for 24 hours in air is 161g m^{-2} If the actual oxidation temperature was 690°C, and the sample platform prevented oxidation of the base of the sample, then (theoretically) the observed mass gain would be about 115g m^{-2}. If the actual oxidation temperature was 710°C, and the sample platform did not affect the oxidation of the base of the sample, then (theoretically) the observed mass gain would be about 184g m^{-2}. Thus at 700°C, the theoretical observed value for the mass gain after 24 hours would be between +14% and -29% of the true value. At lower temperatures, this range would be considerably reduced.

Of the oxidation tests that were repeated (which included nearly all of those done with pure iron), only a very few exhibited a large variation between results. None of the test result variations were of the magnitude indicated by the calculations.

7.1.4 Comparison of Oxidation Results with Published Data

Figures 7.1, 7.2 and 7.3 compare oxidation curves calculated from published values the parabolic scaling constant, with the results obtained for Armco iron at 500°C, 600°C and 700°C. The results obtained during thermo-gravimetry tests, using the thermobalance, do not appear to obey parabolic oxidation laws. Plots of $\log(\Delta m/A_0)$ against log(time), in Figure 7.4, show that both the exponent, n, and the scaling constant, k, in the equation

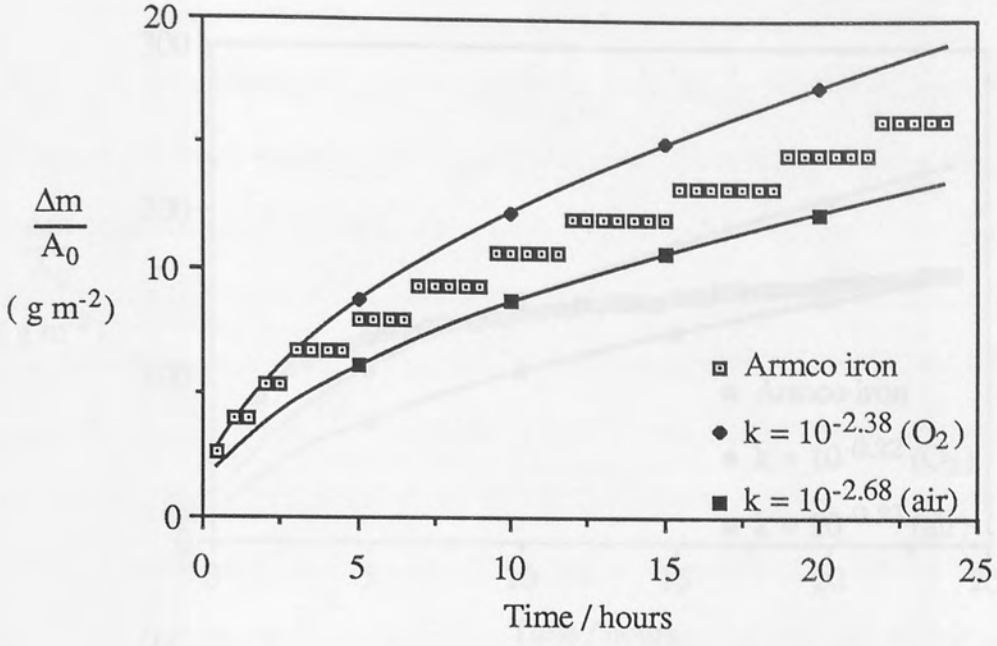

Figure 7.1. Comparison of TGA results for Armco iron oxidised at 500°C, with published parabolic scaling constants.

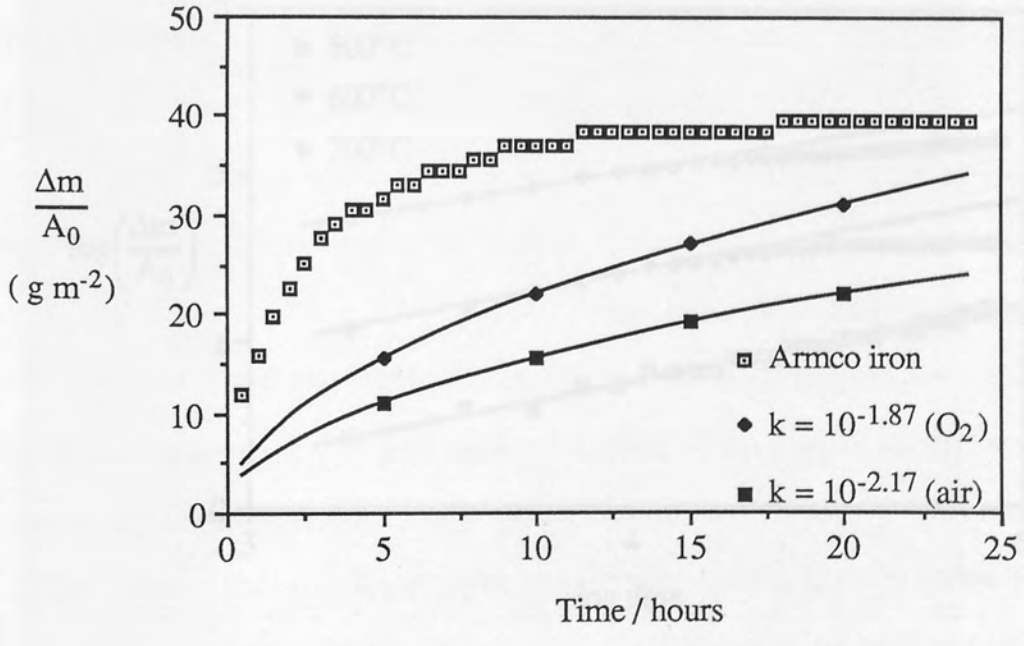

Figure 7.2. Comparison of TGA results for Armco iron oxidised at 600°C, with published parabolic scaling constants.

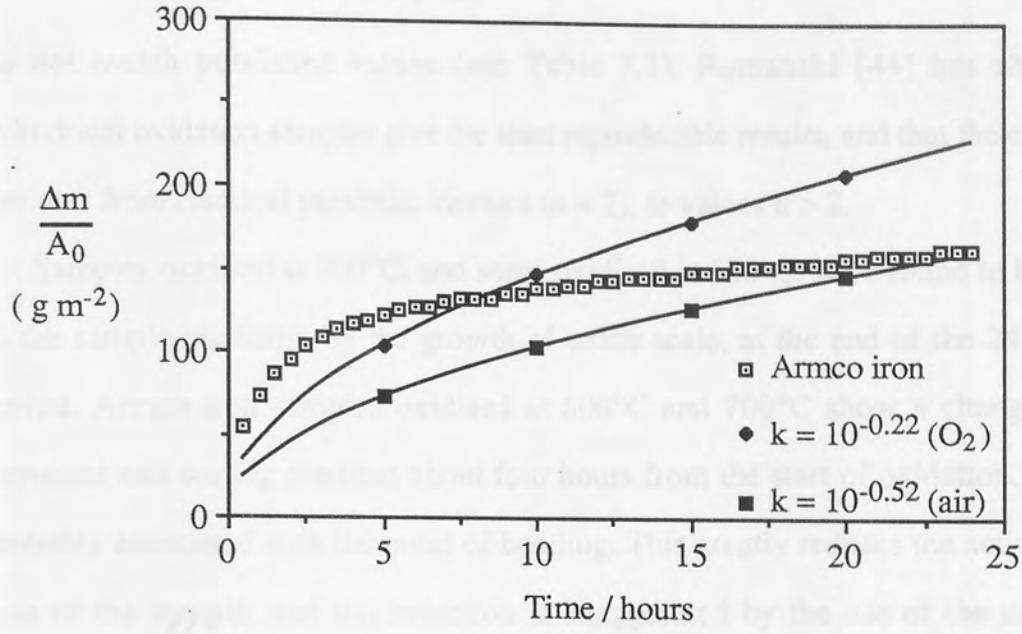

Figure 7.3. Comparison of TGA results for Armco iron oxidised at 700°C, with published parabolic scaling constants.

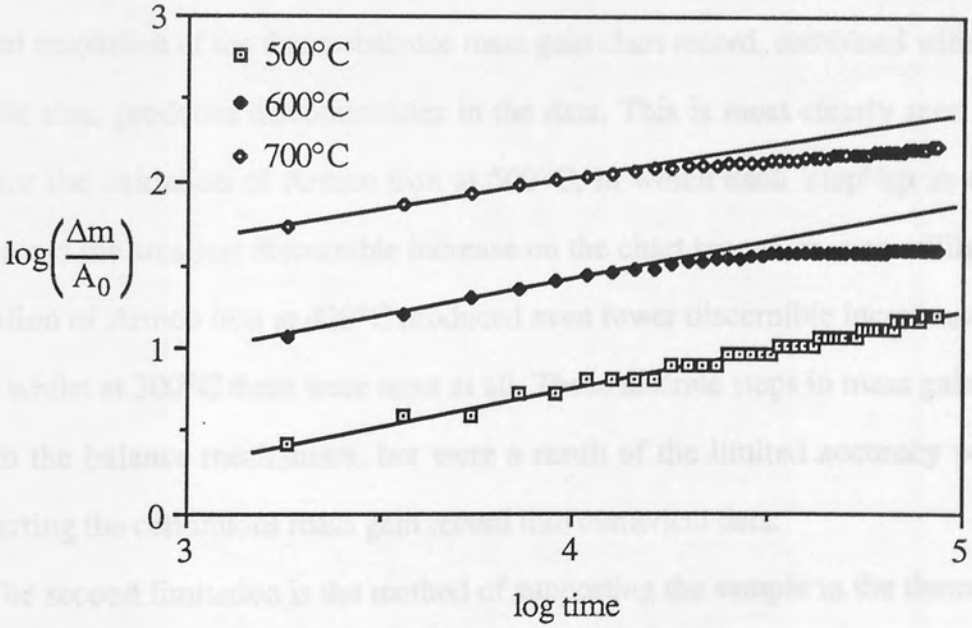

Figure 7.4. Determination of scaling constant and exponent for oxidation of Armco iron samples.

$$\left(\frac{\Delta m}{A_0}\right)^n = k\,t \qquad \text{Eq. 7.8}$$

do not match published values (see Table 7.1). Romanski [44] has shown that cylindrical oxidation samples give the least reproducible results, and that the exponent n deviates from classical parabolic kinetics (n = 2), to values n > 2.

Samples oxidised at 700°C, and some oxidised at 600°C, were found to be bonded to the sample platform, by the growth of oxide scale, at the end of the 24 hour test period. Armco iron samples oxidised at 600°C and 700°C show a change in both exponent and scaling constant about four hours from the start of oxidation., which is probably associated with the onset of bonding. This greatly reduces the active surface area of the sample, and the reduction is exaggerated by the use of the unoxidised surface area, A_0, in the calculation of $\Delta m/A_0$, which leads to an underestimate of the oxidation rate.

The results for Armco iron do not compare well with published values. The comparison reveals two of the limitations of the experimental technique. Firstly, the limited resolution of the thermobalance mass gain chart record, combined with the small sample size, produces discontinuities in the data. This is most clearly seen in Figure 7.1, for the oxidation of Armco iron at 500°C, in which each 'step' up in mass gain represents the smallest discernible increase on the chart record, ie. one milligram. The oxidation of Armco iron at 400°C produced even fewer discernible increments in mass gain, whilst at 300°C there were none at all. These discrete steps in mass gain were not due to the balance mechanism, but were a result of the limited accuracy possible in converting the continuous mass gain record into numerical data.

The second limitation is the method of supporting the sample in the thermobalance furnace during oxidation. Ideally, none of the surfaces to be oxidised should be in contact with any part of the furnace. A common experimental approach is to suspend the oxidation sample by passing a wire through a hole in one corner; a small hole has very little effect on the overall result, and the oxidation of the wire can be easily

Oxidation temperature	Exponent n	Scaling constant k $g^2m^{-4}s^{-1}$	Published values of scaling constant , k, for n = 2 $g^2m^{-4}s^{-1}$	
			Air	Oxygen
500°C	2.18	$10^{-2.34}$	$10^{-2.68}$	$10^{-2.38}$
600°C	2.2	$10^{-0.86}$	$10^{-2.17}$	$10^{-1.87}$
700°C	2.6	$10^{1.23}$	$10^{-0.52}$	$10^{-0.22}$

Table 7.1. Exponents and scaling constants for oxidation of Armco iron.

accounted for. However, it would have been difficult to drill such a hole through the small cylindrical samples used, without damaging the 'as compacted' surfaces.

The choice of sample shape and size were largely dictated by the limitations of the thermobalance. However, the thermobalance was able to provide detailed records of mass gains that varied in magnitude by a factor of about 400 (for example, from the oxidation of Armco iron at 400°C, to the oxidation, at 500°C, of ASC100.29 pure iron powder compacted at 150MPa). Thus despite the fact that oxidation kinetics were influenced to some degree by the experimental apparatus, it was possible to use the same equipment for all the oxidation tests performed.

7.1.5 Validity of Results

It is generally accepted that the oxidation of wrought iron at 400°C, and higher temperatures, in oxygen or air, obeys a parabolic kinetic law. The differences between the current results for wrought iron, and the published data, must therefore arise because of the experimental approach, which has modified the oxidation mechanism. It is reasonable to assume that, on a microscopic scale, the oxidation of the Armco samples does proceed at a parabolic rate. However, oxidation is affected by surface geometry, and physical interaction with the surroundings, so that the cumulative effect, on a macroscopic scale, results in apparently non-parabolic kinetics.

The experimental factors that modify the oxidation of wrought iron will have the same effects on the oxidation of the external surfaces of PM iron. No attempt is made, in this present work, to reconcile the oxidation of the Armco iron samples with published data, because the results have shown that the mass gain of wrought iron is, generally, negligible compared with the mass gain of PM iron. Thus the bulk of oxidation on a porous body must be occurring within the porosity, with only a small contribution from the external surface.

By using the same experimental equipment, and identical samples for tests, the factors that modify the oxidation kinetics should be invariable. Thus comparisons

between results remain valid. The oxidation tests on Armco iron allow the oxidation behaviour of PM iron, and PM iron alloys, to be compared with that of wrought iron, if only on a semi-quantifiable basis. The comparison of oxidation results for Armco iron, with published data, show that the experimental work, presented here, should not be used to quantify the kinetics of oxidation for the PM iron and iron alloys.

In the following discussion, it has been assumed that, on a microscopic scale, oxidation has obeyed a parabolic kinetic law, with the exponent n equal to 2, and published values have been used for the parabolic scaling constant (see Figure 3.4). This has been extended, as a simplifying assumption, to enable calculations concerning oxidation on a macroscopic scale. Geometrical effects have been ignored.

7.2 OXIDATION OF INTERCONNECTED POROSITY

Consideration of the processes involved in the oxidation of a porous body leads to the following observations:

(i) The oxygen in the gas permeating the interconnecting porosity is adsorbed by the pore surfaces. This reduces the gas pressure in the porosity, and also reduces the partial pressure of oxygen in the gas. Subsequent oxidation of pores is dependent on the ingress of oxygen from the external atmosphere. This can occur by two mechanisms, (a) gas pressure equalisation, and (b) diffusion of oxygen, driven by the partial pressure gradient.

(ii) Oxygen diffusing through interconnecting porosity is adsorbed at any metal surface with which it comes into contact. Therefore, it will tend to be adsorbed closer to the external surface (than to the sample core).

(iii) Oxide growth can block the capillaries connecting pores, restricting the ingress of the atmosphere.

(iv) The external scale will grow most rapidly, since the oxygen supply is relatively unrestricted. From observation (iii), it follows that surface

porosity will be filled by oxide growth first, preventing the diffusion of oxygen into the gas permeating the interconnected porosity.

(v) Once internal porosity is sealed from the external atmosphere, the oxide that has already formed on pore surfaces will eventually reach a dynamic equilibrium with the remaining atmosphere, in which the dissociation of oxide is matched by the adsorption of oxygen. Oxygen may still enter sealed porosity, by diffusion from the external surface, and dissociation at the internal oxide/pore interface, or through micro-channels in the oxide scale.

These observations can be used to explain the microstructures revealed by metallography.

7.2.1 Effect of Temperature

7.2.1.1 Oxidation in Porosity at 300°C

The oxidation rate is very low, relative to oxidation at higher temperatures, and the oxide film that is formed, is thin enough to produce interference colours at the external surface. The oxygen in the gas permeating the porosity is replenished faster than it is consumed by the oxidation reaction.

7.2.1.2 Oxidation in Porosity at 400°C

Oxidation is sufficiently slow for oxygen to diffuse into the core of samples with relatively open pore structures, for example, those compacted at between 150MPa and 350MPa. The relatively large interconnecting capillaries allow the passage of sufficient oxygen for the formation of an oxide scale on all exposed surfaces.

Denser samples, compacted at between 350MPa and 550MPa, have a less open pore structure. The interconnecting capillaries are relatively narrower, restricting the flow of oxygen to the core, which appears to remain unoxidised.

7.2.1.3 Oxidation in Porosity at 500°C to 600°C

Pore surfaces close to the external surface adsorb all the oxygen diffusing in from the atmosphere. There is no discernible oxidation of core porosity, because the partial pressure of oxygen is never high enough (after the initial phase of the reaction) to support the reaction. Scale growth on the external surface is also rapid, and tends to seal surface porosity.

7.2.1.4 Oxidation in Porosity at 600°C to 700°C

The growth of wüstite is so rapid that even near-surface porosity does not receive adequate oxygen for the formation of an oxide scale. Lateral growth of the external scale very rapidly seals surface porosity.

Figure 6.4, illustrates the implications of this rapid scale growth. The oxide scale formed at 600°C and 700°C is considerably thicker than the two-layer scales formed at 500°C and below, but the total weight gain is greatly reduced, because oxide growth is largely restricted to the external surface.

7.2.2 Porosity and Scale Adhesion

The sub-surface porosity in a compact provides numerous sinks for the vacancies created at the metal/oxide interface. The experiments of Tylecote and Mitchell [r172] (Section 2.9.1) have demonstrated that vacancy sinks of this type will increase the adhesion of oxide scales. The pores maintain a vacancy concentration gradient in the metal, reducing cavity formation by the condensation of vacancies at the metal/oxide interface.

The effectiveness of this process can be ascertained from the experimental work presented here. 550MPa (12% porosity) compacts oxidised at 600°C or 700°C had non-adherent scales, which flaked during handling after tests. 350MPa compacts (19% porosity) had non-adherent scale on the curved side surface only, whilst 150MPa (31% porosity) compacts had tightly adherent scales on all surfaces, which could not be loosened even when gouged with a pointed metal scribe.

The dependence of scale adhesion on porosity suggests that there is a critical, minimum level below which it (the porosity) does not provide an adequate concentration of vacancy sinks. For the ends of the samples, with flat, unsmeared surfaces, this critical level lies between 12% and 19% porosity. Curvature of the surface, and possibly smearing during the ejection of the compact from the compaction die, increase the critical porosity level for scale adhesion.

Another factor may be the mechanical locking of the scale to the irregular, porous surface. The micro-photographs of cross-sections of oxidised compact surfaces (Plates 6.6, 6.8 and 6.9) show that surface irregularity increases with increasing porosity (or decreasing compaction pressure). The surfaces of samples compacted at 150MPa are clearly going to have more re-entrant angles than samples compacted at 550MPa, and therefore will have more sites that can mechanically anchor a continuous, unbroken scale.

7.2.3 Depth of Oxidation

The depth below the external surface at which oxide is able to form in interconnected porosity has a considerable effect on the mass gain of samples during oxidation. Plate 6.5 shows the macrostructure of a sample compacted at 350MPa and oxidised at 500°C. As previously mentioned (Section 6.10.1), this type of macrostructure was generally only visible in certain lighting conditions, and was difficult to photograph, or measure in a reproducible manner.

The appearance of the macrostructure, which is unetched, is caused by the development of surface relief during the polishing of samples, and is similar to the mechanism illustrated in Figure 5.9. The different hardnesses of the oxide, and the metal, create an irregular surface relief during polishing, which scatters incident light on oxidised areas of the sample. Hence, under certain lighting conditions, areas of the sample containing oxide appear brighter than unoxidised areas. It is possible (occasionally) to determine the depth below the external surface, to which the surfaces

of interconnected porosity have been oxidised, by measuring the bright area.

Many of the samples in which this type of macrostructure was found, exhibited the same characteristics. The smearing of the side surface, during ejection from the powder compaction die, and the partial sealing of surface porosity that it causes, does not appear to have affected the depth of oxidation. The depth is not uniform, tending to be shallowest at the corners. This pattern should be compared to the density distribution obtained by the double-action pressing of a compact, illustrated in Figure 4.3b. Clearly, the depth of oxidation must be related to the permeability of the porosity.

7.2.4 Oxidation in Pores and the Oxide Growth Stress

Iron oxides grow under compression, due to the atomic lattice mismatches between the metal and oxide. At the external surface, the stress may be relieved to some extent by the ability of the scale to expand at a free surface, ie. outwards, and laterally over surface porosity. The retreat of the metal/oxide interface, as metal is consumed by oxide growth on concave surfaces (such as in pores), reduces the compressive growth stress (and can lead to the scale becoming detached, or cracking in tension at the interface) [46].

If the porosity becomes completely filled with oxide, further oxide growth in the pores would exert a compressive stress on the surrounding metal. This would dilate the metal matrix, exerting a tensile stress on interparticle bonds, and increasing the likelihood of their oxidation. However, no evidence of the oxidation of interparticle bonds was found in the metal surrounding oxide-choked pores.

The oxide/atmosphere interface for an oxide-choked pore will be in the capillary connecting it to the external atmosphere. In the experiments conducted, only magnetite was found in fully oxidised pores. This has a very narrow composition range, and so will not grow appreciably in the absence of oxygen, which does not diffuse readily through the Fe_3O_4 lattice. Therefore, any compressive growth stress in the oxide growing on pore surfaces, will be at least partially relaxed (by the retreat of the iron),

and is unlikely to increase when the pores are filled.

The haematite layer of the oxide scale will be reduced to magnetite when the pore is sealed from the external atmosphere. Haematite is less dense than magnetite, so its reduction should lead to a further reduction in any residual compressive stress.

7.2.5 Heat of Oxidation

The quantity of heat generated during oxidation is proportional to the rate of reaction, and the surface area the oxidising body. This effect is therefore most marked during the early stages of oxidation, and most particularly on samples with a large active surface area, namely those compacted at 150MPa for the present work. The magnitude of the effect for these samples caused significant superheating, above the ambient furnace temperature.

Samples compacted at 150MPa (giving 30% porosity), and oxidised at 500°C and 550°C exhibited two periods of superheating. The second period of superheating cannot be due to the exothermicity of the oxidation reaction, since by this stage the active surface area already has a covering of oxide. Therefore it must be due to a change in the oxide itself, as suggested by Fedorchenko *et al* [158]. Whatever that change is, it results in the liberation of energy, and is probably caused by a transformation towards equilibrium.

The formation of a thin layer of wüstite beneath the initial growth of magnetite has been observed at temperatures as low as 400°C [83]. The activation energy for the formation of the wüstite reduces the strain energy due to the lattice mismatch between the iron and magnetite [96]. The initial period of superheating in PM iron will aid the formation of wüstite, by raising the temperature of the sample closer to, or above, the equilibrium temperature for the formation of wüstite. As the oxide scale thickens, strain energy due to the Fe - Fe_3O_4 lattice mismatch becomes less significant, and the wüstite layer is transformed back to magnetite. The excess energy that was bound-up in the non-equilibrium wüstite, is evolved as heat, and hence the second period of superheating.

7.3 KINETICS OF OXIDATION OF PM IRON

The major difference between the oxidation of a plane metal surface (for which most oxidation laws have been derived), and the oxidation of a porous body, is the formation of oxide in regions remote from the ambient atmosphere.

Relating the widely published oxidation laws for plane surfaces, to the oxidation of a porous body would therefore have to take in to account several factors, which are discussed in the following sections.

7.3.1 The Partial Pressure of Oxygen in Porosity

The consumption of oxygen reduces the partial pressure of oxygen in the porosity, and also the pressure of the gas relative to the atmospheric pressure. Thus, in addition to the oxygen partial pressure gradient, there is also a partial vacuum created in the porosity. (To avoid confusion, 'gas' will generally mean the gas in pores, whilst 'atmosphere' will mean the gas outside the porous body.)

7.3.1.1 Influx of Oxygen Due to a Partial Vacuum

The flow of gas through porous structures is complex, and theoretical descriptions of pore characteristics, and their effects on gas flow, are still being developed. These descriptions include some factors that are difficult to quantify (such as the 'tortuosity' of the pore structure) [140]. There does not appear to be any suitable information available with which to estimate the flow rate of gas through a porous body.

The root mean square velocity of gas molecules is given by

$$c_{rms} = \sqrt{\frac{3\,k\,T}{M}} \qquad \text{Eq. 7.9}$$

where M is the molecular weight of the gas. This yields a value of about 820m s^{-1} for 20%O_2/80%N_2 at 500°C. The mean free path of the gas molecules is given by

$$\bar{l} = \frac{k\,T}{\pi\,\sigma^2\,P} \qquad \text{Eq. 7.10}$$

where 2σ is the molecular diameter in collisions (about $0.45 \times 10^{-9} m^2$), and P is the gas pressure [93]. At 500°C and 10^5Pa, the mean free path of gas molecules is 170nm. These values suggest that gas pressure equalisation may be effectively instantaneous at the experimental temperatures, since the velocity of gas molecules is very large relative to the size of the oxidation samples, whilst their mean free path is small relative to the size of capillaries and pores[4].

Consider a typical oxidation sample (diameter 12.7mm, height 12.5mm), compacted at 150MPa, resulting in 30% porosity after sintering. At a partial pressure of 0.2×10^5Pa, and a temperature of 500°C, the pores can contain about 47μg of gaseous oxygen[5]. Figure A.5, Appendix A, shows that such a sample of pure iron gained about 150mg (ie. $\Delta m/A_0 = 200 g\ m^{-2}$) in mass during the first 30 minutes of oxidation at 500°C.

If it is assumed that the external surface of this sample, of about $750mm^2$, has obeyed parabolic oxidation kinetics during this period, with a scaling constant of $k = 10^{-2.38} g^2 m^{-4} s^{-1}$, then the mass gain due to the external surface alone would account for only 1.3% of the observed mass gain (by way of comparison, the mass gain of the Armco iron sample at this temperature was only just large enough to be measured). This suggests that the oxygen content of the gas permeating the porosity was replaced about 3,150 times in the first thirty minutes of oxidation, or approximately once every 0.6 seconds (on average). The formation of oxide at the core of the sample indicates that this supply rate is practical.

The gas drawn into the pores by the partial vacuum is composed of $80\%N_2$ and $20\%N_2$. Therefore, ignoring the effects of oxygen diffusion, the oxygen content of the gas permeating the porosity will decrease as fresh gas is drawn in. In simplistic terms, the oxygen content would be reduced by 80% for each time the adsorbed gas in the porosity is replaced from the atmosphere. Starting from a partial pressure of 0.2×10^5Pa,

4 This does not take into account the effects of gas flow characteristics (eg. lamellar or turbulent), or the indirectness of the path connecting an external surface to the core porosity.

5 Assuming that $20\%O_2/80\%N_2$ behaves as an ideal gas.

it takes only 41 'replacements' for the oxygen partial pressure to fall below the dissociation pressure for iron oxide at 500°C (ie. 0.2×10^5Pa x $0.2^{41} < 10^{-24}$Pa) [180].

Returning to the earlier calculation, for the oxygen consumption of a 30% porous iron compact at 500°C, it would appear therefore that, if there was no oxygen diffusion, the partial pressure of oxygen in the porosity would fall below the oxide dissociation pressure within 25 seconds. This leads to the conclusion that the bulk of the oxygen adsorbed by pore surfaces is transported by gaseous diffusion, and that the creation of a partial vacuum will play only a minor part.

7.3.1.2 Gaseous Diffusion of Oxygen

The oxygen flux is given by

$$j_{O_2} = - D_{O_2} A \frac{C'' - C'}{H} \qquad \text{Eq. 7.11}$$

For the example of the 30% porous sample oxidised at 500°C used in Section 7.3.1.1, the oxygen flux must average 83×10^{-9}kg s^{-1} (ie. 150mg ÷ 30 minutes). The diffusion coefficient for a gas can be approximated by the relationship

$$D \approx \frac{1}{3} c_{rms} \bar{l} \qquad \text{Eq. 7.12}$$

and in binary gases, D is largely independent of composition [10, 93]. Using the previous calculations of c_{rms} and l (Equations 7.9 and 7.10 respectively), the value of D_{O_2} is about $46 \times 10^{-6} m^2 s^{-1}$ at 500°C and 10^5Pa.

If it is assumed that the cross-sectional area of surface porosity, A, of the 30% porous sample is $225 \times 10^{-6} m^2$ (ie. 30% of the external surface area, $750 \times 10^{-6} m^2$), and the length of the concentration gradient, H, is the radius of the sample ($^1/_2 \times 12.7 \times 10^{-3}$m), then the calculated concentration difference (C" - C') would be -0.051kg O_2 m^{-3} (see footnote[6]). This is equivalent to an oxygen partial pressure differential of -50% between the external atmosphere and the core.

The parabolic scaling constant is proportional to the partial pressure of oxygen (see

6 The cylindrical geometry of the surface is ignored here. It is assumed that the sample is a plane body, with a thickness equal to the diameter of the cylinder.

Section 2.6.2), such that

$$k \propto (p_{O_2})^{1/(2(v+1))} \qquad \text{Eq. 7.13}$$

where v is the valency of the oxide cation, and hence for Fe_2O_3 (the oxide layer in contact with the atmosphere) the exponent is equal to $^1/_8$. Thus a 50% reduction of p_{O_2} will cause an 8% reduction of k, equivalent to a 4% decrease of the oxidation rate. For these conditions (30% porosity, at 500°C), therefore, the core porosity will oxidise at nearly the same rate as the external surface.

After oxidation at 500°C for 24 hours, samples with 15% porosity or less (compacted at 450MPa and 550MPa), did not have any oxide in the core porosity. The porosity in these samples was interconnected, which is confirmed by the presence of oxide in pores to some depth below the external surface. However, oxygen diffusing into the porosity, from the furnace atmosphere, did not reach the sample core in great enough quantities to cause the formation of a discernible oxide scale. Therefore it is probable that the partial pressure of oxygen in the core porosity of these samples was close to the dissociation pressure of the oxide, and was thus negligible relative to the partial pressure of oxygen in the atmosphere.

If the oxygen partial pressure at the sample core is negligible, then the oxygen concentration difference, (C'' - C') in Equation 7.11, is equivalent to a pressure difference of -0.2×10^5Pa. At 500°C, this is equivalent to -0.100kg O_2 m^{-3}. During the first 30 minutes of oxidation, the mass gain of the 15% porous sample (compacted at 450MPa) was 62mg (see Figure A.5, Appendix A), of which 2mg are calculated to be due to the oxidation of the external surface. Hence the oxidation of pore surfaces requires an oxygen flux of 33×10^{-9}kg s^{-1} (ie. 60mg ÷ 30 minutes).

To balance for these values in Equation 7.11, the area, A, across which this oxygen flux would be flowing is $45\times10^{-6}m^2$, which accounts for only 40% of the estimated surface porosity of a 15% porous sample (with a surface area of $750mm^2$). This is clearly a measure of the pore structure's efficiency in conveying oxygen to sub-surface porosity by diffusion, and must therefore be related to the permeability.

The penetration of oxygen into porosity, by gaseous diffusion, is dependent on the permeability of the pore structure. For the example of the 30% porous sample, compacted at 150MPa, and also for samples compacted up to 350MPa (20% porosity), oxygen was able to penetrate to the core porosity, and oxidise all surfaces. Samples compacted at 450MPa (15% porosity) and 550MPa did not have any observable oxide in core porosity, but were oxidised to a considerable depth below the external surface. It seems probable, therefore, that more massive compacts of the pure iron powder, with 20% porosity or more, would also have unoxidised cores.

7.3.1.3 Effect of p_{O_2} on the Oxidation Rate of Pore Surfaces

Oxidation within a porous body is sustained by the diffusion of oxygen through the gas permeating the porosity. The partial pressure of oxygen, at any particular point within a porous body, depends on the permeability of the pore structure. At the same time, the rate at which oxygen is adsorbed from the gas, is itself dependent on the oxygen partial pressure (see Section 2.6.2). Thus the restriction of the oxygen supply, by the impermeability of the pore structure, will also reduce the rate of oxidation in the porosity. Additionally, the growth of oxide on pore surfaces will reduce the cross-sectional area of pores and capillaries, which will therefore reduce the permeability as oxidation progresses. The values required for the calculation of the partial pressure of oxygen in the porosity (permeability, oxidation rate) are themselves dependent on the answer to the calculation.

7.3.2 Closure of Porosity

The growth of oxide on pore surfaces reduces the volume of porosity. This will lead to pores becoming choked with oxide, and will reduce the permeability of the pore structure. As has been shown , the partial pressure of oxygen in the porosity decreases with increasing depth below the external surface, and so the oxidation rate will be highest in the surface porosity. Therefore, pore closure is more likely to occur at the

external surface, where the partial pressure of oxygen is close to the ambient.

Pore closure will occur when the growth of oxide above the original metal surface is equal to the radius of the capillary, that is

$$\Delta x = x + x_M = \frac{\Phi}{2} \qquad \text{Eq. 7.14}$$

where x is the thickness of oxide, x_M is the distance moved by the metal/oxide interface (relative to some fixed point in space), and Φ is the diameter of the capillary. The value of Δx at a given time, may be calculated from

$$\Delta x = \frac{\Delta m}{A_0} \times \frac{\left(V_{MO} - V_M\right)}{b\, M_O} \qquad \text{Eq. 7.15}$$

where V is the molar volume (eg. $V_{MO} = M_{MO} / \rho_{MO}$).

The main interest in pore closure is the time at which it occurs, since this will have the most significant effect on the oxidation rate of the porous body. Noting that

$$t = \frac{1}{k}\left(\frac{A_0}{\Delta m}\right)^2 \qquad \text{Eq. 7.16}$$

then the time of pore closure is given by

$$t_c = \frac{1}{k}\left(\frac{\Phi\, b\, M_O}{2\left(V_{MO} - V_M\right)}\right)^2 \qquad \text{Eq. 7.17}$$

From the photo-micrographs of pore structures (eg. Plates 6.6 to 6.9), typical values of Φ lie in the range 5μm to 10μm. Values of t_c have been calculated for these capillary diameters, and are tabulated in Table 7.2.

Oxidation test results (Appendix A) show a rapid decreases in the rate of mass gain at around the times calculated for t_c. The calculations in Table 7.2 are more accurate for samples compacted at 150MPa to 350MPa, whilst the change in mass gain rate occurs earlier than calculated for samples compacted at 450MPa and 550MPa. The change of mass gain rate occurs over a period of time in all cases, because of the range of capillary diameters. A study of capillary diameters (eg. to obtain the statistical mean and distribution of Φ) would enable the effects of pore closure, on mass gain rate, to be

Oxidation temperature	Oxide scale layer thickness ratios $FeO:Fe_3O_4:Fe_2O_3$	Pore closure time t_c / hours	
		Φ = 5μm	Φ = 10μm
400°C	0:1:1	726.6	2906.3
500°C	0:1:1	3.3	13.3
600°C	0:1:1	1.0	4.1
700°C	1:0:0	<0.1	<0.1

Table 7.2. Calculations of pore closure time, by growth of oxide in capillaries of diameter Φ .

calculated on a probabilistic basis.

7.3.3 Active Surface Area During Oxidation

Knowing the active surface area during oxidation is critical to determining the mass gain rate of a porous body. In Section 7.3.1, the effects of oxygen diffusion on mass gain were discussed, and showed that the oxidation of sub-surface porosity depends on the permeability, rather than the interconnectedness, of the pore structure. Hence the active (ie. oxidising) surface area of a porous body may be considerably less than its total surface area.

In Section 7.3.2, it was shown that the growth of oxide scale can block capillaries very rapidly at the higher experimental temperatures. Pore closure will isolate porosity, significantly reducing the surface area exposed to the oxygen diffusing in from the external atmosphere.

Therefore, it appears that knowledge of the effects of permeability on sub-surface oxidation, and pore closure, may allow the active surface area to be estimated. However, as discussed in Section 7.3.1.3, determining partial pressure of oxygen in porosity, and hence the oxidation rate, is difficult because of their interdependence.

Figure 7.5 is an interpretation of the oxidation results obtained for porous samples compacted at 350MPa (shown together in Figure 6.5), in terms of active surface area. From the relationship

$$A_0^2 = \frac{\Delta m^2}{k\,t} \qquad \text{Eq. 7.18}$$

it follows that the instantaneous surface area, A_i, at time t_2, is given by

$$A_i = \sqrt{\frac{\Delta m_2^2 - \Delta m_1^2}{k\,(t_2 - t_1)}} \qquad \text{Eq. 7.19}$$

where Δm_1 and Δm_2 are the mass gains at times t_1 and t_2 respectively, and $t_1 < t_2$. If the mass gain obeys a parabolic law, then $A_i = A_0$. However, for the oxidation of a porous body Equation 7.19 provides an estimate of the active surface area, assuming that the oxidation rate (as opposed to the mass gain rate) is parabolic. During periods when the

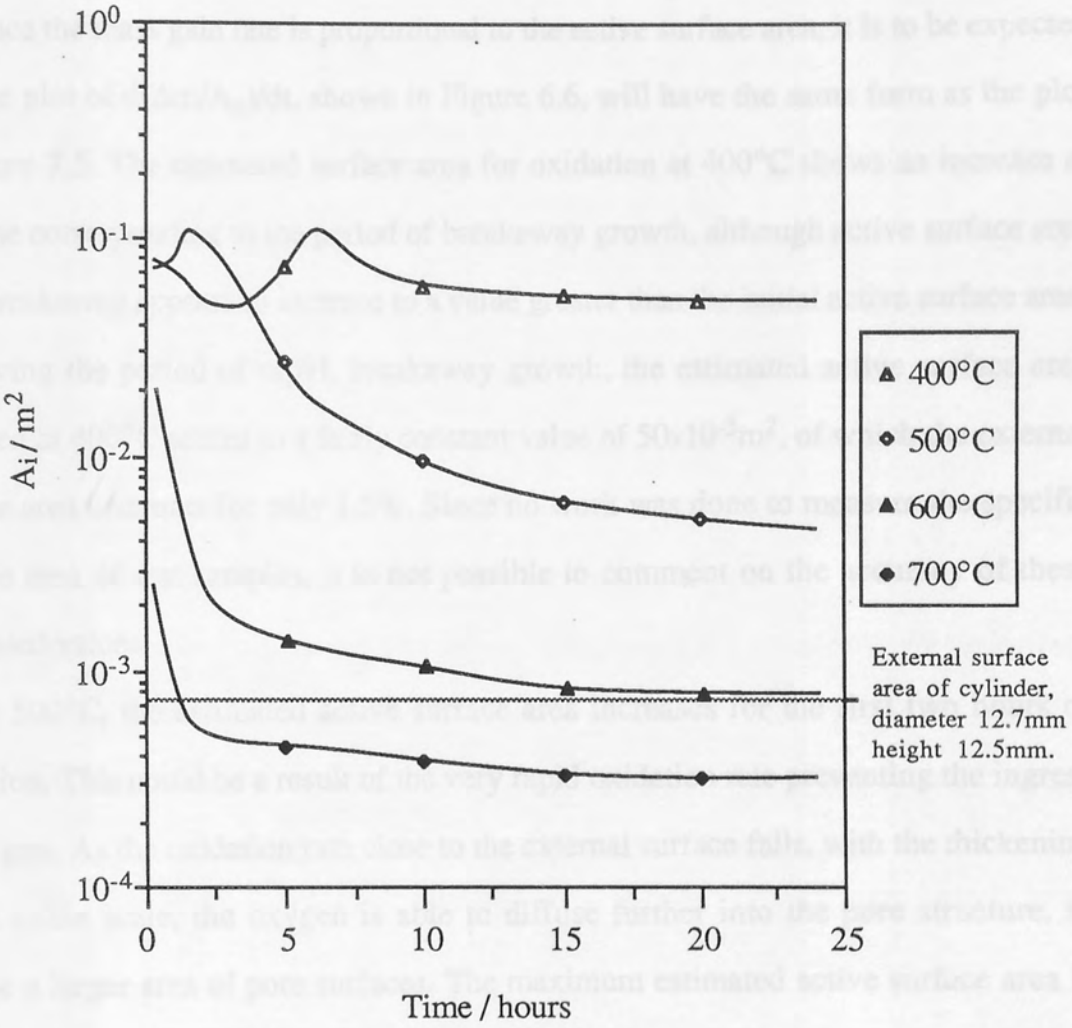

Figure 7.5. Estimated instantaneous active surface area of ASC100.29 (pure iron), compacted at 350MPa, and oxidised at 400°C to 700°C.

$$A_i = \sqrt{\frac{\Delta m_2^2 - \Delta m_1^2}{k\,(t_2 - t_1)}}$$

mass gain rate is changing rapidly, a large time interval will tend to over-estimate the active surface area at time t_2. The data shown in Figure 7.5 is derived using a time interval (t_2 - t_1) of 30 minutes.

Since the mass gain rate is proportional to the active surface area, it is to be expected that the plot of $d(\Delta m/A_0)/dt$, shown in Figure 6.6, will have the same form as the plot in Figure 7.5. The estimated surface area for oxidation at 400°C shows an increase at the time corresponding to the period of breakaway growth, although active surface area after breakaway appears to increase to a value greater than the initial active surface area. Following the period of rapid, breakaway growth, the estimated active surface area oxidised at 400°C settles to a fairly constant value of $50x10^{-3}m^2$, of which the external surface area accounts for only 1.5%. Since no work was done to measure the specific surface area of test samples, it is not possible to comment on the accuracy of these calculated values.

At 500°C, the estimated active surface area increases for the first two hours of oxidation. This could be a result of the very rapid oxidation rate preventing the ingress of oxygen. As the oxidation rate close to the external surface falls, with the thickening of the oxide scale, the oxygen is able to diffuse further into the pore structure, to oxidise a larger area of pore surfaces. The maximum estimated active surface area is about the same as for the sample oxidised at 400°C.

Interestingly, the estimated active surface area, at 500°C, remains large throughout the test period, with a final value of about $4x10^{-3}m^2$, of which the external surface area accounts for 20%. This is despite the calculations for pore closure indicating that, after 24 hours, the surface porosity had been sealed for some time. The measured thickness of this scale (Table 6.12) was 7μm. Oxidation at 600°C, to produce a two layer scale of Fe_3O_4 and Fe_2O_3 with a thickness of 28μm, produced a final estimated active surface area very close to the external surface area of the cylinder. Hence there may be some relationship between the thickness of the external scale and the sample mass gain rate. The two-layer scale produced at 500°C may have been thin enough to be permeable,

allowing the ingress of gaseous oxygen to the internal porosity. At 600°C, the two-layer scale was either impermeable, or the transport pathways through the scale were too long for an appreciable amount of gaseous oxygen to diffuse through.

Oxidation at 700°C produces a very rapid reduction in the estimated active surface area, to a value less than the external surface area of the cylindrical sample. This is probably due to the growth of the wüstite scale around the sample platform in the thermobalance furnace. (The same effect would probably be found for the active surface area of samples that were oxidised at 600°C, and produced a three layer scale with wüstite.) The calculations for pore closure at 700°C indicate that the surface should have been sealed against the ingress of oxygen within a matter of minutes after the start of the test. The relatively high estimate of the initial active surface area may be due to the thin oxide scale formed at this time being permeable, or porous.

One factor that has not been taken into account is surface geometry. As previously discussed (and assumed for calculations), published theories relate to the oxidation of infinite plane surfaces. The surface of a PM body is very complex and convoluted, and this has (as yet) an unquantifiable effect on the growth of an oxide scale.

7.3.4 Modelling the Oxidation of PM Iron

The preceding sections have discussed many of the factors affecting the oxidation of PM iron. Much seems to rest on the permeability of the pore structure. At any given time, this determines the oxygen flux into the porosity, which in turn determines the partial pressure of oxygen. This could then be used to determine the rate of oxidation and the active surface area. (In turn, these two factors will enable the magnitude of the heat of oxidation to be determined, and its effects on the early stages of oxidation gauged.)

Thus, for a particular instant in time, knowledge of the permeability might enable the oxidation rate for any given surface in the pore structure to be estimated. However, firstly the limitations of compaction produce a non-uniform permeability, and this will

be exacerbated by the non-uniform growth of oxide on pore surfaces, due to variations in p_{O_2}.

Assuming that all of the factors affecting oxidation could be modelled mathematically, the final equation would be excessively complex. A more realistic approach would be a probabilistic relationship between time and mass gain, for a given ambient temperature, atmosphere and initial permeability. This would require an accumulation of data for statistical analysis, which has not been attempted in the present work.

7.4 OXIDATION OF PM IRON ALLOYS

7.4.1 Aluminium Addition

Initial attempts at sintering elementally mixed Fe, 1.0Al compacts resulted in small spots of oxide on the sample surfaces, indicating the oxidation of the aluminium powder particles *in situ*. The formation of these oxide particles appeared to be prevented by maintaining a good vacuum in the furnace until it had cooled below 50°C. However, similar spots then appeared on samples when they were oxidised at 500°C. The spots, presumably Al_2O_3, were light grey, and stood proud of the surrounding dark grey iron oxide scale.

At the sintering temperature, 1120°C, the dissociation partial pressure of Al_2O_3 is less than 10^{-27}Pa, compared with a p_{O_2} of about 4×10^{-3}Pa in the furnace vacuum [180]. It seems probable that, even though the aluminium was superheated by nearly 500°C above its melting point at the sintering temperature, the strength of the aluminium oxide skin covering the molten metal was sufficient to prevent wetting of the iron surface. The intimate contact between the droplets of molten aluminium and the iron particles allowed some limited diffusion alloying. Quantitative X-ray analysis indicated that the Al content of the iron was 0.1%, suggesting that 90% of the total addition remained segregated after sintering. The minimum aluminium content required to reduce the oxidation rate of the iron is 0.1% [14] and the PM alloy did have a reduced mass gain rate, compared

with the unalloyed, pure PM iron. However, observations show that most of the elemental aluminium addition remained segregated, and did not contribute to protecting the iron against oxidation. Therefore, although larger additions of aluminium might have increased the oxidation resistance of the iron, it probably would have been at the expense of forming a greater number of non-contributing, second phase particles.

7.4.2 Silicon Addition

7.4.2.1 Sintering of PM Fe-Si Alloys

The iron-silicon system (Figure 3.15) does not produce any liquid phases at the sintering temperature, 1120°C, at equilibrium. A silicon concentration of 1.9% or more in the iron will stabilise α-Fe above this temperature. Diffusion is more rapid in the relatively open body-centred cubic structure of α-Fe, than in the more densely packed face-centred cubic structure of γ-Fe. Thus the stabilisation of α-Fe, relative to γ-Fe, at the sintering temperature, will accelerate sintering mechanisms, promoting pore rounding and densification [153 - 155]. Since sintering tends to isolate pores, and reduce the amount of interconnected porosity, stabilisation of the α-Fe phase at the sintering temperature should reduce the mass gain of PM alloys during oxidation.

For the Fe 1.0Si alloy, this effect was probably confined to the outer layers of iron particles during the early stages of sintering, since homogenisation would have reduced the silicon content below the 1.9% level very quickly. The TMA record (Figure B.3, Appendix B) shows that this alloy shrank by only 0.5%, and that shrinkage had more or less ceased by the end of the sintering period. Therefore, in the early stages of sintering, diffusion alloying would have prevented the outer layers of iron particles from undergoing the α-Fe→γ-Fe transformation, promoting some pore rounding and shrinkage. As diffusion alloying progressed, and the silicon concentration at the iron particle surfaces was reduced, allowing the progressive completion of the α-Fe→γ-Fe transformation. Fe 1.0Si samples underwent the γ-Fe→α-Fe transformation during the cooling phase of the sintering cycle.

The Fe 3.0Si alloy exhibited considerable shrinkage (Figure B.4, Appendix B). The

dimensional change due to the α-Fe→γ-Fe transformation, during the heating phase of the sintering cycle, is of the same magnitude as that exhibited by the Fe 1.0Si alloy (Figure B.3, Appendix B). This suggests that the initial rate of dissolution of the silicon in the iron was the same for both alloys, which is commensurate with diffusion driven by a very steep (initially infinite) concentration gradient. However, unlike the Fe 1.0Si alloy, diffusion alloying in the Fe 3.0Si alloy caused a progressive, and complete reversal of the α-Fe→γ-Fe transformation, of the austenitic cores of iron particles. The γ-Fe→α-Fe transformation was not observed during the cooling phase of the sintering cycle, indicating that the progressive transformation was completed during sintering.

7.4.2.2 Oxidation of PM Fe-Si Alloys

An addition of silicon as small as 0.1wt% was enough to significantly reduce the initial oxidation rate of the pure iron (Figure A.12, Appendix A), but appears, in the long term, only to delay the formation of the same mass of oxide as was formed on pure iron compacts. The reduction in the oxidation rate is caused by the formation of SiO_2 particles, which inhibit the outward migration of iron ions through the oxide scale. The effectiveness of the SiO_2 particles, in reducing the oxidation rate, decreases as they are engulfed by the oxide [5]. The 0.1%Si addition did not reduce the eventual oxidation mass gain of samples, because the concentration of silicon was insufficient to cause appreciable densification during sintering. Thus the permeability of the Fe 0.1Si compacts was probably much the same as for those of pure Fe, and initial differences in surface chemistry during oxidation were quickly overcome by the growth of the oxide scale.

The addition of 1% Si or 3% Si to the pure iron powder caused a considerable reduction in the oxidation rate of the pure iron, so that the heat of reaction in the early stages of oxidation is almost negligible (see Figure C.2, Appendix C). These two alloys fall one on either side of the minimum silicon content, of 2.6% to 3.0% [50, 133], required for the formation of a protective layer of SiO_2, although this compound was

not detected by XRD tests on oxide scales. If densification during sintering can be used as a guide to the reduction of interconnected porosity, then the Fe 3.0Si alloy samples would be expected to have the best oxidation resistance by far. In fact, the extra 2% silicon in the Fe 3.0Si alloy apparently gave only a small improvement over the Fe 1.0Si alloy, and at the expense of much poorer compressibility and considerable dimensional instability during sintering.

The microstructure of the oxide formed on the Fe 1.0Si alloy was thick enough to be resolved into magnetite and haematite layers with a microscope. Furthermore, the oxide scale, although of variable thickness, was enough to block some pores. The oxide film on the Fe 3.0Si alloy was too thin to be detected in the sample microstructure.

The similarity in mass gains of the different alloys can therefore be explained in terms of different active surface areas, affected by different oxidation rates. The surface area of interconnected porosity in the PM Fe 1.0Si alloy is reduced, relative to that of PM pure iron, during sintering, by pore rounding. During oxidation, therefore, the active surface area of porosity in the Fe 1.0Si alloy is less than that for pure Fe. The formation of SiO_2 particles at the metal/oxide interface reduces the oxidation rate, so that the overall mass gain rate of a sample is reduced. However, a fairly thick oxide scale is still formed, and this is sufficient to block some of the capillaries, reducing the amount of porosity interconnected to the external atmosphere, further reducing the mass gain rate for samples.

The PM Fe 3.0Si alloy undergoes considerable densification during sintering, greatly reducing the surface area of interconnected porosity exposed during oxidation, compared with the Fe 1.0Si alloy. However, the formation of a very thin, protective layer of SiO_2 during oxidation prevents the rapid growth of iron oxide in surface porosity. This prevents the isolation of interconnected porosity, so that the active surface area is not reduced appreciably during oxidation, as occurs with the Fe 1.0Si alloy. Thus, even though the oxide film formed on the PM Fe 3.0Si alloy is very thin,

relative to the scale formed on the Fe 1.0Si alloy, it forms over a much greater area. Hence the total mass of oxide formed on a Fe 3.0Si alloy sample is similar to the mass of oxide formed on an Fe 1.0Si alloy sample.

The effects of the 1%Si addition on the mass gain of samples at different temperatures is shown in Figure A.14, Appendix A. For the temperature range studied (400°C to 600°C), an unusual relationship occurs, in that, as the oxidation temperature increases, the mass gain of the sample decreases (for pure iron, the mass gain rises to a peak at about 500°C). This is probably be due to the increase of the oxidation rate with increasing temperature affecting the rate of pore closure in samples. That is, at 400°C the rate of thickening of the oxide scale is relatively slow, so that the active surface area is large. At 500°C, there is an intermediate rate of pore closure, whilst at 600°C the rate is high, so that the active surface area is relatively small.

7.4.3 Iron-Phosphorous Alloys

7.4.3.1 Sintering of PM Fe-P Alloys

The iron-phosphorus system (Figure 3.14) has a low melting point eutectic, (Fe + Fe_3P), at 1050°C and 10.1wt%P. Phosphorus stabilises ferrite, relative to austenite, so that diffusion alloying, of the segregated iron and ferro-phosphorus powder particles in the green compact, will cause the iron particles to undergo the γ-Fe$\rightarrow\alpha$-Fe transformation whilst at the sintering temperature. As with the PM Fe-Si alloys, this transformation will start at the surface of an iron particle, and progress inwards with the diffusion of alloying element towards the particle core. Rapid self-diffusion of iron in ferrite (relative to self-diffusion in austenite) will accelerate sintering mechanisms, promoting pore rounding and densification [153 - 155].

The TMA record (Figure B.5, Appendix B) shows that the PNC60 sample had started to shrink whilst the furnace temperature was still below 800°C, indicating that it can sinter at temperatures much lower than the one used for experimental work (1120°C). The equilibrium phase diagram (Figure 3.14) shows that the phosphorus content required to stabilise α-Fe relative to γ-Fe is about 0.65% at the sintering

temperature, slightly more than that of PNC60 (Fe, 0.60P). The presence of the α-Fe→γ-Fe transformation indicates that the alloy did not become fully homogenised during the heating phase of the sintering cycle. Homogenisation during the sintering period should have caused the phosphorus-stabilised ferrite to undergo the α-Fe→γ-Fe transformation, as the phosphorus content in segregated layers of iron particles fell below the 0.65% level. Although this transformation would have been progressive (ie. it would have occurred over a period of time, and the associated lattice contraction would have been obscured by the sintering shrinkage), the reverse transformation, γ-Fe→α-Fe, was not observed during cooling. This suggests that complete homogenisation did not occur, although the volume of austenite, remaining at the end of the sintering period, must have been too small to cause a discernible expansion when it transformed to ferrite, during cooling. Incomplete homogenisation may have been due to the concentration gradient, of phosphorus in iron particles, falling below some critical level for diffusion alloying

The onset of densification below 800°C in the PNC60 may, in part, be due to its sponge iron powder base (Höganäs NC100.24). This has an irregular particle shape, which is associated with a high surface energy, and this would be used in the activation of sintering mechanisms. The phosphorus content of PNC60 occurs in the form of an admixed Fe_3P powder. In view of this, it seems unlikely that the phosphorus content would be ever sufficiently segregated for the formation of a liquid phase composed of the (Fe + Fe_3P) eutectic.

7.4.3.2 Oxidation of PM Fe-P Alloys

The TCA record for PNC60 (Figure C.4, Appendix C) shows that the heat of reaction, at the start of oxidation, raised the temperature of the sample core above the equilibrium formation temperature for wüstite. Other results for this present work (see Section 7.2.5) indicate that this will cause the formation of wüstite, which transforms into magnetite as the sample core temperature falls below 570°C, causing a second

period of superheating. However, a second period of superheating was not observed for the Fe-P sample, suggesting that phosphorus may inhibit the formation of wüstite.

The core of the PNC60 sample was superheated by nearly 50°C above the furnace temperature, a figure comparable to that of a similar compact of pure iron. This implies similar surface areas of porosity, even though the PNC60 underwent greater densification than the ASC100.29 during sintering. This is possibly due to the more irregular particle shape of the sponge iron powder used to make the PNC60, compared with the atomised pure iron. These irregularities in particle surfaces are small, and would be rapidly filled with oxide, thereby reducing the active surface area of porosity.

Plates 6.9 and 6.17 (pure Fe, and Fe 0.6P, respectively, compacted at 350MPa, and oxidised at 500°C), show that the pure Fe and Fe-P alloy compacts have comparable thicknesses of oxide scale on their external surfaces. The oxidation of these alloys is therefore similar (allowing that there may be a difference due to the purities of the NC100.24, in the PNC60 powder, and the ASC100.29 iron powders), so it can be confirmed that the phosphorus addition does not increase the oxidation resistance of iron. The reduced oxidation mass gain observed for Fe-P compacts, compared with the pure Fe compacts, is therefore due to the reduced active surface area caused by pore rounding and densification during sintering.

7.4.4.3 Fe-P-Si Alloys

Additions of 1%Si and 3% Si were made to the PNC60, to ascertain whether the oxidation resistance of PNC60 could be improved. The TCA records show that the sintering shrinkages of the Fe-P-Si alloys were greater than that of plain PNC60, and are approximately equal to the sum of the shrinkages of the Fe-P alloy and the respective Fe-Si alloys. That is, by adding the shrinkage of the Fe 1.0Si alloy (-0.5%) to that of the PNC60 (-4.0%), one arrives at an approximation of the shrinkage of the Fe 0.6P 1.0Si alloy (-5.0%). Similarly, for the Fe 0.6P 3.0Si,

$$\Delta h/h_0 = -8.0\% \approx -4.5\% \ (\Delta h/h_{0,\ Fe\ 3.0Si}) + -4.0\% \ (\Delta h/h_{0,\ PNC60})$$

Thus it appears that the contributions of silicon and phosphorus to accelerating sintering mechanisms may be substitutional (ie. 0.6% silicon could have much the same effect as 0.6% phosphorus).

The 1%Si addition reduced the mass gain rate, compared to that for plain PNC60, during the first three hours of TGA tests. This was probably due to the increased densification caused by the silicon addition. Subsequently, the mass gain rates of the plain Fe 0.6P, and Fe 0.6P 1.0Si alloys were similar, but because of the initial effect, the overall mass gain of the Fe-P-Si alloy was less than that of the Fe-P alloy.

The 3% silicon addition reduced the oxidation rate of the PNC60 by a considerable amount, but the overall mass gain indicates that the active surface area remained high and that pore closure by oxide growth did not occur. The formation of an oxidation resistant layer of SiO_2 appears, therefore, to be unaffected by the presence of phosphorus, and the XRD tests did not reveal any intermetallic phases, such as SiP.

The heats of reaction during the early stages of oxidation (Figure C.4, Appendix C) of Fe-P-Si compacts is large, compared with those of the Fe-Si alloys. However, since it appears that the silicon and phosphorus did not interact, this effect is probably due to the relatively large surface area of the sponge iron particles in the powder.

7.4.4 Copper Addition

The Fe-Cu alloy was not tested in TMA experiments, since other workers have published extensively on the subject (eg. [150 - 153]). Mass transport mechanisms in sintering are accelerated by the presence of liquid copper above 1085°C. The extent of the liquid phase's effects depend on the rate of dissolution of the copper into the iron. Additions of 4%Cu or more will cause a permanent expansion of PM iron, due to the penetration of interparticle and grain boundaries by liquid copper.

The addition of copper to ASC100.29 produced a slight reduction in the mass gain of samples during oxidation, relative to the pure iron. Copper does not play a direct role

in the oxidation reaction [11], but the pore rounding it causes as a liquid phase during sintering will reduce the surface area of porosity in the compact. The oxide scales produced by the pure Fe, and Fe 1.0Cu (Plates 6.7 and 6.23 respectively) were of similar thickness, indicating that the oxidation rates of the two powders were basically the same. There is a small area of the scale on the alloy, that has become detached (Plate 6.23), exposing the iron substrate, probably caused by cooling stresses. This spalling was not observed on pure iron compacts, so it is possible that the copper reduces scale adhesion.

The additions of copper to Fe-Si, Fe-P and Fe-P-Si alloys were intended as the next stage of the development of the alloys. The purpose was to ascertain whether the shrinkage caused by phosphorus and silicon could be reduced, without affecting the oxidation resistance of the alloys.

The addition of 1.0wt%Cu to PNC60 did not greatly alter its overall mass gain during oxidation (Figure 6.9), but did produce an unusual oxide morphology (Plate 6.24). It would appear that the phosphorus prevented the wetting of the iron surface by the liquid copper, which consequently formed spherical droplets. These droplets were then engulfed by the growth of oxide scale, to give the morphology seen in Plate 6.24. Despite the reduced wettability, the SEM analysis of the alloy indicates that diffusion alloying did occur. It appears that the addition of silicon, to make Fe 0.6P 1.0Cu 1.0Si, prevents this non-wetting.

7.5 COMMERCIAL APPLICATION OF RESULTS

The original inspiration for this work came from the development of a domestic electric hot plate, manufactured by the compaction of iron powder (Introduction, Section 1). The compaction process is a novel technique that incorporates a spiral electric heating element, embedded in the iron powder mass, in a near net-shape compact.

It is therefore appropriate to review how the results may be applied to this commercial process. The present work indicates that there a two approaches to reducing

the oxidation of PM iron by elemental alloying.

The first relies on the closure of pores by oxide growth, to isolate porosity, thereby reducing the mass gain rate to a negligible level. This can be achieved by the oxidation of pure iron at 500°C and above. However, the overall mass gain can be greatly reduced by the addition of elements that promote pore rounding during sintering, producing alloys such as Fe 1.0Si (ASC100.29 + 1.0wt%Si) and Fe 0.6P (PNC60). The disadvantage of this approach is the formation of a thick oxide scale, which may spall during the cyclic oxidation expected of service conditions.

The second approach is to add an adequate amount of an element that increases the oxidation resistance of iron, such as 3wt % Si to ASC100.29 (the Fe 1.0Al alloy can be ruled out on the grounds of its poor aesthetic qualities).This leads to the formation of an oxide film with a very low, or negligible growth rate. Oxidation during service does not cause a reduction of the active surface area by the pore closure mechanism. The growth of a thin oxide film on a large surface (as with the Fe 3.0Si alloy) may produce a similar mass gain to the growth of a thick oxide film on a small surface area (as with the Fe 1.0Si alloy). However, a thin oxide film may be more resistant to cyclic oxidation.

The incorporation of an electric heating element in the hot plate compact requires good compressibility of the powder, and a degree of dimensional stability during sintering. Although the Fe 3.0Si alloy is the most promising alloy from the point of view of oxidation resistance, the silicon addition reduces the compressibility of the base iron powder, and causes considerable shrinkage during sintering. On this basis, the PNC60 powder, and the alloys based on it, can also be ruled out. It is possible that suitable additions of copper could offset the sintering shrinkage caused by silicon or phosphorus. Copper alone does not greatly increase the oxidation resistance of iron.

From consideration of the powder compressibility, dimensional stability during sintering, and oxidation resistance during service, it is apparent that, on the basis of the present work, the most suitable materials for the PM hot plate are pure iron (plain ASC100.29), and Fe 1.0Si (ASC100.29 + 1wt% Si).

However, it must be borne in mind that the experimental samples were sintered in a vacuum. Commercial furnace atmospheres, using 'exo' gas (partially combusted natural gas), 'endo' gas (cracked natural gas), or cracked ammonia, all contain some traces of water vapour. The silicon content of an alloy powder would be substantially reduced by the reaction with oxygen in the water vapour, yielding SiO_2.

Finally, this work has only considered the growth of oxide during a single, specified time period. For example, the effects of cyclic oxidation should also be studied to determine the effects of thermal stresses on the oxide scale.

Section 8
CONCLUSIONS

1. The adsorption of oxygen by pore surfaces creates an oxygen partial pressure gradient between the external atmosphere and the porosity, causing the diffusion of gaseous oxygen into the pores. The flux of oxygen that can diffuse through the pore structure is limited by the permeability of the porosity, which in turn is affected by the growth of the oxide scale on pore surfaces.

2. The interdependence of the permeability of the pore structure, and the oxidation rate of the pore surfaces, can result in the core porosity of PM iron compacts remaining unoxidised, even if it is interconnected with the external atmosphere. Thus the active surface area of porosity may be less than the total surface area of porosity interconnected with the external surface.

3. As a consequence of conclusions 1 and 2, it is not practical to quantify the oxidation of PM iron in terms of a kinetic law. At best, by careful control of experimental variables, results may be considered on a comparative basis.

4. Below the equilibrium temperature for the formation of wüstite ('FeO'), the oxidation of PM iron can extend beyond the external surface of the compact, to the surfaces of pores interconnected with the external atmosphere. Consequently, the oxidation mass gain of PM iron, per unit external surface area, is much greater than that of non-porous wrought iron, for the same experimental conditions.

5. Above the equilibrium temperature for the formation of wüstite ('FeO'), the rapid growth of oxide scale over the external surface of PM iron seals capillaries interconnected with internal porosity, preventing the oxidation of pore surfaces. Consequently, the oxidation mass gain of PM iron, per unit external surface area, is similar to that of non-porous wrought iron, for the same experimental

conditions.

6. The adhesion of an oxide scale to a PM iron surface increases with increasing porosity in the compact, due to the vacancy gradient mechanism [33 - 34]. This confirms H. E. Evans proposal [31] that scale adhesion is dependent on the concentration of vacancy sinks. Magnetite-haematite oxide scales tend to be more adherent than wüstite-magnetite-haematite oxide scales

7. During vacuum sintering in air at a pressure of 20mPa, elemental powder additions of aluminium remain segregated in a pure iron powder matrix, because of an Al_2O_3 skin, which prevents the molten aluminium wetting the surfaces of the iron particles.

8. Elemental powder additions of silicon will alloy, by diffusion, with a pure iron powder matrix, during vacuum sintering in air at a pressure of 20mPa.

9. The oxidation mass gain of PM iron is reduced by the addition of elements that cause pore rounding and isolation during sintering, thereby reducing the active surface area of the compact, such as phosphorus and silicon. The reduced mass gain is not necessarily indicative that the homogeneous PM alloy has any greater oxidation resistance than the base iron powder.

10. A vacuum sintered, elemental powder addition of 3.0wt% Si to pure iron powder is sufficient to form a thin, semi-protective oxide scale during oxidation. The slow growth of this scale retards pore closure during oxidation.

11. The growth of a thick oxide scale over a decreasing surface area can result in a similar sample mass gain to that of a thin oxide film growing over a constant surface area (eg. as with Fe, 1.0wt% Si and Fe, 3.0wt% Si). The thermo-gravimetric study of the oxidation of PM iron alloys therefore must be supplemented by metallography, to differentiate between the two cases.

REFERENCES

1. "Advances in Powder Metallurgy", ed. T. G. Gasbarre and W. F. Jandeska, publ. Metal Powder Industries Federation, Princeton, NJ (1989).
2. "Science Data Book", 9th impression, ed. R. M. Tennent, publ. Oliver and Boyd, Edinburgh (1984).
3. J. Oudar, "Physics and Chemistry of Surfaces", publ. Blackie, Glasgow (1975).
4. P. Kofstad, "High Temperature Oxidation of Metals", publ. John Wiley and Sons, New York, NY (1966).
5. N. Birks and G. H. Meier, "Introduction to the High Temperature Oxidation of Metals", publ. Edward Arnold, London (1983).
6. G. R. Wallwork, "The oxidation of alloys", Rep. Prog. Phys. **39**: 401 - 485 (1976).
7. J. Bénard, "Adsorption of oxidant and oxide nucleation", in "Oxidation of Metals and Alloys: Papers Presented at a Seminar of the ASM (Oct 1970)", publ. ASM, Ohio (1971).
8. K. R. Lawless, "The oxidation of metals", Rep. Prog. Phys. **37**: 231 - 316 (1974).
9. F. P. Fehlner and N. F. Mott, "Oxidation in the thin film range", in "Oxidation of Metals and Alloys: Papers presented at a seminar of the ASM (Oct 1970)", publ. ASM, Ohio (1971).
10. R. E. Reed-Hill, "Physical Metallurgy Principles", 2nd edition, publ. D. Van Nostrand Co., New York (1973).
11. O. Kubachewski and B. E. Hopkins, "Oxidation of Alloys and Metals", publ. Butterworth, London (1963).
12. A. Atkinson, "Transport processes during the growth of oxide films at elevated temperatures", Rev. Mod. Phys. **57** (2): 437 - 470 (1985).
13. N. Cabrera and N. F. Mott, "Theory of oxidation of metals", Rep. Progr. Phys. **21**: 163 - 184 (1949).
14. U. R. Evans, "Corrosion and oxidation of metals", publ. Edward Arnold, London (1960);"Corrosion and oxidation of metals. Supplementary Volume 1", publ. Edward Arnold, London (1968);"Corrosion and oxidation of metals. Supplementary Volume 2", publ. Edward Arnold, London (1976).
15. C. Wagner, "Beitag zur theorie des anlaufvorgangs", Z. physikal Chem. **B21**: 25 - 41 (1933).
16. F. Gesmundo and F. Viani, "The formation of multilayer scales in the

parabolic oxidation of pure metals", Corros. Sci. **18**: 217 - 243 (1978); "Correction to paper", Corros. Sci. **19**: 437 (1979).

17. K. A. Hay and K. H. Jolliffe, "The kinetics of reduction in a two-layer oxide scale", Corros. Sci. **12**: 661 - 667 (1972).
18. C. I. Howe, B. McEnaney and V. D. Scott, "A new kinetic model for the nucleation and growth of duplex oxide scales on iron between 350 and 500°C", Corros. Sci. **25** (3): 195 - 207 (1985).
19. R. D. Shaw and R. Rolls, "The calculation of relative layer thicknesses in a two-component scale", Corros. Sci. **14**: 443 - 450 (1974).
20. G. J. Yurek, J. P. Hirth and R. A. Rapp, "The formation of two phase layered scales on pure metals", Oxid. Met. **8** (5): 265 - 281 (1974).
21. D. L. Douglass, "Exfoliation and the mechanical behavior of scales", in "Oxidation of metals and alloys: Papers presented at a seminar of the ASM (Oct 1970)", publ. ASM, Ohio (1971).
22. N. B. Pilling and R. E. Bedworth, "The oxidation of metals at high temperatures", J. I. Metals **29**: 529 - 591 (1923).
23. A. M. Huntz, "Scale growth and stress development", Mater. Sci. Technol. **4**: 1079 - 1088 (1988).
24. J. Stringer, "Stress generation and relief in growing oxide films", Corros. Sci. **1**: 513 - 543 (1970).
25. F. N. Rhines and J. S. Wolf, "The role of oxide microstructure and growth stresses in the high temperature scaling of nickel", Metall. Trans. **1**: 1701 - 1710 (1970).
26. M. V. Speight and J. E. Haris, "The generation of stresses in oxide films growing by cation diffusion", Acta Met. **26**: 1043 - 1045 (1978).
27. S. Taniguchi, "Stress developed during the oxidation of metals and alloys", Trans. Iron St. Inst. Jpn. **25**: 3 - 13 (1985).
28. U. R. Evans, "The mechanism of oxidation and tarnishing", Trans. Electrochem. Soc. **91**: 547 - 570 (1947).
29. J. M. Hulley and R. Rolls, "High temperature cohesion and adhesion of oxide scales on mild steel", J. I. S. I. **208**: 1029 - 1030 (1970).
30. G. B. Gibbs and R. Hales, "The influence of metal lattice vacancies on the oxidation of high temperature materials", Corros. Sci. **17**: 487 - 507 (1977).
31. H. E. Evans, "Cavity formation and metallurgical changes induced by growth of oxide scale", Mater. Sci. Technol. **4**: 1089 - 1098 (1988).
32. D. Caplan and M. Cohen, "Effect of cold work on the oxidation of iron from 400 - 650°C", Corros. Sci. **6**: 321 - 335 (1966).
33. B. W. Dunnington, F. H. Beck and M. G. Fontana, "The mechanism of scale

formation on iron at high temperature", Corrosion **8**: 2t - 13t (1952).

34. R. F. Tylecote and T. E. Mitchell, "Marker movements in the oxidation of iron and some other metals", J. I. S. I.: 445 - 453 (1960).
35. J. E. Harris, "Vacancy injection during oxidation - a re-examination of the evidence", Acta Met. **26**: 1033 - 1041 (1978).
36. Y. Shida, G. C. Wood, F. H. Stott, D. P. Whittle and B. D. Bastow, "Intergranular oxidation and internal void formation in Ni - 40% Cr alloys", Corros. Sci. **21** (8): 581 - 597 (1981).
37. D. W. Juenker, R. A. Meussner and C. E. Birchenall, "Cavity formation in iron oxide", Corrosion **14**: 39 - 46 (1958).
38. L. B. Pfeil, "The oxidation of iron and steel at high temperatures", J. I. S. I. **119**: 501 - 560 (1929).
39. S. Mrowec, "On the mechanism of high temperature oxidation of metals and alloys", Corros. Sci. **7**: 563 - 578 (1967).
40. A. Brückman, R. Emmerich and S. Mrowec, "Investigation of the high temperature oxidation of Fe-Cr alloys by means of the isotope ^{18}O", Oxid. Met. **5** (2): 137 - 147 (1972).
41. A . Atkinson, "Wagner theory and short circuit diffussion", Mater. Sci. Technol. **4**: 1046 - 1051 (1988).
42. A. Atkinson and D. W. Smart, "Transport of nickel and oxygen during the oxidation of nickel and dilute nickel alloys", J. Electrochem. Soc. **135** (11): 2886 - 2893 (1988).
43. W. W. Smeltzer, "Transport properties and defect structures of oxide scales", in "Oxidation of Metals and Alloys: Papers Presented at a Seminar of the ASM (Oct 1970)", publ. ASM, Ohio (1971).
44. J. Romanski, "Geometrical factors in studies of the oxidation of metals at high temperatures", Corros. Sci. **8**: 67 - 102 (1968).
45. P. Hancock and R. C. Hurst, "The mechanical properties and breakdown of surface oxide films at elevated temperatures", in "Advances in Corrosion Science and Technology", vol. 4, ed. M. G. Fontana and R. W. Staehle, publ. Plenum Press, New York, NY: 1 - 84 (1970).
46. M. I. Manning, "Geometrical effects on oxide scale integrity", Corros. Sci. **21** (4): 301 - 316 (1981).
47. N. Birks, G. H. Meier and F. S. Petit, "High temperature corrosion resistance", J. Metals, **39**(12): 28 - 31 (1987).
48. R. A. Rapp, "Kinetics, microstructures and mechanism of internal oxidation - its effect and prevention in high temperature alloy oxidation", Corrosion **21**: 382 - 401 (1965).

49. C. Wagner, "Formation of composite scales consisting of oxides of different metals", J. Electrochem. Soc. **103** (11): 627 - 633 (1956).
50. A. Atkinson, "A theoretical analysis of the oxidation of Fe-Si alloys", Corros. Sci. **22** (2): 87 - 102 (1982).
51. C. Wagner, "The distribution of cations in metal oxide and metal sulphide solutions formed during the oxidation of steel", Corros. Sci. **9**: 91 - 109 (1969).
52. M. H. Davies, M. T. Simnad and C. E. Birchenall, "On the mechanism and kinetics of the scaling of iron", Trans. A. I. M. E. **191**: 889 - 896 (1951).
53. L. Himmel, R. F. Mehl and C. E. Birchenall, "Self diffusion of iron in iron oxides and the Wagner theory of oxidation", J. Metals **5**: 827 - 843 (1953).
54. L. S. Darken and R. W. Gurry, "The iron - oxygen system", J. Amer. Chem. Soc. **67**: 1398 - 1412 (1945); *ibid.* **68**: 798 - 816 (1946).
55. E. R. Jette and F. Foote, "A study of the homogeneity limits of wüstite (FeO) by x-ray methods", Trans. A. I. M. E. **105**: 276 - 289 (1933).
56. L. B. Pfeil, "The constitution of scale", J. I. S. I. **131**: 237 - 255 (1931).
57. J. Bénard, "Recherches sur les variations de composition du protoxyde de fer", Bull. Soc. Chim. France **16**: D109 - 116 (1949).
58. V. J. Linnenbom, "The reaction between iron and water in the absence of oxygen", J. Electrochem. Soc. **105** (6): 322 - 324 (1958).
59. R. F. Mehl, "Oxide films on iron", Trans. A. I. M. E. **125**: 531 - 553 (1937).
60. D. Caplan, R. J. Hussey, G. I. Sproule and M. J. Graham, "The effect of FeO grain size on the oxidation of Fe", Corros. Sci. **21** (9): 689 - 711 (1981).
61. D. Caplan and M. Cohen, "Scaling of iron at 500°C", Corros. Sci. **3**: 139 - 143 (1963).
62. R. J. Hussey and M. J. Graham, "Some observations on void formation in Fe_3O_4 layers on Fe", Corros. Sci. **21** (8): 255 - 258 (1981).
63. K. Sachs and G. T. F. Jay, "A magnetite seam at the scale/metal interface on mild steel", J. I. S. I.: 180 - 189 (1960).
64. D. Bruce and P. Hancock, "Note on the temperature stability of wüstite in surface oxide films on iron", Br. Corros. J. **4**: 221 - 222 (1969).
65. G. Garnaud and R. A. Rapp, "Thickness of the oxide layers formed during the oxidation of iron", Oxid. Met. **11** (4): 193 - 198 (1977).
66. G. Valensi, Int. Conf. Surf. React.: 156 (1948). Quoted by Kubachewski and Hopkins (p. 137 [11]).
67. W. H. J. Vernon, E. A. Calnan, C. J. B. Clews and T. J. Nurse, "The oxidation of iron around 200°C", Proc. Royal Soc. (A) **216**: 375 - 397

(1952).

68. G. W. Simmons, E. Kellerman and H. Leidheiser, "The oxidation of iron as studied by conversion electron Mössbauer spectroscopy", Corrosion **29** (6): 227 - (1973).
69. A. B. Winterbottom, "Optical studies of the oxidation of iron at temperatures in the range 20 - 265°C", J. I. S. I. **31**: 9 - 22 (1950).
70. D. E. Davies, U. R. Evans and J. N. Agar, "The oxidation of iron at 175°C to 350°C", Proc. Roy. Soc. (A) **225**: 443 - 462 (1954).
71. Z. Szlarska-Smialowska and J. Jurek, "Ellipsometric studies on iron oxide film growth at 100 to 350°C", Corrosion **32** (7): 294 - 297 (1976).
72. E. A. Gulbransen and J. W. Hickman, "An electron diffraction study of oxide films formed on iron, cobalt, nickel, chromium and copper at high temperatures", Trans. A. I. M. E. **171**: 306 - 331 (1947).
73. P. B. Sewell, C. D. Stockbridge and M. Cohen, "An electrometric and electron diffraction study of air-formed oxide films on iron", J. Electrochem. Soc. **108** (10): 933 - 941 (1961).
74. P. B. Sewell and M. Cohen, "The oxidation of iron single crystals around 200°C", J. Electrochem. Soc. **111** (5): 501 - 508 (1964).
75. K. J. Gallagher, W. Feitknecht and U. Mannweiler, "Mechanism of oxidation of magnetite to γ-Fe_2O_3", Nature **217**: 1118 - 1121 (1968).
76. R. P. Frankenthal, P. C. Milner and D. J. Siconolfi, "Long-term atmospheric oxidation of high purity iron", J. Electrochem. Soc. **132** (5): 1019 - 1021 (1985).
77. M. C. Bloom and L. Goldenberg, "γ-Fe_2O_3 and the passivity of iron", Corros. Sci. **5**: 623 - 630 (1965).
78. J. Kruger and H. T. Yolken, "Room temperature oxidation at low pressures", Corrosion **20**; 29t - 33t (1964).
79. P. B. Needham Jr., H. W. Leavenworth Jr. and T. J. Driscoll, "The kinetics of thin oxide film formation on iron using proton-impact-excited x-ray analysis", J. Electrochem. Soc. **120**: 778 - 783 (1973).
80. Gulbransen, "Thin oxide films on iron", Trans. Electrochem. Soc. **81**, 1942: 327 - 337 (1942).
81. M. J. Graham, S. I. Ali and M. Cohen, J. Electrochem. Soc. **117**(4): 513 - 516 (1970).
82. E. K. Oshe, T. Yu. Zimina and M. N. Fokin, "Defect formation in surface iron oxides during thermal oxidation in air", Protection of Metals **23** (3): 292 - 296 (1987).
83. R. Jackson and A. G. Quarrel, "An electron diffraction study of the oxide

films on iron", in "Second Report of the Alloy Steels Research Committee", Special Report Number 24, pp 65 - 105, publ. Iron and Steel Inst., London (1939).

84. J. Barlow, C. W. Tuck and K. Sachs, "Effect of lime on the transformation of scales during cooling", J. I. S. I. **205**: 45 - 50 (1967).
85. H. J. Goldschmidt, "The crystal structures of Fe, FeO and Fe_3O_4 and their interrelations", J. I. S. I. **146**: 157 - 174 (1942).
86. J. Smuts, "Structure of wüstite and the variation of its x-ray diffraction intensities with composition", J. I. S. I. **204**: 237 - 239 (1966).
87. W. L. Roth, "Defects in the crystal and magnetic structures of ferrous oxide", Acta Cryst. **13**: 140 - 149 (1960).
88. H. -J. Engell, "Der konzentrationsgradient der eisenionen-leerstellen in wüstit-zunderschichten und der mechanismus der oxydation des eisens", Acta Met. **6**: 439 - 445 (1958).
89. R. W. G. Wycoff and E. D. Crittenden, "The preparation and crystal structure of ferrous oxide", J. Am. Chem. Soc. **47**: 2876 - 2882 (1925).
90. W. K. Chen and N. L. Peterson, "Effect of the deviation from stoichiometry on cation self-diffusion and isotope effect in wüstite, $Fe_{1-x}O$", J. Phys. Chem. Solids **36**: 1097 - 1103 (1975).
91. E. R. Jette and F. Foote, "An x-ray study of the wüstite (FeO) solid solutions", J. Phys. Chem. **1**: 29 - 36 (1933).
92. L. W. Pinder, "Lattice parameters of wüstite (FeO) and magnetite (Fe_3O_4) grown on mild steel and low chromium alloy steels as a function of formation temperature", ref. SSD/MID/R45/77, publ. C. E. G. B. Scientific Services Dept., Nottingham (1977).
93. A. Cottrell, "An Introduction to Metallurgy", 2nd edition, publ. Edward Arnold, London (1975).
94. P. Hembree and J. B. Wagner, "The diffusion of Fe_{55} in wüstite as a function of composition at 1100°C", Trans. A. I. M. E. **245**: 1547 - 1552 (1969).
95. F. Viani and F. Gesmundo, "The relationship between the different rate constants and the diffusion properties of the oxides in the parabolic oxidation of a metal or a lower oxide to multilayer scales - application to the oxidation of iron", Corros. Sci. **20**; 541 - 554 (1980).
96. K. Sachs, "Marker movements in scale layers", Metallurgia **54** (July): 11 - 17 (1956).
97. J. D. Mackenzie and C. D. Birchenall, "Plastic flow of iron oxides and the oxidation of iron", Corrosion **13**: 783t - 785t (1957).
98. D. Bruce and P. Hancock, "Influence of mechanical properties of surface

oxide films on oxidation mechanisms", J. I. Metals **97**: 140 - 155 (1969).

99. B. Ilschner, B. Reppich and E. Riecke, "High-temperature steady-state creep and atomic disorder in iron oxide", Disc. Farad. Soc. **38**: 243 - 250 (1964).
100. E. A. Gulbransen and R. Ruka, "Kinetics of solid phase reactions in oxide films on iron - the irreversible transformation at or near 570°C", Trans. A. I. M. E. **188**:1500 - 1508 (1950).
101. G. Chaudron, "Réactions réversibles de l'oxyde de carbone sur les oxydes de fer", Comptes Rendus **172**: 152 - 155 (1921).
102. G. Chaudron and H. Forestier, "Étude de la décomposition du protoxyde de fer. Anomalies de dilatation corrélatives de son instabilité", Comptes Rendus **178**: 2173 - 2176 (1924).
103. J. Wingrove, "Identification of iron oxides", J. I. S. I. **208**: 258 - 264 (1970).
104. J. Bénard and G. Chaudron, "Contribition à l'étude de la décomposition du protoxyde de fer", Comptes Rendus **202**: 1336 - 1338 (1936).
105. G. Chaudron and J. Bénard, "L'oxydation des métaux et les réactions dans l'état solide", Bull. Soc. Chim. France **1949**:D89 - 95 (1949).
106. J. K. Stanley, J. von Hoene and R. T. Huntoon, "The oxidation of pure iron", Trans. A. S. M. **43**: 426 - 446 (1951).
107. E. J. W. Verwey and P. W. Haayman, "Electronic conductivity and the transition point of magnetite ("Fe_3O_4")", Physica **8** (9): 979 - 987 (1941).
108. J. Thewlis, "The structure of ferromagnetic oxide", Phil. Mag. **12**: 1089 - 1106 (1931).
109. R. Dieckmann and H. Schmalzried, "Defects and cation diffusion in magnetite", Ber. Bunsenges. Phys. Chem. **81** (3): 344 - 347; *ibid.* **81** (4): 414 - 419 (1977).
110. R. Dieckmann and H. Schmalzried, "Point defects and cation diffusion in magnetite", Z. Phys. Chem. **96**: 331 - 333 (1975).
111. A. Atkinson and R. I. Taylor, "^{55}Fe and ^{18}O tracers in magnetite scales growing on iron and dilute iron-silicon alloys", High Temp. - High Press. **14**: 571 - 580 (1982).
112. N. L. Peterson, W. K. Chen and D. Wolf, "Correlation and isotope effects for cation diffusion in magnetite", J. Phys. Chem. Solids **41**: 709 - 719 (1980).
113. A. Atkinson, M. L. O'Dwyer and R. I. Taylor, "^{55}Fe diffusion in magnetite at 500°C and its relevance to the oxidation of iron", J. Mater. Sci. **18**: 2371 - 2379 (1983).
114. J. E. Castle and P. L. Surman, "The self-diffusion of oxygen in magnetite.

The effect of anion vacancy concentration and cation distribution", J. Phys. Chem. **73** (3): 632 - 634 (1969).

115. C. Gleave, J. M. Calvert, D. G. Lees and P. C. Rowlands, "A study of the mechanism of corrossion of some ferritic steels in high pressure carbon dioxide with the aid of oxygen-18 as a tracer. I. Low silicon mild steel", Proc. Roy. Soc. (A) **379**: 409 - 427 (1982).
116. D. A. Channing and M. J. Graham, "A study of iron oxidation processes by Mössbauer spectroscopy", Corros. Sci. **12**: 271 - 289 (1972).
117. W. E. Boggs, R. H. Kachik and G. E. Pellisier, "The effect of oxygen pressure on the oxidation of zone-refined iron", J. Electrochem. Soc. **112**: 539 - 546 (1965).
118. F. DeBoer and P. W. Selwood, "The activation energy for the solid state reaction γ-Fe_2O_3 - α-Fe_2O_3", J. Electrochem. Soc. **76**, 1954: 3365 - 3367.
119. E. A. Harrington, "X-ray diffraction measurements on some of the pure compounds concerned in the study of Portland cement", Am. J. Sci. **13**: 467 - 479 (1927).
120. D. J. M. Bevan, J. P. Shelton and J. S. Anderson, "Properties of some simple oxides and spinels at higher temperatures", J. Chem. Soc.: 1729 - 1741 (1948).
121. K. A. Hay, F. G. Hicks and D. R. Holmes, "The transport properties and defect structure of the oxide $(Fe, Cr)_2O_3$ formed on Fe-Cr alloys", Werkstoffe Korros. **21**: 917 - 924 (1970).
122. W. C. Hagel, "Oxygen-ion diffusion in hematite", Trans. A. I. M. E. **236**: 179 - 184 (1966).
123. R. Francis and D. G. Lees, "Some observations on the growth mechanism of haematite during the oxidation of iron at 823K", Corros. Sci. **16**: 847 - 855 (1976).
124. A. Bruckman and G. Simkovich, "Concerning the mechanism of scale growth due to cation diffusion in Fe_2O_3 and CuS", Corros. Sci. **12**: 595 - 601 (1972).
125. U. Colombo, F. Gazzarini, G. Lanzavecchia and G. Sironi, "Magnetite oxidation: A proposed mechanism", Nature **147**: 1033 (1965).
126. I. David and A. J. E. Welch, "The oxidation of magnetite and related spinels: Constitution of gamma ferric oxide", Trans. Farad. Soc. **52**: 1642 - 1650 (1956).
127. C. -T. Chen and B. D. Cahan, "The nature of the passive film on iron: I. Automatic ellipsometric spectroscopy studies", J. Electrochem. Soc. **129:** 17 - 26 (1982); B. D. Cahan and C.-T. Chen, "The nature of the passive film on

iron: II. A-C impedance studies", J. Electrochem. Soc. **129:** 474 - 480 (1982); B. D. Cahan and C.-T. Chen, "The nature of the passive film on iron: III. The chemi-conductor model and further supporting evidence", J. Electrochem. Soc. **129:** 921 - 925 (1982).

128. C. D. Stockbridge, P.B. Sewell and M. Cohen, "Cathodic behaviour of iron single crystals and the oxides Fe_3O_4, gamma-Fe_2O_3, and alpha-Fe_2O_3", J. Electrochem. Soc. **108** (10): 928 - 933 (1961).
129. S. I. Ali and G. C. Wood, "Oxidation at room temperature", Br. Corros. J. **4**: 133 - 137 (1969).
130. U.R. Evans, "Electrochemical mechanism of atmospheric rusting", Nature **206**: 980 - 982 (1965).
131. C. E. Birchenall, "Oxidation of alloys", in "Oxidation of Metals and Alloys: Papers presented at a seminar of the ASM (Oct 1970)", publ. ASM, Ohio (1971).
132. J. Takada, S. Yamamoto, S. Kikuchi and M. Adachi, "Determination of diffusion coefficient of oxygen in γ-iron from measurements of internal oxidation in Fe-Al alloys", Metall. Trans. **17A**: 221 - 229 (1986).
133. C. W. Tuck, "Non-protective and protective scaling of a commercial $1^3/_4$% silicon - iron alloy in the range 800°C - 1000°C", Corros. Sci. **5**: 631 - 643 (1965).
134. T. Adachi and G. H. Meier, "Oxidation of iron silicon alloys", Oxid. Met. **27** (5/6): 347 - 366 (1987).
135. I. Svedung and N. G. Vannerberg, "The influence of silicon on the oxidation properties of iron", Corros. Sci. **14**: 391 - 399 (1974).
136. R. L. Sands and C. R. Shakespeare, "Powder Metallurgy. Practice and Applications", publ. George Newnes Ltd, London (1966).
137. M. J. Koczak and H. Chung, 'The effects of elemental alloying and sintering temperature on the cold forming of powder metallurgy Ni steels', Powd. Metall. Int., **7**(2): 71 - 74 (1975).
138. M. J. Fleetwood, "Rapid solidification processes", Met. Matls. **3**(1): 14 - 20 (1987).
139. R. W. Heckel, R. D. Lanam and R. A. Tanzili, "Techniques for the study of homogenization in compacts of blended powders", in "Perspectives in Powder Metallurgy, Volume 5: Experimental Techniques in Powder Metallurgy", ed. J. S. Hirschhorn and K. H. Roll, publ. Plenum Press, London: 139 - 188 (1970).
140. R. M. German, "Powder Metallurgy Science", publ. Metal Powder Industries Federation, Princeton, NJ (1984).

141. G. Pitt, "The effect of production variables on the mechanical properties of a sintered nickel steel", undergraduate project, supervisor L. W. Crane. unpublished, Aston University (1980).
142. R. A. Thompson, "Mechanics of powder pressing", Bull. Am. Ceram. Soc. **60**: 237 - 251 (1981).
143. V. T. Morgan, "Techniques for the evaluation of powders III. Observations on compacts", Powd. Metall. 1961 (7): 44 - 65 (1961).
144. P. Duwez and L. Zwell, "Pressure distribution in compacting metal powders", Trans. A. I. M. E. **185**: 137 - 144 (1949).
145. D. Yarnton and T. J. Davies, "The effect of lubrication on the compaction and sintering of iron powder compacts", Int. J. Powd. Metall. **8** (2): 51 - 67 (1972).
146. R. J. Sajdak, R. P. McNally, M. D. Nasta and J. K. Beddow, "Two methods for characterizing the compaction and ejection behavior of metal powders in a die", Int. J. Powd. Metall. **6** (2): 13 - 23 (1970).
147. B. A. James, "Die wall lubrication for powder compaction: A feasible solution?" Powd. Metall. **30** (4): 273 - 280 (1987).
148. G. Arthur, "Porosity and permeability changes during the sintering of copper powder", J. I. Metals, **83**: 329 - 336 (1954-55).
149. R. G. Benard, "Processes involved in sintering", Powd. Met. (3): 86 - 103 (1959).
150. Y. Trudel and R. Angers, "Properties of iron copper powders made from elemental or prealloyed powders", Int. J. Powd. Metall. and Powd. Technol. **11** (1): 5 - 16 (1975).
151. W. A. Kaysser, W. J. Huppmann and G. Petzow, "Analysis of dimensional changes during sintering of Fe-Cu", Powd. Metall. (2): 86 - 91 (1980).
152. K. Tabeshfar and G. A. Chadwick, "Dimensional changes during liquid phase sintering of Fe-Cu compacts", Powd. Metall. **27** (1): 19 - 24 (1984).
153. B. A. James, "Liquid phase sintering in ferrous powder metallurgy", Powd. Metall., **28** (3): 121 - 130 (1985).
154. V. Gemenetsis, "Homogenization and sintering in multiphase iron-base alloys", Powd. Metall. Group, Metals Soc. (1979).
155. A. Cias, J. Frydrych and T. Pieczonka, "Liquid phase sintering of iron-phosphorus model system", Powd. Metall. Int. **21** (3): 13 - 15 (1989)
156. D. R. Gabe, "Corrosion and protection of sintered metal parts", Powd. Metall. **20** (4): 227 - 231 (1977).
157. O. Hoffman, "Improving the corrosion resistance of sintered steel components", Anti-Corrosion (August):16 - 18 (1969).

158. I. M. Fedorchenko, A. P. Lyapunov and V. V. Skorokhod, "Phenomena taking place during oxidation of porous metals at elevated temperatures", Powd. Metall. (12): 27 - 43 (1963).
159. P. C. Searson and R. M. Latanision, "The corrosion and oxidation resistance of iron- and aluminium-based powder metallurgical alloys", Corros. Sci. **25** (10): 947 - 968 (1985).
160. R. L. Sands, G. F. Bidmead and D. E. Oliver, "The corrosion resistance of sintered austenitic stainless steel", in "Modern Developments in Powder Metallurgy", vol. 2, ed. H. H. Hausner, publ. Plenum Press, New York, NY:73 - 83 (1966).
161. N. A. Siddiqi, A. Hafiz, M. A. Siddiqi and M. Hamiuddin, "Effects of dopants and steam treatment of sintered ferrous alloys", Powd. Metall. Assoc. India. Newsletter **10** (1): 14 - 18 (1984).
162. K. Razavizadeh and B. L. Davies, "Influence of powder type and density on pore closure and surface hardness changes resulting from steam treatment of sintered iron", Powd. Metall. **22** (4): 187 - 192 (1979).
163. F. W. Regel, "The steam treatment of sintered iron parts", Engineers Digest **24** (11): 91 - 93 (1963).
164. V. B. Phadke and B. L. Davies, "Ageing and steam oxidation of furnace cooled Fe - 2% Cu alloy", Powd. Metall. Int. **9** (4): 168 - 169 (1977).
165. T. H. Sanderson, "Steam atmsophere heat treatment", Heat Treat. Met. (4): 109 - 112 (1975).
166. N. J. Cory and T. Herrington, "The location of hydrogen in the kinetics of oxidation of ferrous alloys by superheated steam", Oxid. Met. **29** (1/2): 135 - 152 (1988).
167. P. Franklin and B. L. Davies, "The effects of steam oxidation on porosity in sintered iron", Powd. Metall. **20** (1): 11 - 16 (1977).
168. K. Volenik, H. Volrabova, J. Neid, M. Seberini and J. Cirak, "Structure of oxidation products of sintered steel in superheated steam", Powd. Metall. **21** (3): 149 - 154 (1978).
169. A. Gallo, V. Sergi and E. Del Giudice, "Physical and mechanical properties of P/M compacts pressed or pressed and steam oxidized", in "Horizons of Powder Metallurgy. Proceedings of the International Conference on Powder Metallurgy. Dusseldorf, 1986", ed. W. A. Kaysser and W. J. Huppmann, publ. Verlag Schmid, FDR (1986).
170. A. Molinari, L. Fedrizzi, P. L. DeBortoli and A. Tiziani, "Study of the oxide layers obtained by steam treatment on iron sinterd to different densities", in

"Horizons of Powder Metallurgy. Proceedings of the International Conference on Powder Metallurgy. Dusseldorf, 1986", ed. W. A. Kaysser and W. J. Huppmann, publ. Verlag Schmid, FDR (1986).

171. L. Fedrizzi, A. Molinari, E. Ramous and S. De Bortoli, "Influence of copper on the corrosion resistance of steam treated sintered iron", in "Horizons of Powder Metallurgy. Proceedings of the International Conference on Powder Metallurgy. Dusseldorf, 1986", ed. W. A. Kaysser and W. J. Huppmann, publ. Verlag Schmid, FDR (1986).
172. R. M. German, "The use of phase diagrams in predicting sintering behavior", in "Horizons of powder metallurgy. Proceedings of the international conference on powder metallurgy. Dusseldorf, 1986", ed. W. A. Kaysser and W. J. Huppmann, publ. Verlag Schmid, FDR (1986).
173. R. J. Hussey, P. E. Beaubien and D. Caplan, "The metallography of oxide scales on metals", Metallography **6**: 27 - 36 (1973).
174. D. V. Miley and A. E. Calabra, "A review of specimen mounting methods for metallography", in "Metallographic Specimen Preparation: Optical and Electron Microscopy," Proc. 1973 Metallographic Symposium, California, ed. J. L. McCall and W. M. Mueller, publ. Plenum Press, New York, NY (1974).
175. S. Guruswamy, J. P. Hirth and G. W. Powell, "Oxidation behaviour of Fe-Si-Al alloys at 1173-1373°K", Oxid. Met, **19** (3/4): 77 - 98 (1983).
176. W. C. Coons, "The evaluation of final polishing abrasives," in "Metallographic Specimen Preparation: Optical and Electron Microscopy," Proc. 1973 Metallographic Symposium, California, ed. J. L. McCall and W. M. Mueller, publ. Plenum Press, New York, NY (1974).
177. N. M. Hodgkin, "Specimen preparation techniques for scanning electron microscopy," in "Metallographic Specimen Preparation: Optical and Electron Microscopy," Proc. 1973 Metallographic Symposium, California, ed. J. L. McCall and W. M. Mueller, publ. Plenum Press, New York, NY (1974).
178. "Powder Diffraction File of Inorganic Compounds," publ. International Center for Diffraction Data, Pennsylvania (1978).
179. "Binary Alloy Phase Diagrams", ed. T. B. Massalski, publ. ASM, Ohio (1986).
180. D. R. Gaskell, "Introduction to Metallurgical Thermodynamics", 2nd ed., publ. McGraw Hill (1981).

APPENDIX A

THERMO-GRAVIMETRIC ANALYSIS RESULTS

The following graphs are taken from continuous chart records of sample mass gain during oxidation in the Stanton Thermobalance. Where one graph has been used to display several test results, the different oxidation curves are identified by a unique symbol, placed at intervals of five hours.

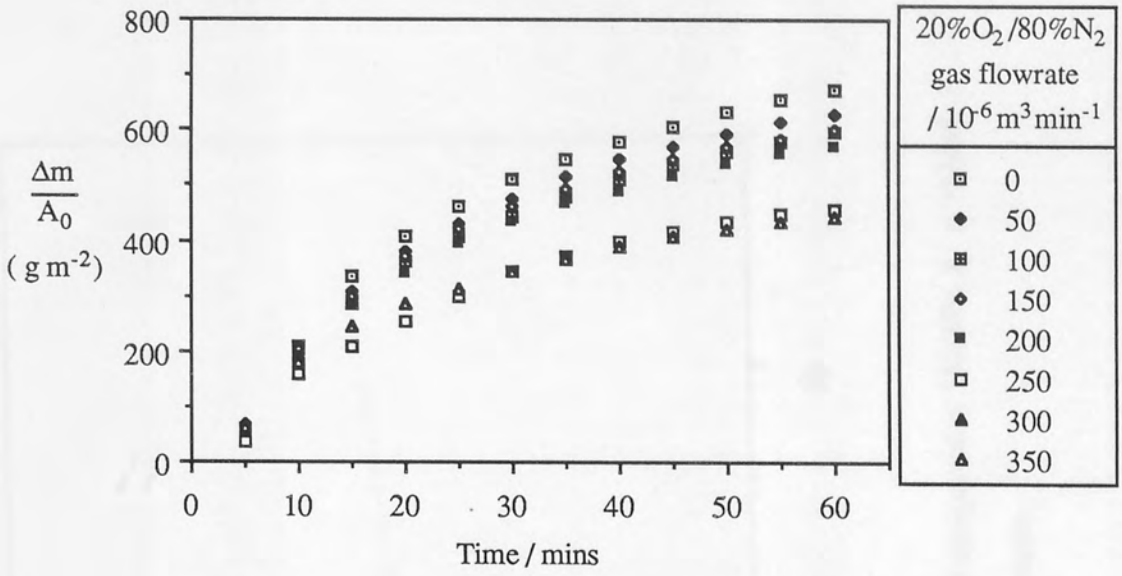

Figure A.1. Effect of gas flow rate on the oxidation at 500°C of pure iron (ASC100.29) compacted at 150MPa.

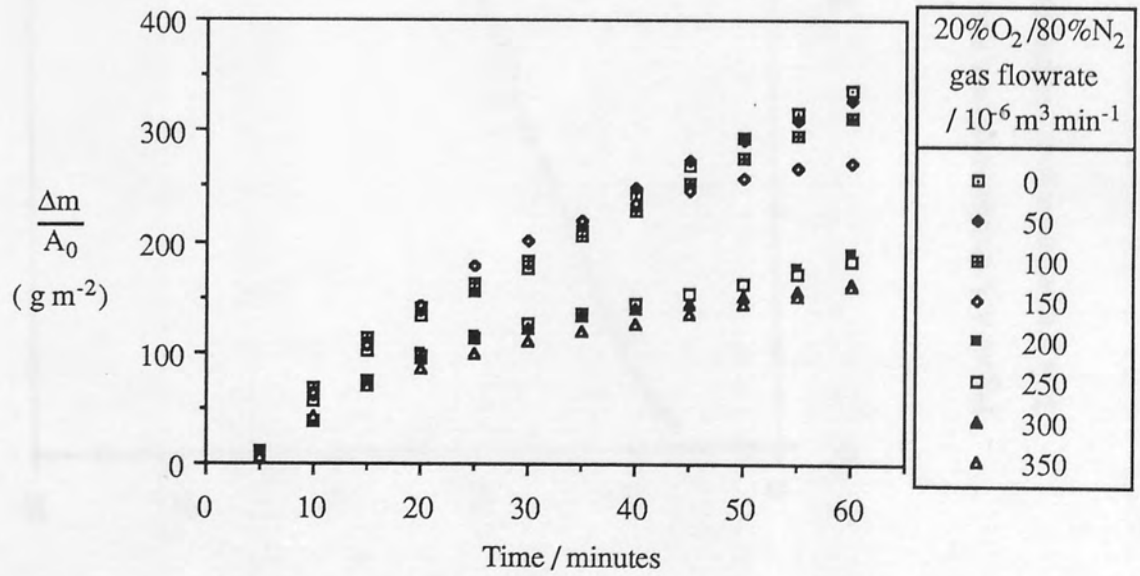

Figure A.2. Effect of gas flow rate on the oxidation at 500°C of pure iron (ASC100.29) compacted at 350MPa.

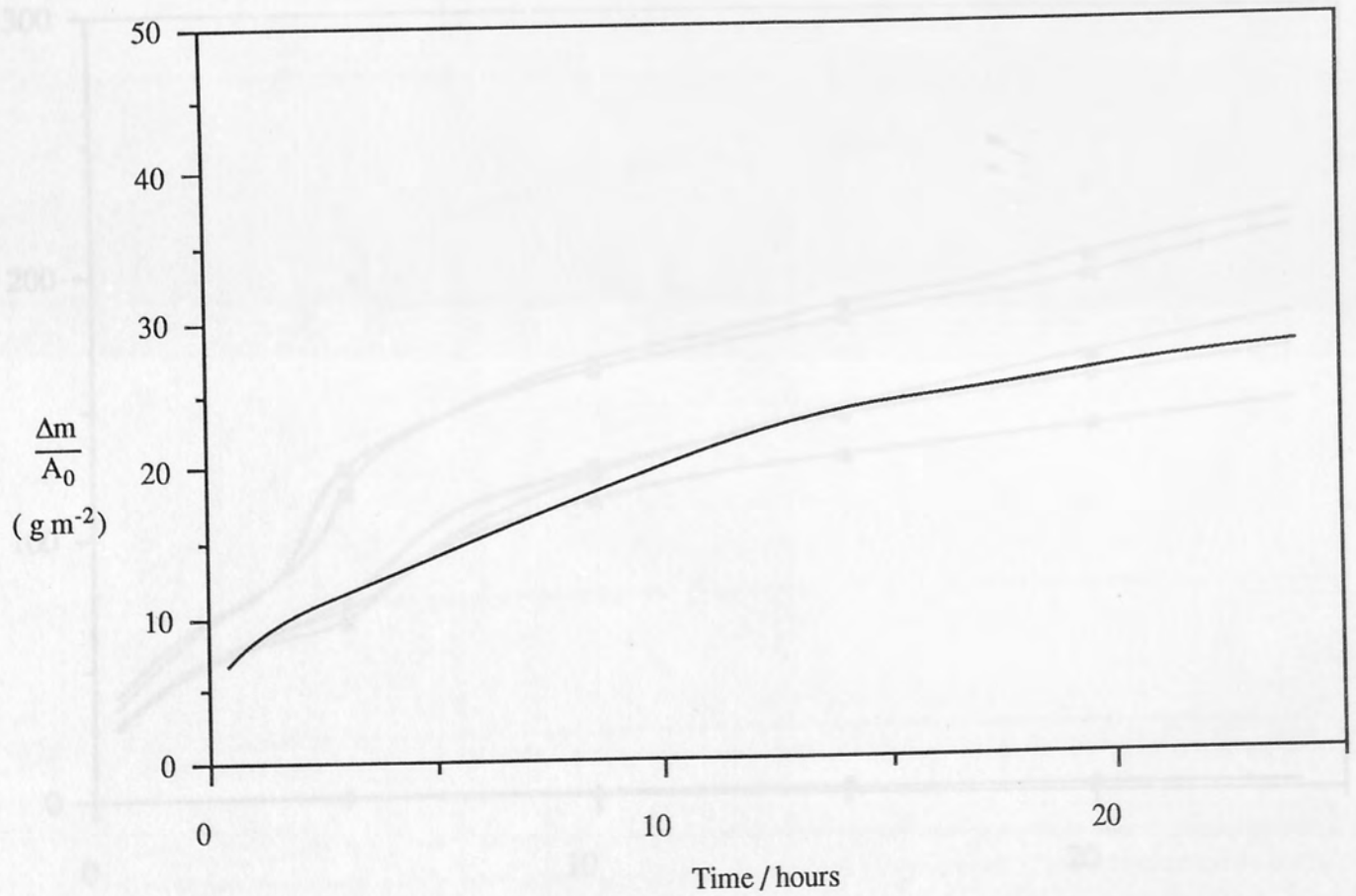

Figure A.3. Oxidation of pure iron at 300°C (ASC100.29 compacted at 350MPa, A_0 = 762mm^2)

This is representative of samples compacted at other pressures.

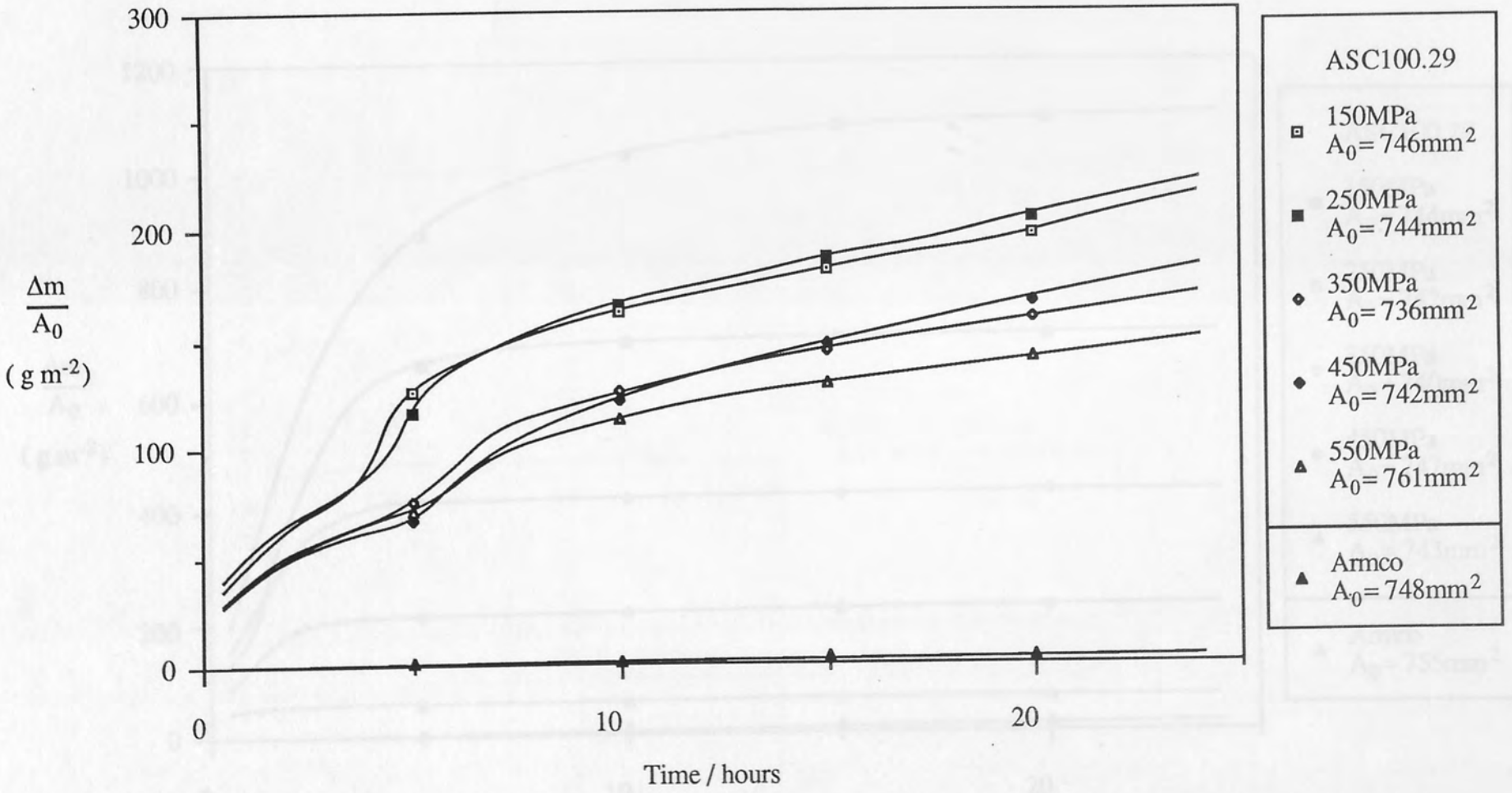

Figure A.4. Oxidation of pure iron (ASC100.29 and Armco) at 400°C.

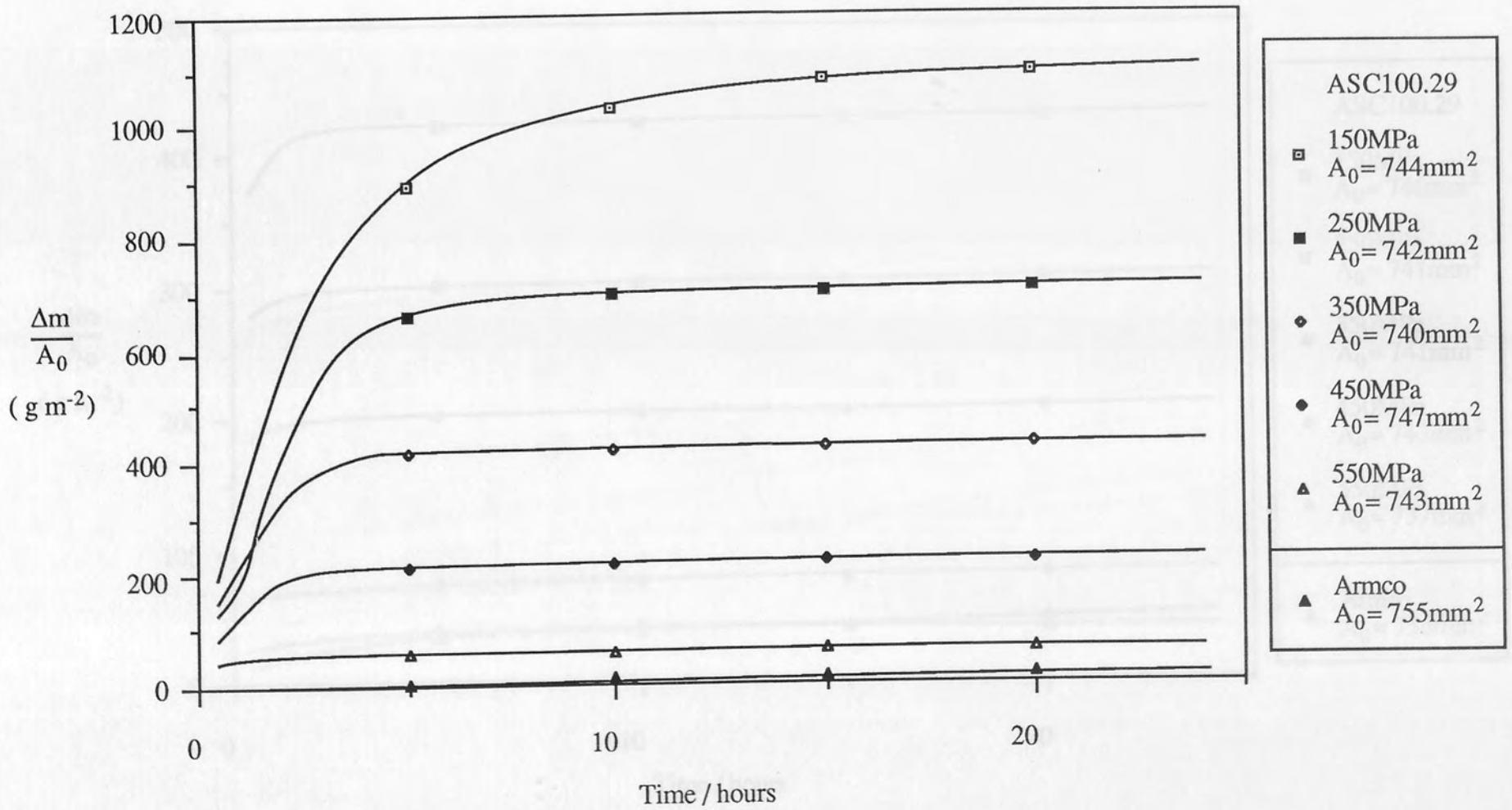

Figure A.5. Oxidation of pure iron (ASC100.29 and Armco) at 500°C.

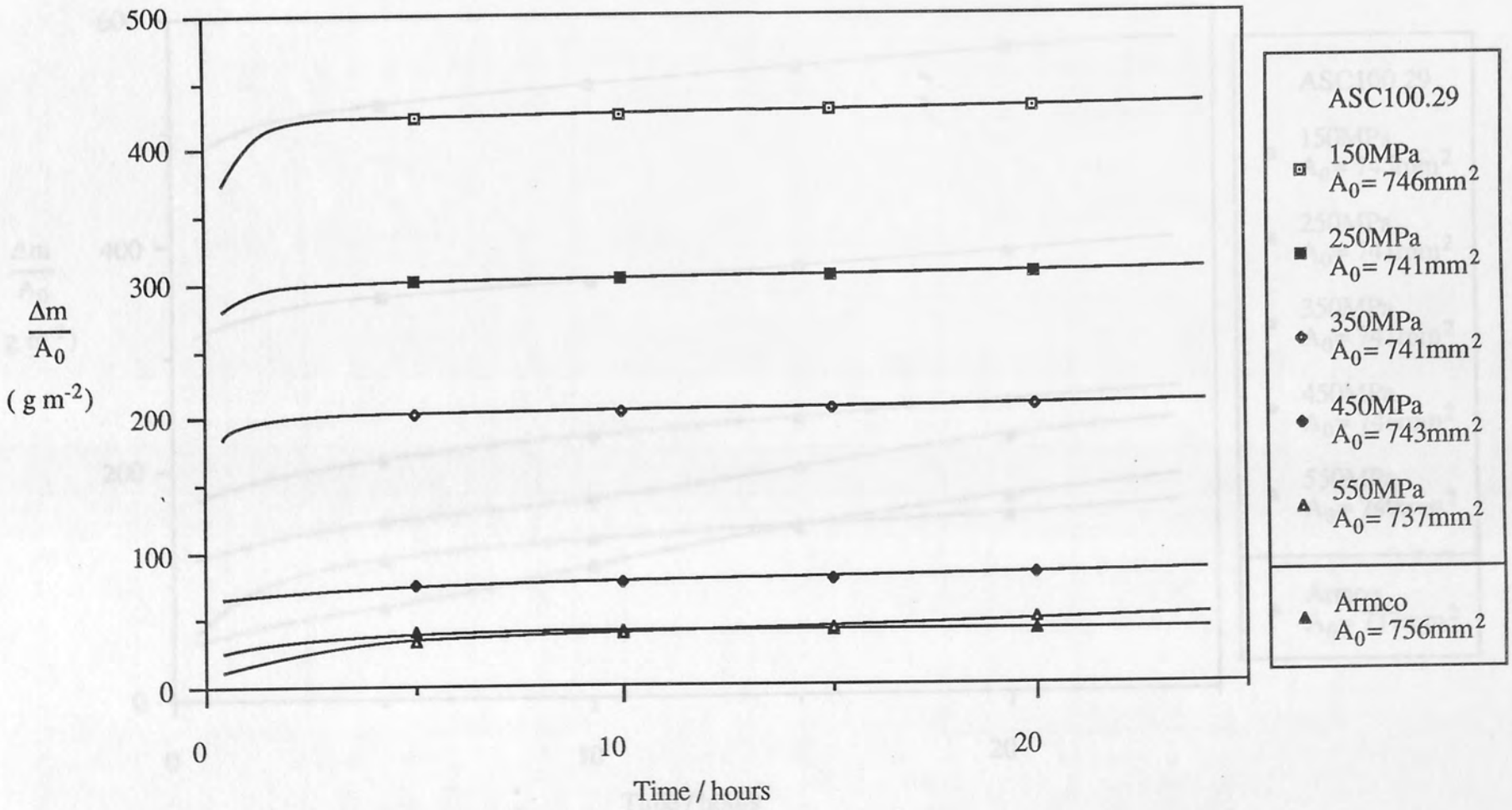

Figure A.6. Oxidation of pure iron (ASC100.29 and Armco) at 600°C.

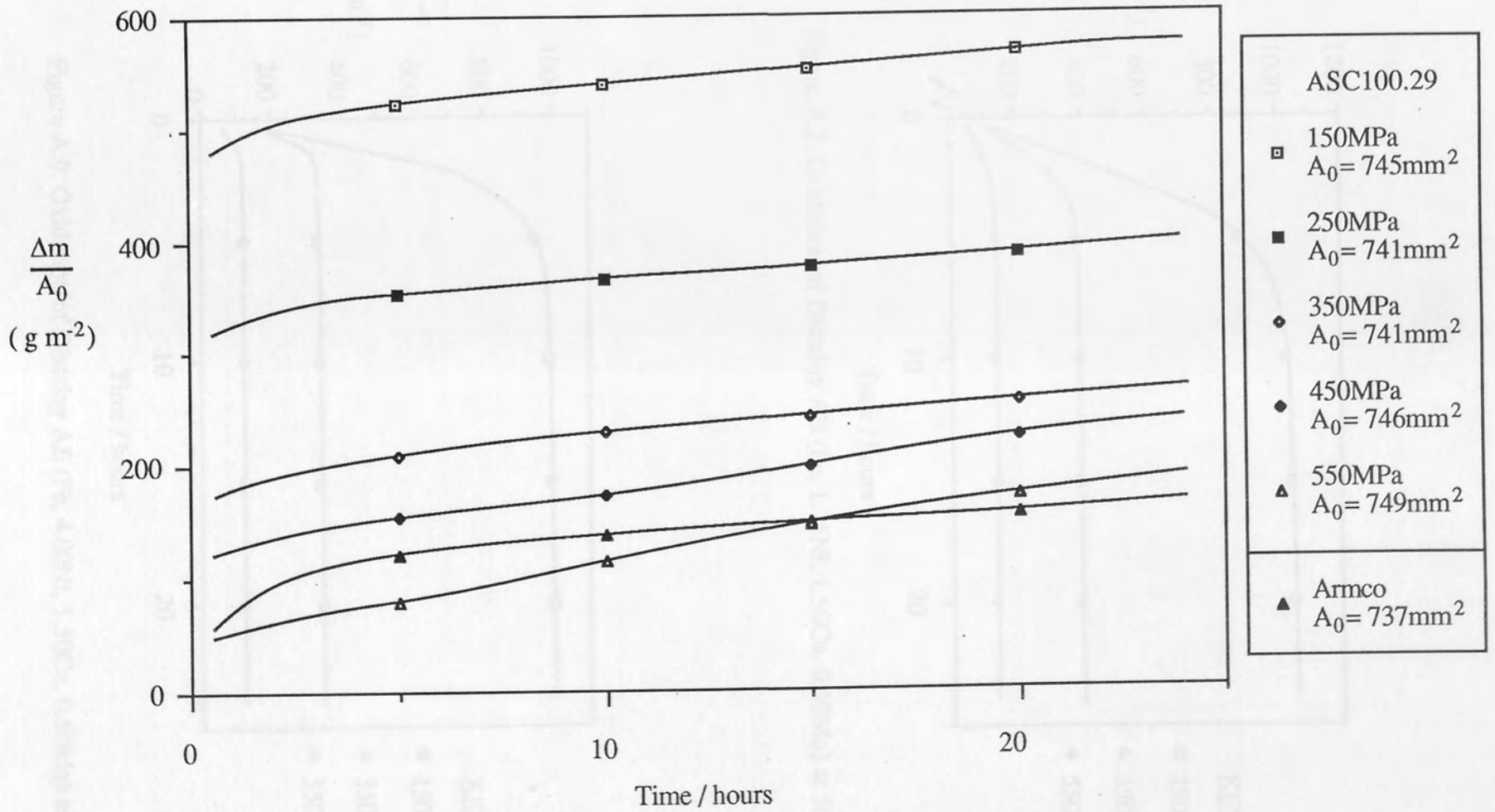

Figure A.7. Oxidation of pure iron at 700°C.

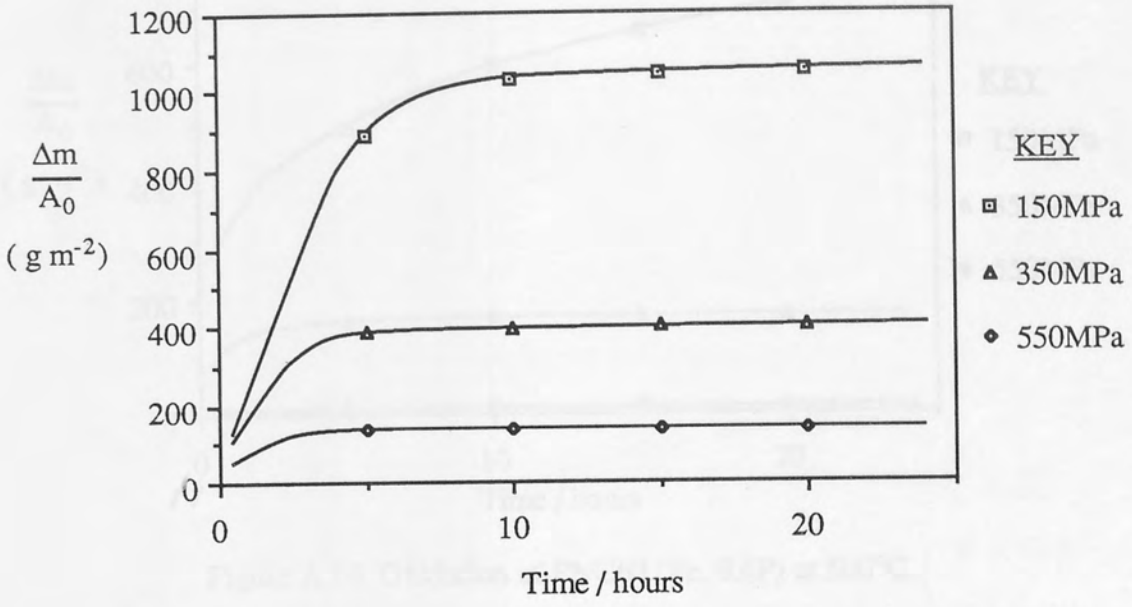

Figure A.8. Oxidation of Distaloy AB (Fe, 1.75Ni, 1.50Cu, 0.50Mo) at 500°C.

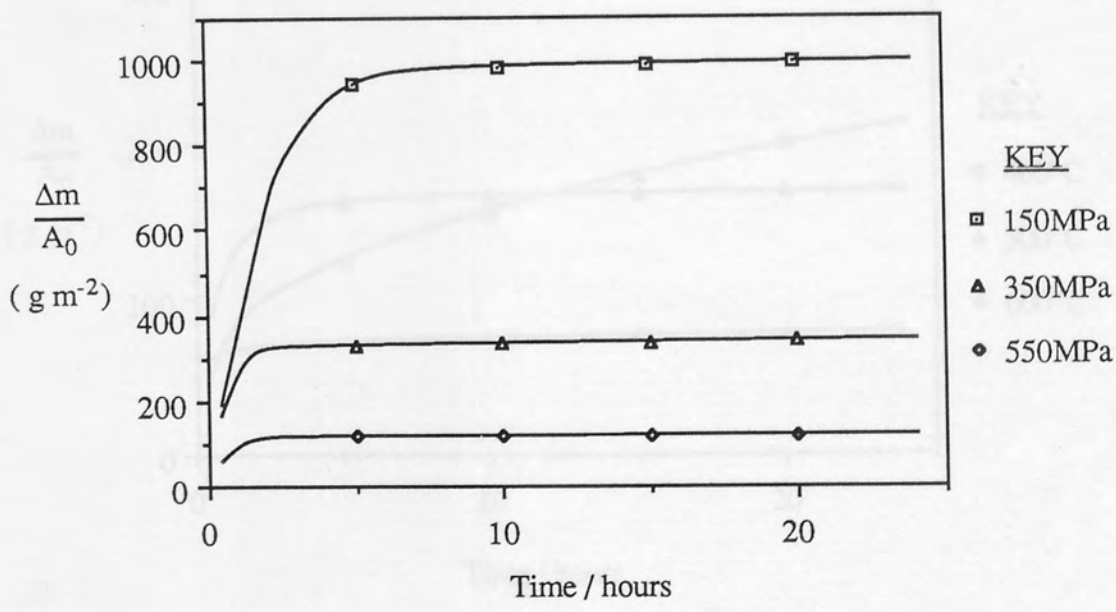

Figure A.9. Oxidation of Distaloy AE (Fe, 4.00Ni, 1.50Cu, 0.50Mo) at 500°C.

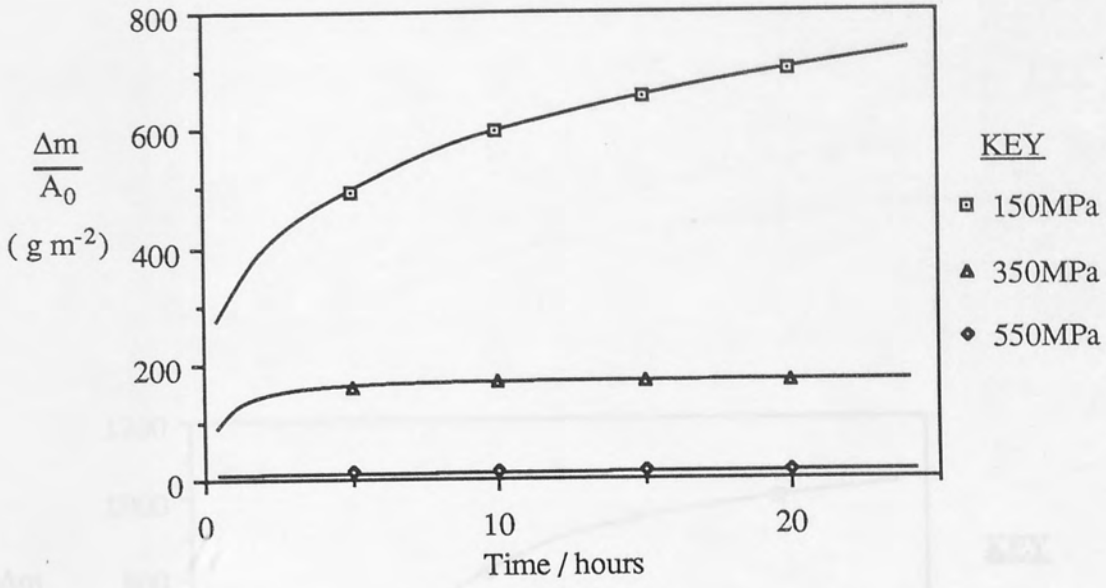

Figure A.10. Oxidation of PNC60 (Fe, 0.6P) at 500°C.

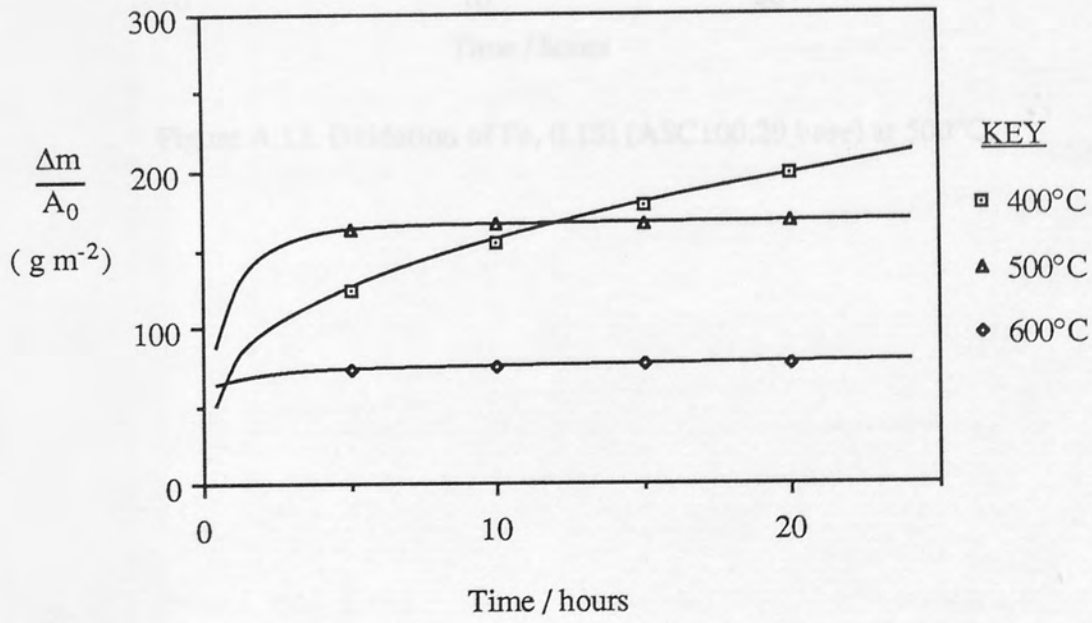

Figure A.11. Oxidation of PNC60 (Fe, 0.6P) compacted at 350MPa.

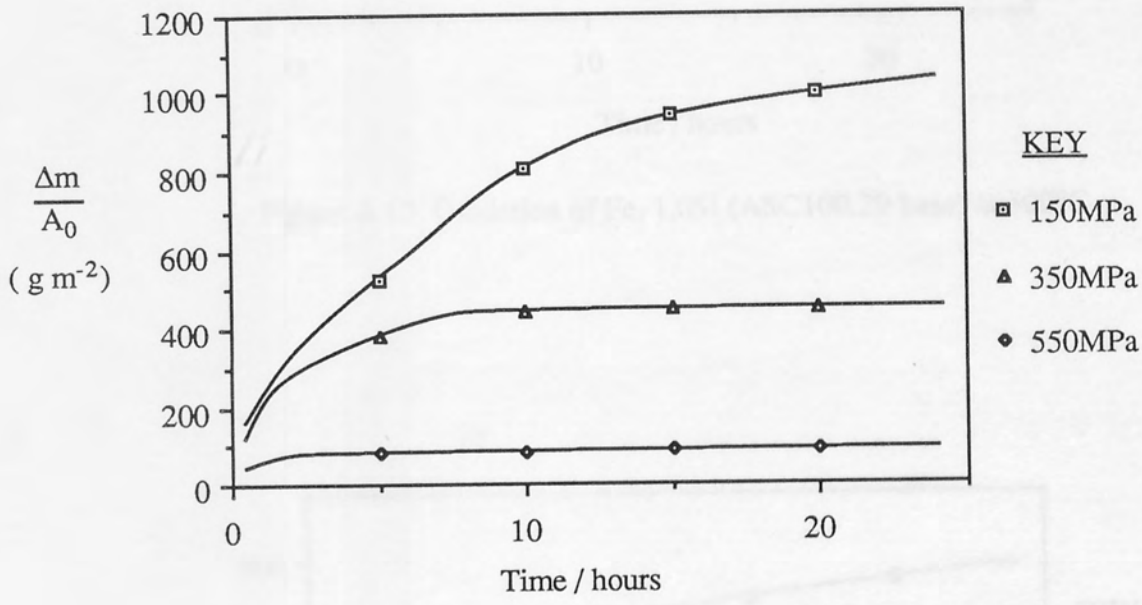

Figure A.12. Oxidation of Fe, 0.1Si (ASC100.29 base) at 500°C.

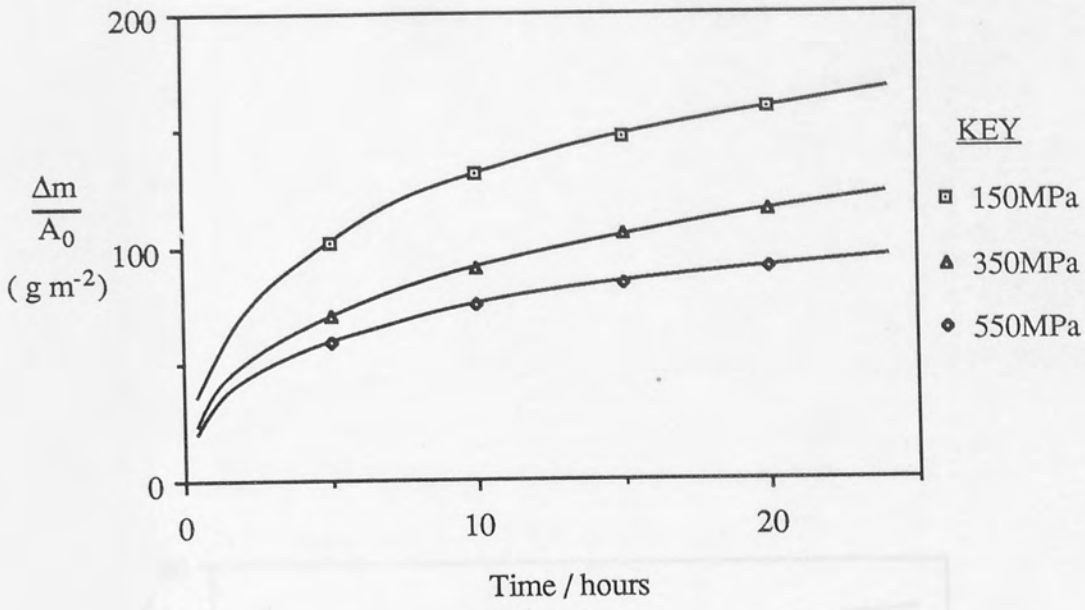

Figure A.13. Oxidation of Fe, 1.0Si (ASC100.29 base) at 500°C.

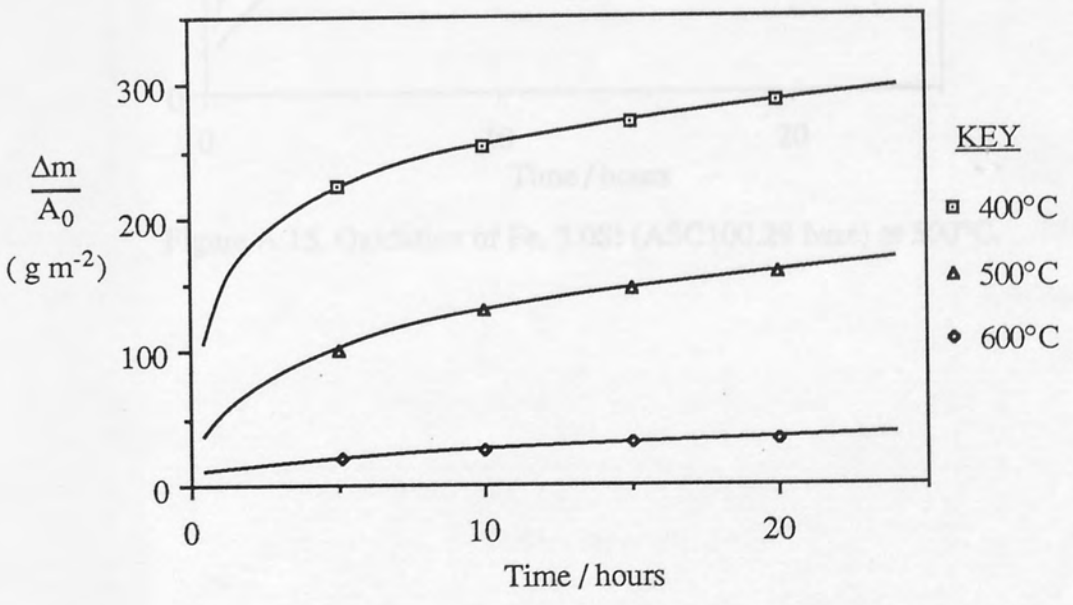

Figure A.14. Oxidation of Fe, 1.0Si (ASC100.29 base) compacted at 350MPa.

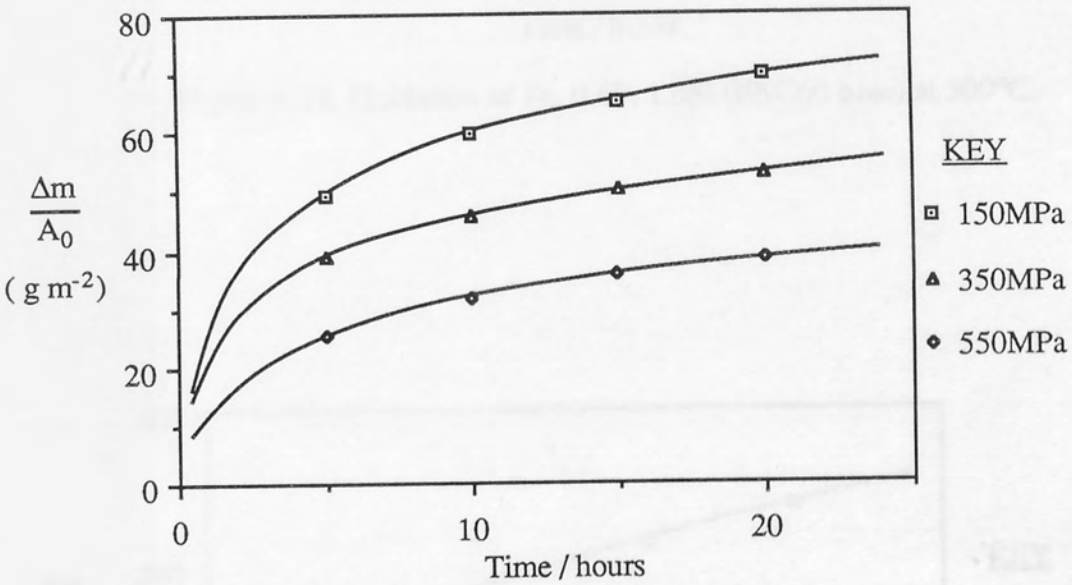

Figure A.15. Oxidation of Fe, 3.0Si (ASC100.29 base) at 500°C.

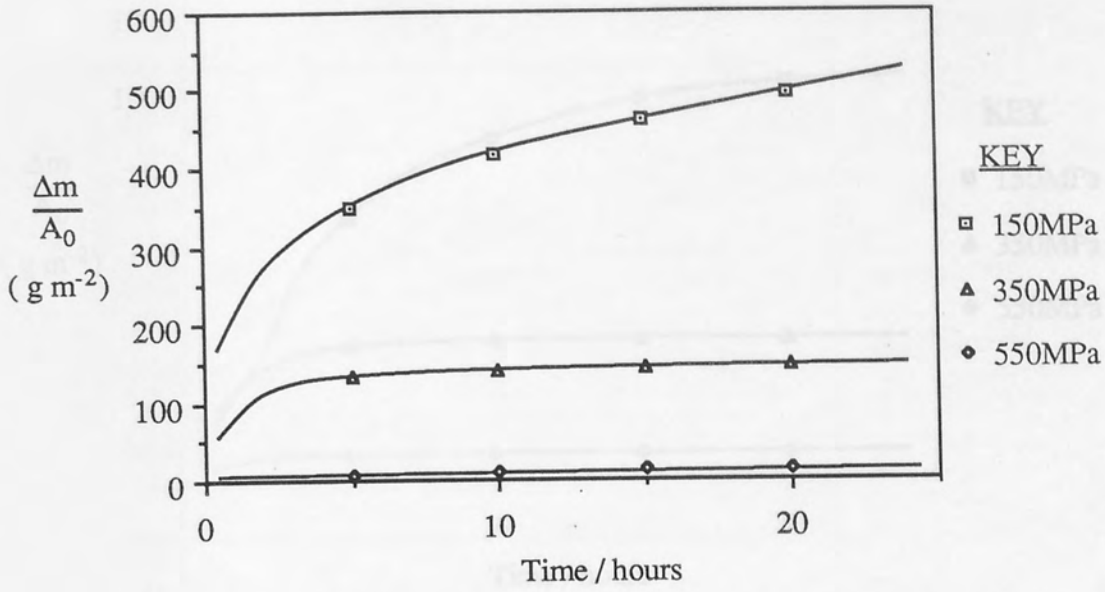

Figure A.16. Oxidation of Fe, 0.6P, 1.0Si (PNC60 base) at 500°C.

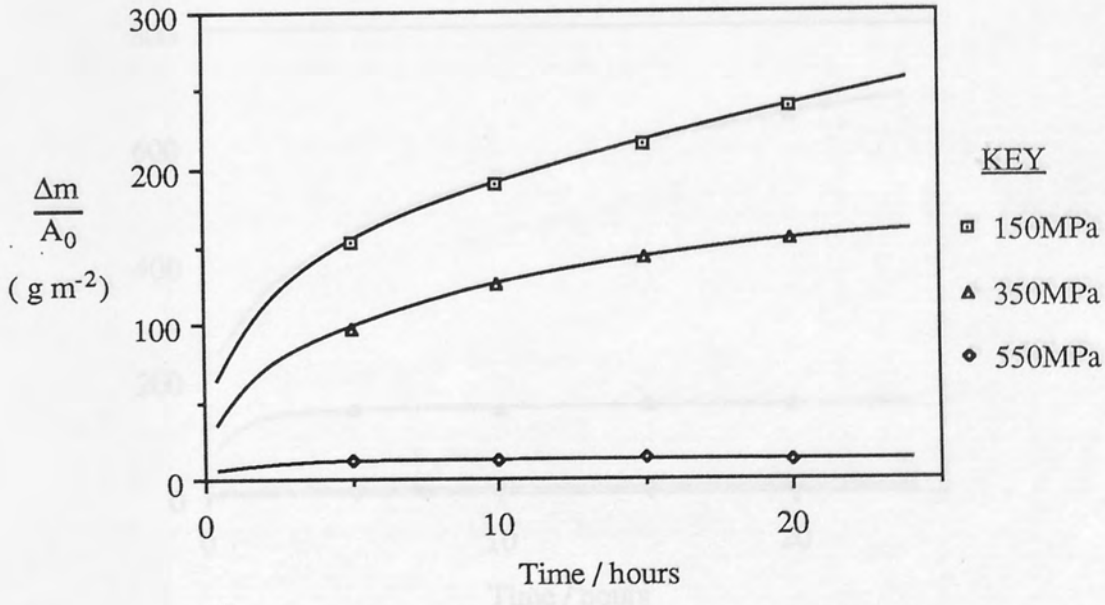

Figure A.17. Oxidation of Fe, 0.6P, 3.0Si (PNC60 base) at 500°C.

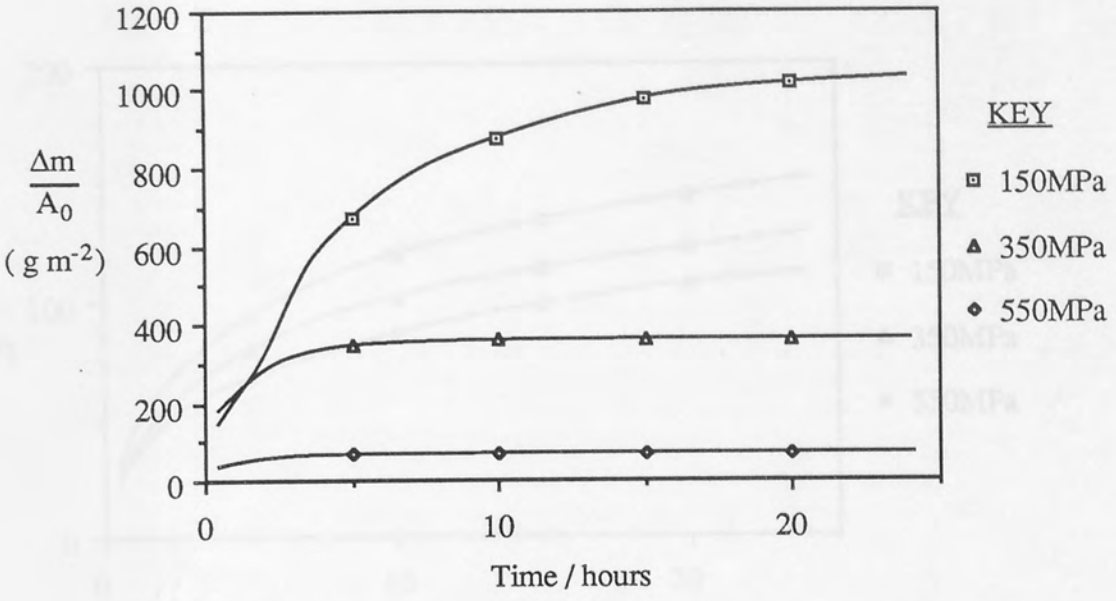

Figure A.18. Oxidation of Fe, 1.0Cu (ASC100.29 base) at 500°C.

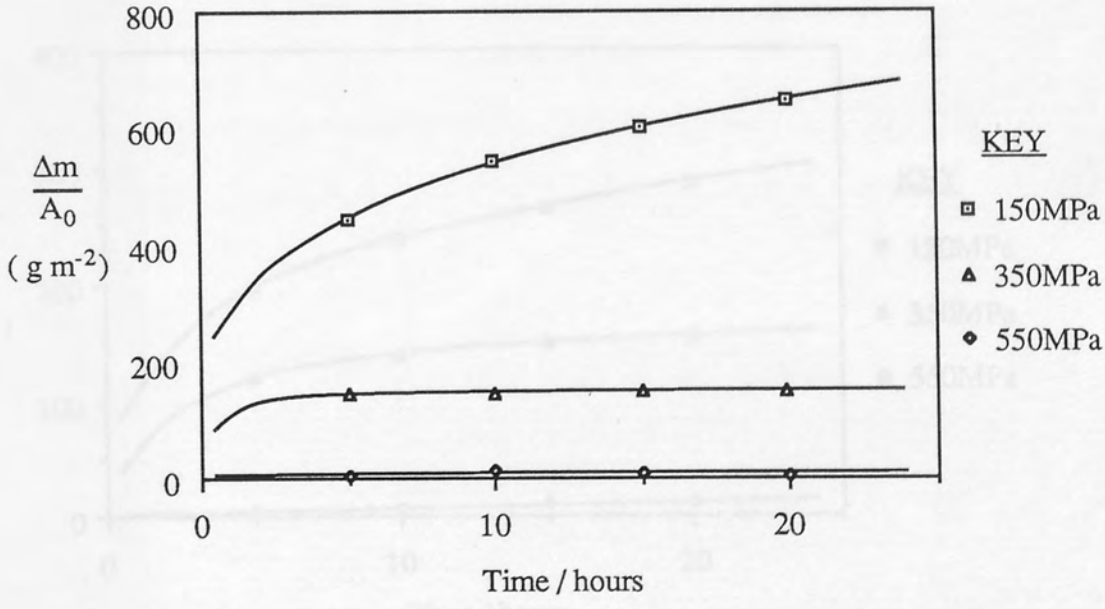

Figure A.19 Oxidation of Fe, 0.6P, 1.0Cu (PNC60 bas) at 500°C.

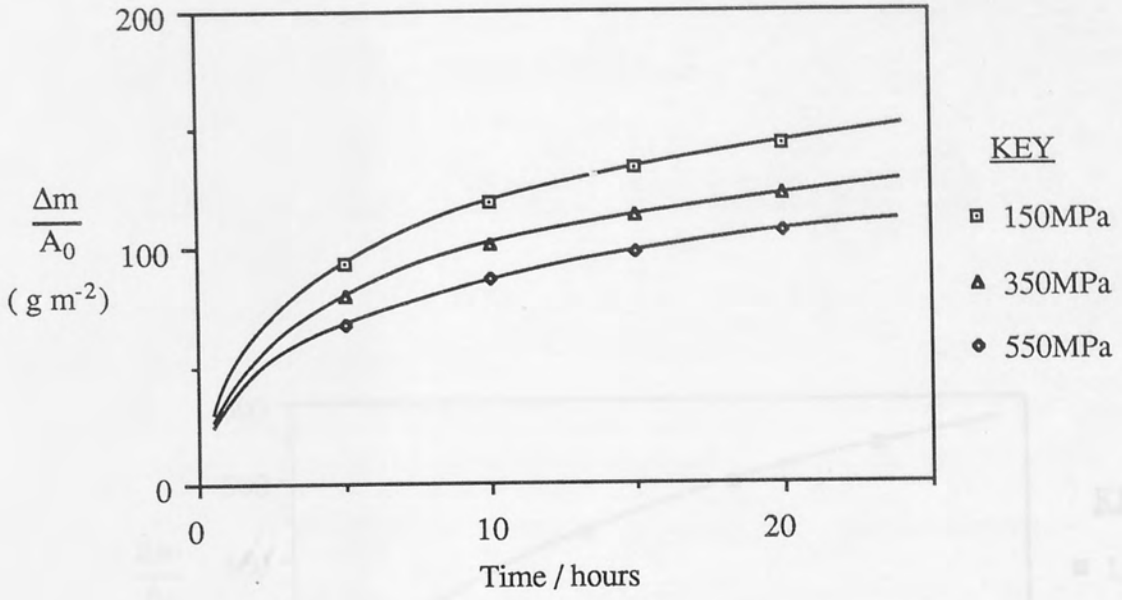

Figure A.20. Oxidation of Fe, 1.0Cu, 1.0Si (ASC100.29 base) at 500°C.

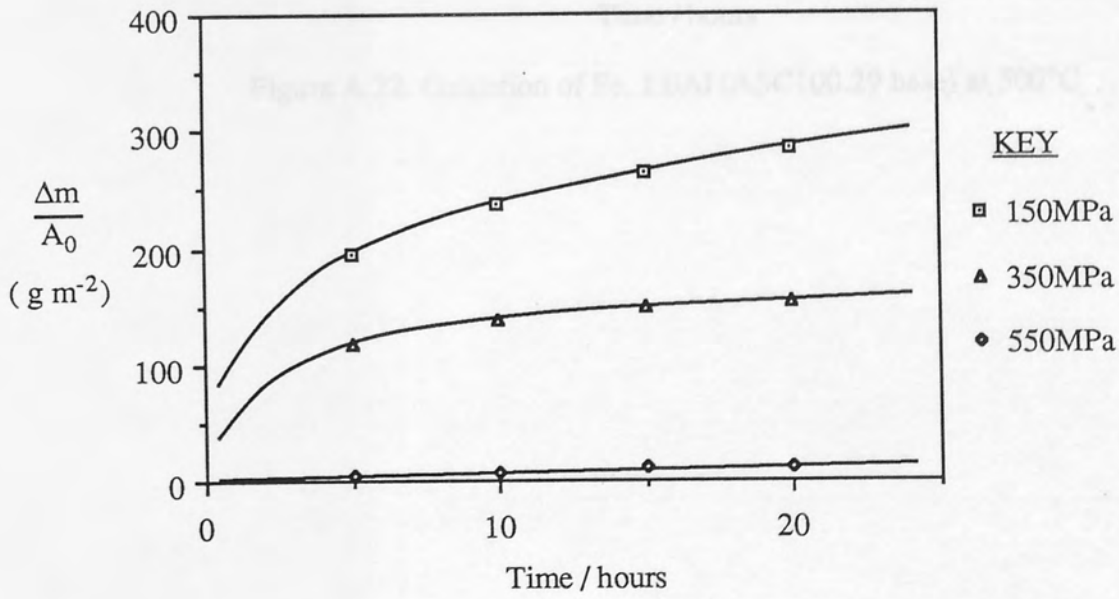

Figure A.21. Oxidation of Fe, 0.6P, 1.0Cu, 1.0Si (PNC60 base) at 500°C.

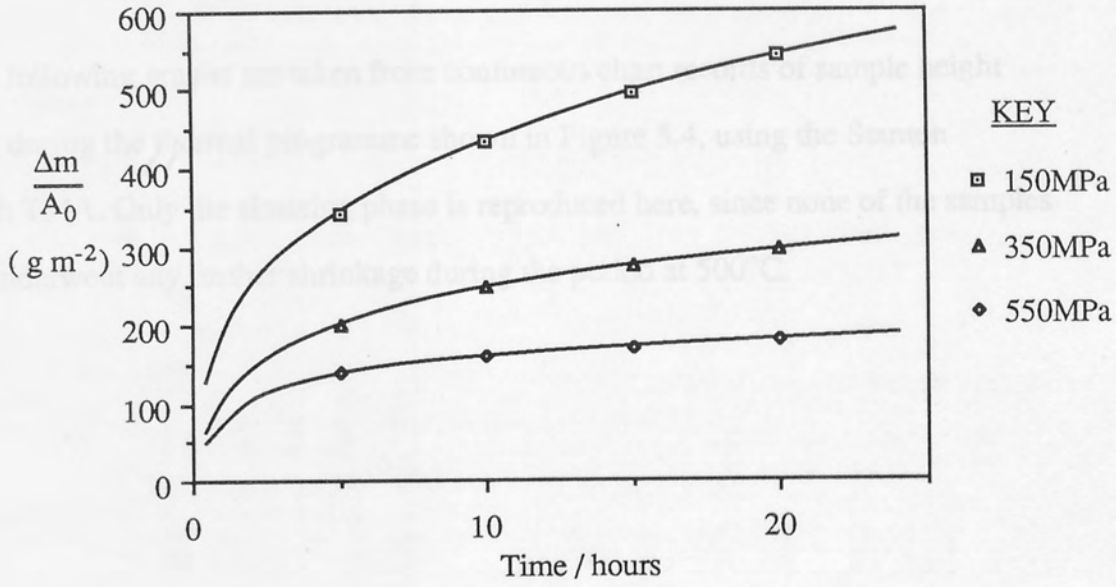

Figure A.22. Oxidation of Fe, 1.0Al (ASC100.29 base) at 500°C

APPENDIX B

THERMO-MECHANICAL ANALYSIS RESULTS

The following graphs are taken from continuous chart records of sample height change, during the thermal programme shown in Figure 5.4, using the Stanton Redcroft TMA. Only the sintering phase is reproduced here, since none of the samples tested underwent any further shrinkage during the period at 500°C.

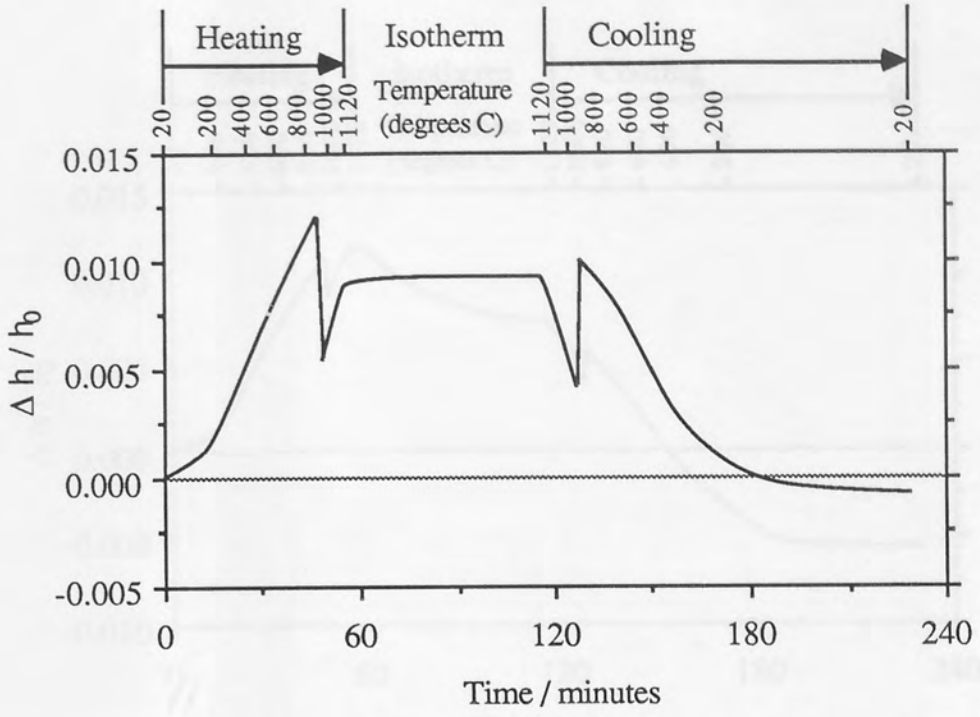

Figure B.1. Dimensional changes in Armco Iron during sintering cycle.

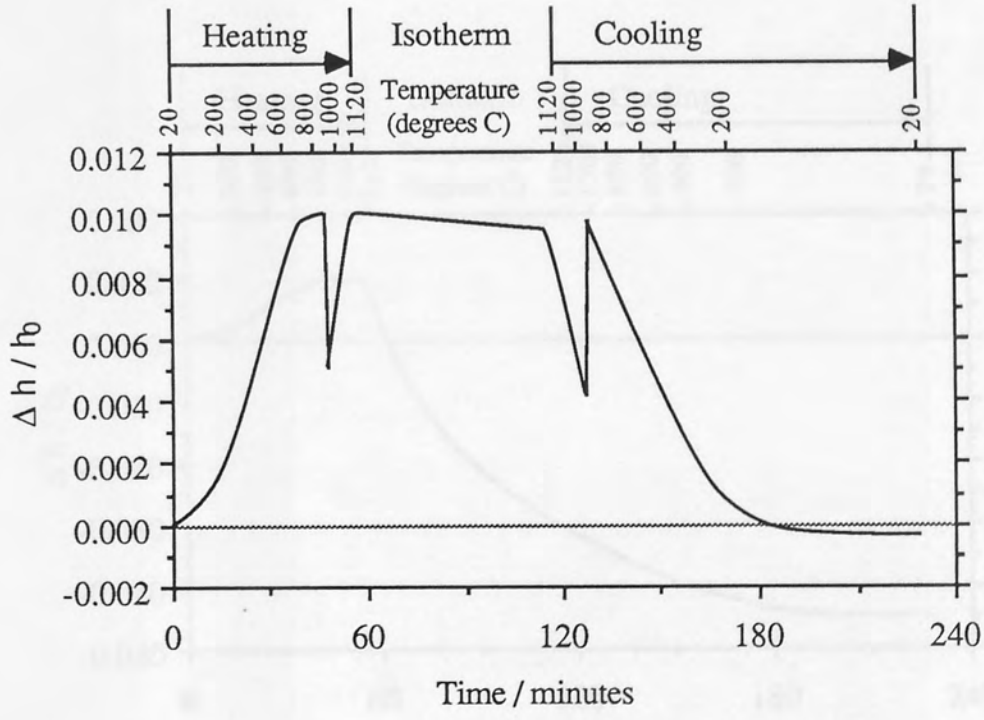

Figure B.2. Dimensional changes in pure iron (ASC100.29) compact during sintering cycle.

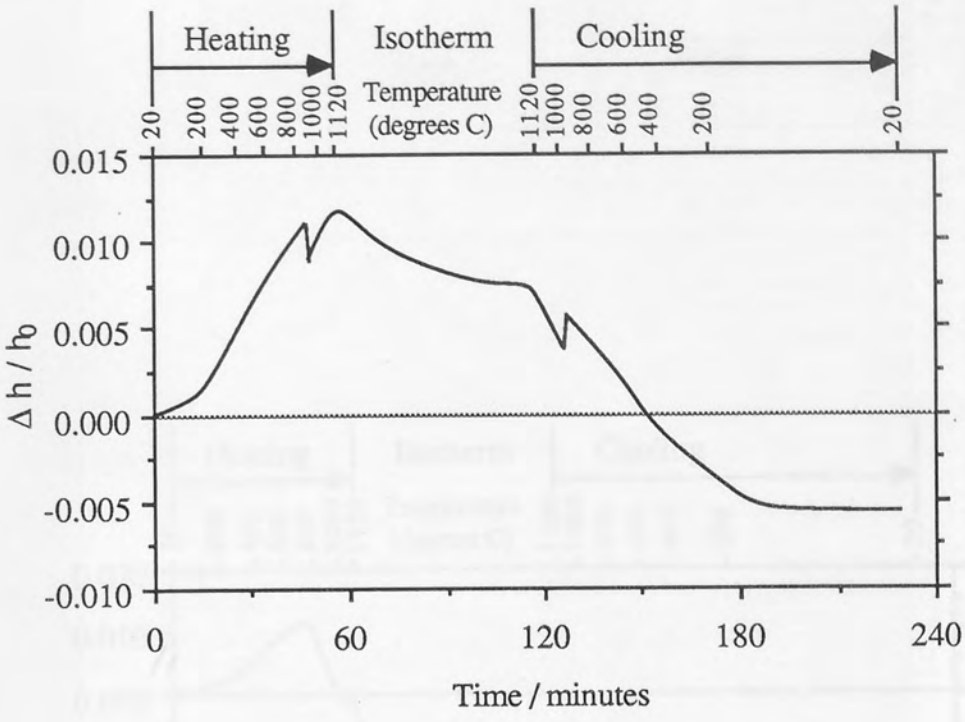

Figure B.3. Dimensional changes in Fe, 1.0Si (ASC100.29 base) during sintering cycle.

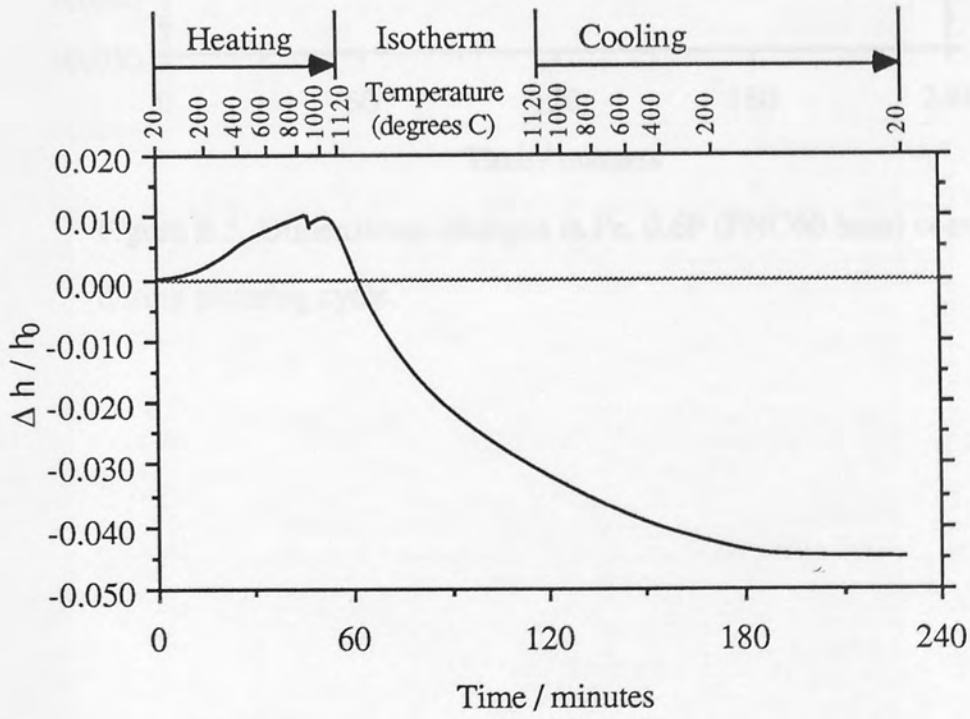

Figure B.4. Dimensional changes in Fe, 3.0Si (ASC100.29 base) during sintering cycle.

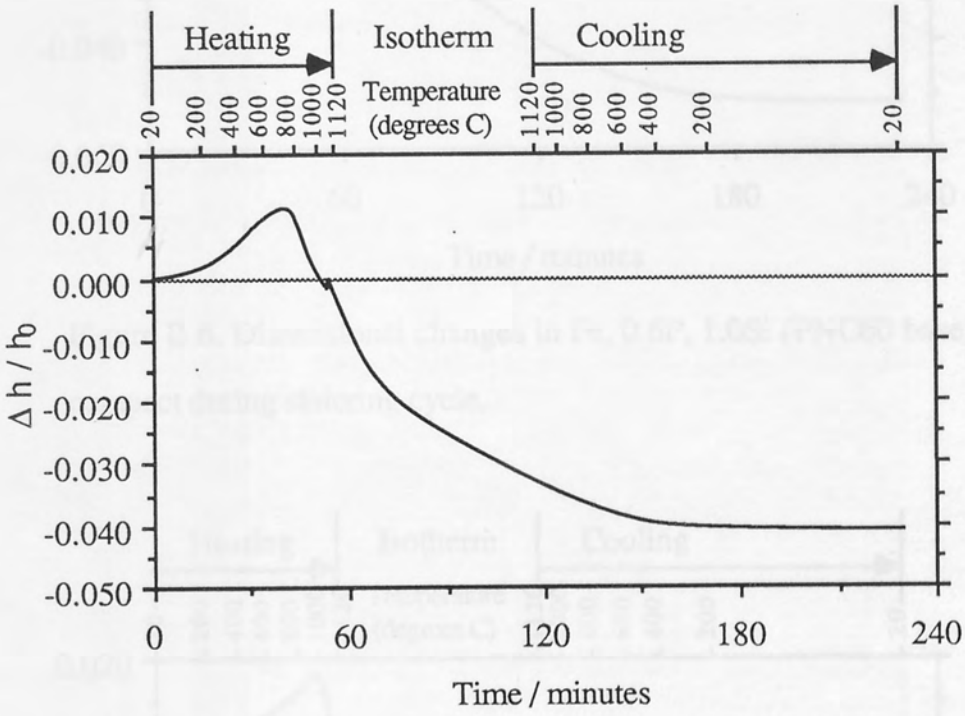

Figure B.5. Dimensional changes in Fe, 0.6P (PNC60 base) compact during sintering cycle.

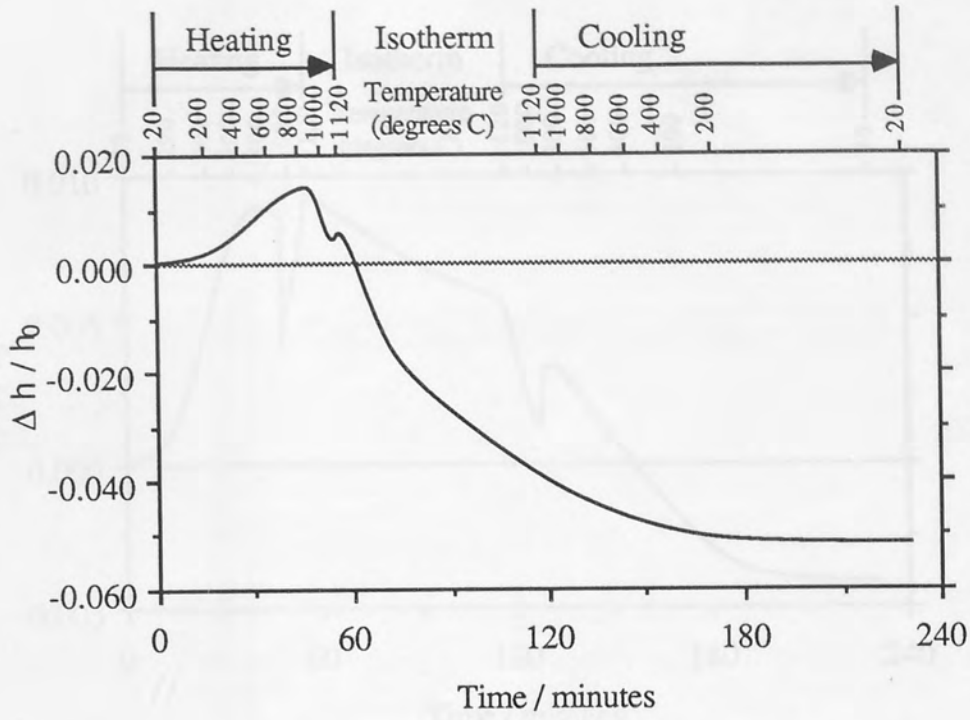

Figure B.6. Dimensional changes in Fe, 0.6P, 1.0Si (PNC60 base) compact during sintering cycle.

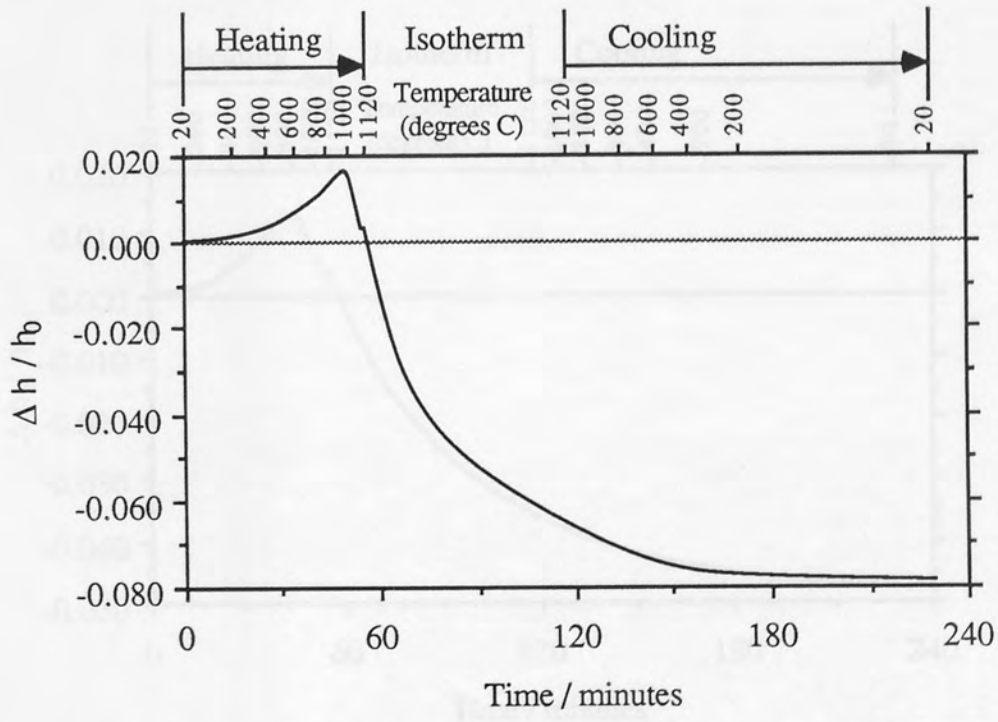

Figure B.7. Dimensional changes in Fe, 0.6P, 3.0Si (PNC60 base) compact during sintering cycle.

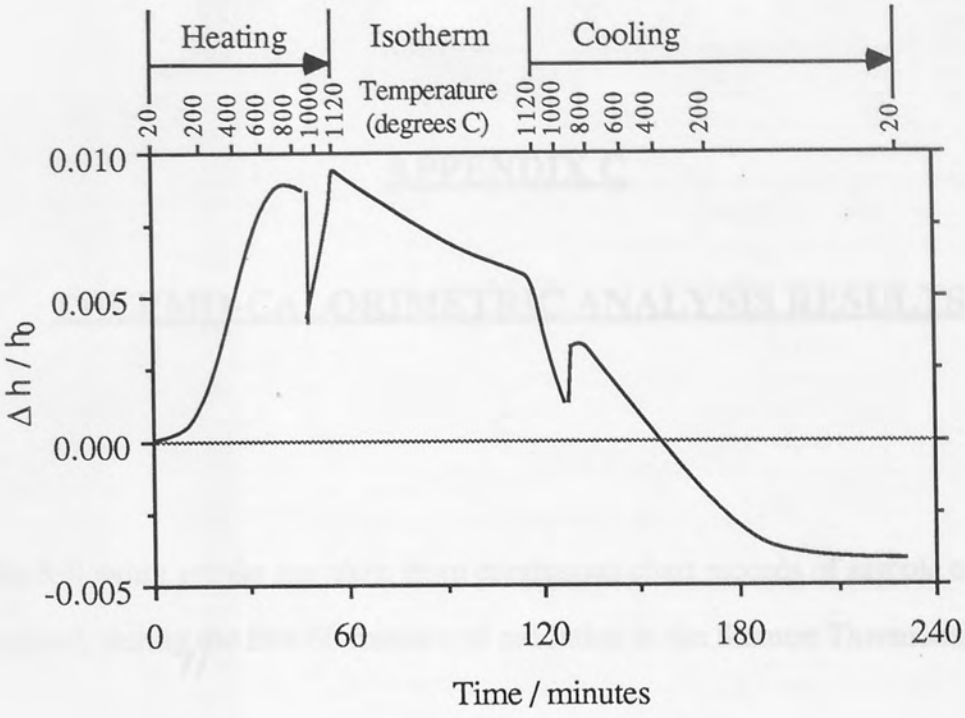

Figure B.8. Dimensional changes in Fe, 1.0Cu, 1.0Si (ASC100.29 base) compact during sintering cycle.

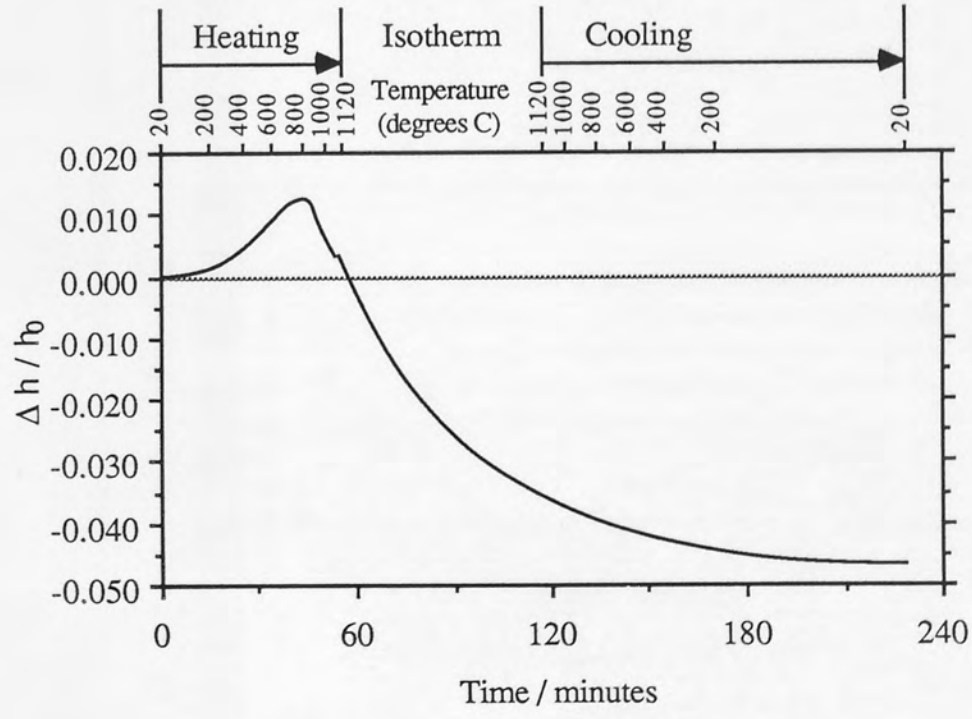

Figure B.9. Dimensional changes in Fe, 0.6P, 1.0Cu, 1.0Si (PNC60 base) compact during sintering cycle.

APPENDIX C

THERMO-CALORIMETRIC ANALYSIS RESULTS

The following graphs are taken from continuous chart records of sample core temperature, during the first 60 minutes of oxidation in the Stanton Thermobalance.

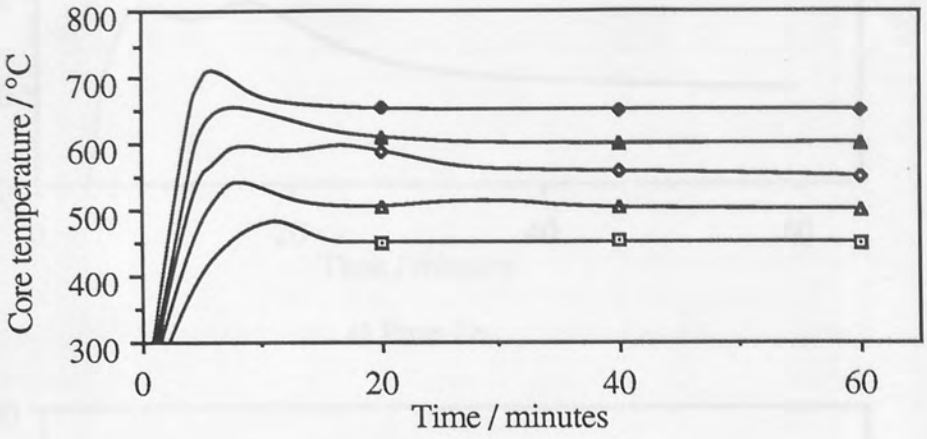

a) Compacted at 150MPa.

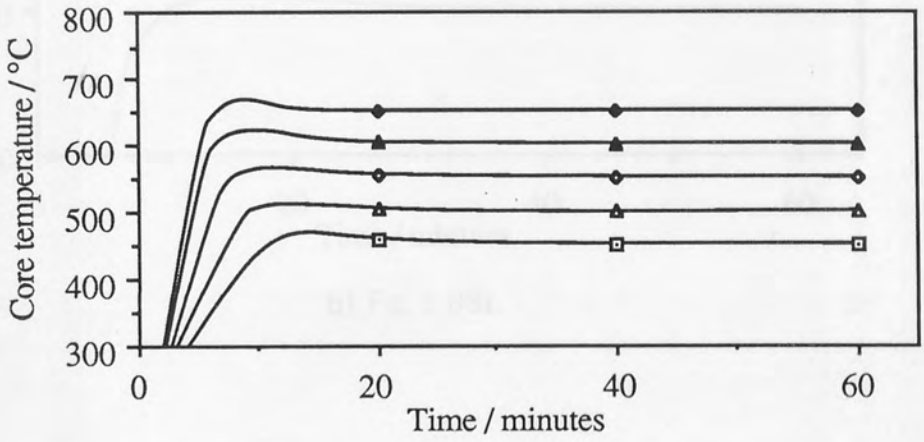

b) Comapcted at 350MPa

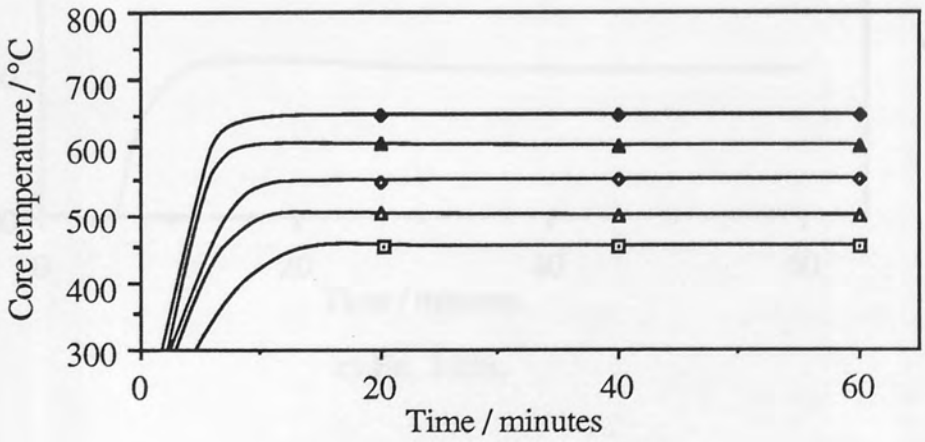

c) Compacted at 550MPa

KEY - Furnace temperature

▫ 450°C ▲ 500°C ◆ 550°C ▲ 600°C ◆ 650°C

Figure C.1. Core temperature of cylindrical ASC100.29 compacts during oxidation at 450°C to 650°C.

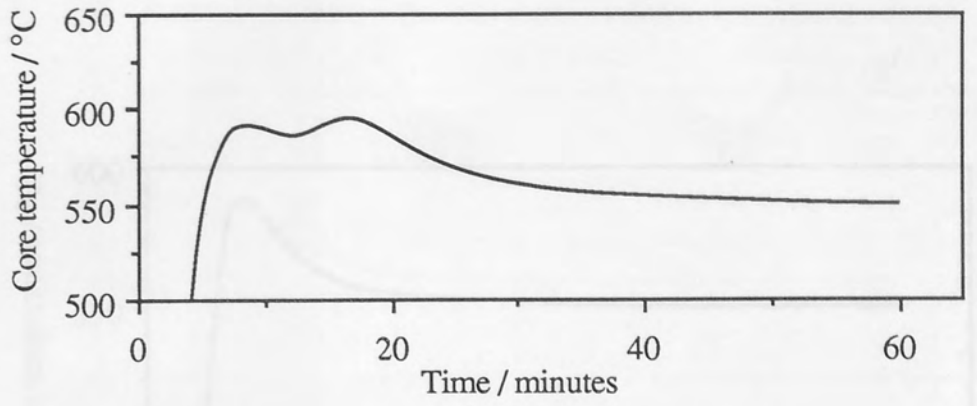

a) Pure Fe.

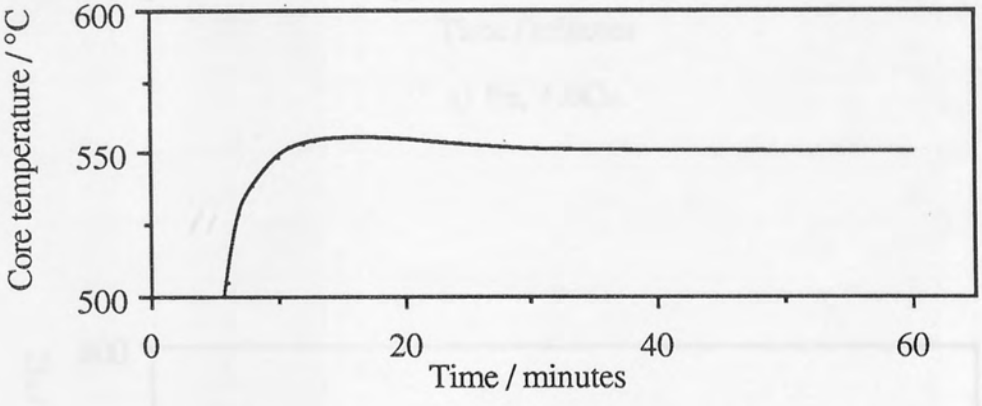

b) Fe, 1.0Si.

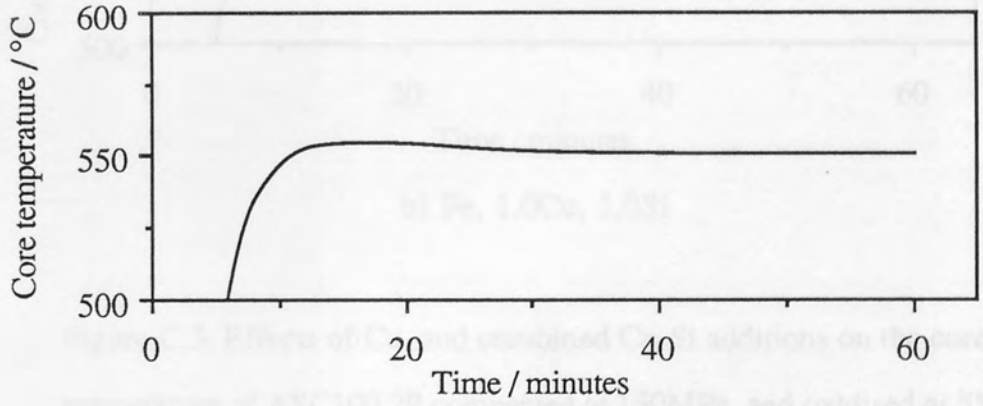

c) Fe, 3.0Si.

Figure C.2. Effects of Si additions on the core tempertaure of ASC100.29 compacted at 150MPa, and oxidised at 550°C.

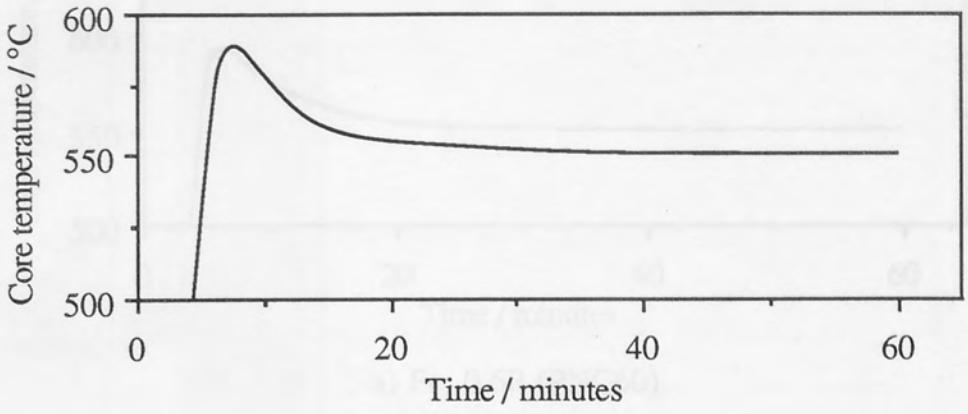

a) Fe, 1.0Cu.

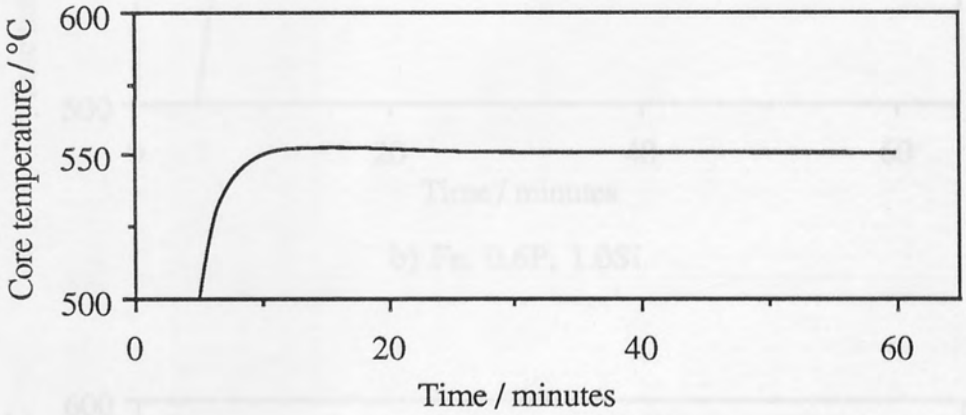

b) Fe, 1.0Cu, 1.0Si

Figure C.3. Effects of Cu, and combined Cu-Si additions on the core temperature of ASC100.29 compacted at 150MPa, and oxidised at 550°C.

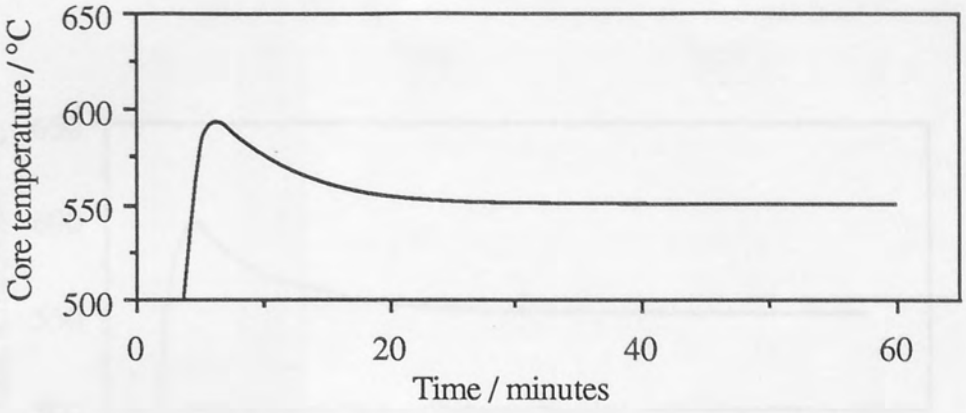

a) Fe, 0.6P (PNC60).

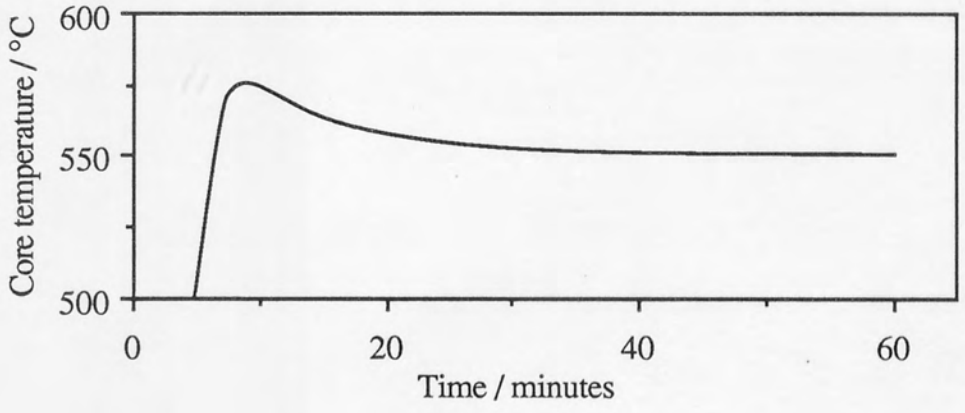

b) Fe, 0.6P, 1.0Si.

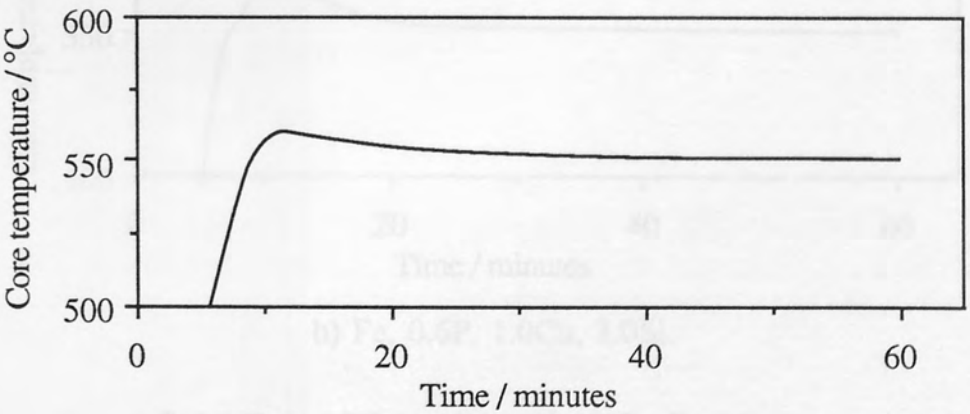

c) Fe, 0.6P, 3.0Si.

Figure C.4. Effects of Si additions on the core temperature of PNC60 compacted at 150MPa, and oxidised at 550°C.